Spectroscopic and Computational Chemistry Studies on Terpene Related Compounds

Thesis submitted for the degree of

Doctor of Philosophy

At the University of Leicester

By

Stephanie Marie Allpress, MChem (Leicester)

Department of Chemistry

University of Leicester

August 2015

UNIVERSITY OF
LEICESTER

STATEMENT OF ORIGINALITY

This work in this thesis was conducted by the author in the Department of Chemistry at the University of Chemistry during the period between October 2011 and August 2015 and is original unless otherwise acknowledged in the text or reference.

None of the work has been submitted for another degree at this or any other university.

Signed ——————————   Date ——————————

Abstract

The millimetre wave spectrum of linalool ($C_{10}H_{18}O$) was recorded and assigned in the region 48-63 GHz whilst the millimetre wave spectrum of verbenone ($C_{10}H_{14}O$) was recorded and assigned in the region 48-69 GHz. Calculations at the MP3/6-31++g(d,p) and B3LYP/aug-cc-pVTZ levels of theory on both molecules, identified around 60 conformers of linalool and a single conformer of verbenone. The lowest energy conformers of linalool and verbenone are in good agreement with the fitted rotational and centrifugal distortion constants. Calculations using the B3LYP functional with the 6-31G(d,p) and 6-31++G(d,p) basis sets investigated the barrier for internal rotation of the methyl groups to explore the potential splitting of the spectral lines. The barrier for internal rotation for linalool (305 cm^{-1}) resulted in the splitting of the spectral lines, whereas the barrier for internal rotation for verbenone (741 cm^{-1}) did not result in such splitting.

There have been no previous theoretical studies examining the products of the ozonolysis of terpinolene. The reaction mechanism for the ozonolysis of terpinolene has been explored at the B3LYP/6-31++G(d,p) and MPW1K/6-31++G(d,p) levels of theory. Single point calculations of the energy minima, transition state structures and possible reaction products were conducted at the MPW1K/6-31++G(3df,3dp) in order to improve the electronic energies.

Work was also carried out on a White-type multi-traversal absorption cell. The old 4 m cell possessed a leak, which inhibits it from being used to study terpinolene ozonolysis products over prolonged time periods. Alterations to improve this system were discussed and resulted in the design and construction of a new 64 m absorption cell in which to study these ozonolysis products.

Table of Contents

List of Tables

List of Figures

Chapter One

Introduction

1.1 Introduction

This work utilises both microwave spectroscopy and theoretical computational calculations to investigate the properties of two terpenes, linalool and verbenone. Calculations are also used in combination with infrared spectroscopy to explore the reaction products between the terpene terpinolene, and the atmospheric oxidant ozone. The introduction of these subjects is followed by chapters including detailed methodology and the theory used to help discuss the varying spectra and reaction analysis.

1.2 Tropospheric Chemistry

1.2.1 Terpenes

Terpenes are organic compounds that are produced by a variety of flora and fauna, and are directly emitted into the atmosphere, with lifetimes ranging from minutes to days. [1, 2] Terpenes are regarded as atmospherically important molecules as their estimated total annual global emission is between 825 and 1150 Tg C yr^{-1}[*], a vast quantity next to the comparably low <100 Tg C yr^{-1} emitted from anthropogenic sources[3, 4, 5], making biogenic emissions more important to atmospheric chemistry than anthropogenic sources.[6] Terpenes are derived from units of isoprene (C_5H_8) so have the general formula $(C_5H_8)_n$ and encompass several wide classes of compounds: hemiterpenes, made of a single isoprene unit (C_5H_8), monoterpenes, made of two isoprene units ($C_{10}H_{16}$) and sesquiterpenes, made of three isoprene units ($C_{15}H_{24}$).[7, 1] Also emitted into the atmosphere are terpenoids, which are similar to terpenes but include the addition of a functional group (such as –OH) and can be subdivided into categories, again based on the number of isoprene units present.

Monoterpenes are highly reactive and account for 11% of the total global emission of non-methane volatile organic compounds (NMVOC)[8], making them highly important to atmospheric chemistry. Monoterpenes, including isoprene, are believed to contribute ~55% of the total global terpene emission.[9] Their estimated global emission is between 30 and 127 Tg C yr^{-1} and have atmospheric lifetimes ranging from minutes to days depending on the individual monoterpene.[10]

---

[*] Tg C yr^{-1} – teragrams of carbon per year

Sesquiterpenes are of particular atmospheric importance due to their high reactivity towards ozone and thus their potential to form aerosol[11]; these can cool the global climate by reflecting the heat from the Sun back into space. They are thought to be emitted at approximately 15 Tg year^{-1} [12], which is low in comparison to monoterpenes. Whilst the atmospheric importance of sesquiterpenes stems from their rapid reactions with ozone, the speed of this reaction also accounts for the uncertainty in their total annual emission.[13]

As sesquiterpenes are abundantly present in ambient air due to vast emissions from vegetation, in future it is believed they should be considered when discussing secondary organic aerosol (SOA) formation from biogenic hydrocarbon sources.[3] Sesquiterpenes contribute to SOA production via oxidation reactions with O_3, OH radicals and NO_3 radicals, forming less volatile products (in comparison to the parent hydrocarbon) which readily condense onto particles already present in the atmosphere and produce SOA.[14, 15] Aerosols can influence atmospheric chemistry as their particles act as cloud condensation nuclei (CCN) upon which water droplets can condense and form cloud droplets. Increased build-up of cloud droplet would result in a wetter climate.

1.2.2 Atmospheric Oxidants

The photochemical oxidation of volatile organic compounds (VOC) is initiated by the common atmospheric oxidants: ozone (O_3), hydroxyl (OH) radicals and nitrate (NO_3) radicals, which play an important role in the chemistry of the lowest layer of the Earth's atmosphere (troposphere). Organic molecules will preferentially react with OH radicals during the day and NO_3 radicals during the night-time, when OH radicals are almost non-existent. The formation of OH radicals is dependent upon radiation from the Sun; solar radiation photolyses ozone to form oxygen atoms which then react with water to for OH radicals. At night-time there is no solar radiation in order to initiate this reaction sequence, causing the drop in OH radical concentration. The reaction with O_3 can occur throughout the day and night, and is believed to be a potential source of night-time OH radicals.[16]

In oxidation reactions involving O_3, OH radicals and NO_3 radicals and terpenes, the process is expected to proceed through the addition of the oxidant to the C=C double bond(s).[15] For terpenes that contain a single double bond, the first oxidation step is rate-limiting and the low volatility first-generation products form aerosols. For terpenes with multiple double bonds, the second oxidation step is rate-limiting and the growth of the secondary organic aerosols is resultant from the second-generation products.[17] These

compounds are also significantly decomposed by O_3, due to their highly unsaturated character.[18]

The high reactivity of OH radicals causes the lifetime of organic species, such as terpenes, to be between 30 minutes and 4 hours. This means that OH radicals are the controlling factor of many chemical processes in the troposphere. The global average concentration of OH radicals is between 10^5 and 10^6 molecules cm^{-3}, dependent upon natural atmospheric perturbations.[19] Peeters *et al.*[20] explore the addition of OH radicals to isoprene, they show that the OH radicals preferentially add to the lesser substituted end of the C=C double bond, forming OH-terpene radicals. Peeters *et al.*[20] then describe a further addition of O_2 to the second double C=C of isoprene; the stability of the resulting structure is dependent upon the hydrogen-bonding between the –OH and OO$^\bullet$ groups.[20]

Tropospheric sources of O_3 include the stratosphere, *in situ* photochemical production and reaction sinks.[18] High concentrations of ozone in the troposphere are damaging to plants and cause respiratory irritation in humans. The production of aerosols from the ozonolysis of VOCs has been recorded since the 1960's.[22] The structure of ozone has been widely reported - a bent C_{2v} structure with O-O bond distances of 1.28 Å and an angle of ~116°.[21, 23, 24] The oxidation reaction proceeds through the cycloaddition of the O_3 unit to the unsaturated C=C double bond to form a 5-membered ring, known as a primary ozonide (POZ). This POZ undergoes unimolecular decomposition to yield a Criegee intermediate (CI) and an aldehyde. The fate of the Criegee intermediate follows two paths: either a ring closure to form a dioxirane or a H-migration yielding a hydroperoxide, which further decomposes into OH and RCO radicals.[17]

1.3 Experimental and Theoretical Methods

1.3.1 Microwave Spectroscopy

Spectroscopy is an essential tool when developing an understanding of almost all compounds. Microwave spectroscopy observes the rotational transitions of molecules that have a non-zero electric dipole moment. Both emission and absorption type spectrometers are utilised, where the later monitors the intensity of the radiation after it has passed through a sample. The absorption type spectrometer in this investigation is combined with Stark modulation, which applies an electric field to a polar molecule causing a shift of the absorption frequencies due to the Stark effect, to improve the sensitivity of the

spectrometer. In this investigation the experimentally obtained spectra are matched to a variety of constants, enabling the assignment of the microwave spectra for the given molecules. Further details of the microwave spectroscopy methods used can be found in Chapter 2.

1.3.2 Infrared Spectroscopy

Infrared spectroscopy observes the vibrational transitions of molecules that experience a change in dipole moment during the vibrational motion. For a simple harmonic oscillator the selection rule for a vibrational transition is $\Delta v = \pm 1$. Infrared spectroscopy is used to determine which molecules are present in a given sample; the position of a peak is indicative of the molecular composition, including the identification of functional groups and the type of bonds present. In this investigation Fourier transform infrared (FTIR) spectroscopy would be utilised to follow the ozonolysis reaction of a terpene. More details of the infrared spectroscopy method used can be found in Chapter 2.

1.3.2.1 White Type Multipass Cell

A White type multipass system passes the radiation back and forth through the same sample volume a designated number of times. They are of particular use when only a small amount of sample is available or if the sample has a high boiling point. Rather than heating the cell, in a multipass system the radiation passes repeatedly through the same sample, offering an improved accuracy of the measurement. Such systems have previously been used to monitor trace atmospheric species. In this investigation the multipass system will be used in conjunction with an infrared spectrometer in order to monitor the ozonolysis reaction mechanism of the terpene terpinolene. Further details of the development of this system are discussed in Chapter 4.

1.3.3 Theoretical Study of Molecules

By understanding the principles of quantum mechanics a number of theoretical methods have been developed for predicting molecular properties of a variety of systems. The fundamental basis of these quantum mechanical techniques is founded upon the Schrödinger Wave Equation (SWE). It is used to describe the properties of molecular structure in quantum mechanical terms, thus providing a foundation for many of the quantum chemical calculation methods.

Such calculations can be divided into two categories: *ab initio* and semi-empirical. *Ab initio* techniques rely on first principles and do not use any empirical parameters. Conversely semi-empirical methods rely on a parameterisation, especially those that can fit theoretical data to the corresponding experimental observation. The use of these techniques can assist with the elucidation of any ambiguous experimental results.

With the use of modern computers, quantum chemical calculations allow for the accurate simulation of almost any system. Both *ab initio* and semi-empirical methods have been used in this investigation to optimise the geometry of a variety of terpene structures and analysis their harmonic vibrational frequencies. These vibrational frequencies play a key role when analysing ozone-terpene reaction schemes, as they help to differentiate between energy minima and transition state structures. Full details of the theoretical methods utilised in this investigation are presented in Chapter 3.

1.4 Thesis Aims and Contents

The first aim of this investigation is to analyse the proof of concept for microwave spectroscopy analysis of terpenes. Although microwave spectroscopy offers improved accuracy of spectra it does not possess the greatest sensitivity, therefore, this thesis looks to ascertain whether microwave spectroscopy is a suitable method for studying terpenes.

Other aims are to develop a new White type multipass system to be used in conjunction with an infrared spectrometer to monitor the ozonolysis reaction of terpenes. This multipass system will be used in conjunction with quantum chemical calculations to establish the reaction pathways for the ozonolysis of terpinolene.

The content of the remainder of this thesis is as follows. In Chapter 2, the fundamental concepts and experimental procedures of the microwave and infrared spectroscopic techniques used are discussed. In Chapter 3, the fundamentals of the quantum chemical calculations used are described. Chapter 4 discusses the development of a 64 m White type multipass cell to be used in conjunction with a Fourier transform infrared (FTIR) spectrometer. Chapters 5 and 6 focus on the theoretical studies of the terpenes linalool and verbenone as well as the microwave spectroscopic analysis of both terpenes. Chapter 7 discusses previous theoretical work examining the ozonolysis reactions of terpenes, and acts as a proof of concept for the theoretical examination of the ozonolysis of terpinolene detailed in Chapter 8.

1.5 References

1. A. Lee, A. H. Goldstein, M. D. Keywood, S. Gao, V. Varutbangkul, R. Bahreini, N. L. Ng, R. C. Flagan, J. H. Seinfeld, *Journal of Geophysical Research*, 2006, **111**, D07302.

2. A. Lee, A. H. Goldstein, M. J. H. Kroll, N. L. Ng, V. Varutbangkul, R. C. Flagan, J. H. Seinfeld, *Journal of Geophysical Research*, 2006, **111**, D17305.

3. T. Hoffmann, J. R. Odum, F. Bowman, D. Collins, D. Klockow, R. C. Flagan, J. H. Seinfeld, *Journal of Atmospheric Chemistry*, 1997, **26**, 189-222.

4. C. Amelynck, N. Schoon, T. Kuppens, P. Bultinck, E. Arijs, *International Journal of Mass Spectrometry*, 2005, **247**, 1-9.

5. R. Atkinson, J. Arey, *Atmospheric Environment,* 2003, **37**, S197-S219.

6. P. Dominguez-Taylor, L. G. Ruiz-Suarez, I. Rosas-Perez, J. M. Hernández-Solis, R. Steinbrecher, *Atmospheric Environment*, 2007, **41**, 2780-2790.

7. N. L. Ng, J. H. Kroll, M. D. Keywood, R. Bahreini, V. Varutbangkul, R. C. Flagan, J. H. Seinfeld, *Environmental Science and Technology*, 2006, **40**, 2283-2297.

8. E. Martínez, B. Cabanas, A. Aranda, P. Martín, S. Salgado, *Journal of Atmospheric Chemistry*, 1999, **33**, 265-282.

9. J. Zhao, R. Zhang, *Advances in Quantum Chemistry, Vol 55: Applications of Theoretical Methods to Atmospheric Science*, 2008, **55**, 177-213.

10. J. Rimetz-Planchon, F. Dhooghe, N. Schoon, F. Vanhaecke, C. Amelynck, *Rapid Communications in Mass Spectrometry*, 2011, **25**, 647-654.

11. R. Winterhalter, F. Herrmann, B. Kanawati, T. L. Nguyen, J. Peeters, L. Vereecken, G. K. Moortgat, *Physical Chemistry Chemical Physcis*, 2009, **11**, 4152-4172.

12. T. L. Nguyen, R. Winterhalter, G. Moortgat, B. Kanawati, J. Peeters, L. Vereecken, *Physical Chemistry Chemical Physcis*, 2009, **11**, 4173-4183.

13. M. Jaoui, S. Leungsakul, R. M. Kamens, *Journal of Atmospheric Chemistry*, 2003, **45**, 261-287.

14. M. Jaoui, M. Lewandowski, T. E. Kleindienst, J. H. Offenberg, E. O. Edney, *Geophysical Research Letters*, 2007, **34**, L05816.

15. Y. Shu, R. Atkinson, *Journal of Geophysical Research*, 1995, **100**, 7275-7281.

16. V. G. Khamaganov, R. A. Hites, *Journal of Physical Chemistry A*, 2001, **105**, 815-822.

17. D. M. Bakalyar, J. V. James, C. C. Wang, *Applied Optics*, 1982, **21**, 2901-2905.

18. B. R. J. Muhyedeen, *European Journal of Scientific Research*, 2007, **16**, 490-505.

19. F. W. Went, *Nature*, 1960, **187**, 641-643.

20. J. Peeters, T. L. Nguyen, L. Vereecken, *Physcial Chemistry Chemical Physics*, 2009, **11**, 5935-5939

21. B. Flemming, P. T. Wolczanski, R. Hoffmann, *Journal of American Chemical Society*, 2006, **127**, 1278-1285.

22. P. G. Burton, *Journal of Chemical Physics*, 1979, **71**, 961-972.

23. D. Zhang, R. Zhang, *Journal of American Chemical Society*, 2002, **124**, 2692-2703.

24. A. Calogirou, B. R. Larsen, D. Kotzias, *Atmospheric Environment*, 1999, **33**, 1423-1439.

Chapter Two

Rotational and Vibrational Spectroscopy

2.1 Introduction

2.1.1 Molecular Spectroscopy

Simplistically, spectroscopy is the study of how electromagnetic radiation interacts with matter as a function of frequency or wavelength. Spectroscopy can be utilised through either emission or absorption processes; proceeding via radiation passing through a sample with the intensity monitored by a detector; if the sample interacts with the radiation then characteristic peaks appear. This spectrum measures the variation in intensity of the sample's response to the radiation, as the frequency (or wavelength) of the radiation is scanned.

Spectroscopists study the interactions between the sample and the radiation as discrete or quantised values. In order to examine the quantised energy levels of a molecule, the energy of stationary states (where energy is independent of time) are represented by a Hamiltonian. These are complicated operators which symbolise measurable properties, which then act upon a given wavefunction (a function of spatial and time-based coordinates).

In order to better understand the processes involved in molecular spectroscopy, we must consider molecules as a collection of charged particles, which move under the influence of electrostatic forces. Charged particles within the nuclei are comprised of the electrons and the nuclei, which are subjected to forces of similar magnitude. As molecular nuclei are considerably larger than an electron, they move much more slowly, so we assume that the nuclei are fixed with rapid motion of electrons around them. This Born-Oppenheimer approximation, simplifies the Schrödinger equation by reducing the number of coordinates making the determination of energy levels easier.[1]
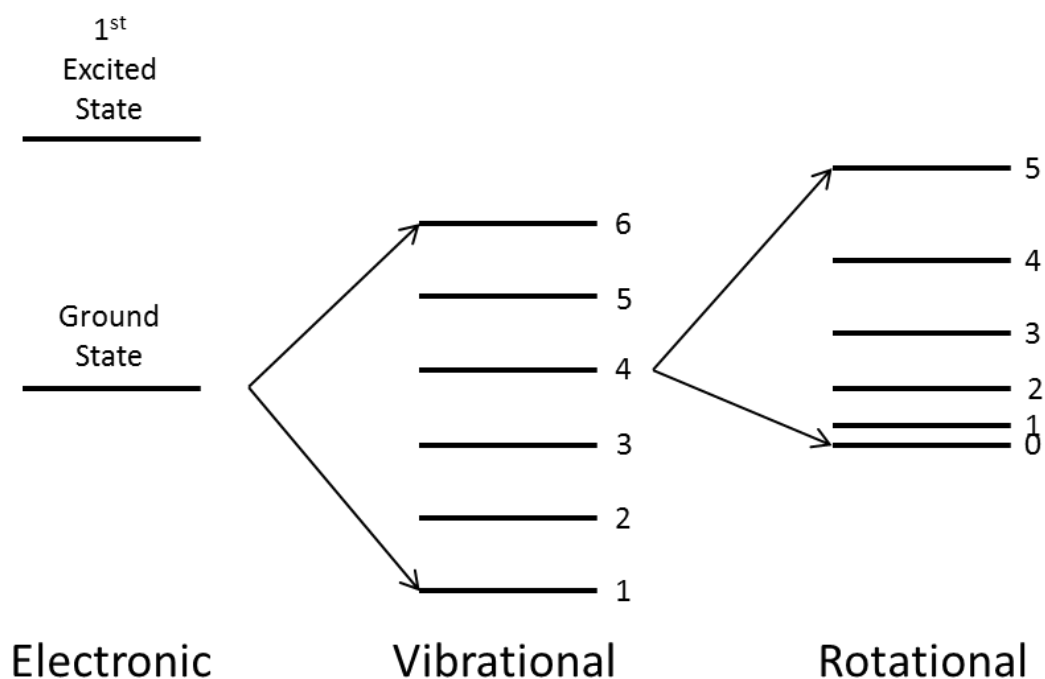
Figure 2.1: Arrangement of the energy levels for a diatomic molecule, showing the Born-Oppenheimer approximation

As can be seen in Figure 2.1 each electronic state supports a set of vibrational energy levels which in turn supports a set of rotational energy levels. The separation between the electronic states is larger than those between the vibrational energy levels which are in turn larger than the separation between the rotational energy levels. The total energy of the system takes into account the energy from all three states

$$E_{tot} = E_{el} + E_{vib} + E_{rot} \tag{2.1}$$

where,

$$E_{el} \gg E_{vib} \gg E_{rot} \tag{2.2}$$

In order for a spectroscopic transition to occur a molecule must change from one quantum state to another. There are a variety of selection rules that must be considered depending on the nature of the spectroscopic transition: for an electronic transition the selection rule is $\Delta\Omega = 0, \pm1$, where Ω is the total orbital and spin angular momentum quantum number. An infrared active vibrational transition requires a change in dipole moment during the vibrational motion and for a simple harmonic oscillator the selection rule is $\Delta v = \pm1$; For a pure rotational transition the molecule requires a non-zero electric dipole moment and

the selection rules depending on whether a linear, spherical, symmetric or asymmetric rotor are being considered.[1]

2.1.2 Classification of Molecules

In relation to spectroscopic techniques, molecules can be categorised into four classes depending on their moments of inertia (the measure of a molecule's resistance to rotate). The class of the molecule is conditional on the spatial context of the nuclei, which are taken to be point masses (m_i) with coordinates x_i, y_i and z_i in relation to any set of Cartesian axes. The origin of these axes is set to the molecule's centre of mass and the axes fixed relative to the nuclei so that as the molecule rotates, so do the axes. The moments of inertia for these so called molecule-fixed axes are given by[2]

$$I_x = \sum_i m_i(y_i^2 + z_i^2)$$

$$I_y = \sum_i m_i(x_i^2 + z_i^2) \tag{2.3}$$

$$I_z = \sum_i m_i(x_i^2 + y_i^2)$$

where m_i is the mass of a given nucleus. Considering the molecule as three-dimensional structure, the products of inertia (I_{xy}, I_{yz} and I_{xz}) can be represented using a momental ellipsoid, where a and b, and b and c, are the major and minor axes in the xy- and yz-planes, respectively. The axes a, b and c are known as the principal inertial axes and I_a, I_b and I_c the principal moments of inertia, for which I_a is the minimum moment of inertia and I_c is the maximum, with an axis perpendicular to that of I_a. The axis of I_b must be perpendicular to those of both I_a and I_c.[2]

2.1.2.1 Linear Molecules

Linear molecules, such as HCN, have two degenerate modes of rotation, $I_c = I_b$ and $I_a = 0$. As I_a is the minimum moment of inertia we know that

$$I_c = I_b > I_a = 0 \tag{2.4}$$

as the distance of nuclei from the molecular axis is zero, $I_a = 0$. As the two rotational modes are degenerate they are indistinguishable from one another so only a single

rotational quantum number, J, is required to describe the rotation of the molecule. For polyatomic linear molecules Equation 2.5 shows the quantised energy levels for a rigid rotor

$$E_r = h^2 J \frac{(J+1)}{(8\pi^2 I)} \tag{2.5}$$

where h is Planck's constant, J is the rotational quantum number and I is the moment of inertia. Experimentally spectroscopists measure the frequency or the wavenumber of a transition rather than the energy of a transition between energy levels (ΔE). Equation 2.6 shows how ΔE is proportional to the wavenumber ($\tilde{\nu}$)

$$\Delta E = hc\tilde{\nu} \tag{2.6}$$

Taking this into consideration it is advantageous to convert Equation 2.5 into a term value expression with the units of wavenumbers (or frequency)

$$F(J) = \frac{E_r}{hc} = hJ \frac{(J+1)}{(8\pi^2 cI)} \tag{2.7}$$

where h is Planck's constant, J is the rotational quantum number, c is the speed of light and I is the moment of inertia. The rotational constant B, is given by

$$B = \frac{h}{8\pi^2 I} \tag{2.8}$$

when expressed as a frequency. B can also be expressed in wavenumbers by dividing by the speed of light (c). For diatomic molecules the moment of inertia is equal to the reduced mass (μ) multiplied by the square of the bond length (r)

$$I = \mu r^2 \tag{2.9}$$

The reduced mass is calculated by dividing the product of the masses by the summation of the two masses

$$\mu = \frac{m_1 m_2}{m_1 + m_2} \tag{2.10}$$

Taking all of this into consideration Equation 2.7 can be simplified to read as[2]

$$F(J) = BJ(J+1) \tag{2.11}$$

Rotational selection rules dictating the conditions for an allowed transition are as follows

1. The molecule must have a permanent dipole moment
2. Selection rule $\Delta J = \pm 1$. The frequency (or wavenumber) difference between the upper (J') and the lower (J'') quantum states is written as $F(J') - F(J'') = F(J+1) - F(J) = 2B(J+1)$, therefore allowed transitions are separated by 2B
3. $\Delta M_J = 0, \pm 1$, which is an important selection rule if the molecule is present within either an electric or magnetic field

2.1.2.2 Symmetric Rotors

Symmetric rotors are molecules which contain two equal moments of inertia, which can be further split into two sub-categories, where the third is either greater or smaller than the equal moments of inertia. If the unequal moment of inertia is less than the other two

$$I_c = I_b > I_a \qquad (2.12)$$

then the molecule is known as a prolate symmetric rotor and is said to be cigar shaped. In the case of methyl iodide (CH_3I) the heavier iodine atom lies on the a-axis and therefore makes no contribution towards I_a (as the moment of inertia is dependent upon the distance of the atom (i) from the axis) making it clear that I_a is smaller. The other moments of inertia, I_c and I_b, are equal as they have a circular cross section perpendicular to the a-axis.[2]

However, if the unequal moment of inertia is greater than the other two

$$I_c > I_b = I_a \qquad (2.13)$$

then the molecule is known as a oblate symmetric rotor and is said to have a discus shape. In the cases of the square planar $[PtCl_4]^{2-}$ and benzene it is clear that the a- and b- axes, which are in the plane of the molecule, produce equal moments of inertia (due to the C_4 and C_6 axes, respectively) therefore I_c must be larger than both of them.

As these molecules contain two axes that possess equal moments of inertia, symmetric rotors are described by two independent rotational quantum numbers. J is the total angular momentum quantum number for the molecule, for which the selection rule is $\Delta J = \pm 1$, whilst K relates to the to the angular momentum of the axis that has a different moment of inertia (I_a for a prolate rotor and I_c for an oblate rotor). As K relates to the axis through

which the molecule is symmetric, there is no perpendicular dipole moment (which is required in order to observe a rotational transition) thus there is no torque along this axis, so the selection rule is $\Delta K = 0$.[2]

2.1.2.3 Asymmetric Rotors

The vast majority of molecules preside in the asymmetric rotor category as they contain no equal principal moments of inertia.

$$I_c \neq I_b \neq I_a \tag{2.14}$$

However, the majority of asymmetric rotors have two moments of inertia that are nearly equal, splitting this group into two sub-categories, where the third moment of inertia is either greater or smaller than the almost equal moments of inertia. If the larger moments of inertia are nearly equal

$$I_c \approx I_b > I_a \tag{2.15}$$

then the molecule is known as a prolate near-symmetric rotor. Positioning of the heavier atoms makes I_a smaller in comparison to I_c and I_b. However, if the smaller moments of inertia are nearly equal

$$I_c > I_b \approx I_a \tag{2.16}$$

then the molecule is known as an oblate near-symmetric rotor. As these molecules possess no equal moments of inertia, asymmetric rotors are described using three rotational quantum numbers. Again J is used to describe the total angular momentum of the molecule for which the selection rule is $\Delta J = 0, \pm 1$. Transitions where $\Delta J = -1$ are referred to as P-branches, where $\Delta J = 0$ are referred to as Q-branches and where $\Delta J = +1$ are referred to as R-branches. Asymmetric rotors are molecules in which the total angular momentum has no constant component along any axis, so the selection rule for symmetric tops of $\Delta K = 0$ loses meaning, so new quantum numbers K_a and K_c are introduced. K_a represents the K value of the prolate near-symmetric rotor, while K_c represents the K value of the oblate near-symmetric rotor.[2, 3] There are a variety of permitted transitions with regards to K_a and K_c (Table 2.1), that can be classified according to which component of the dipole moment make the transition allowed.[2]

Table 2.1: Selection rules regarding the rotational quantum numbers K_a and K_c

Dipole Component	ΔK_a	ΔK_c
$\mu_a \neq 0$	$0, \pm 2 \ldots$	$\pm 1, \pm 3 \ldots$
$\mu_b \neq 0$	$\pm 1, \pm 3 \ldots$	$\pm 1, \pm 3 \ldots$
$\mu_c \neq 0$	$\pm 1, \pm 3 \ldots$	$0, \pm 2 \ldots$

Note: $\mu_a \neq 0$ is along the axis of smaller moment of inertia, $\mu_b \neq 0$ is along the axis of intermediate moment of inertia and $\mu_c \neq 0$ is along the axis of greatest moment of inertia[4]

Ray's asymmetry parameter[5] (κ), is used to measure the degree to which a molecule deviates from being a symmetric rotor.

$$\kappa = \frac{(2B - A - C)}{(A - C)} \tag{2.17}$$

Using the rotational constants of the given molecule the asymmetry parameter (κ) is calculated so that $-1 \leq \kappa \leq 1$, in order to determine whether the molecule is a prolate or oblate near-symmetric rotor and thus which representation (Table 2.2) is required in order to assign the microwave spectra.

Table 2.2: The ordering of inertial axes *a*, *b*, *c* with respect to Cartesian axes *x*, *y*, *z* for the various different representations of the Hamiltonian operator for asymmetric top molecules[3]

	$\mathbf{I^r}$	$\mathbf{II^r}$	$\mathbf{III^r}$	$\mathbf{I^l}$	$\mathbf{II^l}$	$\mathbf{III^l}$
x	*b*	*c*	*a*	*c*	*a*	*b*
y	*c*	*a*	*b*	*b*	*c*	*a*
z	*a*	*b*	*c*	*a*	*b*	*c*

I^r to III^r identifies *a*, *b*, *c* with *x*, *y*, *z* with three permutations of right-handed axes, whereas I^l to III^l identify them using left handed axes.[3] When the asymmetry parameter is approximately -1 then $C \approx B$ meaning that a prolate near-symmetric rotor is being considered and the I^r representation is used. When the asymmetry parameter is approximately 1 then $B \approx A$ meaning that a oblate near-symmetric rotor is being considered and the III^l representation is used.

2.1.2.4 Spherical Rotors

The final classification for molecules are the highly symmetric molecules, such as those belonging to the tetrahedral or octahedral point groups (CH_4 or SF_6) which have three equal moments of inertia, $I_a = I_b = I_c$.[2]

2.1.3. Centrifugal Distortion

The above classifications presume the molecule to be rigid rotors (a mechanical model used to explain a rotating system), which in reality is not the case. During the rotation of a given molecule its geometry slightly distorts, due to the centrifugal forces (those operating away from the molecule's centre of mass) acting upon it. This distortion of the molecular geometry is considered through the use of centrifugal distortion constants, which are of the order of a few kHz, depending on the rigidity of the molecule and the strength of the bonds, making them approximately six orders of magnitude smaller than the rotational constants discussed previously. In order to obtain these centrifugal distortion constants from a microwave spectrum of an asymmetric top, Watson's A or S reductions[6] could be used, depending on how close to a symmetric rotor the molecule is. The Hamiltonian for an asymmetric top sums the Hamiltonians for the rigid top (H_r) and the centrifugal distortion (H_d)

$$\hat{H}^{(a)} = H_r + H_d^{(4)} \tag{2.18}$$

where

$$H_d^{(4)} = -\Delta_J P^4 - \Delta_{JK} P^2 P_a^2$$

$$-\Delta_K P_a^4 - 2\delta_J P^2 (P_b^2 - P_c^2) - \delta_K$$

$$x \left[P_a^2 (P_b^2 - P_c^2) + (P_b^2 - P_c^2) P_a^2 \right] \tag{2.19}$$

where P_a, P_b and P_c are the angular momenta about the axes a, b and c. In order to fully describe and reproduce the microwave spectrum of a prolate asymmetric top, five centrifugal distortion constants, found in Equation 2.19 are required: Δ_J, Δ_K, Δ_{JK}, δ_J and δ_K. Higher order sextic constants also exist, however they are not required for lower J values.

2.1.4 Internal Rotation

Even after classification of the molecule into one of the four categories and taking into account the centrifugal distortion, there is another important phenomenon that has the ability to greatly affect the microwave spectrum of a given molecule – the internal rotation of methyl groups.[7-10] When a methyl group rotates about a single bond, through which it is bound to the rest of the molecule, it can result in complications in the spectrum as it leads to splitting of the rotational energy levels. However, these complications have the potential to be useful, as they could assist with the determination of the internal rotation barrier height and with the differentiation between different conformers.[11] The kinetic energy for this rotation can be written as

$$T = \frac{1}{2}\vec{\omega}^\dagger I \vec{\omega} \qquad (2.20)$$

where $\vec{\omega}$ is the generalised angular velocity vector and ω_a, ω_b, ω_c are the angular velocities about to the inertial axes

$$\vec{\omega} = \begin{pmatrix} \omega_a \\ \omega_b \\ \omega_c \\ \dot{\alpha} \end{pmatrix} \qquad (2.21)$$

$\vec{\omega}^\dagger$ is the corresponding transposed vector

$$\vec{\omega}^\dagger = (\omega_a, \omega_b, \omega_c, \dot{\alpha}) \qquad (2.22)$$

and $\dot{\alpha}$ is the angular velocity of the internal rotor. The moment of inertia tensor is increased to four dimensions to take into account the moment of inertia and internal rotation angle of the methyl rotor with regards to the principal axes

$$I = \begin{pmatrix} I_a & 0 & 0 & \lambda_a I_a \\ 0 & I_b & 0 & \lambda_b I_a \\ 0 & 0 & I_c & \lambda_c I_a \\ \lambda_a I_a & \lambda_b I_a & \lambda_c I_a & I_a \end{pmatrix} \qquad (2.23)$$

The Hamiltonian function is described as

$$H = \frac{1}{2}\vec{P}^\dagger I^{-1}\vec{P} + V \qquad (2.24)$$

with the angular momentum

$$\vec{P}^\dagger = \begin{pmatrix} P_a \\ P_b \\ P_c \\ p \end{pmatrix} \tag{2.25}$$

and the transposed momentum

$$\vec{P}^\dagger = (P_a, \ P_b, P_c, p) \tag{2.26}$$

where p is the angular momentum of the internal rotor

The potential energy for this rotation is written as a periodic function of the rotation angle and expressed as a Fourier expansion[2, 4]

$$V(\varphi) = \frac{1}{2} \sum_n V_n \left(1 - \cos n\varphi\right) \tag{2.27}$$

where φ is the angle of rotation, V_n is the energy of the internal torsional barrier and n is an integer, which in this instance is 3, as the torsional motion for a methyl group produces three maxima. Besides the magnitude of the internal rotation barrier, the splitting of the spectral lines can provide information of the molecular geometry as the internal axis rotation and principle axes of inertia are parameterised in Equation 2.23.

Three different instances of internal methyl rotation can be characterised; a negligible barrier for internal rotation would result in the methyl group being treated as a free rotor, whereas an infinite barrier would act as a harmonic torsional oscillator producing three isolated oscillators (Figure 2.2a) about the single bond where the rotation is occurring. Each of these oscillators is located at a minimum as tunnelling between them is forbidden, so the energy levels are threefold degenerate.

The final scenario is an internal rotation that is hindered by a finite periodic potential with an intermediate barrier height. Whether describing an infinite or an intermediate barrier, the rotation of a methyl rotor results in three equal minima (due to the threefold symmetry possessed by a methyl group); however, if the intermediate barrier is low enough, then tunnelling becomes possible resulting in the partial lifting of the degeneracy of the energy levels. This gives states with different symmetries one non-degenerate A-species and a degenerate pair with E- symmetry as seen in Figure 2.2b.[11] The A level is the lower energy level.
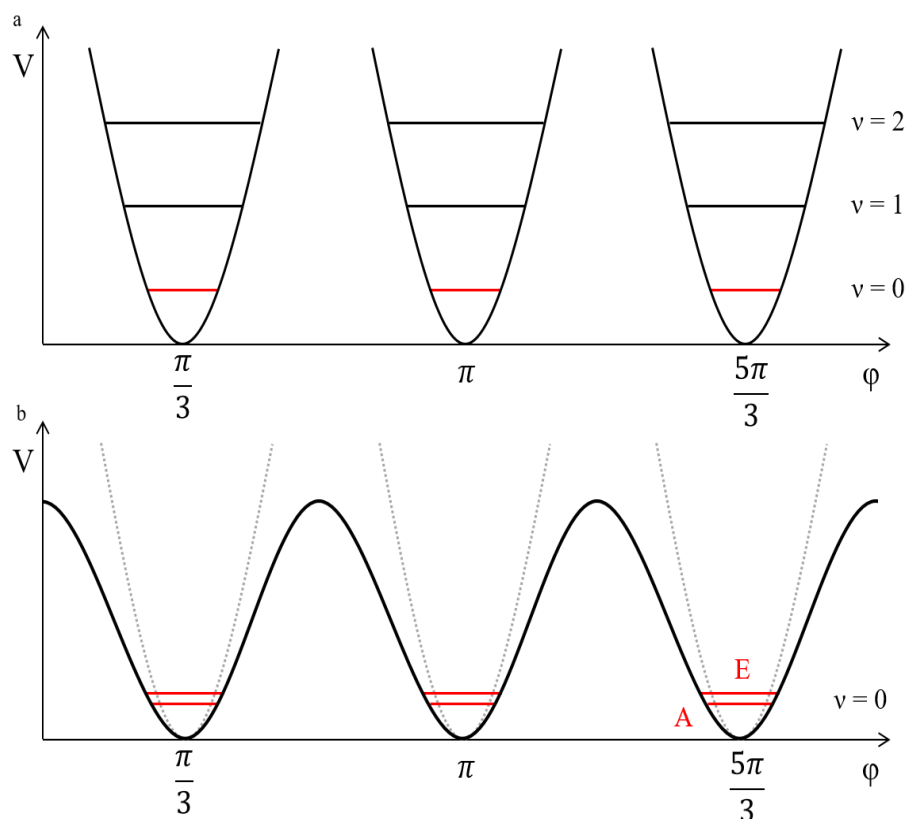
Figure 2.2: a) Isolated harmonic oscillators with threefold degenerate energy levels, resulting from an infinite barrier for internal rotation, b) Finite, intermediate barrier partially lifting the energy levels' degeneracy of the ground state resulting in a tunnelling effect resulting in *A*- and *E*-species[11]

Coriolis interactions result in a slight difference in the rotational levels of the *A*- and *E*-species as can be seen in Figure 2.2b. These Coriolis interactions are taken from terms in the Hamiltonian that contain both the angular momentum operator of the internal rotor ($\hat{p}$) and a component of the overall angular momentum operator ($\hat{p}_a, \hat{p}_b \ or \ \hat{p}_c$), that are obtained through the evaluation of Equation 2.24. Direct transitions between the *A*- and *E*- states are forbidden.[11] So far this finite barrier has merely been described as intermediate in size, but by assigning the transitions belonging to both the *A*- and *E*-species in the microwave spectrum, the accurate determination of this rotational barrier can be obtained.[11]

Should this internal rotation be determined to possess a sufficiently low barrier then this would cause the splitting observed in a microwave spectrum. In more general terms the magnitude of the rotational barrier and the resulting splitting (Figure 2.3) are inversely

proportional, so the lower the internal rotation barrier the larger the splitting observed in the microwave spectrum.[11]
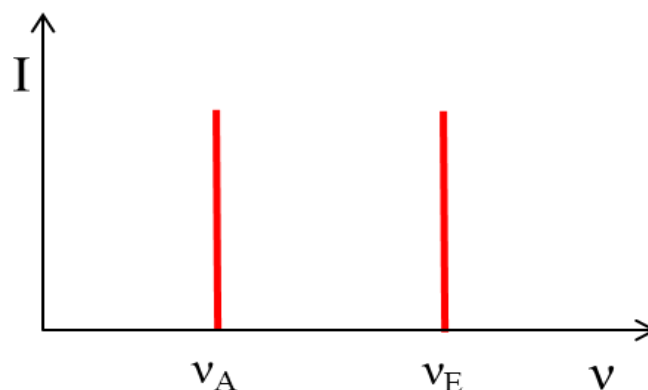
Figure 2.3: Resulting A-E doublet in the rotational spectrum

It is important to note that any calculated barrier height for internal rotation is highly dependent on the method and basis set used and so cannot always be accurately calculated. However, Mouhib [10] describes general rules of thumb to help predict the barrier heights: for an ester the alcohol group is expected to have a rotation barrier of ~400 cm^{-1}, whereas the acid group has ~100 cm^{-1} barrier; methyl rotation in a ketone is expected to have a barrier of ~180 cm^{-1}; finally for alkenes a methyl rotor in the *trans*-position has a rotational barrier of ~700 cm^{-1} and a methyl in the *cis*-position has a lower barrier of ~400 cm^{-1}. Theoretical predictions of the internal rotation barrier height are useful as they give an indication as to whether splitting of the spectral lines would be expected; if the theoretical barrier is established to be >900 cm^{-1}, then such splitting would not be expected to be observed, especially if using molecular beam experiments.[11]

2.2 Rotational Spectroscopy

2.2.1 Absorption Type Microwave Spectrometers

Most traditional absorption type spectrometers comprise of a coherent microwave source, which produces radiation that passes through an absorption cell, usually a waveguide of a couple of meters in length[12], containing the gas of interest before reaching a detector and a spectrum is recorded.[11, 13]

These systems are simple and convenient as long as the absorption lines are strong; however, many lines are weak even with long waveguides and as most gases have absorption coefficients of between 10^{-5} to 10^{-12} cm^{-1}. The sensitivity of these

spectrometers is very low. Other factors degrading the overall sensitivity of absorption spectrometers are: random fluctuations of power caused by noise resulting from current flowing in the detector crystal, variations in the oscillator output and noise in the amplifying circuit; systematic variation of power with the oscillator frequency causes variable oscillator power as a function of frequency and loss of signal power as the microwave signal is converted into a lower-frequency signal by the detector. The intensity of individual spectral lines is primarily dependent on the number of molecules which exist in the energy level that gives rise to that line.
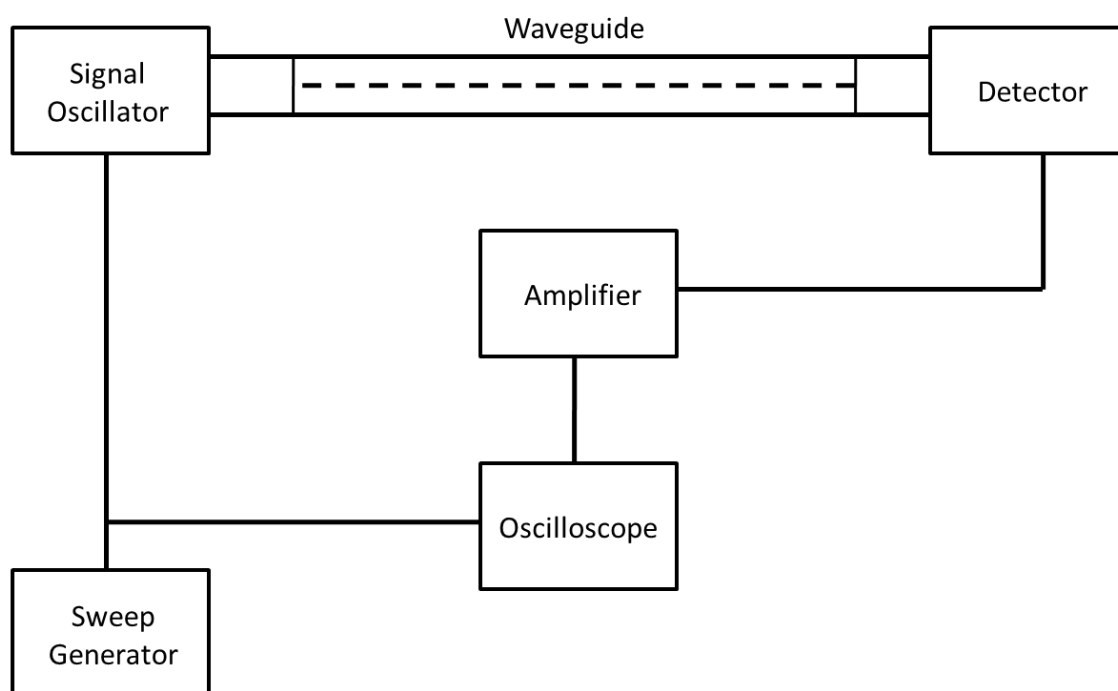
Figure 2.4: A traditional absorption type spectrometer[13]

2.2.1.1 Stark Modulation

In order to improve the sensitivity a modulation technique needs to be included. Introduced by Hughes and Wilson in 1947[14], Stark modulation applies an electric field to a polar molecule causing a shift of the absorption frequencies due to the Stark effect. Chantry describes the Stark effect by imagining a spectrometer where the gas is pumped out suddenly and then reintroduced instantaneously. The detector only sees the variation in absorption of the gas. In practice, a gas cannot be siphoned in this manner at a sufficient rate, so an electric field is applied to the gas.[15] When an electric field is applied to an electric dipole moment (a requirement for rotational transitions) torque is applied by the electric field changing the rotational motion[1], thus displacing the rotational energy levels

and changing the absorption frequencies.[13, 15] By switching the field in-and-out of coincidence with the beam frequency you can mimic the rapid removal and reintroduction of the gas.

Stark modulation is by no means perfect; firstly the modulating field used must be larger than the line width of the spectra. Spectra could contain misleading artefacts, known as Stark lobes that lie where an absorption line appears. Although comparatively weak, Stark lobes and an inappropriate modulating field could both result in overlap with the true absorption lines resulting in distortion of the peaks, a decrease in their intensity or an asymmetric profile.[13, 15]

2.2.1.2 Stark Modulated, Continuous Jet Millimetre Wave Absorption Spectroscopy

During the investigations of the terpenes linalool and verbenone (Chapters 5 and 6) a Stark modulated, continuous jet millimetre wave absorption system, located at Monash University in Victoria, Australia, was used in order to record their microwave spectra [16].
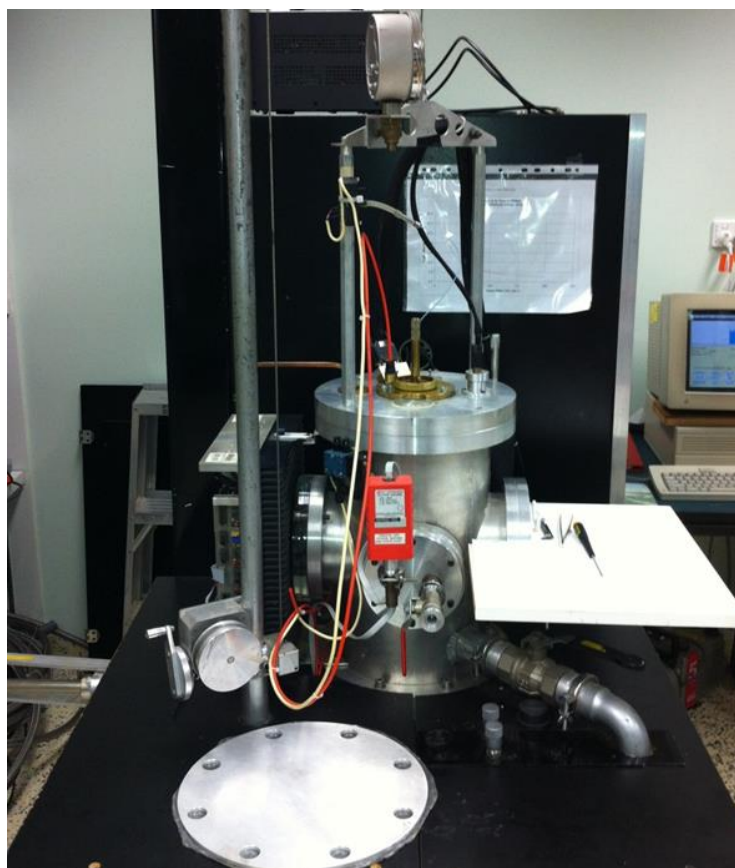
Figure 2.5: The Stark modulated, continuous jet millimetre wave absorption spectrometer, located at Monash University, Victoria, Australia

This instrument uses a solid state sweep oscillator, rather than a klystron (a specialised linear-beam vacuum tube that is used to amplify microwave frequencies to produce a low-power reference signals as well as high-power carrier waves[13]), as it enables an extended frequency range to be recorded with improved tuning ability.

The sample, encased in a small vial, sits inside a small bulb which is located below the central mount atop the spectrometer. The sample is entrained in hot argon at ~30 kPa, which is introduced into the system via the red tube (Figure 2.5 and 2.6). The argon-terpene mixture enters the spectrometer via a 350 μm diameter pinhole nozzle, which is heated to 10 °C higher than the vaporisation temperature of the given terpene. Under these conditions the rotational temperature of the molecular beam is *ca.* 10 K and no evidence of thermal decomposition is observed.
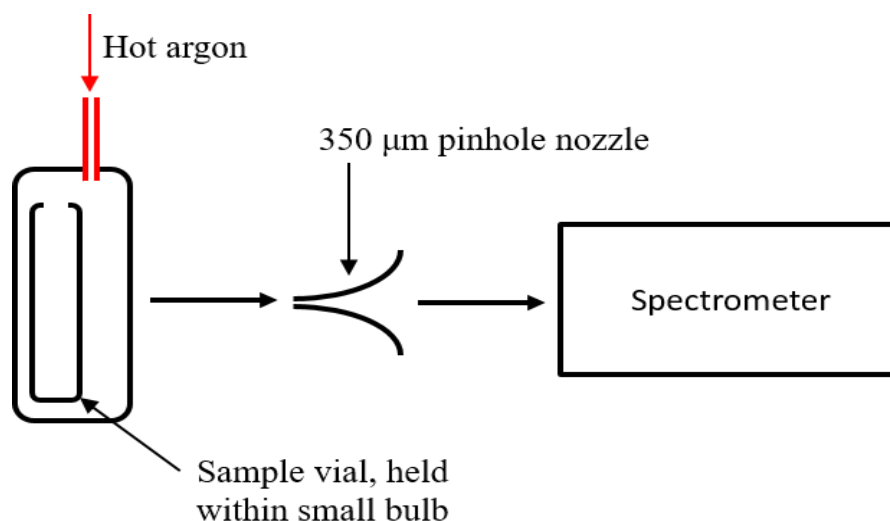
Figure 2.6: Diagram of sample entry mechanism for the Stark modulated, continuous jet millimetre wave absorption spectrometer, located at Monash University, Victoria, Australia

The Stark modulation in this system is provided at 33 kHz, using plates at *ca.* 3.5 cm apart. Initially the electric field, used to cause the torque on the electric dipole moment and thus altering the molecule's rotational spectrum, was set to 2000 V cm^{-1}, in order to maximise the Stark modulation. However, electric fields as low as 15 V cm^{-1} were used in order to investigate the resultant Stark effect (the shifting and splitting of the spectral lines) to ascertain which electric field conditions best recorded the microwave spectrum of a given terpene, as explained in Chapters 7 and 8.

Firstly a low resolution search spectrum was first recorded over a wide frequency range using a strip chart. Observed lines were then individually recorded through a repetitive narrow-band scan and then digitally averaged. A Lorentzian line-shape function was fitted to each of the line profiles

$$y = y_\emptyset + \left(\frac{2A}{\pi}\right) x \left(\frac{\omega}{4(x - x_c)^2}\right) + \omega^2 \qquad (2.28)$$

where x_c is the peak width, ω is linewidth, A is the peak area and $y_\emptyset$ is the offset from the y-axis

2.2.2 Emission Type Spectrometers

Emission type spectrometers use generated microwave pulses that are tuned to match the frequency of the sample cavity. In most cases a Fabry-Pérot resonator is used as the sample cell. A Fabry-Pérot resonator consists of two parallel, spherical, concave mirrors[17], which are connected to a brass plate via two mounts. One mirror is fixed whilst the other is able to move axially, sliding in a well-fitting bore in the mount. A motor-driven micrometer translates the moveable mirror across the cavity length.[18, 19] Generally before a microwave pulse is applied to the sample, the individual dipole moments of the molecules rotate independently, preventing a measurable dipole moment. When the pulse is applied the molecules' dipole moments align yielding a macroscopic dipole moment. This emits microwave radiation, when the radiation stops, corresponding to the difference between the two rotational energy levels, which is collected and undergoes a Fourier transform resulting in a spectrum. Emission type spectrometers are used preferentially over absorption type spectrometers when studying molecules with very low dipole moments.[11]
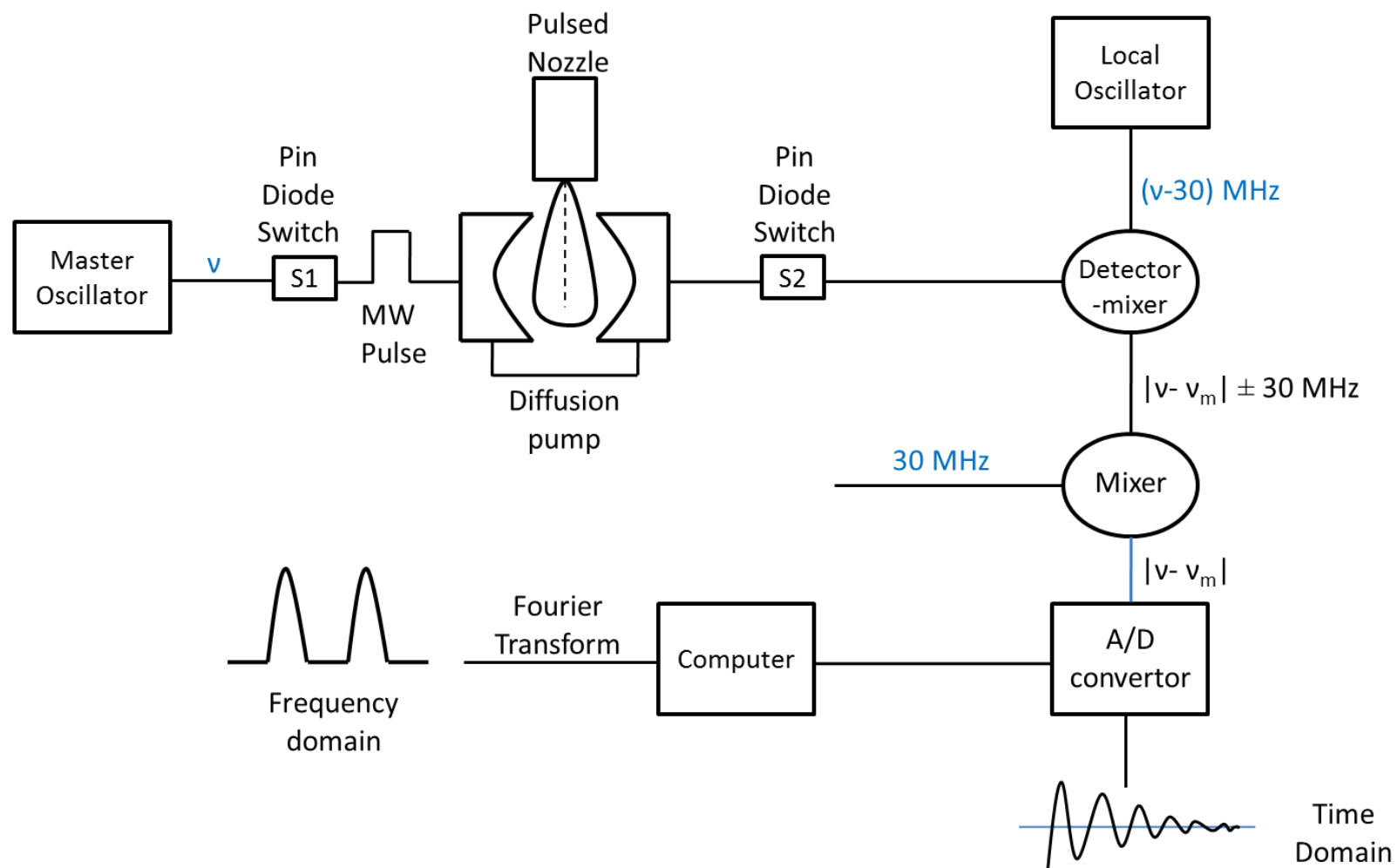
Figure 2.7: Fourier transform Emission type spectrometer[17]. Phase coherent radiation is shown in blue

The Fourier transform microwave spectrometer shown in Figure 2.7 consists of four main elements: three sources of phase coherent radiation (shown in blue), the nozzle source, the Fabry-Pérot cavity and the detection and processing of the microwave emission. Switch one (S1) pulses the microwave radiation, of frequency v, into the cavity and coupled with the gas of interest. Before the microwave pulse the individual molecules rotate independently; however, when the microwave pulse is applied rotations of the molecular dipole moments coordinate, and can yield a macroscopic dipole moment if the molecules are in resonance with the transition frequency. Switch 2 (S2) then opens once the pulse has finished and allows the spectrum to be recorded. When the spectrum is displayed v is simply added back on.[20]

After the pulse has been completed, the molecule relaxes back down to its ground state and emits radiation forming a field induction decay (FID). The emissions are detected using a double superheterodyne detection system, before the signal passes to an analogue-to-digital converter which is coupled to a computer. The frequency pulse is converted down to a lower frequency range for easier processing, before the FID signals are averaged and then Fourier transformed in order to create the final spectrum.

2.2.2.1 Pulsed-Supersonic Jet, Fabry-Pérot Type Resonator High Resolution Fourier Transform Microwave Spectroscopy

During the investigation into the terpene verbenone (Chapter 6) a pulsed-supersonic jet, Fabry-Pérot type resonator high resolution Fourier Transform Microwave System located at Gottfried-Wilhelm-Leibniz-Universität in Hannover, Germany [16], was used in order to record the microwave spectrum.

The instrument is equipped with an automated broadband setup with a coaxially orientated beam-resonator so that the molecular jet expands coaxially to the axis of the near confocal spherical mirrors. Extending the transit time of the molecular jet using this arrangement results in longer lasting signals which are capable of producing extremely narrow line widths (3 kHz FWHM) when using neon as a carrier gas. The resolving power of this system is approximately 5 kHz with experimental uncertainties <500 Hz for unblended lines.

In order to obtain sufficient vapour pressure, terpenes require heating in a 1.5 mm orifice reservoir nozzle situated at the rear of one of the Fabry-Pérot resonator reflectors. The

spectra were recorded with a nozzle temperature similar to the samples' vaporisation temperature, with a backing pressure of approximately 100 kPa and a pulse repetition rate of 20 kHz with neon carrier gas. Under these conditions the rotational temperature of the molecular beam was <2 K. A Lorentzian line-shape function (Equation 2.28) was fitted to each of the line profiles.
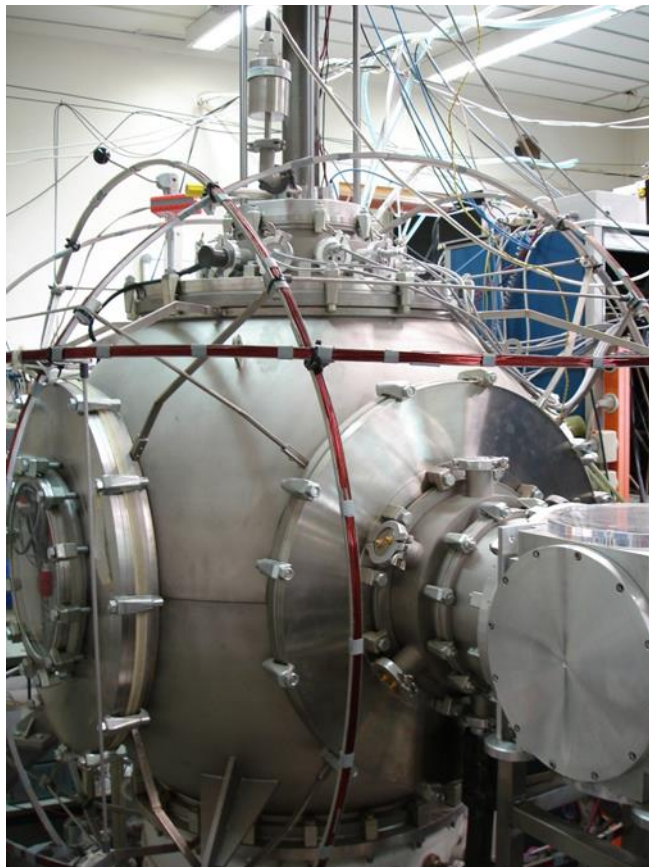
Figure 2.8: Pulsed-supersonic jet, Fabry-Pérot type resonator high resolution Fourier Transform Microwave System located at Gottfried-Wilhelm-Leibniz-Universität in Hannover, Germany[16]

2.3 Vibrational Spectroscopy

2.3.1 Fundamentals of Vibrational Spectroscopy

As mentioned previously vibrational transitions, that can be recorded using infrared (IR) spectroscopy, require a change in dipole moment during the vibrational motion. There are two different energy contributors associated with vibrational motion: kinetic energy, originating from the motion of the nuclei; and potential energy, which arises from the bond compression/expansion from its equilibrium value. As the nuclei move back and

forth, the energy of the system transfers between these two forms; the energy is entirely in the kinetic form when the nuclei are at their equilibrium separation and in the potential form (Figure 2.9) when the nuclei are stationary at the turning point of the compression/expansion motion.[1]
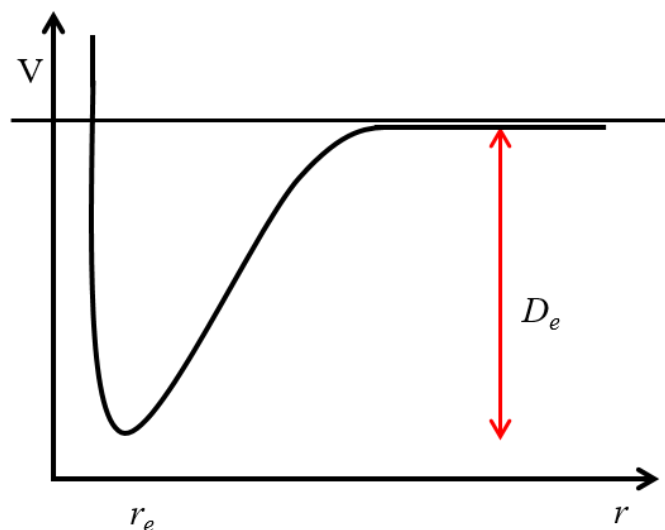
Figure 2.9: Vibrational potential energy function (V) plotted with respect to the bond length (*r*), where r_e is the equilibrium bond distance and D_e is the dissociation energy

The dissociation energy (D_e) depicted in Figure 2.8 shows the difference between the bottom of the potential energy curve and the bond dissociation limit. At short internuclear distances, below r_e, the molecular energy increases rapidly as the charged particles in the molecule experience strong repulsive forces when they are close together. At large internuclear distances, the bond has the possibility to stretch enough so that it breaks. Upon bond breakage the potential energy of the system becomes constant as it is the sum of the energies of the two individual atoms. For a chemical bond, the potential energy curve is an approximate parabola near the minimum (r_e); when the parabolic description of the curve is only an approximation the vibrational motion is confirmed as that of a harmonic oscillator.[1]

The vibrational motion of a given particle in a harmonic oscillator is confined by the boundaries of the potential energy curve and the energy levels associated with this motion are quantised

$$E_v = \left(v + \frac{1}{2}\right) h\nu \qquad (2.29)$$

where the vibrational quantum number (v) is 0, 1, 2, 3… and the harmonic frequency (in Hz or s^{-1}) is stated as

$$v = \frac{1}{2\pi}\left(\frac{k}{\mu}\right)^{\frac{1}{2}} \tag{2.30}$$

However, in vibrational spectroscopy rather than hertz the unit of wavenumbers (cm^{-1}) are usually used and are distinguished from the frequency by the vibrational wavenumber ω_e

$$E_v = \left(v + \frac{1}{2}\right)hc\tilde{\omega}_e \tag{2.31}$$

2.3.2 Infrared Spectroscopy

Infrared spectroscopy can be used to determine which molecules are present in a given sample. If the frequency of the absorbed infrared radiation coincides with the frequency of a molecular vibration, then absorption can occur. As each vibrational frequency relates to a specific molecular motion, infrared spectroscopy has the potential to provide information on the various bonds present in a molecule. Peak position in an infrared spectrum relates to the molecular structure and molecular composition, such as what functional groups and what type of bonds (single, double, triple) are present. Infrared spectroscopy can also be used to determine the concentration of a molecule within a sample, by firstly recording the spectrum of samples with known concentration and producing a calibration plot. This plot can then be used to determine the concentration of an unknown sample.[21]

The first advantage of infrared spectroscopy is that it is almost universal, it has the capability of recording the spectra of solids, liquids, gases, semi-solids, polymers and biological materials to name a few. Infrared spectra are information rich: peak positioning gives structural information about the sample, while peak intensities give the concentration of the molecules within the sample and the peak widths are indicators of pH or the presence of hydrogen bonding. Another key advantage of infrared spectroscopy is its sensitivity, a measure of the minimum amount of material required to produce a usable spectrum; infrared spectroscopy has the ability to detect picograms of a sample. Other advantages are the comparative ease and speed at which infrared spectra can be obtained and at a relatively low cost.[21]

Disadvantages of infrared spectroscopy include its inability to detect all vibrational modes, where the absorbance of infrared light does not generate excitations resulting in a change in dipole moment. Infrared spectroscopy is also incapable of observing vibrational modes undergoing the Raman Effect, which are dependent upon electric dipole polarisation. In the instance of homonuclear diatomic molecules, this is not always considered a disadvantage; it means that N_2 and O_2 (the most common species present in the air) do not appear in a spectrum, reducing artefacts, however it could result in incomplete spectra for other molecules. The biggest practical disadvantage of infrared spectroscopy is mixtures; it complicates the spectrum and means it is more difficult to ascertain which peaks are from which molecule. Finally, water poses a big problem for infrared spectroscopy due to the broad and intense peaks it produces in the liquid phase, which can disguise peaks from a solute dissolved in the water. Water also poses an issue for materials used in sample preparation; KBr and NaCl are commonly used as the windows for infrared cells; however, both are highly soluble in water, so are damaged in the presence of water.[21]

2.3.2.1 Fourier Transform Infrared Spectroscopy

At the heart of every Fourier transform infrared (FTIR) spectrometer is an interferometer, which measures the interference pattern between two light beams. When the infrared radiation enters the interferometer it splits the single light beam into two, by a device called a beamsplitter, which then follow two paths of different lengths (Figure 2.10).
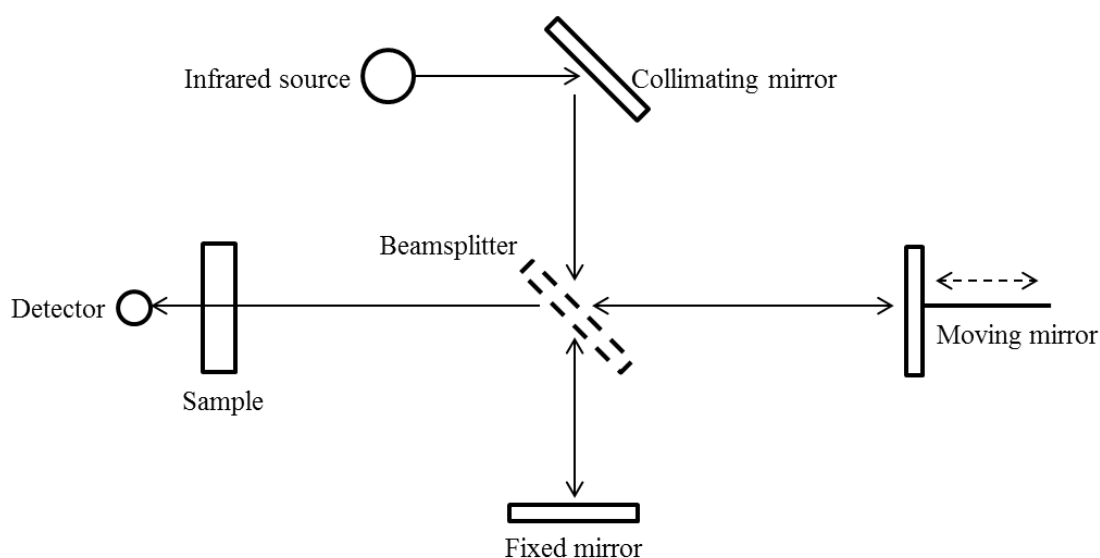
Figure 2.10: Optical diagram of an interferometer[21]

The light transmitted by the beamsplitter travels to the fixed mirror, whilst the light reflected by the beamsplitter travels towards the moving mirror. A single traversal of this mirror back and forth is called a scan. Once the light has reached these mirrors it reflects back to the beamsplitter, and recombines into a single beam. The two light beams recombine through interference of the two waves so that the two amplitudes add together to form a single wave. This single beam leaves the interferometer, interacts with the sample and finally hits the detector. The plot of the light intensity versus the optical path difference (for the mirror moving away from the beamsplitter) is known as an interferogram. These then undergo a Fourier transform to yield the infrared spectrum.[21]

There are multiple advantages to using Fourier transform infrared spectroscopy (FTIR) over a conventional IR spectrometer, firstly the high signal-to-noise ratio (SNR) of the spectral peak. The signal relates to the peak size and the noise is the error associated with this; the use of a Fourier transform improves the SNR. Fourier transform spectrometers are able to produce large SNRs due to a throughput advantage; as the infrared radiation doesn't have to pass through prisms, slits and grating within the spectrometer it means that high intensity radiation reaches the detector. A second benefit of FTIR is the multiplex advantage; increasing the number of scans and adding them together improves the SNR, which is a convenient and simple method of a spectral improvement. The final advantage of FTIR over other types of IR spectrometers is its wavenumber precision; FTIRs contain a laser which acts as an internal wavenumber standard so that the peak positions of the sample can be measured reproducibly. Alternatively the resultant spectrum could be calibrated against a known standard.[21]

The main disadvantages of FTIR spectroscopy are artefacts, which are features present in the spectrum that are not from the sample; some of the most common artefacts are water vapour and carbon dioxide. Absorbance and %Transmission spectra are calculated through a ratio of a background spectrum and that of the sample. If the amount of water vapour and carbon dioxide are equal in both spectra then the two will ratio out and yield an artefact free spectrum. However, in FTIRs the background and sample spectra have to be measured at different times, and therefore if there is a change in water vapour and/or carbon dioxide concentrations during this time period then peaks from these gases will appear as artefacts in the sample spectrum. Whilst these artefacts are an annoyance the advantages of FTIR over other spectrometers means that they are widely used for the analysis of samples.[21] For this particular investigation atmospheric water vapour and

carbon dioxide would not be of particular concern as the spectrometer will proceed under a vacuum and only a small amount of atmospheric water vapour and carbon dioxide will be present in the gas cell.

2.3.2.2 Bruker Infrared system

During the investigation into the terpene terpinolene (Chapter 8) a Bruker IFS 66v/S infrared spectrometer, located at The University of Leicester, was used in order to record the infrared spectrum of the ozonolysis products of terpinolene.

A schematic diagram of the Bruker system is shown in Figure 2.10. The infrared radiation is emitted from the source (S1) and reflected off a spherical mirror (SPH R125) through an aperture before hitting a parabolic mirror (PAR F153). The radiation is then split into two beams that then recombine via a beamsplitter, as described above. The material of the beamsplitter is dependent upon the type of infrared source being used. The Bruker system is commonly used with either mid-infrared (MIR) or near-infrared (NIR) beamsplitters made from KBr or CaF_2.

The recombined beam then reflects off a second parabolic mirror (PAR F180) into the sample chamber. For the ozonolysis reaction of terpinolene an additional component will be added to the sample chamber; a multipass White cell will sit atop the sample chamber so the infrared radiation will need to be diverted into this system where it will interact with the sample and upon its exits will then be diverted out of the cell and into the detector chamber of the spectrometer. Full details of this component and radiation diversion can be found in Chapter 4.

Upon exiting the sample chamber the infrared radiation passes to a preselected detector; the Bruker system contains two: a deuterated triglycine sulfate (DTGS) detector and a mercury cadmium tellurium (MCT) liquid nitrogen cooled detector. To reach the DTGS detector (D1) the radiation from the sample chamber is reflected from the elliptical mirror (ELL F250/40). DTGS detectors use the variation in the distribution of charges with temperature so that a current flows when the temperature is changed. This current is measured by electrical contacts placed on the surface of the detector. DTGS use accompanies a KBr beamsplitter looking at the mid-infrared region (400 – 4000 cm^{-1}). Whilst DTGS are relatively inexpensive and don't require any special treatment they are known as slow and noisy detectors. They are slow to respond to any change in infrared

intensity and due to the greater amount of noise generated in the spectrum they are typically only used for routine analysis as they are considered useless for demanding applications.[21]

For the terpinolene investigation the MCT detector (D2) will be used. MCT is a photoconductor, so when IR radiation is absorbed, electrons are released creating an electrical current in the alloy, the more intense the radiation the larger the current produced.[21] The detector element is cooled with liquid nitrogen in order to reduce the noise in the infrared spectrum. This cooling process adds both cost and complexity to this detector. Unfortunately the spectral range for a MCT is not as good as a DTGS; it tends to cut off at 700 cm^{-1}, removing some of the mid-infrared region, which is problematic if the sample produces a peak in this region. A MCT detector is dramatically more expensive than a DTGS but it is four times faster and gives a tenfold improvement on the spectral noise level, enabling it to be used for more demanding applications.[21]

In the Bruker system the radiation from the sample chamber reaches the MCT detector, via reflection from a parabolic mirror (PAR F180). The radiation is then reflected from two flat mirrors onto a final parabolic mirror (PAR F43) and onto the MCT detector (D2).

Regardless of the specific atmospheric reaction being studied with this system, the infrared spectrum produced will be from a mixture, which is problematic as it is difficult to ascertain which peaks are generated by which molecule. Other investigations (involving mixtures) have used Band Target Entropy Minimization (BTEM) to reconstruct spectra of the pure components from the mixture spectrum. The BTEM algorithm is able to reconstruct each of the components spectra without prior knowledge of their spectra or their concentration profile, removing the problems of older techniques that involved background subtractions.[22] The algorithm targets individual features from a vector-space decomposition of the observations and then uses these features to reconstruct the pure spectra. Another advantage of BTEM is that is reduces the noise of the spectra, as with each cycle the spectra become more refined.[23]
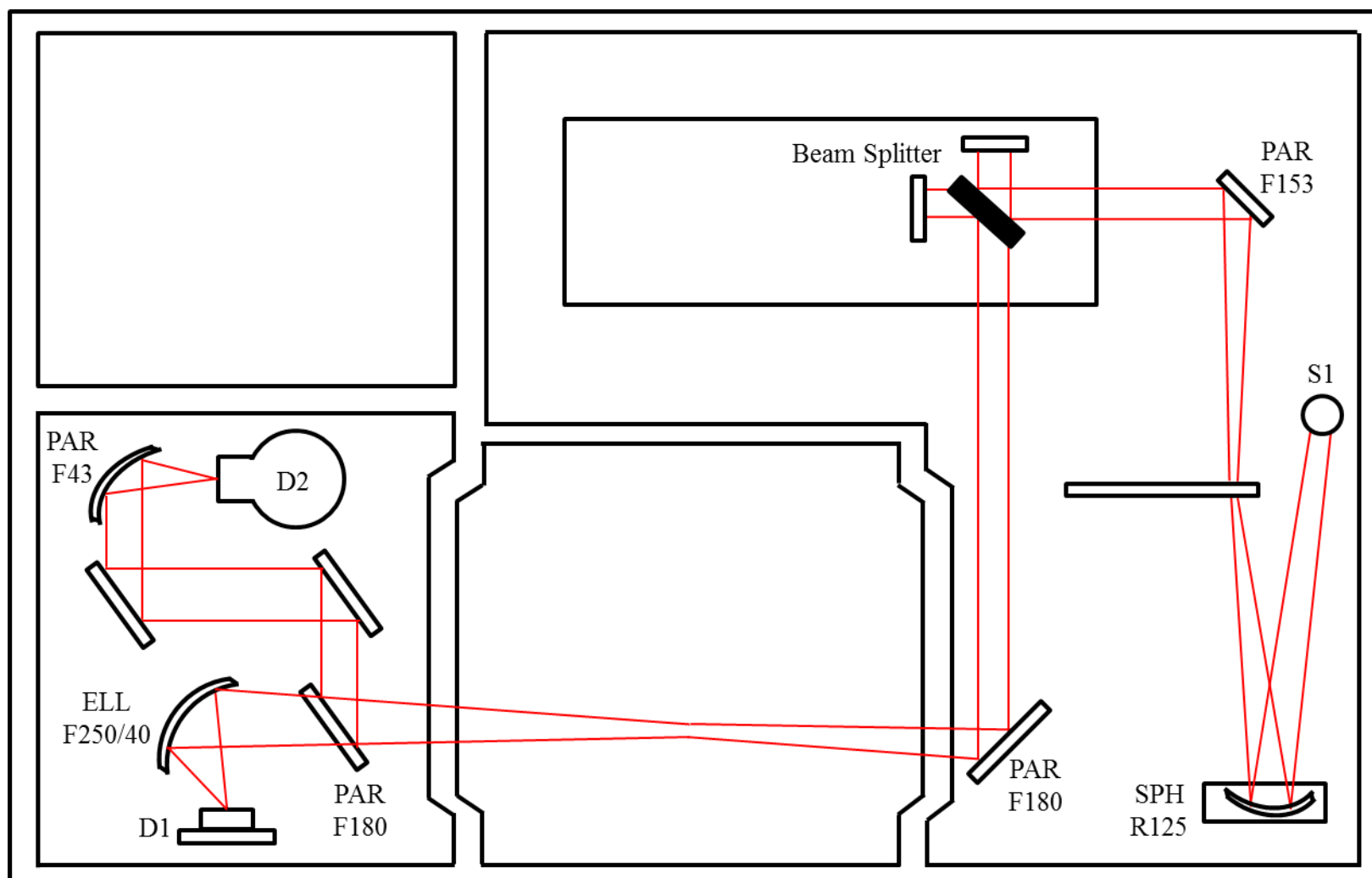
Figure 2.11: Schematic diagram of Bruker IR system

2.4 References

1. M. B. Brown, *Molecular Spectroscopy*, Oxford University Press, New York, 1998.

2. J. M. Hollas, *High Resolution Spectroscopy Second Edition*, Wiley, Chichester, 1998.

3. G. W. King, R. M. Hainer and P. C. Cross, *Journal of Chemical Physics*, 1943, **11**, 27-42.

4. W. Gordy and R. L. Cook, *Microwave Molecular Spectra Third Edition Techniques of Chemistry*, Wiley, New York, 1984.

5. B. S. Ray, *Zeitschrift für Physikalische Chemie*, 1932, **78**, 74.

6. J. K. G. Watson, *Vibrational Spectra and Structure : A series of Advances, ed J.R. During, Elsevier, Amsterdam*, Elsevier, Oxford, 1977.

7. D. Jelisavac, D. C. C. Gomez, H. V. L. Nguyen, L. W. Sutikdja, W. Stahl and I. Kleiner, *Journal of Molecular Spectroscopy*, 2009, **257**, 111-115.

8. H. V. L. Nguyen and W. Stahl, *Journal of Molecular Spectroscopy*, 2010, **264**, 120-124.

9. H. V. L. Nguyen, H. Mouhib, W. Stahl and I. Kleiner, *Molecular Physics*, 2010, **108**, 763-770.

10. H. Mouhib, D. Jelisavac, W. Stahl, R. Wang, I. Kalf and U. Englert, *ChemPhysChem: A European Journal of Chemical Physics and Physical Chemistry*, 2011, **12**, 761-764.

11. H. Mouhib, *Journal of Physics B-Atomic Molecular and Optical Physics*, 2014, **47**.

12. J. Ekkers, *Review of Scientific Instruments*, 1976, **47**, 448.

13. C. H. Townes and A. L. Schawlow, *Microwave Spectroscopy*, McGraw-Hill Book Company, New York, 1955.

14. E. B. Wilson and R. H. Hughes, *Physical Review*, 1947, **71**, 562-563.

15. G. W. Chantry, *Modern Aspects of Microwave Spectroscopy*, Academic Press, London, UK, 1979.

16. D. McNaughton, P. D. Godfrey, J.-U. Grabow, *Journal of Molecular Spectroscopy*, 2012, **274**, 1-4

17. A. C. Legon, *Annual Review of Physical Chemistry*, 1983, **34**, 275-300.

18.   U. Harbarth, J. Kowalski, R. Neumann, S. Noehte, K. Scheffzek and G. Z. Putlitz, *Journal of Physics E-Scientific Instruments*, 1987, **20**, 409-412.

19.   S. Zvanovec, P. Cerny, P. Piksa, T. Korinek, P. Pechac, M. Mazanek, J. Varga, J. Koubek and S. Urban, *Journal of Molecular Spectroscopy*, 2009, **256**, 141-145.

20.   J. C. McGurk, H. Mader, R. T. Hofmann, T. G. Schmalz and W. H. Flygare, *Journal of Chemical Physics*, 1974, **61**, 3759-3767.

21.   B.C. Smith, *Fundamentals of Fourier Transform Infrared Spectroscopy*, CRC Press, New York, 2011.

22.   H. Zhang, M. Garland, *American Society for Mass Spectrometry*, 2003, **14**, 1295 -1305.

23.   W. Chew, E. Widjaja, M. Garland, *Organometallics*, 2002, **21**, 1982-1990

Chapter Three

Computational Chemistry

3.1 Introduction

Advances in computational chemistry have led to developments in the computational systems and the size and complexity of molecular systems that can be regularly studied. There are three approaches for quantum chemical calculations: *ab initio*, semi-empirical and molecular mechanics techniques.

Ab initio techniques are based on solutions to the SWE and don't rely on any empirical parameter. Derived from Latin *ab initio* means "*from the beginning*" and can be thought of as operating from first principles. Conversely semi-empirical methods rely on parameterisation, typically those that can fit theoretically acquired data to the corresponding data obtained experimentally. A popular example, Density Functional Theory (DFT), uses a set of mathematical functions to accurately describe many-electron systems, using electron density rather than wavefunctions. Molecular mechanics is used to model large molecular systems using a single energy expression, such as a harmonic oscillator; however, these calculations require the constants to be obtained from experimental data.

3.2 Schrödinger Wave Equation

The Schrödinger Wave Equation (SWE) forms the basis of all quantum chemical calculations and its solution supports the understanding of the molecular properties. The Hamiltonian operator $(\widehat{H})$ consists of terms that describe the electron-nuclei and electron-electron interactions that are built into both kinetic and potential energy terms.[1]

$$\widehat{H}\varPsi = E\varPsi \tag{3.1}$$

The Born-Oppenheimer approximation assumes the nuclei are effectively stationary relative to the motion of the electrons, and is used to simplify Equation 3.1. This simplification takes the form of an electronic Hamiltonian that is used in the majority of quantum chemical calculations.

$$\widehat{H} = \sum_{i=1}^{n} h_i + \sum_{i=1}^{n}\sum_{j>1} g_{ij} + \sum_{a}\sum_{a>b} \frac{Z_a Z_b}{|R_a R_b|} \tag{3.2}$$

where h_i and g_{ij} are the one- and two-electron terms that describe the motion of the individual electrons in a static electric field (originating from the nuclei) and the repulsion

between the electrons respectively. The nuclear repulsion term is independent of the electron positioning; within a given geometry this positioning remains constant regardless of the value of the electronic term.

$$h_i = -\frac{1}{2}\nabla_{ij}^2 - \sum_a \frac{Z_a}{|R_a - r_i|} = \hat{T} + \hat{V}_{Ne} \tag{3.3}$$

$$g_{ij} = \frac{1}{|r_i - r_j|} \tag{3.4}$$

Here Z is the nuclear charge, R is the electron-nucleus distance, r is the electron-electron distance, ∇^2 is the Laplacian operator[2] and g_{ij} is the electron-electron operator.

In order to create a suitable wavefunction (Ψ) that satisfies the SWE, an appropriate operator must be calculated in order to generate an eigenvalue. Equation 3.1 shows that the energy in the SWE is dependent on a wavefunction; however, this wavefunction requires some knowledge of the energy. An iterative process is therefore required in order to optimise the wavefunction with respect to the energy.

3.3 Levels of Theory

3.3.1 Hartree-Fock Theory

The SWE can only be solved exactly for one-electron systems; however, all but the simplest systems have more than one electron, so in order to solve the SWE for multi-electron cases some approximations must be used. The combination of the product of a single electron wavefunction and a spin function results in spin-orbitals, which form the building blocks of electronic wavefunctions.[3]

The simplest approximation used to solve SWE for a polyelectron system is the Hartree-Fock (HF) approximation, this forms the basis of all *ab initio* techniques. The wavefunction in this instance is formed from a single Slater determinant using a finite set of atomic spin-orbitals (also known as atomic basis functions) that contribute towards the basis set. The general form of the Slater determinant is shown in Equation 3.5 and explicitly accounts for the antisymmetry with respect to electron exchange

$$\psi_{SD} = \frac{1}{\sqrt{n!}} \begin{vmatrix} \phi_1(1) & \phi_2(1) & \cdots & \phi_n(1) \\ \phi_1(2) & \phi_2(2) & \cdots & \phi_n(2) \\ \vdots & \vdots & \ddots & \vdots \\ \phi_1(n) & \phi_2(n) & \cdots & \phi_n(n) \end{vmatrix} \tag{3.5}$$

where $\phi_i(n)$ is the spin-orbit function (i is the orbital index and n is the electron index) and $\frac{1}{\sqrt{n!}}$ is a normalization constant. The spin-orbit function is orthonormal to satisfy the equation

The Slater determinant can be used to describe the ground state wavefunction of any atom or molecule. HF theory uses a wavefunction to form a trial wavefunction in a variation to the SWE. The energy is minimised with respect to the variation in the spin-orbitals to give the HF equation

$$\hat{F}_i \phi_i = \varepsilon_i \phi_i \tag{3.6}$$

where ε_i is the energy of electron i, and $\hat{F}_i$ correspond to the Fock operator by

$$\hat{F}_i = \frac{1}{2} \nabla_{ij}^2 - \sum_{A=1}^{M} \frac{Z_A}{r_{iA}} + v^{HF}(i) \tag{3.7}$$

where v^{HF} is the HF potential, which represents the mean field potential experienced by the ith electron, due to presence of other electrons. This is dependent on the spin-orbitals of the electrons in the system, so the Fock operator is reliant on its own eigenfunction; this route used to solve the HF equation is cyclic, so cannot be solved analytically. Therefore a numerical approach is required with an initial guess in order to provide the first approximation of the spin orbitals.

The field that each electron is subjected to is then calculated using approximate functions for h_i and g_{ij}, which are used to solve the eigenvalue in the HF equation (Equation 3.6). The eigenfunction is used to generate a new set of spin-orbitals and the process is repeated. This practice continues until there is no further change in the mean field or the optimisation criteria are met. The wavefunction is deemed optimised when the energy is minimised.

Combining all the elements of the Fock operator yields the Fock matrix, which can be composed through a combination of basis functions (which in turn is a linear combination of elementary functions) with unknown coefficients. The determination of each orbital

within the Slater determinant, results in a series of simultaneous equations which must solved to determine the coefficients for each function with an orbital description.

The major shortcoming of HF is the great expense (with regards to both time and computational cost) in calculating two-electron integrals. It is assumed that each electron interacts with the averaged charge from the sum of all other electrons distributed within the molecular orbitals. The Coulomb integrals fail to explicitly evaluate the electron-electron repulsion; this repulsion is evaluated between the individual electrons and the average charge arising from the other electrons orbiting the positively charged nucleus. To improve the accuracy of electronic structure calculations, a method accounting for the electron correlation must be incorporated.

3.3.2 Post Hartree-Fock Methodologies

More complex wavefunctions cannot be created directly, but can be estimated through a simpler wavefunction. An iterative process, known as the self-consistent field (SCF), can then be used to solve the SWE. This process leads to a more accurate representation of the orbitals. These orbitals are then used to solve the SWE, yielding an even more accurate representation of the orbitals. This process continues until the results reach convergence.[2]

A trial wavefunction is then created and optimised using an iterative process. At this point a choice needs to be made: either continue using the wavefunction (on the assumption that the guess of the geometry is sufficiently good) or continue the iteration process by minimising the energy with respect to the change in the nuclear coordinates. These iterations continue until a change in nuclear coordinates no longer reduces the energy of the wavefunction; this geometry is then considered to be optimised. In order to confirm that these coordinates represent a minimum or stationary point on the potential energy surface (PES) a harmonic vibrational frequency calculation is performed; the presence of an imaginary frequency is indicative of a saddle point or a transition state.

3.3.2.1 Perturbation Theory

In quantum mechanics small perturbations are introduced into the Hamiltonian in order to introduce electron correlation.[4] It is assumed that this perturbation is small in comparison to the unperturbed system.

The most popular routine that is able to adequately include the effects of the electron correlation is Møller-Plesset (MPn) perturbation theory.[5] This method takes the zero-order HF Hamiltonian and incorporates a small perturbation that models the effects of electron correlation

$$\hat{H}_{Pert} = \hat{H}_0 + \sum_{n=1}^{\infty} \lambda^n \hat{H}_n \qquad (3.8)$$

where $\hat{H}_0$ is the unperturbed reference for which the solution is known and λ is some coefficient that describes the extent of the perturbation (0 indicates an unperturbed system and 1 represents a full perturbation). It is widely understood that $\hat{H}_n$ must be smaller than $\hat{H}_0$ in order for the Hamiltonian to work. From Equation 3.9 it can be seen that the perturbation $(\hat{H}_n)$ must be multiplied by the factor λ, which is representative of the perturbation strength; if λ were to equal zero then the Hamiltonian $(\hat{H}_{Pert})$ would be equal to the unperturbed reference $(\hat{H}_0)$.[4]

In order to utilise MP perturbation theory, a suitable selection of $\hat{H}_0$ must firstly be undertaken. The common practice for this is to take the sum of the Fock operators[4, 6], which are effective one-electron energy operators. Fock operators describe the kinetic energy of an electron, its attraction to the nucleus as well as its repulsion to all other electrons. They are associated with variation in total energy rather than the exact energy itself. The Hamiltonian operator in these cases does not relate to the sum of Fock operators[4], as previously stated this becomes the case in MP perturbation theory. Summation of the Fock operators counts the average electron-electron repulsion twice, so that the perturbation $(\hat{H}_n)$ becomes the exact electron-electron operator minus twice the electron-electron operator $\langle V_{ee} \rangle$ as shown in Equation 3.10. Whilst this does not satisfy the assumption that $\hat{H}_n$ is vastly smaller than $\hat{H}_0$, it does fulfil the requirement that $\hat{H}_0$ is a known quantity.[4]

$$\hat{H}_n = V_{ee} - 2\langle V_{ee} \rangle \qquad (3.9)$$

This perturbation theory can be corrected to the *first-*, *second-*, *third*-order or further, allowing the effectiveness of the perturbation on the HF energies to be assessed. When a perturbation operator is included in the wavefunction, the result is a series of expansion values that are related to the Fock operator expectation values

$$\hat{H}_0\psi = E_{MP0}\psi = \sum_{i=1}^{n} \varepsilon_i\psi \tag{3.10}$$

$$\hat{H}_1\psi = E_{MP1}\psi = -\langle V_{ee}\rangle\psi \tag{3.11}$$

$$\hat{H}_2\psi = E_{MP2}\psi \cdots \tag{3.12}$$

The use of unperturbed operators results in a series of eigenvalues that represent the orbital energies (ε_i) for each of the occupied orbitals included in the HF wavefunction. Expectation values that describe the averaged electron-electron repulsion, are generated through perturbations of the summation of first-order corrections.

Møller-Plesset perturbation theory is indicated through the notation MPn, where n is the index of the correction. The first real correction is a second order correction notated as MP2; this second order correction represents the excitation of two electrons from the occupied orbitals labelled i and j into the virtual orbitals labelled a and b

$$E_{MP2} = \sum_{i<j}^{occ} \sum_{a<b}^{vir} \frac{\left[\langle \phi_i\phi_j|\phi_a\phi_b\rangle - \langle \phi_i\phi_j|\phi_b\phi_a\rangle\right]^2}{\varepsilon_i + \varepsilon_j - \varepsilon_a - \varepsilon_b} \tag{3.13}$$

This expression describes the energy contribution from the doubly excited determinants; the excitation of a pair of electrons from a single occupied orbital into a single virtual orbital and is responsible for 80% of the correlation energy. The second order correction (in MP2) described the interaction between various electron pairs.

To use further corrections, such as MP3 and MP4, their necessity must be justified as they have a substantial computational cost. It is generally unfeasible to use such calculations as the increase in the order of the correction does not necessarily result in an improvement in convergence; this small gain in accuracy is not considered worthwhile considering the cost involved.[4, 6]

3.3.3 Density Functional Theory

The basis of density functional theory (DFT) methods is that the ground-state electronic energy is determined solely by the electron density[4], rather than taking into account of wavefunctions like the Hartree-Fock (HF) and MPn methods; consequently there is a one-to-one connection between electron energy (E) and density (ρ), via a function (F) that needs to be determined (Equation 3.15).

$$E = F[\rho(x)] \qquad (3.14)$$

The electron density is equal to the square of the wavefunction and is integrated over N-1 electron coordinates.

The description of DFT, in which it requires the location of F, does not appropriately describe the process; using Equation 3.14 it has been proven that different densities would yield different ground-state energies; however, the connecting function is unknown. Rather than 'finding' F, DFT methods aim to design a variety of functions to connect the electron's density and energy. DFT uses the Kohn-Sham Theory (1965) to calculate kinetic energy and a determinant for the Kohn-Sham orbitals. The equation for which is the Schrödinger equation of a fictitious system (Equation 3.15)

$$E_{DFT}[\rho] = T[\rho] + E_{ne}[\rho] + J[\rho] + E_{xc}[\rho] \qquad (3.15)$$

where $E_{DFT}[\rho]$ is the exact energy, $T[\rho]$ is the electronic kinetic energy, $E_{ne}[\rho]$ is the nuclei-electron Coulombic energy, $J[\rho]$ is the electron-electron Coulombic energy and $E_{xc}[\rho]$ is the electron-electron exchange energy. $E_{xc}[\rho]$ is the part that is left after subtracting the non-interacting kinetic energy and the potential energy terms $E_{ne}[\rho]$ and $J[\rho]$. The system is described as fictitious as it works on the assumption of non-interacting electrons, which in reality are interacting.[4]

It is possible to calculate the energy in this manner as the difference between the exact kinetic energy and the kinetic energy assuming no orbital interactions, is small. Excess kinetic energy is absorbed into an exchange-correlation term, meaning that the exact energy ($E_{DFT}[\rho]$) can be calculated from the general DFT expression (Equation 3.15). In order to actually calculate the exact kinetic energy, orbitals must be reintroduced into the system. Deriving suitable exchange-correlation terms is problematic as $J[\rho]$ and $E_{xc}[\rho]$ functions are totally dependent on density, this means that the determination of the involved orbitals is an iterative process.[4]

Whilst there are problems with DFT, the previously mentioned requirement of finding F and deriving exchange-correlation terms, the strengths of this type of calculation are that it only takes density into consideration and that it has the potential of including computationally difficult parts of wave mechanics and correlation energies at similar computational effort and cost as for HF calculations[4], which is why it is so popular for computational analysis of molecular systems.

Commonly, DFT methods use the *Local Spin Density Approximation* (LSDA) which can be used interchangeably with the *Local Density Approximation* (LDA), which assumes local density can be treated as an electron gas or a slowly varying function. The two are able to be used interchangeably as in the most common closed-shell systems the two approximations are equal. However, approximations are not perfect and LSDA can be improved with the incorporation of the *Gradient Corrected or Generalized Gradient Approximation* (GGA). GGA assumes that the exchange and correlation energies are dependent not only upon the electron density but also on the derivatives of the density, thereby considering the density as a non-uniform electron gas.[4]

In order to utilise DFT to its fullest potential using the Gaussian 03 software package[7] the inclusion of the key term '*int=ultrafinegrid*' is required. The first part to define is *int*, which '*modifies the computational method to use two-electron integrals and their derivatives*'; the second part to examine is *grid*, which '*specifies the integration grid to be used for numerical integration*'; and the final part to define is *ultrafine* which relates to the size of the 'pruned' grid. Pruned grids are those which have been optimised to reduce the number of points required to generate a given level of accuracy. An ultrafine grid has 99 radical shells and 590 angular points per shell (Notation: 99,590).

Another key term used in order to maximise the use of DFT is '*SCF=tight*'. *Self-Consistent Field* (SCF) calculations that include diffuse functions require the *tight* instruction must be included in order to obtain tight SCF convergence. Ordinarily SCF calculations are run with a modest convergence as it is quicker; however, "tight" SCF calculations include more steps than normal to determine the convergence, which is more costly. The general way in which a SCF method proceeds, is firstly the integrals are evaluated, then the Fock matrix is formed, the density matrix is then solved and finally the convergence is tested. If this convergence fails then the next iteration begins; however, if it succeeds then other parts of the calculation are performed.[6]

3.3.4 Failures of B3LYP, a DFT method – A Literature Review

Over the past 20 years DFT has become the computational workhorse due to its lower computational cost in comparison to wave function theory[8] and more recently functionals have been developed showing great improvement in the calculation of reaction barrier heights and transition state geometries,[9] a fact of key importance in this investigation. Unlike wavefunctions, DFT methods are not improved through the addition of more

electron configurations, so there is no 'best' DFT method,[10] just the most appropriate to obtain the information required.

Hybrid density functionals are not uncommon as they combine various amounts of HF non-local exchange operators with DFT exchange-correlation[9, 11] to improve the results of DFT calculations. They are much less sensitive to the basis set in use than the *ab initio* techniques.[9] One of the most popular hybrid methods is B3LYP[12, 13], which is not the best performing DFT process, but has the capability of performing to the accuracy of *ab initio* techniques.[10] The B3LYP functional combines the Becke 3-parameter, which incorporates exchange-correlation containing local-spin-density, gradient and exact-exchange information[12] and the correlation functional of Lee, Yang and Parr. This functional utilises the non-local correlation from the LYP expression and the local correlation from Vosko, Wilk and Nusair (VWN) functional III.[13]

The B3LYP functional is the most popular method for synthetic and mechanistic concepts amongst organic chemists as it accurately describes their systems[10] however, this is not a finding supported by theoretical chemists. Check and Gilbert describe the poor account that the B3LYP functional gives of van der Waals molecules and hydrogen-bonded systems as well as the generally inaccurate evaluation of organic systems, especially as the number of C-C bonds increases. The large and chemically relevant errors such as: dissociation reactions and enthalpies of formation[14, 15] of organic systems, found by Check and Gilbert are supported by the findings of Grimme *et al.*; however, Grimme *et al.* do recommend the use of diffuse functions in the basis set in order to obtain the best results with B3LYP.[16] Multiple studies state that B3LYP has large errors in bond distances and angles particularly for loose saddle points (energy maximum on the potential energy surface) , leading to an underestimation of the barrier heights.[9, 19] The underestimation of the reaction barrier height stems from the unreliable transition state geometries generated by the B3LYP functional, meaning that it is not a recommended method for transition state location.[8]

B3LYP is a commonly used functional for the location of ozonolysis transition state geometries, when reacted with terpenes, such as: α- and β-pinene[18, 19], camphene[20], sabinene[21], isoprene[22, 23] and β-caryophyllene.[24] All of these studies comment on the known defect of B3LYP – its inability to show ozone a singlet open-shell biradical, resulting in the calculated energy of the entrance channel transition state being

underestimated by ~10 kcal mol^{-1}. This literature review, based on the study by Xu *et al.* [8] which looked at the ability of density functionals to predict internuclear distances within transition states, considers alternatives to the B3LYP functional in order to decipher the ozonolysis reaction mechanism for the terpene, terpinolene.

3.3.4.1 Wave-Function Methods

Wave-function methods include those that have been mentioned earlier in this chapter. Møller-Plesset second order perturbation theory (MP2)[5] has a propensity to underestimate the sum of the bond distances for the bond breakage and formation at the saddle point resulting in an overestimation of the barrier height, the opposite trend displayed by B3LYP.[9] Unlike the DFT methods MP2 experiences large basis set effects[9, 17], contributing towards the inaccuracy of the calculated reaction barrier height.

Quadratic configuration interaction with single and double excitation (QCISD)[25] is believed to calculate well balanced optimised geometry structures, particularly with respect to loose structures, a notable failing of B3LYP. QCISD is exceptional expensive computational technique unless only small systems are being considered, which does not align with the ambitions of this investigation.[8]

A new multi-coefficient correlation method (MCCM), the balanced multicoefficient method based on coupled cluster theory with single and double excitations (BMC-CCSD), has been developed with a recorded error of 0.7 kcal mol^{-1} for reaction barrier heights, a vast improvement on that of B3LYP.[26] Although BMC-CCSD, which is more expensive than the other wavefunction methods, is recommended for systems when high accuracy is required[8], other MCCMs that were developed have a threefold improvement in the error associated with the calculated bond energies.

3.3.4.2 Generalised Gradient Approximations

The BLYP functional is obtained by adding gradient corrections to the local-density approximation (LDA), specifically the exchange correction of Becke[27] and the correlation function of Lee, Yang and Parr (LYP).[28] When dealing with reversible reactions and if the reverse barrier height is small, such as the H transfer of methanol, the use of this functional results in the barrier vanishing completely as it significantly underestimates the barrier height.[8]

The MOHLYP functional contains metal-adjusted optimised exchange potentials (MOptX or MO) and uses half of the LYP correctional functional (HLYP). The half-LYP correlation is favoured over the full LYP function as it offers improved results.[29] Similarly to BLYP, the use of this functional on a small barrier for a reverse reaction results in the barrier vanishing completely[8], which would not assist this investigation. The MOHLYP2 functional[30] is the only GGA that was able to locate all of the transition states for the reactions explored by Xu *et al.* Unfortunately this functional produces a large mean deviation from the average mean unassigned deviation (AMUD). The mean assigned deviation (MUD) is obtained through comparison to the most accurate available reference data, whilst the AMUD averages over all of the MUDs in the dataset.[8]

Perdew, Burke and Ernzehof have developed a parameter-free GGA (PBE) in which all the parameters are fundamental constants using only the general features detailing the underlying construction the of Perdew-Wang 1991(PW91) GGA. Improvements over PW91 include more accurate descriptions of the linear response of an uniform electron gas, correct behaviours under uniform scaling and the construction of smoother potentials.[31] Similarly to other functionals PBE is described as producing equally accurate results as MP2.[10]

Zhao and Truhlar have developed a second order generalised gradient approximations (SOGGA) in which they enforce a complete restoration of the gradient expansion for both the exchange and correlation to the second order.[32] To achieve this they require a more flexible functional exchange form of the GGA. The best performance of the SOGGA functional is for heavy atom transfer reactions, making it an inappropriate method for this investigation. Similarly to the previous techniques in this section, the use of SOGGA on reverse reaction barriers causes them to vanish.[8]

Generalised gradient approximations (GGAs) are generally thought of as not good enough to obtain reliable structures for transition states geometries and any instances with a low reaction barrier height, where essentially no reaction barrier is present, GGAs are unable to locate transition state structures. These techniques are not recommended for locating transition state structures due to errors in the geometry causing an underestimation of the barrier height.[8]

3.3.4.3 Meta – Generalised Gradient Approximations

Meta-GGAs are akin to GGAs, but the exchange-correlation energy density is at a point in space that is dependent on the spin kinetic energy densities.[8, 33] The M06-L functional contains a local function without any HF exchange, allowing the use of highly efficient algorithms to reduce the computational cost of larger systems.[8, 33, 34] It is described as having good overall results for thermochemistry, thermochemical kinetics, organometallics, metallics, biological and non-covalent interactions as well as good predictions on geometries and vibrational frequencies. It is thought to be an improvement on known local and hybrid functions and it outperforms B3LYP. Specific advantages of M06-L functional have been listed as: good performance for unimolecular and association barrier height (a benefit also possessed by B3LYP) and the weighted mean unassigned error is better than other hybrid functionals. The primary recommendation for the use of M06-L is for the investigation of transition metal bonding, which does not coincide with the ambitions of this investigation.[33, 34] Similarly to GGAs, meta-GGAs are not advised for transition state location as they underestimate the reaction barrier heights.[8]

3.3.4.4 Hybrid Generalised Gradient Approximations

Hybrid GGAs possess an exchange energy term that also has a non-local component, which in the study by Xu *et al.* is HF exchange. They were developed to provide a cost-effective way to incorporate non-locality for the exchange-correlation.[35] These hybrid GGAs can be further separated into four categories: global hybrid GGAs, global GGAs combined with molecular mechanics, range separated hybrid GGAs and range separated hybrid GGAs combined with molecular mechanics.

The global hybrid GGAs includes the common B3LYP functional for which this review is attempting to discover an alternative to. The modified Perdew-Wang 1-parameter model for kinetics (MPW1K)[36] yields much better performance for kinetic calculations and bond energies for improved long-range behaviour of the modified Perdew-Wang density function in the mPW1PW91 functional.[9] The mPW1PW91 functional performs marginally better than the B3LYP functional but has a large error in its calculated bond distances and predicted geometries of loose saddle points caused by its systematic underestimation of the barrier heights.[9, 10]

The main difference between the MPW1K and mPW1PW91 functionals is the amount of exact exchange employed to give best agreement with MP2.[10] Xu *et al.* tested the MPW1K, mPW1PW91, B3LYP and BH&HLYP functionals and only recommended the MPW1K functional for locating transition state geometries. The MPW1K functional produced the lowest error in bond length and predicted more reliable saddle point geometries with augmented, polarized double-zeta basis sets and at a lower cost than MP2.[8, 9] The MPW1K functional is recommended for the calculation of reaction barrier height as it reduces the error of such calculations by a factor of three in comparison to the B3LYP functional.[36]

The BH&HLYP[12] functional has a 50% HF exchange potential, resulting in more accurate barrier heights in comparison to B3LYP but decreases the accuracy of calculated bond and reaction energies. This results in a large error in bond lengths and loose structures, making its use to locate transition state structures questionable. The B1LYP functional uses a ratio between HF and the density functional exchange, which has been predetermined using theoretical knowledge and does not require further addition of other parameters. However, it is believed to perform at a similar level to B3LYP so does not offer an improvement.[37]

The B97-3 functional is formed to improve the quality of conventional semi-empirical hybrid exchange-correlation DFT functionals, by including expansion parameters which are iterated to convergence. This has resulted in a functional with a moderate amount of orbital exchange and a lower mean absolute error than B3LYP, but it lacks the appropriate physics to adequately describe van der Waals interactions and one-electron systems.[38] A parameter free density functional (PBE0) has been developed by combining the PBE generalized gradient functional with a predetermined amount of exact exchange, to provide a widely applicable method for quantum chemistry calculations.[39] With predicted interaction energies and equilibrium distances sufficiently close to the experimental values, PBE0 has proven itself to be an cheaper alternative to MP2.[8, 39]

Xu *et al.* describe all of these functionals and mPW1PW[40] as having similar or better performance than MP2. Besides MPW1K, all the other functionals including B98, are explicitly not recommended for the location of transition state structures due to the underestimation of the corresponding reaction barrier height.

For the second category, global hybrid-GGAs with molecular mechanics, Xu *et al.* only analyse a single functional, B97-D.[41] This functional is based upon the Becke GGA functional introduced in 1997[42] but has been explicitly parameterised to include damped atom-pair dispersion corrections. Xu *et al.* describe this functional as the worst of the hybrid methods tested as unreliable transition state geometries are produced. Similarly to some of the GGAs mentioned previously, this functional fails to characterise small reversible barrier heights in fact causing them to vanish completely. This functional like so many others, underestimates reaction barrier heights, so is unable to locate the transition state of a small barrier and thus is not recommended for a transition state search.[8]

The third category identified by Xu *et al.* is known as the range separated hybrid GGAs. The functionals, ωB97 and ωB97X model long-range, corrected hybrid density functionals. They show great accuracy when calculating thermochemistry and kinetics in addition to more precisely representing noncovalent interactions in comparison to other hybrid functions. The difference between the two functionals is the inclusion of a small fraction of the short-range HF exchange (denoted by the X).[35] Whilst no direct comparison to B3LYP has been reported, ωB97 is thought of as the best hybrid method and together with ωB97X is considered to perform to a better or similar standard to MP2, with a smaller computational cost.[8]

For the final category, range separated hybrid-GGAs with molecular mechanics, Xu *et al.* only analyse a single functional, ωB97X-D. This functional originates from a re-optimisation of the long-range corrected hybrid density functional; those that retain all the HF exchange for long-range electron-electron interactions, which resolves a significant part of the self-interaction problems associated with global hybrid functionals.[43] The ωB97X-D functional also includes empirical atom-atom dispersion corrections. This enables the new functional to offer significant improvement for non-bonding interactions, over the ωB97X functional. The development of such functionals is required as B3LYP does not qualitatively resolve the problems of long-range charge-transfer excitations. Xu *et al.* describe this functional like so many other hybrid GGAs, as a similar or better performer than MP2, while achieving a lower computational cost.

3.3.4.5 Hybrid Meta – Generalised Gradient Approximations

Hybrid meta-GGAs contain exchange energy that has a non-local component, which in the review by Xu *et al.* was the Hartree-Fock exchange. In hybrid meta density functionals, energy is dependent upon the occupied orbitals through both the HF exchange (as for a hybrid GGA) and also through the non-interacting spin kinetic energy densities (as in meta-GGAs). This combination has shown an enhanced performance over the hybrid GGAs.[44]

The Minnesota 2005 (M05) functional incorporates kinetic energy density into the exchange and correlation functionals whilst removing self-correlation effects. Zhao *et al.* designed this functional to show broadly applicability to organometallics and metallics, non-metallic bonding, thermochemistry, thermochemical kinetics, and non-covalent interactions as well as satisfying the uniform electron gas limit.[45] Xu *et al.* do not recommend this functional for transition state location, as like so many of the hybrid GGAs, it underestimates the reaction barrier height.[8] Whilst the M05 functional is parameterised with both metal and non-metals, the M05-2X functional[46] is a high non-locality functional with double the amount of the non-local exchange (hence 2X) and is only parameterised for non-metals. This functional has the best performance when calculating thermochemical kinetics, non-covalent interactions and alkyl bond dissociation.[45] Xu *et al.* promote this functional as it performs better or similarly to MP2 with a lower computational cost.[8]

The M06-HF functional use full HF-exchange and eliminates the self-exchange interaction at long range and satisfies the uniform electron gas limit.[47] M06-HF has been praised for its calculation of non-covalent interactions and long-range charge-transfer via time-dependent DFT (TDDFT); however, it is considered to have reasonably good overall performance even though it has full HF-exchange.[47, 48] M06-HF performs better than doubly hybrid functionals (that will be discussed later) and the hybrid GGA – B3LYP when investigating ground-electronic-state energetics. Generally M06-HF behaves better than MP2 whilst operating at a lower computational cost.[8, 47]

Similarly to the M05 and M05-2X functionals the M06 functional is parametrised including both transition metals and non-metals and is recommended for organo- and metallics chemistry for non-covalent interactions and the M06-2X functional contains double the amount of non-local exchange and parameterised by non-metals.[48] M06-2X is

considered the best application for main-group thermochemistry, kinetics, non-covalent interactions and electronic excitations energies to valence states.[48] Xu *et al.* states that M06-2X is one of the better hybrid meta-GGA, and both functionals are considered better or similar performers to MP2.[8]

The Minnesota 2008 high-HF exchange (M08-HX) functional has improved the problem of accuracy over other functionals, including calculations on large-molecule atomization energies, non-covalent interaction energies, conformational energies in aromatic peptides, barrier heights, multiplicity-changing excitation energies and bond lengths in large molecules. This functional was developed to achieve further improvements with the use of a more flexible functional. The M08-SO functional follows the same form as M08-Hx but is optimised with an additional function which enforces gradient expansion to second order (SO). It is also believed to perform slightly worse than the M08-HX functional.[44] Both functionals are considered better or equal performers to MP2, but Xu *et al.* states that M08-HX is one of the better hybrid meta-GGAs and they highly recommend its use due to its excellent performance and lower cost when compared to doubly hybrid functionals.

The 6-parameter functional based on the Perdew-Wang-91 (PW91) exchange and Becke 95 correlation (PW6B95) obtains the best results for thermochemistry calculations and those involving non-bonding interactions. The PWB6K functional is based upon the same exchange and correlation but offers an improvement on non-bonding interactions for kinetics (K)[49], resulting in it being recommended as a suitable method to calculate reaction barrier heights as it produces reliable transition state structures.[8] Both functionals are considered to be improvements upon MP2[8], yet only PW6B95 is noted as having an improvement on B3LYP for main group covalent bond energies.[49]

The Becke88-Becke95 1-parameter model for kinetics (BB1K) uses the Becke88 (B) gradient correct exchange functional and the Becke95 (B95) kinetic-energy-dependent dynamical correlation functional, that Zhao *et al.* promote as an excellent technique to locate saddle point geometries and calculate the corresponding reaction barrier heights. The authors also endorse this functional with claims that it outperforms all other DFT and hybrid DFT methods by a considerable margin and is the best functional in use for thermochemical kinetics.[50] Zhao *et al.* are less enthusiastic, suggesting that BB1K is only a reasonably accurate DFT functional, but due to its better performance than MP2 with a

lower computational cost it is a recommended technique for the determination of transition state structures.[50]

Based on the modified Perdew and Wang exchange functional (MPW) and Becke's 1995 correlation functional (B95) MPWB1K depends on not only the kinetic energy density but the density and the gradient of density as well. This functional yields good results for thermochemistry, thermochemical kinetics, hydrogen-bonding and other weak interactions, enabling it to produce excellent saddle point geometries.[49] The Boese-Martin functional for kinetics (BMK) is able to produce transition state barrier height with an accuracy of ~2 kcal mol^{-1}; however, this is achieved at the expense of the equilibrium parameters. The variable exact exchange within this functional enable it to be relied upon for both relative stabilities of geometries as well as barrier heights.[52]

The τHCTHhyb functional includes kinetic energy density (τ) to enhance its performance resulting in a highly accurate functional that is capable of operating with or without the use of exact exchange. The inclusion of kinetic energy density has the potential to simulate delocalised exchange, which offers an improvement to this GGA.[53] However, Xu *et al.* describe τHCTHhyb as the worst meta-hybrid GGA as it is not good enough to produce reliable transition state structures, resulting in an underestimation of the reaction barrier height. This means that transition states for small reaction barriers cannot be located as this functional would not be able to calculate the barrier.[8]

Most of the hybrid meta-GGAs, including TPSS25B95[54] are considered to produce better predictions for transition state geometries than GGAs and hybrid GGAs. With the exception of τHCTHhyb, these functionals are considered a cheaper alternative to MP2 as they produce results of a similar or better quality.[8]

3.3.4.6 Doubly Hybrid Functionals

Doubly hybrid density functionals are like a hybrid functional but have an additional non-local component to the correlation and exchange energies. In the review by Xu e*t al.* this non-local component is an orbital-dependent term with the form of the MP2 correlation energy, computed using either the Hartree-Fock or the Kohn-Sham orbitals, which are both functionals of the electron density.

Two multi-coefficient correlation and density functional methods, MC3BB and MC3MPW, are based on a mixed scaling-all-component theory and hybrid meta density

functional theory with empirical parameters. The multi-coefficient 3-parameter Becke88-Becke95 including kinetic energy density (MC3BB) functional is a more accurate technique in comparison to other methods that operate with a similar computational cost.[55] Xu *et al.* appreciated the overall reasonable accuracy of the MC3BB functional as well as the multi-coefficient 3-parameter modified Perdew-Wang not including kinetic energy density (MC3MPW) functional. Both methods represent a good compromise between the accuracy, cost and ease of use of the procedure during calculations.[55]

The B2PLYP functional includes two parameters and two orders of perturbation theory and a perturbative correlation with the LYP functional (PLYP).[56] Whilst Grimme *et al.* regards B2PLYP as the best general purpose density functional, Xu *et al.* state that it is a poorer performer than both MC3BB and MC3MPW. However, B2LPYP has been described as an improvement upon M06-L, specifically when calculating reaction barrier heights; this improvement has been attributed to the 47% HF exchange that the B2PLYP functional contains exchange.[33]

Xu *et al.* suggest that all three of these doubly hybrid methods all perform better than the expensive QCISD wavefunction method. However, due to the poor performance of the MP2 component, the results of doubly hybrid GGAs are worse than those of the hybrid meta GGAs, especially when considering heavy atom transfer.

3.3.4.7 Which Functionals are Recommended for Locating Transition States?

Xu *et al.* concluded that the GGAs, the meta-GGA and the majority of the hybrid functionals, are not recommended for the location of transition state structures due to the errors in the geometries that these functionals produce. These geometrical errors are attributed to the underestimation of the barrier heights. The findings of this study supports those investigating the ozonolysis of terpenes in that B3LYP is not a suitable functional for transition state location.[8, 18-24] Wave-function methods would be impractical for transition state location due to their increased computational costs. Hybrid-meta GGAs are recommended over the GGA's and most hybrid GGAs; however, there is only a single functional that Xu *et al.* recommend over B3LYP – MPW1K. The error generated by a calculation conducted with the MPW1K functional offers a threefold improvement over the equivalent B3LYP calculation. The MPW1K functional produces this increase in accuracy with a similar performance to MP2, with a lower computational cost.

3.4 Basis Sets

A basis set is defined as *'the mathematical representation of molecular orbitals within a molecule'* and can be thought of as a spatial restriction imposed on an electron, such as an atomic orbital. A Linear Combination of Atomic Orbitals (LCAO) or basis function, are used to construct molecular orbitals, described by Equation 3.16, where ψ_{mol} is the molecular orbital, ϕ_a are the functions contained within the basis set and c_{ia} are the atomic orbital coefficients.

$$\psi_{mol} = \sum_{i=1}^{n} c_{ia}\phi_a \tag{3.16}$$

Basis sets can be simple combinations of orbitals or be more complex, including better descriptions of the diffuse and/or polarizability of the orbitals. Additions of diffuse functions are important when attempting to obtain a balanced treatment of bond energies across multiple bond types[57]; however, they significantly slow the SCF convergence for larger molecules.[58] With chemical knowledge of the system being investigated, basis sets can be tailored to describe the various physical properties of interest. The types of atomic orbital combinations used in the LCAO approximation fall into two categories: Slater-type orbitals (STO) and Gaussian type orbitals (GTO).

3.4.1 Slater Type Orbitals

The general form for the STO[59] uses spherical polar coordinates

$$\chi_{\zeta nml}(r,\theta,\phi) = NY_{lm}(\theta,\phi)r^{n-1}e^{-\zeta r} \tag{3.17}$$

where N is a normalisation constant, Y_{lm} are spherical harmonics, r is the electron-nucleus distance and ζ describes the spatial extent of the orbital. STOs are primarily used when considering atomic and diatomic systems, where high accuracy is required.[4]

3.4.2 Gaussian Type Orbitals

The form for GTO using the same spherical polar coordinates used for STO is shown in Equation 3.19

$$\chi_{\zeta nml}(r,\theta,\phi) = NY_{lm}(\theta,\phi)r^{(2n-2-l)}e^{-\zeta r^2} \tag{3.18}$$

The general form for the GTO[57] uses Cartesian coordinates

$$\chi_{\zeta, l_x, l_y, l_z}(x, y, z) = N x^{l_x} y^{l_y} z^{l_z} e^{-\zeta r^2} \tag{3.19}$$

where the sum of l_x, l_y and l_z determines the angular momentum of the orbital. Unfortunately the dependence on r^2 in the exponential function results in poor behaviour of the wavefunction about the nucleus, rapidly dropping off as the distance from the nucleus increases. Although a large number of GTOs are required to replicate a result using STOs, they are more commonly used to construct a basis set as they easily evaluate two-electron intervals, a failing of STOs.

3.4.3 Basis Set Construction

A basis set is required to have sufficient functions to describe all of the electrons for a neutral atom. First row elements are represented by two *s*-orbitals (1*s* and 2*s*) and three *p*-orbitals (2*p_x*, 2*p_y*, 2*p_z*), portrayed by either a STO or a linear combination of GTOs. Though this accurately describes atomic orbitals it fails to fully describe a molecular system, so additional functions are required.

Each atomic orbital of the first row elements can be described by two functions *1s*, *1s'*, *2s*, *2s'*, *2p* and *2p'*; basis sets that include these two functions are known as double-zeta basis sets. The difference between *1s* and *1s'* arises from the different orbital exponent values (ζ, Equations 3.19 and 3.20). A basis set in which these two functions are used to describe the atomic orbitals is referred to as a double-zeta basis set. It is possible to split the basis set further into triple-, quadruple-zeta and larger. This split basis is not used to describe every orbital; as core electrons do not contribute to the same extent as the valence electrons, computational cost is saved by only using a single function for the core electrons. There are two main types of these basis sets: Pople[60] and Dunning.[61]

The general form of Pople style basis sets is

k-nlm++G**

using primitive GTOs, denoted by the letters: k, n, l and m. These represent the core electrons (k), inner valence orbitals (n), medium valence orbitals (l) and outer valence orbitals (m). Gaussian functions are used to denote the atomic orbital, which are then expanded with the use of split valence functions (6-31G), differentiating the treatment of the core and valence electrons. Pople basis sets are further extended by the introduction of diffuse functions (6-31+G) and polarisation functions (6-31G(d)). Diffuse functions

are important in systems where the electrons are distant from the nucleus, as it allows the orbitals to occupy a larger region of space. The addition of a single + adds a diffuse function to the heavier atom, whereas ++ also add diffuse functions to the hydrogen atom. Polarisation functions incorporate the addition of angular momentum to an orbital, meaning that it is able to change shape beyond the usual requirements for the ground-state. The addition of one polarisation function (a single * in the form above) adds a *1d* polarisation function to the heavy atom and an *f* function for transition metals. The addition of a second polarisation function (two ** in the form above) incorporates a *1p* polarisation function on the hydrogen atom.[6]

The general form of Dunning style basis sets is

$$cc\text{-}pVXZ$$

where *cc* refers to the correlation consistent basis, *p* shows the system is polarised, *V* represents the valence electrons, *X* is double (D), triple (T), quadruple (Q) etc. and *Z* shows a zeta potential. Dunning's basis sets systematically converge the correlation energies to the basis set limit; as more basis functions are added a better representation of the wavefunction is achieved. The energy is at its lowest when the number of basis functions is infinite, this is the complete basis set (CBS) limit.

Further augmentations have been added by Dunning *et al.*[62], with the form *aug-cc-pVXZ*, and are typically seen in conjunction with high-level electron-correlation wavefunction methods. The introduction of augmentations make the basis set 5-7 times more costly than their non-augmented counterparts.[16]

The choice of basis set is a compromise between the basis set size, its accuracy to the true energy value and the computational cost. The more basis functions that are included the better the physical description of the system. Common practice involves a series of calculations being conducted in sequence while systematically increasing the size of the basis set e.g. (cc-pVDZ, cc-pVTZ, cc-pVQZ); with each addition of basis functions the difference between the computed and true values will decrease until a saturation point where no further changes is observable.

3.5 Geometry Optimisation

In order to obtain the accurate energies of a given system, geometry optimisation calculations are utilised. The principle of a geometry optimisation is to calculate the energy of a molecular system using the given nuclear coordinates using the desired level of theory and basis set. Geometry optimisation calculations then search for the minimum energy structure (global minimum), which they achieve through an iterative process. The initial optimisation is conducted on the original nuclear coordinates, the nuclei positions are then relocated and the energy recalculated. This process continues until a stationary point on the potential energy surface is located.

Such optimisations are simple for diatomic molecules as only a single variable is to be altered; however, larger molecular systems can have a large number of degrees of freedom. The potential energy surface of larger molecules could contain several local minima or saddle points which the optimisation may locate, rather than the global minimum. To help assist the location of the global minimum the original nuclear coordinates must be carefully selected as will the convergence criteria of the optimisation.

3.6 Vibrational Frequency Analysis

After the stationary point has been located on the potential energy surface, vibrational frequency analysis is used to differentiate between energy minima and saddle points, which is relatively easy to undertake. When multiple degrees of freedom are being considered the second derivatives of the potential energy function of a system, in relation to its equilibrium coordinates is required. The second derivatives are then used to calculate the harmonic vibrational frequencies.

Following the calculation of all the normal modes of vibration, the potential energy minima and saddle points are identified. Potential energy minima correspond to the most physically stable structure, and possess vibrational frequencies that are all positive. Saddle point geometries, relate to transition state structures and represents an energy maximum along a single coordinate. This is indicated through the presence of an imaginary (negative frequency). The order of the saddle point is shown through the number of imaginary frequencies e.g. a third order saddle point would produce three imaginary frequencies.

The major shortcoming of harmonic vibrational analysis is that it fails to account for vibrational anharmonicity, resulting in the computed frequencies being larger than those obtained experimentally. The common correctional method is the use of a scaling factor, which brings the calculated and recorded frequencies into better agreement.[62]

3.7 Transition State Optimisation

In the cases described in Chapters 7 and 8, where reaction pathways are being investigated, it is important to determine the transition state structures that join each of the energy minima on the potential energy surface (PES). The optimisation of a transition state structure not only gives geometrical data, but the energetics involved with the structure that leads to the determination of the reaction barrier height. A common method for searching for transition states requires the minimum energy structures of the reactants and products involved in the given reaction step; the Quadratic Synchronous Transit (QST) method searches for energy maxima along the PES that connect the reactants and products.[11] Similarly to the QST2 method, the QST3 method uses the minimum energy structures of the reactant and product; however, it also requires an estimated geometry of the transition state.

Besides the QST methods, geometry optimisation calculations are utilised in order to obtain the accurate energies of the given system. Geometry optimisation calculations usually search for the minimum energy structure on a potential energy curve; however, transition states are energy maxima along one coordinate. In order to obtain these structures a TS calculation is used; these calculations optimise to transition structures rather than converging on a local minimum. In conjunction with this calculation the CalcFC instruction is used; this command results in the force constants being calculated at the first point. A NoEigenTest calculation provides an alternative to the TS calculation. This calculation supresses the curvature of the Berny optimisation (which by default is converging towards a minima), overcoming the test for a single imaginary frequency and allows the continuation of the optimisation calculation, even with the presence of an imaginary frequency, otherwise the optimisation calculation would fail.

For confirmation that a transition state structure is appropriate for the reaction process of interest, the Intrinsic Reaction Path is used. A reaction path is defined as curve on a potential energy surface connecting the reactants and products through a transition state; the curve is located by following the steepest decent path or minimum energy path (MEP)

from transition state toward reactants and products.[4, 63, 64] It is much easier to find the MEP by following PES downhill from a transition state structure than uphill from a minimum.[58] The use of mass-weighted Cartesian coordinates, results in the path generating an Intrinsic Reaction Coordinate (IRC).[63, 64]

In order to utilise the IRC method, a transition state structure must firstly be identified to compute rather than estimate the initial force constants and then a frequency calculation on this optimised structure is then carried out. This frequency calculation *i*) verifies that a transition structure has indeed been found as it possess an 'imaginary' vibrational frequency, *ii*) determines the zero-point energy of the transition state and *iii*) generates the force constant data required for the IRC calculation.[6]

Molecules react with each other while vibrating about an equilibrium configuration and rotating as a whole about the centre-of-mass, whilst exchanging energies in all degrees of freedom. The IRC represents the vibrationless-rotationaless motion path of the reacting system.[66] Unfortunately reaction paths are notoriously difficult to follow[66], which can result in an IRC calculation not reaching the desired reactant or product, as it is possible that multiple transition states exist along the reaction path.[63] However, Fukui suggests that as long as the calculation begins with the transition state structure and the neighbouring points are successfully plotted by numerical gradients, the solution is easily obtained.[65]

3.8 Computational Details

High-level calculations require sufficient processors and large amounts of system memory, therefore PC-based *ab initio* packages are often too slow, so high performance computer systems were utilised for the calculation reported in this thesis. These are based on multiprocessor systems offering high speed disk drives to facilitate proficient calculations. The cluster utilises a GNU/Linux based operating system and has the following specification.

ALICE: 208 standard compute nodes

A pair of eight-core Intel Xeon Ivy Bridge CPUs running at 2.6GHz and 64GB of RAM per node

Approximately 428GB of local storage per node

High performance Panasas storage system provides 550TB, accessible to all nodes

SPECTRE: 32 compute nodes

A pair of 4-core 2.6Ghz Intel Xeon Nehalem CPUs and 24GB RAM per node

Approximately 400GB of local storage per node

High performance Panasas storage system provides 550TB, accessible to all nodes

ALICE and SPECTRE are High Performance Computing (HPC) clusters at the University of Leicester. ALICE was purchased through a £2 million CIF (Capital Infrastructure Fund) award. It is a research facility available to all academic staff, postdoctoral researchers and postgraduate research students. SPECTRE (Special Computational Teaching and Research Environment) provides an interactive and batch Linux environment for staff and students.

3.9 References

1. N. J. B. Green, *Quantum Mechanics 1: Foundations*, Oxford University Press, Oxford, 1997

2. G. B. Arfken, H.-J. Weber, *Mathematical Methods for Physicists*, 4th ed., Academic Press, San Diego, 1995

3. P. W. Atkins, *Molecular Quantum Mechanics*, 3rd ed, Oxford University Press, Oxford, 1997.

4. F. Jenson, *Introduction to Computational Chemistry*, Wiley, Chichester, 1999

5. C. Møller and M. S. Plesset, *Physical Review*, 1934, **46**, 618-622.

6. J.B. Foresman and Æ. Frisch, *Exploring Chemistry with Electronic Structure Method: A Guide to Using Gaussian*, Gaussian, Inc. Pittsburgh, PA, **1993**

7. M. J. Frisch, G. W. Trucks, H. B. Schlegel, G. E. Scuseria, M. A. Robb, J. R. Cheeseman, J. A. M. Jr., T. Vreven, K. N. Kudin, J. C. Burant, J. M. Millam, S. S. Iyengar, J. Tomasi, V. Barone, B. Mennucci, M. Cossi, G. Scalmani, N. Rega, G. A. Petersson, H. Nakatsuji, M. Hada, M. Ehara, K. Toyota, R. Fukuda, J. Hasegawa, M. Ishida, T. Nakajima, Y. Honda, O. Kitao, H. Nakai, M. Klene, X. Li, J. E. Knox, H. P. Hratchian, J. B. Cross, V. Bakken, C. Adamo, J. Jaramillo, R. Gomperts, R. E. Stratmann, O. Yazyev, A. J. Austin, R. Cammi, C. Pomelli, J. W. Ochterski, P. Y. Ayala, K. Morokuma, G. A. Voth, P. Salvador, J. J. Dannenberg, V. G. Zakrzewski, S. Dapprich, A. D. Daniels, M. C. Strain, O. Farkas, D. K. Malick, A. D. Rabuck, K. Raghavachari, J. B. Foresman, J. V. Ortiz, Q. Cui, A. G. Baboul, S. Clifford, J. Cioslowski, B. B. Stefanov, G. Liu, A. Liashenko, P. Piskorz, I. Komaromi, R. L. Martin, D. J. Fox, T. Keith, M. A. Al-Laham, C. Y. Peng, A. Nanayakkara, M. Challacombe, P. M. W. Gill, B. Johnson, W. Chen, M. W. Wong, C. Gonzalez and J. A. Pople, Gaussian, Inc., Wallingford CT, 2004, vol. Revision E.01.

8. X. Xu, I. M. Alecu, D. G. Truhlar, *Journal of Chemical Theory and Computation*, 2011, 7, 1667-1676.

9. B. J. Lynch, D. G. Truhlar, *Journal of Physical Chemistry A*, 2001, **105**, 2936-2941.

10. C. E. Check, T. M. Gilbert, *Journal of Organic Chemistry*, 2005, **70**, 9828-9834.

11. B. R. J. Muhyedeen, *European Journal of Scientific Research*, 2007, **16**, 490-505.

12. A. D. Becke, *Journal of Chemical Physics*, 1993, **98**, 5648-5652.

13. P. J. Stephens, F. J. Devlin, C. F. Chabalowski and M. J. Frisch, *Journal of Physical Chemistry*, 1994, **98**, 11623-11627.

14. S. Grimme, *Angewandte Chemie (International Edition)*, 2006, **45**, 44600-4464.

15. P. C. Redfern, P. Zapol, L. A. Curtiss, K. J. Raghavachari, *Journal of Physical Chemistry A*, 2000, **104**, 5850-5854.

16. S. Grimme, M. Steinmetz, M. Korth, *Journal of Organic Chemistry*, 2007, **72**, 2118-2126.

17. S. E. Wheeler, D. H. Ess and K. N. Houk, *Journal of Physical Chemistry A*, 2008, **112**, 1798-1807.

18. D. Zhang and R. Zhang, *Journal of Chemical Physics*, 2005, **122**, 114308.

19. T. L. Nguyen, J. Peeters and L. Vereecken, *Physical Chemistry Chemical Physics*, 2009, **11**, 5643-5656.

20. R. C. D. Oliveira and G. F. Bauerfeldt, *Journal of Chemical Physics*, 2012, **137**, 134306.

21. Y. Zhao, R. X. Zhang, H. Wang, M. X. He, X. M. Sun, Q. Z. Zhang, W. X. Wang and M. Y. Ru, *Journal of Molecular Structure:Theochem*, 2010, **942**, 32-37.

22. R. Gutbrod, E. Kraka, R. N. Schindler and D. Cremer, *Journal of the American Chemical Society*, 1997, **119**, 7330-7342.

23. D. Zhang and R. Y. Zhang, *Journal of the American Chemical Society*, 2002, **124**, 2692-2703.

24. T. L. Nguyen, R. Winterhalter, G. Moortgat, B. Kanawati, J. Peeters and L. Vereecken, *Physical Chemistry Chemical Physics*, 2009, **11**, 4173-4183.

25. J. A. Pople, M. Head-Gordon, K. Raghavachari, *Journal of Chemical Physics*, 1987, **87**, 5968.

26. B. J. Lynch, Y. Zhao, D. G. Truhlar, *Journal of Physical Chemsitry A*, 2005, **109**, 1643-1649.

27. A. D. Becke, *Physical Review A*, 1988, **38**, 3098-3100.

28. C. Lee, W. Yang, R. G. Parr, *Physical Review B*, 1988, **37,** 785-789.

29. N. E. Schultz, Y. Zhao, D. G. Truhlar, *Journal of Physical A,* 2005, **109**, 11127-11143.

30. J. Zheng, Y. Zhao, D. G. Truhlar, *Journal of Chemical Theory and Computation*, 2009, **5**, 808-821.

31. J. P. Perdew, K. Burke, M. Ernzerhof, *Physical Review Letters*, 1996, **77**, 3865-3868.

32.   Y. Zhao, D. G. Truhlar, *Journal of Chemical Physics*, 2008, **128**, 184109.

33.   Y. Zhao, D. G. Truhlar, *Journal of Chemical Physics*, 2006, **125**, 194101.

34.   Y. Zhao, D. G. Truhlar, *Accounts of Chemical Research*, 2008, **41**, 157-167.

35.   J.-D. Chai, M. Head-Gordon, *Journal of Chemical Physics*, 2008, **128**, 084106.

36.   B. J. Lynch, P. L. Fast, M. Harris, D. G. Truhlar, *Journal of Physical Chemistry A*, 2000, **104**, 4811-4815.

37.   C. Adamo, V. Barone, *Chemical Physics Letters*, 1997, **274**, 242-250.

38.   T. W. Keal, D. J. Tozer, *Journal of Chemical Physics*, 2005, **123**, 121103.

39.   C. Adamo, M. Cossi, V. Barone, *Journal of Molecular Structure (Theochem)*, 1999, **493**, 145-147.

40.   C. Adamo, V. Barone, *Journal of Chemical Physics*, 1998, **108**, 664-675.

41.   S. Grimme, *Journal of Computational Chemistry*, 2006, **27**, 1787-1799.

42.   A. D. Becke, *Journal of Chemical Physics*, 1997, **107**, 8554.

43.   J.-D. Chai, M. Head-Gordon, *Physcial Chemistry Chemical Physics*, 2008, **10**, 6615-6620.

44.   Y. Zhao, D. G. Truhlar, *Journal of Chemical Theory and Computation*, 2008, 4, 1849-1868.

45.   Y. Zhao, N. E. Schultz, D. G. Truhlar, *Journal of Chemical Physics*, 2005, **123**, 161103.

46.   Y. Zhao, N. E. Schultz, D. G. Truhlar, *Journal of Chemical Theory and Computaiton*, 2006, **2**, 364-382.

47.   Y. Zhao, D. G. Truhlar, *Journal of Physical Chemistry A Letters*, 2006, **110**, 13126-13130.

48.   Y. Zhao, D. G. Truhlar, *Theoretical Chemical Accoutns*, 2008, **120**, 215-241.

49.   Y. Zhao, D. G. Truhlar, *Journal of Physical Chemistry*, 2005, **109**, 5656-5667.

50.   Y. Zhao, D. G. Truhlar, *Journal of Physcial Chemsitry A*, 2004, **108**, 2715-2719.

51.   Y. Zhao, D. G. Truhlar, *Journal of Physcial Chemistry A*, 2004, **108**, 6908-6918.

52.   A. D. Boese, J. M. L. Martin, *Journal of Chemical Physics*, 2004, **121**, 3405.

53.   A. D. Boese, N. C. Handy, *Journal of Chemical Physics*, 2002, **116**, 9559.

54.   M. M. Quintal, A. Karton, M. A. Iron, D. Boese, J. M. L. Martin, *Journal of Physical Chemistry A*, 2006, **110**, 79-716.

55.   Y. Zhao, B. J. Lynch, D. G. Truhlar, *Journal of Physcial Chemistry A*, 2004, **108**, 4786-4791.

56.   S. Grimme, *Journal of Chemical Physics*, 2006, **124**, 034108.

57.   S. F. Boys, *Proceedings of the Royal Society of London A*, 1950, **200**, 542.

58.   P. Sinha, S. E. Boesch, C. M. Gu, R. A. Wheeler , A. K. Wilson, *Journal of Physical Chemistry A*, 2004, **108**, 9213.

59.   J. C. Slater, *Physical Review*, 1930, **36,** 57.

60.   W. J. Hehre, R. F. Stewart, J. A. Pople, *Symposia of the Faraday Society*, 1968, **2**, 15.

61.   T. H. Dunning, *Journal of Chemical Physics*, 1971, **55**, 716.

62.   T. H. Dunning, *Journal of Chemical Physics*, 1989, **90**, 1007.

63.   C. Gonzalez, H. B. Schlegel, *Journal of Physical Chemsitry*, 1990, **94**, 5523-5527.

64.   P. Tao, J. D. Larkin, B. R. Brooks, *Some Applications of Quantum Mechanics*, Prof. Mohammad Reza Pahlavani (Ed.), ISBN: 978-953-51-0059-1.

65.   K. Fukui, *Accounts of Chemical Research*, 1981, **14**, 363-368.

66.   C. Gonzalez, H. B. Schlegel, *Journal of Chemical Physics*, 1991, **95**, 5853-5860.

Chapter Four

Construction of a New Multipass Cell

4.1 Introduction

4.1.1 Beer-Lambert Law

Infrared spectra are often presented in absorbance units, which depends on the amount of light absorbed by a given sample.[1] The absorbance of a sample is calculated by

$$A = log\left(\frac{I_0}{I}\right) \tag{4.1}$$

where A is the absorbance, I_0 is the initial intensity and I is the detected intensity. The absorbance is related to the concentration of the sample through the Beer-Lambert law

$$A = \varepsilon l c \tag{4.2}$$

where ε is the molar absorption coefficient of the sample, l is the path-length and c is the concentration of the absorber. This relationship clearly shows that sensitivity is maximised through the use of a long path-length; these can be created using a multipass system[2], where the radiation is passed back and forth through the sample via a set of mirrors. This method improves sensitivity without the need to increase the concentration of the sample. If the concentration was increased then there would be more molecules to absorb the radiation so the overall absorbance would increase. However, if the concentration were to increase to a sufficiently high level then the Beer-Lambert law begins to break down.

4.1.2 What is a Multipass Reflection Cell?

There are two commonly documented types of multipass reflection systems. Herriot cells consist of two spherical mirrors that are facing one another; each reflection of the radiation between these mirrors creates an ellipse shaped image. The radiation enters and exits this type of cell via a hole made into one of the mirrors. The number of traversals is determined by the distance between the two mirrors. Although Herriot cells are the simplest type of multipass system and provide outstanding opto-mechanical stability, if longer optical path-lengths are required then larger sized mirrors would also be required.[3] This is not an issue for White type multipass reflection cells.

White cells enable the use of an optical system, when only a small amount of sample is available, by passing the radiation back and forth through the same sample volume a great number of times. It has been extensively reported that the most fundamental components

of such a system is the three spherical concave mirrors which all have the same radius of curvature.[2-7] The three mirrors are arranged with two optical mirrors, which are very close together, positioned at a distance from a singular field mirror[3], on which images are produced, so that the length of the cell is equal to the radii of curvature.[2, 3] The radiation is reflected between these mirrors until the required path-length has been obtained.[5]

McManus *et al.* explored the use of astigmatic mirrors which possessed differing radii of curvature so the reflected beams would have a different focus. They found that the reflected radiation better fills the volume of the cell so that the created images better fill the area of the field mirror, so smaller volume and mirrors could be used. Whilst the use of an astigmatic cell seems greatly advantageous, extreme precision is required during the production of the mirrors; the two differing radii of curvature have been stated as requiring an accuracy of 1 part in 10^4 to ensure that reflections proceed as needed.[8]

4.1.3 How do White Type Multipass Systems Work?

White Cells operate via radiation entering a cell close to a field mirror (B) and reflecting backwards and forwards between this field mirror and the two optical mirrors (A and A'), as show in Figure 4.1 (taken from White's paper published in 1942).[4]
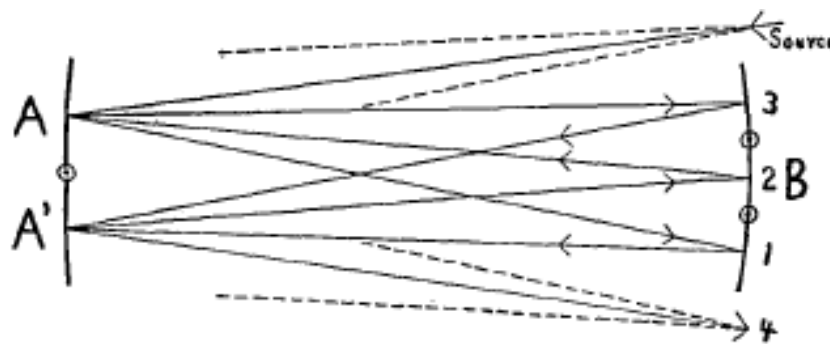
Figure 4.1: White cell schematic showing reflection of radiation between the field mirror (B) and the optical mirrors (A and A'), resulting in images 1-4[4]

Each of the successive images (1-3) created on the field mirror is offset to one side or another until an image falls beyond the edge of the mirror; this is known as the exit image (4).[4] As with the entrance of the radiation the exit image is also found near the edge of the field mirror.[4] In the original design of White cells the three concave mirrors were circular in shape; however, as development of the technique has progressed, it has been found that altering the shape of the field mirror is more advantageous. The use of 'T-

shaped' field mirror allows two rows of images to be produced, doubling the potential path-length of the original White cells[6]; this is well depicted using an image published by Edwards in 1961[6] (Figure 4.2).
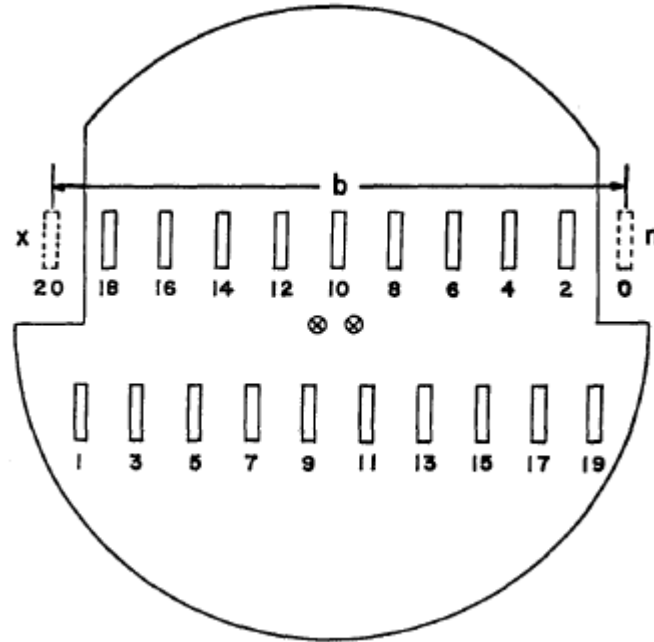
Figure 4.2: 'T-shaped' field mirror, showing 20 images resulting from 40 passes. *n* and *x* show the entrance and exit images respectively and b is the total distance between these images. The crossed circles show the centre of curvature of the back mirrors[6]

The field mirror shown in Figure 4.2 allows for 40 traversals through the cell (where a single traversal is either the reflection from the field mirror to one of the optical mirrors or from one of the optical mirrors to the field mirror), which produces a total of 20 images. The radiation enters the cell at *n* (image 0) before reflecting off one of the optical mirrors resulting in image 1, a further two traversals results in image 2. The sequence of traversals continues until the radiation exits (image 20) the cell at *x* and travels to a detector. Using numerous traversals is advantageous[6]; however, the maximum number of traversals is governed by the width of the field mirror[5] and the separation between the centres of curvature of the two optical mirrors. This adjustment controls the number of times the radiation can pass through the cell.[4] It is important to note Bakalyar's observation that the signal-to-noise ratio (SNR) produced by White cells is independent of the path-length of the cell.[9] Instead the authors suggest that the SNR for a laser source is dependent on the relative magnitudes of the contributors to noise

$$SNR = \frac{\Delta I(v)}{\sqrt{N_1^2 + N_2^2 + N_3^2 + N_4^2}} \qquad (4.3)$$

where $\Delta I(v)$ is the ac signal registered in the average, N_1 is the shot noise proportional to $\sqrt{I(v)} \approx \sqrt{I_0'}$, N_2 is the background noise of the instrument, N_3 is the laser amplitude fluctuations proportional to I_0' (the transmitted laser intensity) and N_4 is the atmospheric turbulence proportional to $I_0'l$ (the product of the transmitted laser intensity and path-length of the White cell). If a lobar source is being used then limits such as aperture size will result in a low SNR.

The number of traversals can also be controlled by mounting the three mirrors on spring-loaded holders; with the use of micrometre screws each mirror can be moved around on both the horizontal and vertical axes[10] giving tunability to the number of passes. Such controllability allows for good correction of aberrations[6], the failure of a mirror (or lens) to bring rays of light coming from a source to a single focus, resulting in a distorted image.

4.1.4 Why are White Type Multipass Systems Useful?

White cells are able to limit the final image to the size of the mirror, and produce quite sharp images even after numerous traversals. White adds that the only loss of intensity is through either absorption or scattering on the reflecting surfaces. He also states a number of advantages for the use of long optical paths when used within restricted volumes[4]: the number of traversals can be easily adjusted through simple manipulation of the optical mirrors (A and A' Figure 4.1); this does not affect the positioning of the exit image so no further adjustments are required on the wider optical system. Light losses on the surfaces of the mirrors are kept to an absolute minimum and besides the entrance and exit windows the radiation does not have to pass through any other optical material, which could account for other losses.

The increased number of traversals used in White type cells makes them extremely useful. When characterising high boiling point compounds there were two potential approaches: to heat the absorption cell; which reduces the accuracy of the absorption measurement, or to use a very long absorption cell.[4] By reflecting the radiation multiple times through the same compact sample volume, the requirement for cell heating is negated[10, 11], thus increasing the accuracy of the absorption in comparison to older measurements. The use of reflected radiation is also advantageous when only a small amount of sample is

available[4]; in such low concentration systems, passing the radiation back-and-forth enhances what would have otherwise been weak spectra, as described by the Beer-Lambert law.[6, 11]

4.1.4.1 Use of White Cells with Fourier Transform Infrared Spectroscopy

Fourier Transform Infrared (FTIR) spectroscopy is a common method for environmental chamber investigations. The high sensitivity of FTIR assists with the identification of minor product channels. Sensitivity is related to absorbance via the Beer-Lambert law (Equation 4.2).

White cells tend to be mounted vertically on top of the spectrometer's sample compartment[12]; this requires transfer optics in order to divert the radiation firstly into the cell and then from the cell to the spectrometer's detector. The mirrors used within the cell itself require a gold coating 99.1 – 99.3% reflection in the infrared.[10, 11] As these multipass cells are mounted onto infrared spectrometers, it is important to maintain a stable alignment of the optic system through both pressure and temperature cycles and any vibrations caused by the pumping system[2], something older systems had a greater susceptibility to, resulting in enlarged reflection images.[11]

4.1.4.2 Uses in Research

Multipass optical systems have been used previously to study the chemistry of the atmosphere; White developed his multipass system enabling it to detect 1 part per billion of many common atmospheric pollutants and later Robert used this to aid with the detection of trace atmospheric species.[3, 11] Armerding *et al.* tested a multipass system under both tropospheric conditions and within a laboratory and found that such a system had exciting applications for both environments as he managed to achieve a 1.2 km path-length outside and a 2.5 km path-length within the laboratory.[7] Bakalyar *et al.* utilised the system specifically to monitor hydroxyl radicals (OH) in the troposphere; they found the use of a White cell a particularly useful method for calibrating their fluorescence instrument for the measurement of OH radicals, which the indirect approach of laser-induced fluorescence does not yield.[9]

4.1.5 Limitations and Disadvantages

The success of the multipass system is highly dependent upon the mirrors used within the White cell; the two optical mirrors and the field mirror must have the same focal length.[4] The adjustments made to the precise positioning of the mirrors are also critical in order to maximise the number of traversals of the system.[11] Disadvantage inherent to all multi-reflection equipment, are the potential for a certain amount of the radiation to be scattered into the reflected beam without having traversed the cell the desired number of times[3] and the foreseeable loss of signal occurring after many traversals.[11] Astigmatism limits the maximum number of traversals the multi-reflection system is capable of, which can cause enlargement of successive images until the images eventually begin to overlap.[10] Rather than just focussing on the cell, White felt it important to note that the system is at the mercy of the uniformity and potential interference from the sample.

4.2 Current White Type Cell with a 4 m Path-length

4.2.1 Limitations and Proposed Improvements of the Current Multipass System

The old White type cell was designed and constructed by Mark Daniels, a MChem project student. To keep the costs manageable, the cell was a 5 mm thick plastic tube, which was 405 mm in length and had an internal diameter of 110 mm (Figure 4.3). Three metal ports have been threaded onto the tube: the bottom port to connect to the pump to evacuate the cell, a centre port in order to inject the molecule of interest and finally a top port through which the reactant gas, such as ozone, could be introduced into the cell. This system utilised three circular mirrors with a focal length of 200 mm, with the 2 optical mirrors set at a distance of 0.4 m from the field mirror. In order to achieve the 4 m optical path length, 10 passes between these mirrors is required.
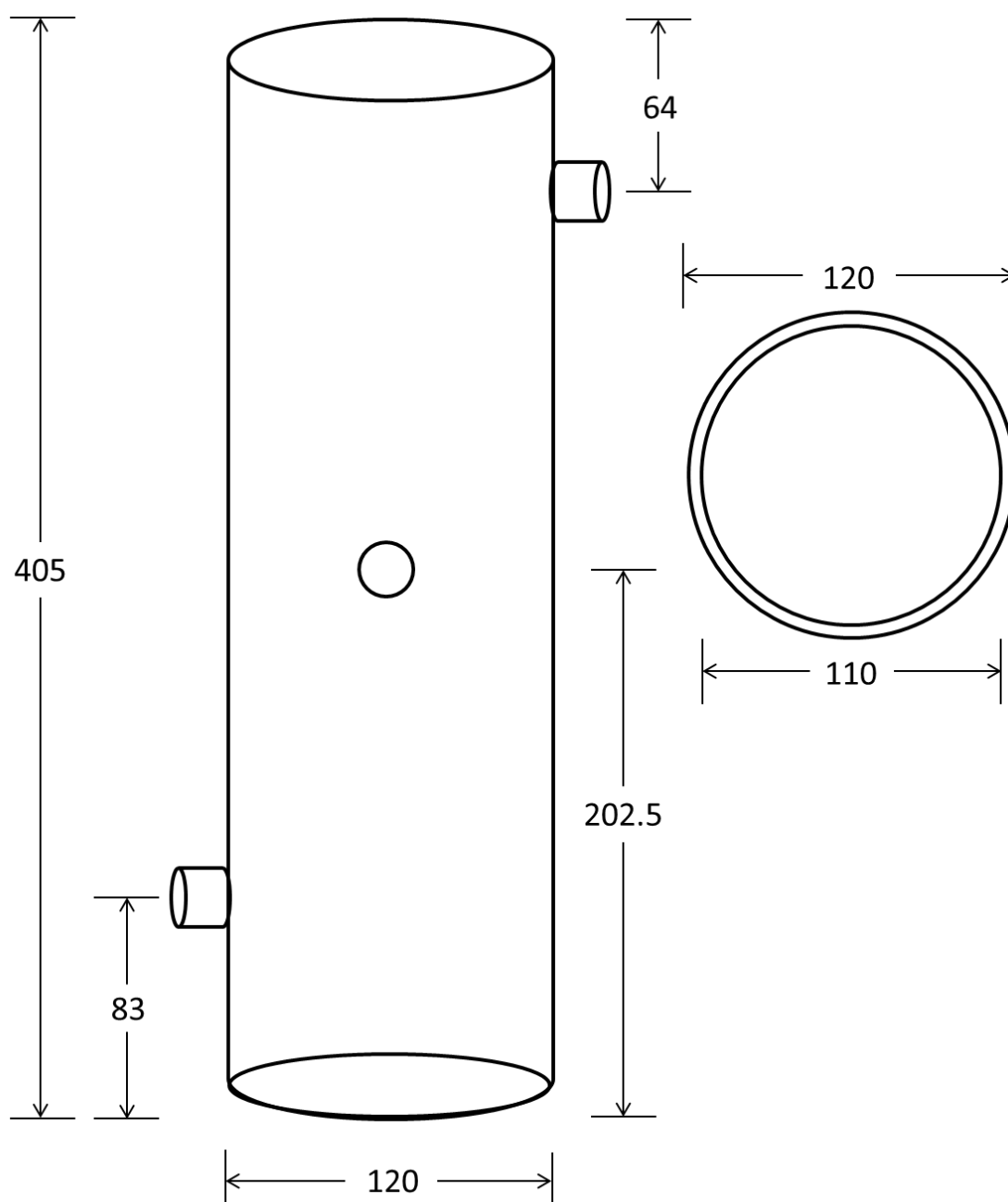
Figure 4.3: Dimensions (mm) for the 4 m White type multipass cell

Whilst the primary objective of the current project is to create a new multi reflection system with an increased path-length of 64 m, other shortcomings of the current setup needed to be overcome. The main issue with the existing 4 m system was that it was prone to leaking; therefore monitoring a reaction over any period of time was impossible. Many potential sources for leaks were examined: the top plate of the cell, which had many fixtures drilled into it in order to hold the optical mirror adjusters and the pressure sensor; the ports on the cell through which the reactants could be introduced; as the cell was a cylinder the walls were curved meaning the ports could not be fitted flush against the cell

wall, so a tight seal could not be guaranteed and a lack of a small lip on either end of the cell meant that the cell sat directly on the top and bottom (which sat on top of the IR spectrometer) metal plates and a seal was only created by squeezing an rubber O-ring against the cell using a circular clamp.

It was found early on that leaks from this current system did not originate from the bottom metal plate; the only potential source for a leak on this plate would be the two NaCl windows through which the radiation passes from the spectrometer into the cell. As the pressure within the White cell is unaffected by the evacuation and venting of the IR spectrometer, it was assured that no reactant was leaking from the cell via these seals.
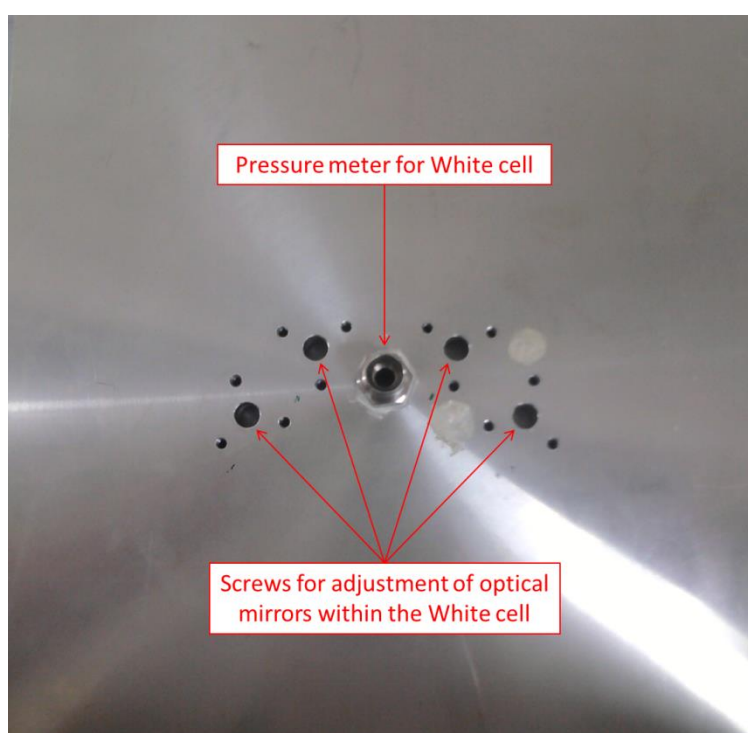
Figure 4.4: Top plate of the original 4 m White cell, showing the pressure gauge port and the four adjusters for the two optical mirrors

As can be seen from Figure 4.4, the top metal plate of the multipass cell generates the greatest potential for leaks from the cell, due to the increased number of attachments and alterations to this plate: the central port attaches the pressure sensor to the cell and the screws used to adjust the optical mirrors within the cell pass through the four larger holes on the top plate. The adjustment screws are held in position via circular clamps which are attached to the top plate via three smaller screws in a triangular orientation. The seals between the top plate and the adjustment screws and pressure sensor also involve rubber

O-rings in order to minimise reactants leaking from the cell. Figure 4.4 also shows two incorrectly positioned holes for the adjustment screws which had to be plugged using a vacuum sealant. A vacuum test suggested that it was poor fitting of the adjustment screws rather than these errors that were the major source of reactant leak, showing a key area of improvement for the proposed new White cell.

4.2.2 Maximising the Path-length of the Current Multipass System
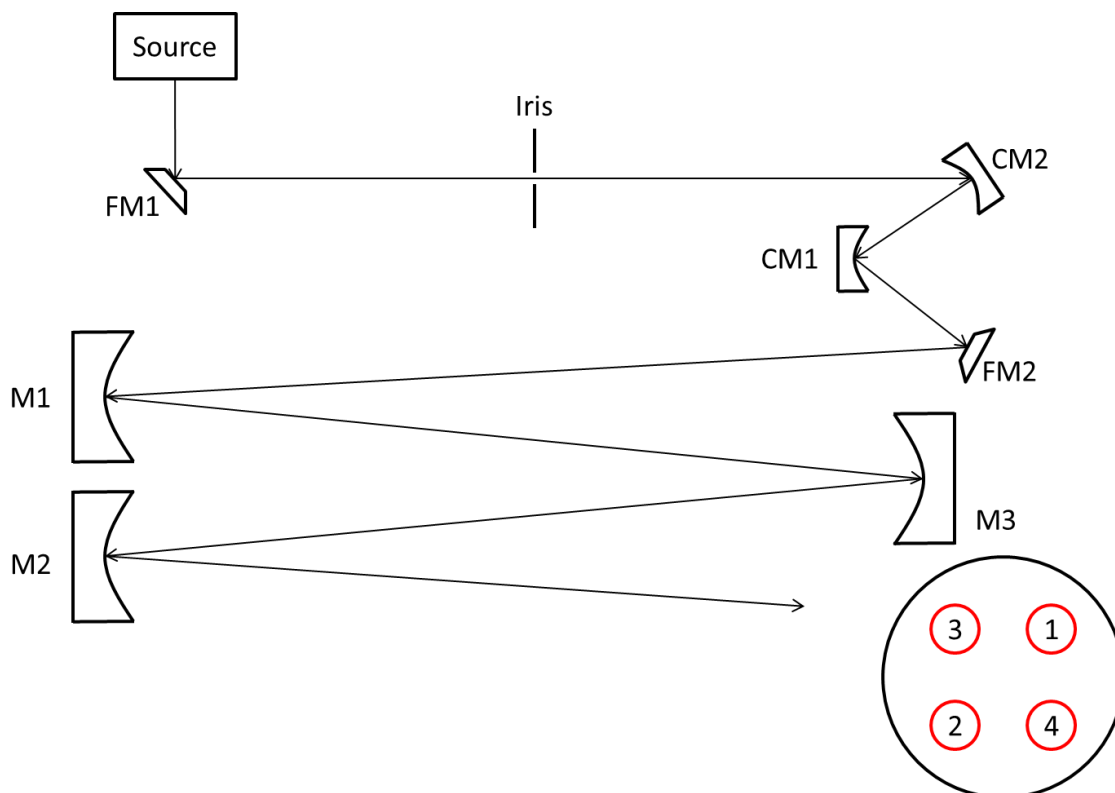
Figure 4.5: Experimental set-up whilst investigating the path-length of the old 4 m multipass system; the flat (FM1 and FM2) and curved mirrors (CM1 and CM2) divert the radiation into the multipass system, which reflects between the optical mirrors (M1 and M2) and the field mirror (M3)

To better understand the required dimensions of the new multipass cell, it is advantageous to maximise the internal mirror configuration of the current system. A visible light source was used in place of IR radiation, so the images created on the field mirror could be seen, the number of passes could be counted and thus the path-length monitored. An iris was used to narrow the white light beam and minimise losses; a wider beam would create images too large for the mirrors, preventing the radiation being reflected back. Besides testing the optical and field mirrors of the multipass system, an additional set of three

mirrors will be analysed that in practice would be used to divert the IR radiation from the spectrometer and into the White cell (Figure 4.5).

The first flat mirror (FM1) is simply used to divert the white light from the source to the three mirror configuration as there was not sufficient room to have all the components set-up at the appropriate distances apart. In the old 4 m system two mirrors in an L-shape configuration are used to divert the IR radiation into the multipass cell; this formation was not deemed to be particularly accurate. Instead a three mirror system optically matched to the field and optical mirrors would assist in the maximisation of the path-length of the new White cell. This new three mirror configuration involves reflection between two curved mirrors (CM1 and CM2) before a second flat mirror (FM2) diverts the radiation into the multipass system.

The optical mirrors (M1 and M2) within the multipass system were placed 0.01 m apart and at a distance of 0.4 m from the field mirror (M3). Using the white light source, this mirror arrangement enabled 10 passes between the optical and field mirrors and the image pattern created on the field mirror can be seen in Figure 4.5. Achievement of 10 passes between the multipass system mirrors set 0.4 m apart, results in a 4 m path length, showing that this mirror arrangement is suitable for achieving the desired number of passes within a White cell.

4.3 Construction of a New White Cell with a 64 m Path-length

4.3.1 Development of the 64 m Mirror Configuration

In order to increase the sensitivity of the current 4 m White Cell, a set of three mirrors, were obtained from Infrared Analysis, Inc., California, USA[13], with the aim to create a 64 m multipass cell. This set of concave mirrors included a T-shaped field mirror and two D-shaped objective mirrors (dimensions of which can be seen in Figure 4.6), which have a radius of curvature of 32 inches and are covered in protective, gold optical coating. The use of a T-shaped field mirror is important as it allows two lines of images to be produced and doubles the potential path length of any given White cell.
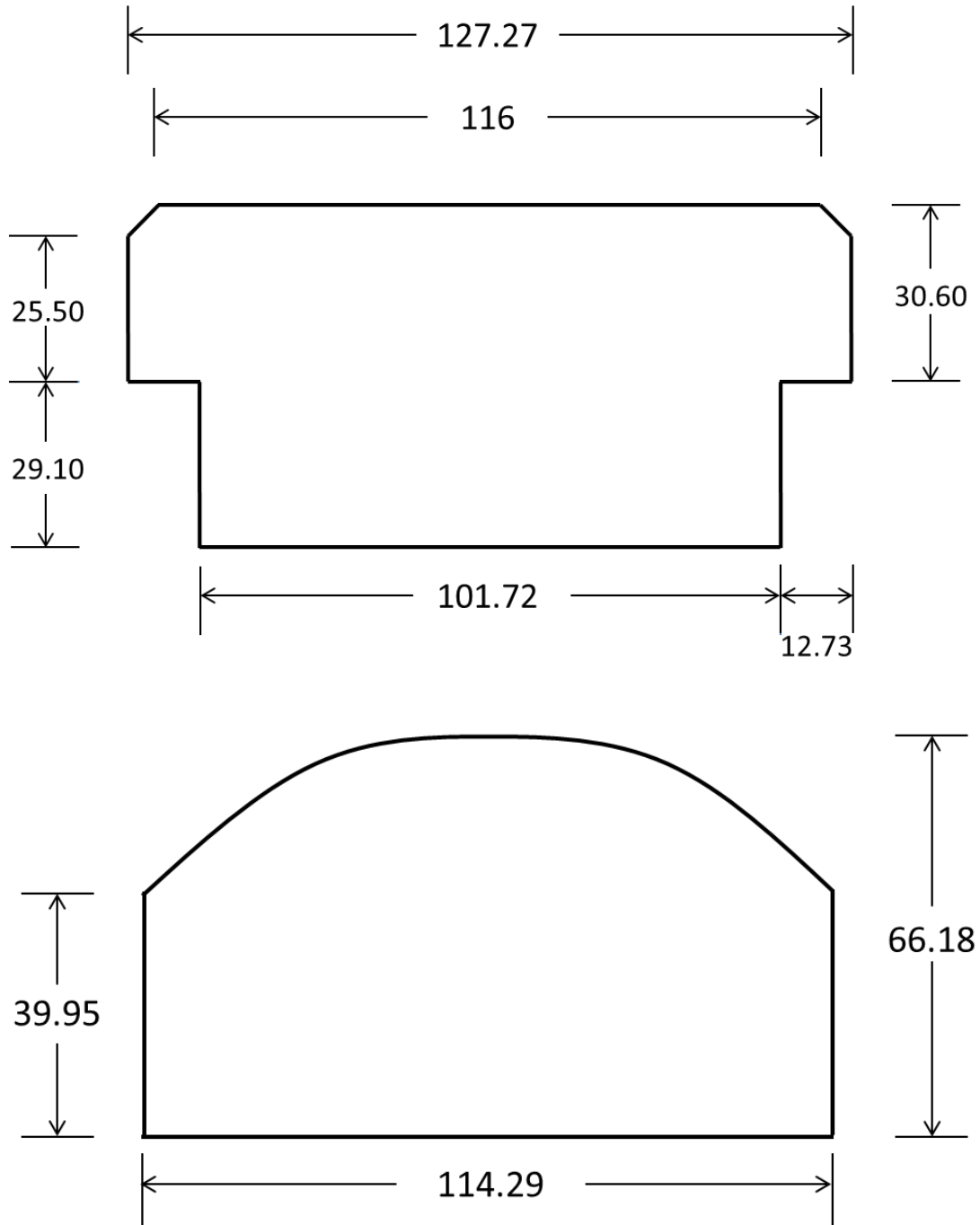
Figure 4.6: Dimensions (mm) for the new field and optical mirrors, with a radius of curvature of 32"

The mirrors were set at a distance of 32" (~0.8 m) with 0.01 m between the optical mirrors, to ascertain whether the required number of passes could be obtained between the mirrors. In order to obtain a path length of 64 m, with mirrors set 0.8 m apart, 80 traversals are required. A HeNe laser was used in place of IR radiation, so the images created on the field mirror could be seen, the number of passes could be counted and thus the path length monitored. In order to maximise the number of traversals the first image

must be close to the edge of the field mirror, as in Figure 4.7. As the number of traversals increases the intensity of the images decreases; whilst later images are difficult to see in the figure below, they can be made more apparent with the use of white card. The appropriate number of passes has been achieved, confirming that the mirror configuration is suitable for a 64 m path length.

Figure 4.7: Image pattern created on the field mirror, at a distance of 0.8 m from the optical mirror, using a HeNe laser

After confirming the correct number of passes using the HeNe laser, a white light source was used as this would better mimic the behaviour of the IR radiation within the spectrometer. The same mirror arrangement was used for this second investigation, with the HeNe laser simply replaced by the white light source. Due to the large divergence of the white light beam, a greatly reduced number of images were created on the field mirror; lenses were used to expand the diameter of the laser beam to approximately that of the IR radiation and again 80 traversals were achieved.

4.3.2 Considerations for the design of the 64 m Multipass System

Before considering the finer details of the system, the dimensions of the glass casing of the cell needed to be determined. The principle of a White cell is based upon three mirrors with the same radius of curvature, placed at a distance equal to this radius, which in this case is 32 inches. Besides this distance the thickness of the mirrors (0.01 m) and the thickness of the material used to create backing plates to hold the mirrors must also be considered whilst determining the height of the glass cell. The width of the cell is highly dependent upon the radius of the optical mirrors; the two optical mirrors were placed with

their flat edges beside each other at a distance of 0.01 m. Additional width must also be taken into account to accommodate any clamps used to hold the mirrors onto the back plates as well as the arc of the mirror as it is adjusted.

The cell is to be constructed using 7 mm thick glass; this thickness must be included when calculating the width of the cell as outer diameters are listed in material catalogues. Wall diameters of less than 7 mm were thought too thin to be used with great stability for a vacuum system, so would be unsuitable for use in a White cell.

As identified in section 4.2.1 the joint between the cell and the top and bottom plates needs to be improved from squeezing an O-ring against the cell wall using a circular clamp; a lip on either end of the cell with an O-ring groove cut into it would improve the seals at both of these joints. The material of the O-rings must also be considered; the O-rings must be chemically inert to both ozone and the reaction products from terpene ozonolysis, which include: aldehydes, ketones and ester.

The top metal plate, to which the optical mirrors will be fixed, includes a variety of components so materials and positioning must be contemplated. Similarly to the O-rings, any material used to fix the optical mirror and their adjustment mechanism to the top metal plate must also be chemically inert to both ozone and the ozonolysis products. Each of the optical mirrors requires three adjusting screws in order to obtain the full range of motion that could be required in order to maximise the path length of the cell. With the optical mirrors positioned 10 mm apart, there is sufficient space for the mirrors to undergo adjustment to their maxima in every direction as well as place an additional window in which a laser can be passed through to confirm the number of traversals within the White cell. The field mirror must be aligned to the centre of the optical mirrors between two IR windows and secured to the bottom plate, so that it does not move out of place. Finally McCubbin *et al.* and Sung *et al.* both recommend increasing the overall stability of the cell with the use of metal bars positioned around the cell.[12, 14]

4.3.3 Assembly of the 64 m White Type Multipass System

The dimensions and fittings of the glass vacuum cell, made by Glass Solutions[15], can be seen in Figure 4.8. Unlike the old cell where metal fittings were threaded through the plastic tube, the various fittings on this new cell are also made of glass so are built into the construction of the cell, so that there is no longer a joint present between the cell and

the fittings, eliminating the potential for a leak from this components. The use of KF25 flanges gives the opportunity for other atmospherically important experiments, such as laser photolysis, to be undertaken in the future. The three Youngs FS29 clear ball joints are utilised for the same purposes as the old cell: connection to the evacuation pump and for the introduction of the reactants.

It should be noted that rather than an O-ring groove cut into the lips of the cell, due to financial reasons a 5 mm groove has instead been cut into the stainless steel plates that go on either end of the cell. The O-rings used on both plates were 180 Viton 75 O-rings, supplied by Leicester Bearings Co Ltd[16], which are chemically inert to ozone, a quality vital for the use in this cell.
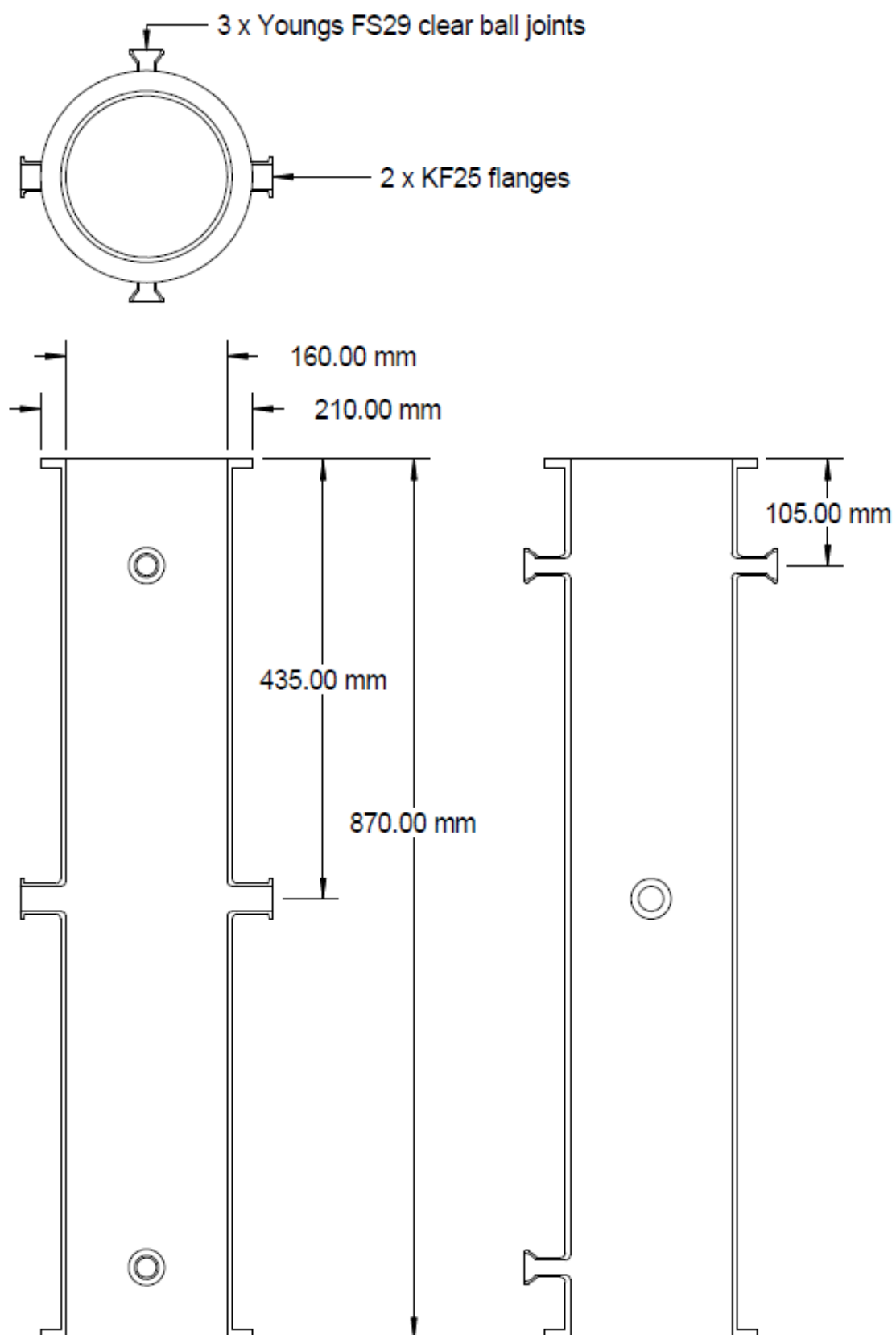
Figure 4.8: Dimensions and fittings of the glass vacuum cell, produced by Glass Solutions[15]

Small stainless steel pegs have been used to hold the field mirror in position, between the IR windows, as can be seen in Figure 4.9.
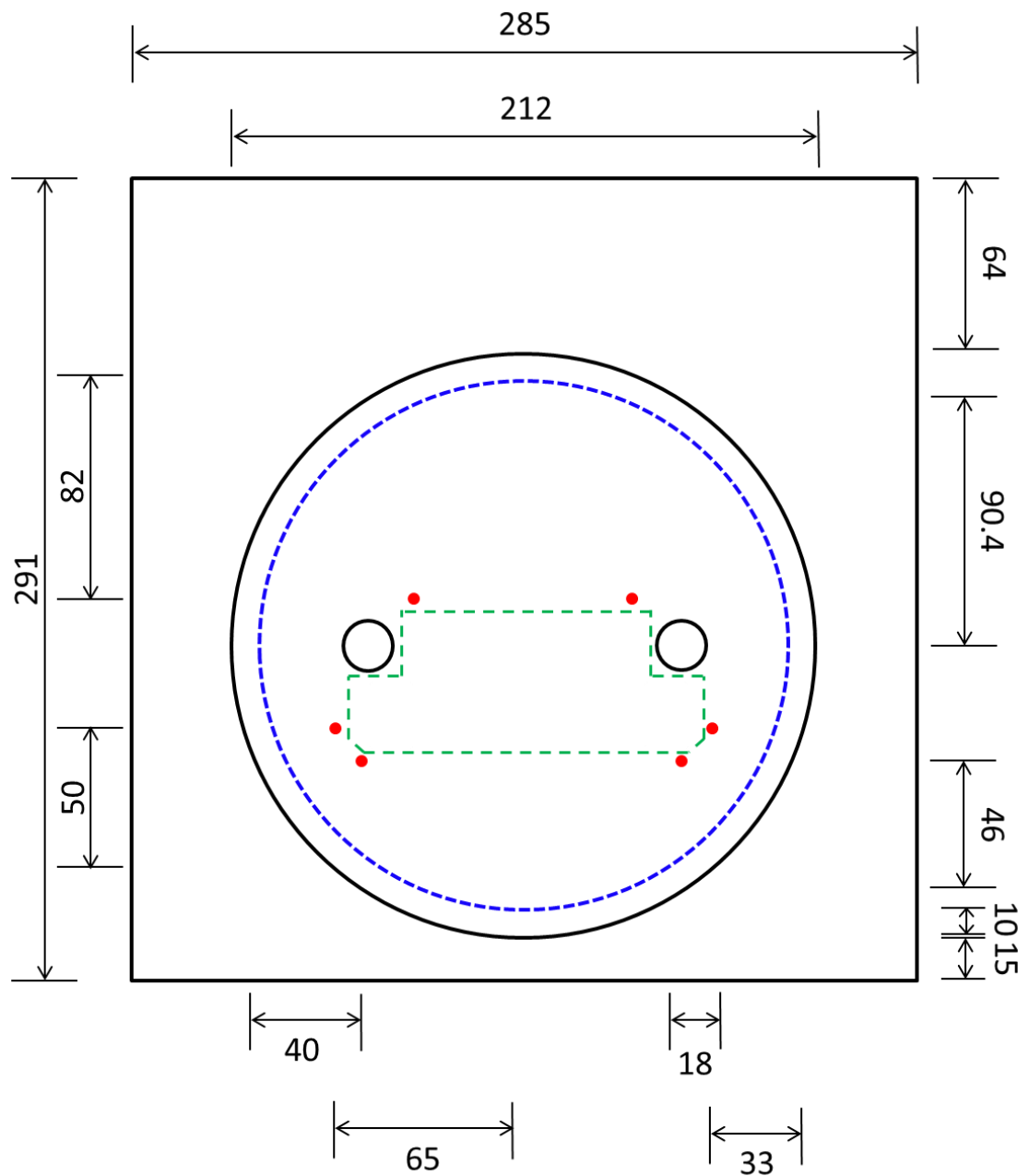
Figure 4.9: Dimensions (mm) for the new bottom plate: the solid black lines demonstrates the boundary of the cell lip and the two IR windows, the dashed blue line shows the 5 mm O-ring grove and the red circles show the holding pins

More consideration was required for the design of the new top stainless steel plate, as this required the correct positioning of the optical mirror adjustment system so that they were not only aligned to the field mirror below but at an adequate distance that they could be manipulated to maximise the path-length of the cell.
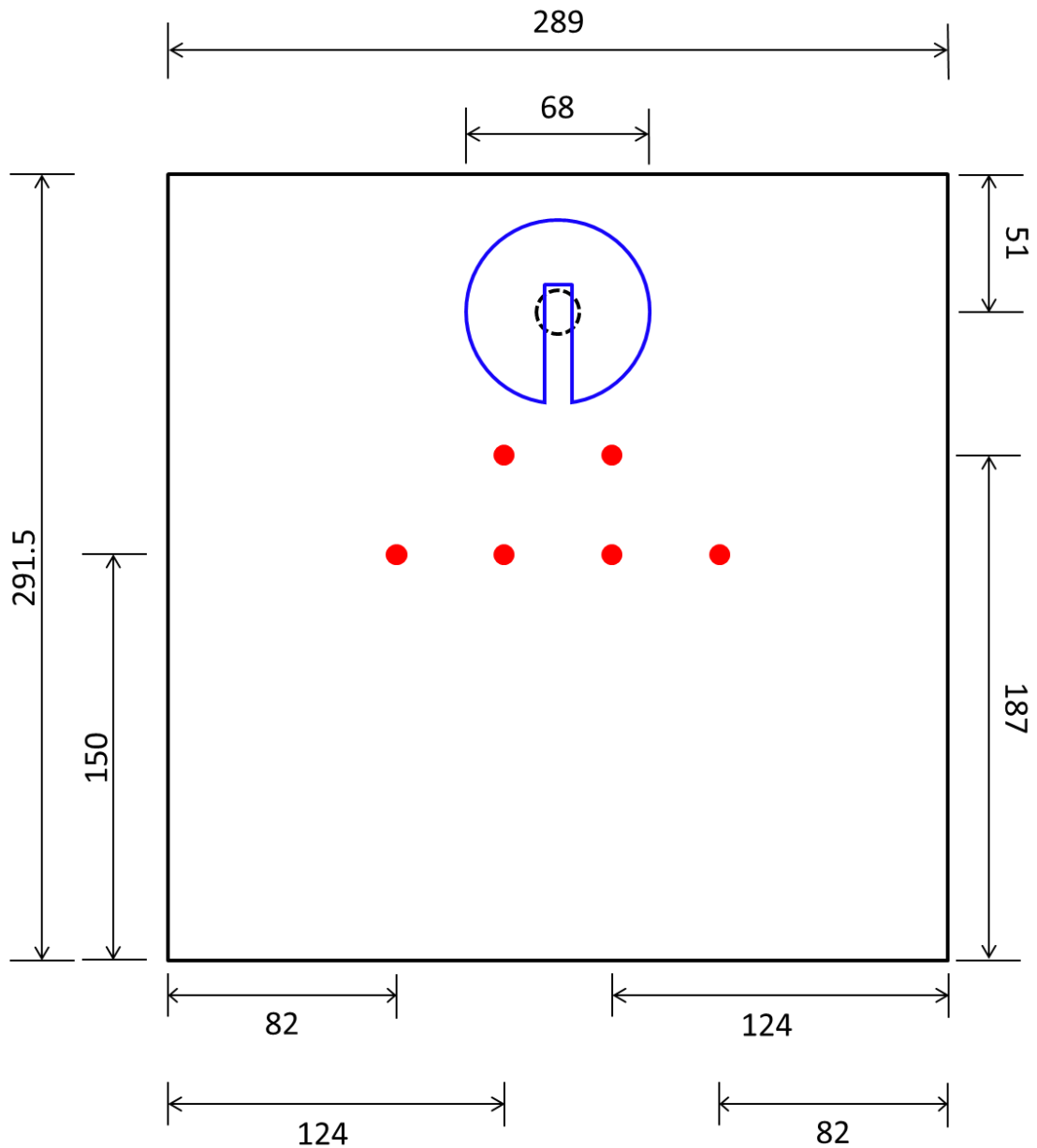
Figure 4.10: Dimensions (mm) for the new top plate: the dotted black line demonstrates the connection of the pressure gauge, the solid blue line shows the C-shaped clamp and the red circles show the adjustment screws for the optical mirrors

The connection for the pressure gauge (Figure 4.10) has been indented into the stainless steel plate and the joint reinforced using a C-clamp to eliminate the potential for any leaks, like those experienced by the original top plate. At the heart of the optical mirror adjustment mechanism are three kinematic table platforms purchased from Edmund Optics.[17] The kinematic platforms were screwed onto the underside of the bottom plate whilst three elongated screws were threaded through the top plate onto each of these platforms to allow for the mirror manipulation across three axes. By simply threading

screws through the top plate the alterations to the plate are kept to a minimum and with that the risk of any potential leaks of the cell contents. All joints on both stainless steel plates were created with an O-ring seal.

Figure 4.11: Clamping mechanism used to hold the optical mirrors

Additional clamps were required in order to attach the optical mirrors to the kinematic table platforms; these clamps were to be fashioned from acetal natural sheet as Direct Plastics advertised the good chemical resistance of this co-polymer.[18] However, Ozone Solutions and Plastics International both comment on the moderate effects ozone has on acetal, continuous use of ozone leads to softening of the acetal, causing it to swell resulting in a loss of strength and ultimately a limited lifespan.[19, 20] Monitoring of ozonolysis reactions is to be the primary use of this multipass system, so a material vulnerable to ozone would require regular replacement thus compromising the overall stability of the pressure vessel. Each clamp was constructed from aluminium and consisted of a backing plate shadowing the shape of the optical mirror, which was attached to the kinematic platforms and three adjustable pegs which could be securely fixed to keep the mirror in place during experimentation but would also allow for the mirror to be removed for cleaning or recoating (Figure 4.11).

4.3.4 Deflection of the Radiation from the IR Spectrometer into the Multipass Cell

As the multipass White cell will be sat atop an IR spectrometer, an optical system needs to be devised in order to deflect the radiation from its usual path through the spectrometer and into the multipass system. As seen in Figure 4.5 a three mirror system, including two curved and one flat mirror, will be used as it is successfully able to deflect the radiation into the multipass system and still achieved the desired number of traversals. Whilst the concept of this three mirror system has been established, its position within the sample chamber of the IR spectrometer needs to be correctly established. The focal point of the IR radiation is at a length of 184 mm, 106 mm along the width and at a height of 111 mm, indicating the position of the first mirror in this diversion system.

Not only is a three mirror system required to divert the radiation into the multipass system, an additional three mirrors are required to divert the radiation from the White cell to the IR detector. In order to keep these two mirror systems in position an additional stainless steel plate was screwed into the underside of the bottom plate, so that the positioning would not be affected by the evacuation and venting of the IR spectrometer. The mirrors were mounted onto L-shaped brackets, which attached to the backing plate through a series of thread holes. These holes were positioned an inch apart in both the horizontal and vertical directions, to allow adaptability of the mirror positioning along the *x*- and *y*-axes. In order to manipulate the mirrors along the *z*-axis, a slot was cut into the mirror brackets, so that the mirrors could be adjusted to the optimum position. An important consideration for each of the six mirrors involved is not to block the radiation passing from the other mirrors.

4.4 Current Status of the Multipass System

Unfortunately due to time constraints, the optimum positioning of the two mirror systems allowing the radiation to enter and exit the White cell, was not completed. Besides these mirror systems the White cell is almost complete; including the top and bottom plates that are used to hold the field and optical mirrors respectively. The adjustment system on the top plate to manoeuvre the optical mirrors is completed as is the additional plate, attached to the underside of the bottom plate, for the additional mirror systems mentioned above.

4.5 How could the White Cell be utilised?

Before this multipass system could have been used to observe the ozonolysis reaction terpinolene, the system would have first been tested on a smaller terpene. Isoprene is the smallest terpene, providing a simpler ozonolysis process than for terpinolene, but has also been more widely studied providing a plethora of information to help ascertain the accuracy of this newly developed system. Inclusion of BTEM analysis (as described in Chapter 2) could be applied to the spectra acquired, in order to differentiate between the different molecules present in the reaction mixture.

4.6 References

1. B.C. Smith, *Fundamentals of Fourier Transform Infrared Spectroscopy*, CRC Press, New York, 2011.

2. J. U. White, *Journal of the Optical Society of America*, 1942, **32**, 285-288.

3. C. Robert, *Applied Optics*, 2007, **46**, 5408-5418.

4. H. J. Bernstein and G. Herzberg, *The Journal of Chemical Physics*, 1948, **16**, 30-39.

5. T. H. Edwards, *Journal of the Optical Society of America*, 1961, **51**, 98-102.

6. W. Armerding, J. Walter and F. J. Comes, *Fresenius Journal of Analytical Chemistry*, 1991, **340**, 661-664.

7. D. R. Glowacki, A. Goddard and P. W. Seakins, *Applied Optics*, 2007, **46**, 7872-7883.

8. J. B. McManus, P. L. Kebabian and W. S. Zahniser, *Applied Optics*, 1995, **34**, 3336-3348.

9. D. M. Bakalyar, J. V. James and C. C. Wang, *Applied Optics*, 1982, **21**, 2901-2905.

10. D. Horn and G. C. Pimentel, *Applied Optics*, 1971, **10**, 1892-&.

11. J. U. White, *Journal of the Optical Society of America*, 1976, **66**, 411-416.

12. K. Sung, R. A. Toth, L. R. Brown and T. J. Crawford, *Journal of Quantitative Spectroscopy & Radiative Transfer*, 2009, **110**, 2082-2101.

13. Infrared Analysis, Inc., http://www.infraredanalysisinc.com/, 2011.

14. T. K. McCubbin Jr and R. P. Grosso, *Applied Optics*, 1963, **2**, 764-765.

15. Glass-solutions.co.uk, Scientific Glass and Equipment Specialists, http://www.glass-solutions.co.uk/, 2013.

16. The Leicester Bearing Co Ltd., http://www.leics-bearings.co.uk/, 2014.

17. Edmund Optics Worldwide, http://www.edmundoptics.co.uk/, 2012.

18. Direct Plastics Limited, http://www.directplastics.co.uk/, 2014.

19. Ozone Solutions, Material Compatibility with Ozone, http://www.ozoneapplications.com/info/ozone_compatible_materials.htm, 2013.

20. Plastics International, http://www.plasticsintl.com/, Accessed 2014.

Chapter Five

Microwave Spectroscopy of Linalool

5.1 Introduction

5.1.1 Structure and Household Uses of Linalool

Linalool ($C_{10}H_{18}O$) is a doubly unsaturated terpene alcohol with a highly flexible structure: with multiple bonds capable of undergoing torsion (Figure 5.1a), methyl rotor groups able to undergo internal torsion (Figure 5.1b) and a chiral centre (Figure 5.1c), resulting in a combination of the *(R)* and *(S)* enantiomers.
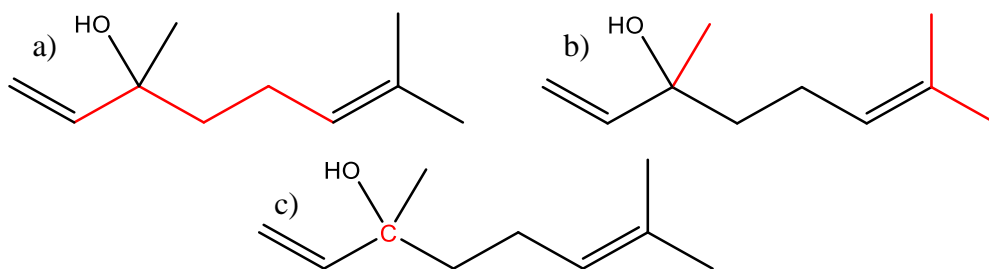
Figure 5.1: Skeletal structure of linalool highlighting a) bonds capable of undergoing torsion, b) internal rotors and c) the chiral centre

Whilst both *(R)* and *(S)* enantiomers of linalool [3,7-dimethylocta-1,6-dien-3-ol] are equally stable, they are distinguishable by their scents; the *(R)* enantiomer smells of lavender whilst the *(S)* enantiomer smells of oranges.[1-4] The fresh, floral aromas of both enantiomers of linalool make it an important fragrance compound. Linalool can be found in a wide variety of scented, household products such as soaps, detergents, cosmetics and toiletries.[1, 5] Studies have highlighted the commonality of linalool in such products; it was found in 97% of deodorants and 61% of domestic and occupational products[4], such as soaps, fabric conditioners and furniture polish with a mean concentration of 147.9 ± 107.5 ppm.[6]

5.1.2 Contact Dermatitis

Fragrances, of which linalool is one of the five most used along with limonene, citronellol, eucalyptol and α-pinene[6], are among the most common causes of contact dermatitis (a rash or skin inflammation after exposer to allergens). Due to its commonality in household products it is important to comment on the role linalool plays in this condition.

Linalool is a weak allergen[2], and is an unsaturated hydrocarbon which means that it is susceptible to oxidation in the presence of air[4], a common reaction bearing in mind the customary use of linalool in everyday products. These autoxidation products incorporate

oxygen into their structures, creating an electrophilic site. Although a variety of primary and secondary oxidation products have been identified, hydroperoxides formed through the primary oxidation of linalool are categorised as the strongest allergens.[2, 4]

5.1.3 Atmospheric Chemistry of Linalool

Linalool is also an important compound with respects to atmospheric chemistry, as it is one of the main substituents emitted from pine trees, particularly *Pinus Pinea*[7-9], common in the Mediterranean region, with observed emission rates of between 1.5 and 5.1 μg g^{-1} h$^{-1\ddagger}$ which accounts for up to 50% of all volatile terpenoids[7] and *Pinus taeda* (lob lolly pine) common to North America, which has the lower emission rate of 82 ng C g^{-1} h$^{-1\S}$.[10] Linalool is also emitted from *Pinus patula* (patula pine)[11] and *Pinus halepensis* (Aleppo pine) accounting for nearly 30% of the emission.[12]

Besides pines, linalool is emitted from *Quercus ilex* (Mediterranean Holm Oak)[7], *Fagus sylvatica L.* (European/common beech)[13] and *Daphne mezereum L.*(Dutch mezereon – a deciduous, evergreen shrub).[14] While most atmospheric studies only catalogue the emission of linalool (without specifying a particular enantiomer), the study by Born-Karlson in 1995 specifically characterises the emission from *Daphne mezereum* as the (*S*)-linalool enantiomer. Simon *et al.* show that the emission rate of linalool is highly dependent upon the visible light available, unlike the emission rate of *α*-pinene, which is dependent upon the temperature of the leaf. Monoterpene emission rates that are reliant on light have a significant effect on regional emissions.[12]

Due to its doubly unsaturated structure, linalool readily reacts with a variety of common tropospheric oxidants: O_3, OH radicals and NO_3 radicals, with an expected lifetime of up to one hour.[9] Reaction at the more substituted double bond ($C_6=C_7$) dominates over the lesser substituted $C_1=C_2$[7] (see Figure 5.2) double bond; reaction at the $C_6=C_7$ double bond has a reaction barrier with ozone of 2.13 kJ mol^{-1}, which is a lower reaction barrier than 7.24 kJ mol^{-1} for ozone reacting with the $C_1=C_2$ double bond.[15] Reaction between linalool and OH radicals also dominates at the more substituted double bond with 77% of this oxidation occurring here and only 23% occurring at the $C_1=C_2$ double bond.[16]

$\ddagger$$\mu$g g^{-1} h^{-1} – micrograms of linalool per gram of air per hour
$\S$ng C g^{-1} h^{-1} – nanograms of carbon per gram of air per hour

Alkene chemistry, in particular electrophilic additions, is dependent upon the substituents bound to the unsaturated carbons, following Markovnikov's rule "*In the addition of HX to an alkene, the H attaches to the carbon with fewer alkyl substituents and the X attaches to the carbon with more alkyl substituents*". Addition at the more highly substituted end of the alkene produces a more highly substituted carbocation intermediate, which is not only more stable but forms faster than the less substituted carbocation so is able to rapidly form the product. Using this basis, the observation that the $C_6=C_7$ double bond preferentially reacts with ozone can be explained; the $C_6=C_7$ double bond is more substituted than the $C_1=C_2$ double bond, thus would form the more stable carbocation, hence addition would occur at the $C_6=C_7$ double bond.[17]
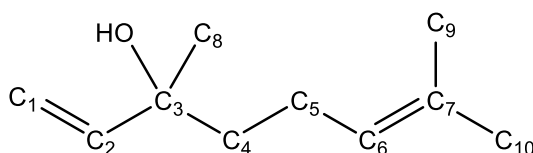
Figure 5.2: Skeletal structure of the terpene alcohol linalool

Various groups have sought to measure the rate constants between linalool and each of the common atmospheric oxidants; in 1995 Calogirou *et al.* made the observation that the oxidation reaction occurred at the more substituted double bond.[7] This observation was later matched by Grosjean *et al.* in 1998, who also recorded a rate constant of $3.15 \pm 0.23 \times 10\text{-}^{16}$ cm^3 molecule^{-1} s^{-1} when linalool was reacted with 50 ppb of ozone.[18] This study also concluded that linalool ozonolysis leads to a variety of carbonyl and carboxylic acid products that could undergo rapid removal from the atmosphere through either reaction with OH or photolysis and that the expected lifetimes of unsaturated oxygenated linalool was less than 30 minutes.[18] In 1999 Calogirou *et al.* conducted another investigation which enabled the comparison of the rate constants of the three common atmospheric oxidants; the largest rate coefficient occurred between linalool and OH radicals (1.59×10^{-10} cm^3 molecule^{-1} s^{-1}), the smallest was between linalool and O_3 (4.3×10^{-16} cm^3 molecule^{-1} s^{-1}) and the reaction between linalool and NO_3 radicals possessed an intermediary rate coefficient (1.12×10^{-11} cm^3 molecule^{-1} s^{-1}).[19]

Rather than focussing on reaction rates between linalool and various atmospheric oxidants other groups prefer to focus on the production of secondary organic aerosols (SOA) from the oxidation of linalool. Lee *et al.* established that the photooxidation of linalool produced much higher SOA yields (13%) in comparison to linalool ozonolysis

(1%)[16], an observation that could be supported by Chen *et al.* who concluded that in order to obtain high SOA yields via linalool ozonolysis then linalool had to be in excess over ozone in a ratio of 1:2.[20]

5.1.4 Insect Pheromones

Whilst not as prevalent as other terpenes such as verbenone, the role of linalool in insect behaviour has also been discussed. As previously mentioned linalool is emitted from *Daphne mezereum*, which has strongly fragrant flowers that develop before the leaves in order to attract pollinators and produces the highest proportion of linalool oxides towards the end of the flowering season. Male *Andrena cinerea* and *A. haemorrhoa* (ashy and early mining bees respectively) are slightly attracted to the enantiomer (*S*)-(+)-linalool; however, the same cannot be said for *A. vaga*, another species of mining bee.[14] Later studies have also commented on the presence of linalool oxides not only being found extensively in nature, but having strong biological significance in certain pollination systems as they act as attraction pheromones.[5]

Many species of solitary bees and bumble bees produce linalool in their mandibular glands (sac-like structures attached to the mandibles which are a pair of appendages near the mouth); both males and female *Colletes cunicularius* (vernal bee) produce (*S*)-linalool, that acts as an aggregation pheromone for the males of this species.[14] These aggregation pheromones attract male vernal bees to a nesting site, increasing the density of the species. Borg-Karlson *et al.* monitored the response of male vernal bees to each of the two linalool enantiomers and discovered that (*S*)-linalool was a much more effective aggregation pheromone.[14] Interestingly linalool has not only been recorded as a signifier of attraction but also infection; linalool emissions were recorded from *Fagus sylvatica L.* (European/common beech) as the result from the infection of *Phyllaphis fagi L.* (woolly beech aphid), which are recorded to release both linalool and *α*-farnesene.[13]

5.1.5 Previous Spectroscopic and Theoretical work on Linalool

A plethora of previous experimental and theoretical work has been carried out on linalool, the majority of which focus on vibrational spectroscopy. In the late 1980's Bacon and van der Maas recorded the infrared spectrum of linalool in the liquid phase, using CCl_4 as a solvent. Of particular interest was the O-H stretching vibration, present in the tertiary alcohol group of linalool. The vibrational frequency was recorded at 3539.5 cm^{-1} due to

the hydrogen-bonding interactions between the alcohol group and the unsaturated $C_1=C_2$ double bond (Figure 5.2) at the α-β position. Interactions with the $C_6=C_7$ double bond (Figure 5.2) in the γ-δ position resulted in the presence of another vibrational band at 3610.5 cm^{-1}. They finally considered the presence of the three possible conformers due to the rotation about the C-O bond.[21]

In the late 1990's Shu *et al.* used infrared spectroscopy to monitor the gas-phase linalool oxidation products from reactions with O_3, OH radicals and NO_3 radicals. The main product from the linalool ozonolysis was identified as 5-ethenyldihydro-5-methyl-2(3H)-furanone, (Figure 5.3). The vibrational analysis of this product showed: a O-H stretching vibration at 3645 cm^{-1}, a vinyl C-H stretch is at 3096 cm^{-1}, two aldehydic C-H stretches at 2715 and 2812 cm^{-1} (present within the known range for aldehydic C-H stretches 2830-2695 cm^{-1}) and a weak C=O stretch at 1742 cm^{-1}, present at a slightly higher frequency characteristic of an aliphatic ketone such as cyclopentenone.[9]
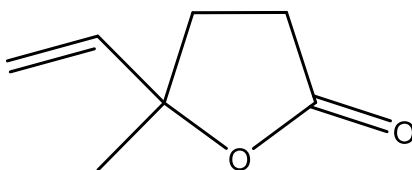
Figure 5.3: Linalool ozonolysis product, 5-ethenyldihydro-5-methyl-2(3H)-furanone

At the turn of the millennia Schulz *et al.* used a variety of vibrational spectroscopy methods to obtain rapid classification of basil chemotypes. Chemotypes are chemically distinct molecules emitted from plants. Basil chemotypes can be differentiated through their differing scents; European basil has a sweet aroma whilst Reunion basil has a woody scent. The group used Fourier transform Raman spectroscopy in order to characterise the C-C vibrations of linalool at 1643 cm^{-1} and 1675 cm^{-1} and Fourier transform infrared spectroscopy to characterise the out-of-plane C-H bending of linalool at 918 cm^{-1} and 994 cm^{-1}.[22]

More recently Sandasi *et al.* used vibrational spectroscopy as a quality control method for geranium oil, for which linalool is a constituent. Unlike the previous investigations, the C=C bond was characterised by the band at 1641 cm^{-1}, although the intensity of this peak was dependent of the number of double bonds present within the molecule, their positioning and the influence of any neighbouring groups within the structure. Moving into the fingerprint region a variety of C-H vibrations present in linalool were

characterised; methyl bending vibrations at 1400 cm^{-1} and 1000-675 cm^{-1} for the (*C-H*) and the (*CH$_2$*) wagging vibrations respectively.[23]

In 2011 Sun *et al.* [15] used density functional theory (DFT) to study the reaction mechanism of linalool with ozone in the atmosphere. Geometry optimisations and harmonic vibrational frequencies (to confirm the presence of both energy minima and maxima) were carried out at the B3LYP/6-31G(d) level of theory, whilst the single point energies used to construct the potential energy surfaces for the reactions were calculated using the B3LYP/6-311+G(3df,2pd) level of theory. A range of physiochemical parameters for each of the competing reaction channels were calculated: enthalpy changes, Gibbs free energy changes and reaction barriers. As mentioned previously, knowledge of energy barriers enables the prediction of the dominant reaction path; reaction at the less substituted terminal double bond has a reaction barrier of 7.24 kJ mol^{-1}, which is much higher than for the more substituted internal double bond, which proceeds through a barrierless addition. The calculation of negative activation energy seems erroneous, and although not mentioned by this investigation the probable cause is through the known defect in the B3LYP functional in the description of the isolated ozone molecule – it struggles to show the singlet open-shell biradical character of ozone.[24, 25] This study concludes by stating the different contributions to the formation of SOA: nucleation, hydration or absorption.[15]

After the original findings of this work was presented at the Ohio High Resolution Spectroscopy Conference, another study of linalool (which referenced the presentation at this conference) combining microwave spectroscopy and quantum chemical calculations was published. This study recorded the microwave spectrum of linalool in the 9-16 GHz range using Fourier transform microwave spectroscopy (FTMW) rather than a Stark Modulated, Continuous Jet Millimeter Wave Absorption System (48-63 GHz). Nguyen *et al.* carried out a total of 34 different computational calculations utilising both MP2 and B3LYP with a wide variety of different basis sets on 15 different conformers of linalool, in order to examine the relative energies between the conformers and also their rotational constants. Potential energy surface (PES) scans were also completed at the MP2/6-311++G(d,p) level of theory, to investigate the internal rotation barrier around each of the methyl groups and explore the impact such rotation could have on the microwave spectrum of linalool. In total the authors assigned 83 transitions, which they used to fit

the microwave spectrum of linalool[26] using two different programs, XIAM[27] and BELGI-C1.[28, 29]

5.2 Experimental

5.2.1 Microwave Spectroscopy

Full details of the experiment are discussed in Chapter 2, but briefly the recording of the microwave spectrum (48-63 GHz) of linalool on the Monash system is discussed here. Linalool was purchased from Sigma-Aldrich (97%) and used without further purification. A sample of linalool was vaporised at a temperature of 110 ºC, in a stream of argon at a pressure of 30 kPa. A low resolution search spectrum was first recorded over a wide frequency range (48-63 GHz) using a strip chart, before the individual lines were recorded and digitally averaged. A Lorentzian line shape was fitted (see Figure 5.4) to each peak with a full width half height (FWHH) for transitions of 50-300 kHz.
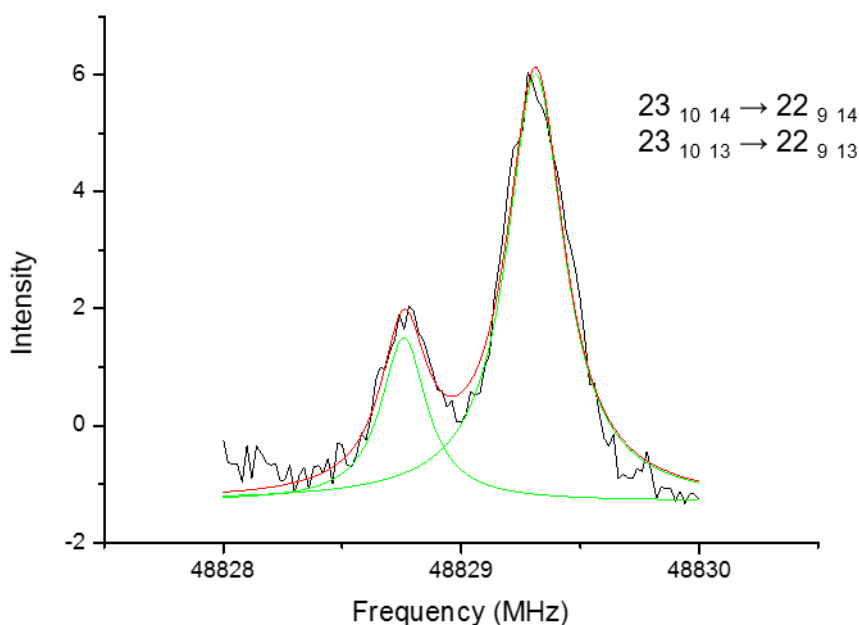
Figure 5.4: Rotational transitions of linalool at 48828.7 and 48829.3 MHz, fitted using a Lorentzian line shape function

Lines were fitted using Watson's A-reduced Hamiltonian with an I^r representation[30] using the PGopher simulation and fitting program written by C.M. Western.[31]

5.2.2 Computational Details

A crude conformational search was conducted at the Hartree-Fock (HF)[32, 33] level of theory with a STO-3G basis set[34], using the Spartan Pro program.[35] This analysis suggested the presence of more than 100 conformers of linalool. Of these preliminary structures, the 10 lowest energy structures were systematically optimised at the HF/6-31(d,p) and MP2/6-31G(d,p) and visualised using Chemcraft[36], a graphical program for working with quantum chemistry computations. These preliminary structures were then used as the basis of geometry optimisation and harmonic frequency calculations using the B3LYP[37, 38] functional with the aug-cc-pVTZ basis set[39] and second- and third-order Møller-Plesset perturbation theory (MP3)[40, 41] with the 6-31++G(d,p) basis set[42], using the Gaussian 03 software package.[43] Tight optimizations and SCF convergence were used for each of these calculations in addition to an ultrafine pruning grid for the DFT calculations. The centrifugal distortion constants of linalool were also calculated at the B3LYP/aug-cc-pVTZ and MP2/6-31++G(d,p) levels of theory. As these preliminary structures were unable to assign the millimetre-wave spectrum of linalool the search was expanded to incorporate the 40 structures with the lowest relative energy at the HF/STO-3G level of theory.

Potential energy surface (PES) scans were carried out to investigate the potential for internal rotation of each of linalool's internal rotors. Relaxed potential energy surface scans were created in Molden[44], a pre- and post-processing program of molecular and electronic structure; rotation around the dihedral angles associated with each of the methyl rotors, (H_{22}-C_{20}-C_{15}-C_{13}, H_{18}-C_{16}-C_{15}-C_{13} and H_{27}-C_{24}-C_6-C_4), the OH rotor (H_{29}-O_{28}-C_6-C_{24}) and the rotation of the terminal $C(H)=C(CH_3)_2$ unit via the H_{14}-C_{13}-C_{10}-H_{11} dihedral angle (Figure 5.5), were analysed at the B3LYP/6-31G(d,p) level of theory. To generate the potential energy surface each dihedral angle was rotated between 0° and 360° with a step size of 10°, the angle was fixed while the remaining structure was optimised at each step. All potential energy surface scans and final optimised structures were visualised with GaussView 5.0 graphical interface.[45]

5.3 Results and discussion

5.3.1 Initial Assignment of the Microwave Spectrum of Linalool

The assignment of the microwave spectrum (48-63 GHz) of linalool was far from straightforward. The chirality, internal rotors and bond torsion present in linalool resulted in a vast number of conformers of both (*R*)- and (*S*)- linalool being identified at the HF/STO-3G level of theory. As (*R*)- and (*S*)- enantiomers possess equal rotational constants, they are usually indistinguishable using microwave spectroscopy[26], so further quantum chemical calculations were only carried out on the (*S*)-linalool enantiomer.

The lowest lying conformer identified was conformer **I** (Figure 5.5) at the B3LYP/aug-cc-pVTZ level of theory.
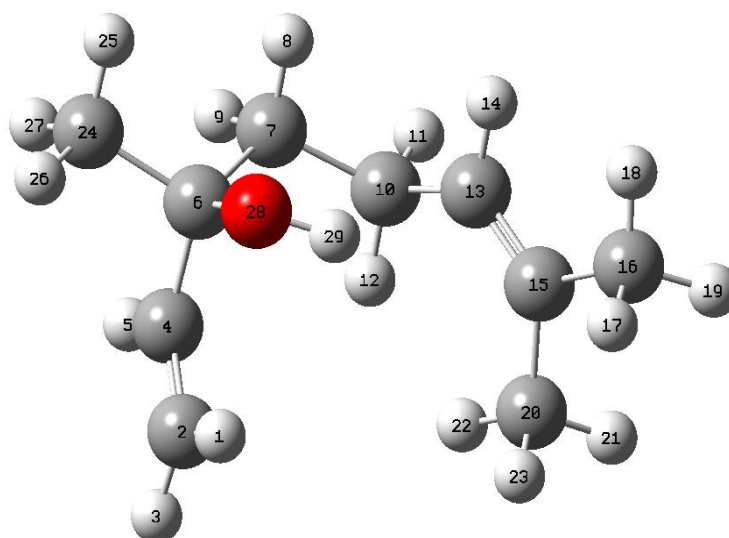
Figure 5.5: Optimised structure of linalool calculated at the B3LYP/aug-cc-pVTZ level of theory

Linalool can be classed as a prolate near-symmetric rotor as it possesses one principal moment of inertia that is significantly smaller than the other two. The asymmetry parameter (κ) of -0.876 makes it a prolate near-symmetric top. A Watson's *A*-reduce Hamiltonian using an I^r representation was used to fit the spectroscopic parameters (including the dipole moments $x = 1.0960$, $y = -0.0284$, $z = -1.8333$)obtained from the Stark modulated continuous jet millimetre wave absorption system using the PGopher[31] program (Figure 5.6).

In this initial fit the rotational constants from the 141 *b*-type transitions, with the selection rule $\Delta J=+1$, $\Delta K_a = \pm 1, \pm 3$ and $\Delta K_c = \pm 1, \pm 3$, were fitted to the molecular parameters of conformer **I**; however there remained many unassigned transitions. The quantum chemical calculations predict only a single spectral line present at each transition frequency (blue trace in Figure 5.7); however, the recorded linalool spectrum proposes that there are in fact two spectral lines (red trace in Figure 5.7). These additional spectral lines, which suggests either the presence of a second conformer, a contamination or splitting caused by an internal rotor, are of a lower intensity than those fitted to conformer **I**. As the two spectral lines are in such close proximity to each other, it would be reasonable to assume that they are resultant from similar molecular parameters, which would imply similar structural geometries.
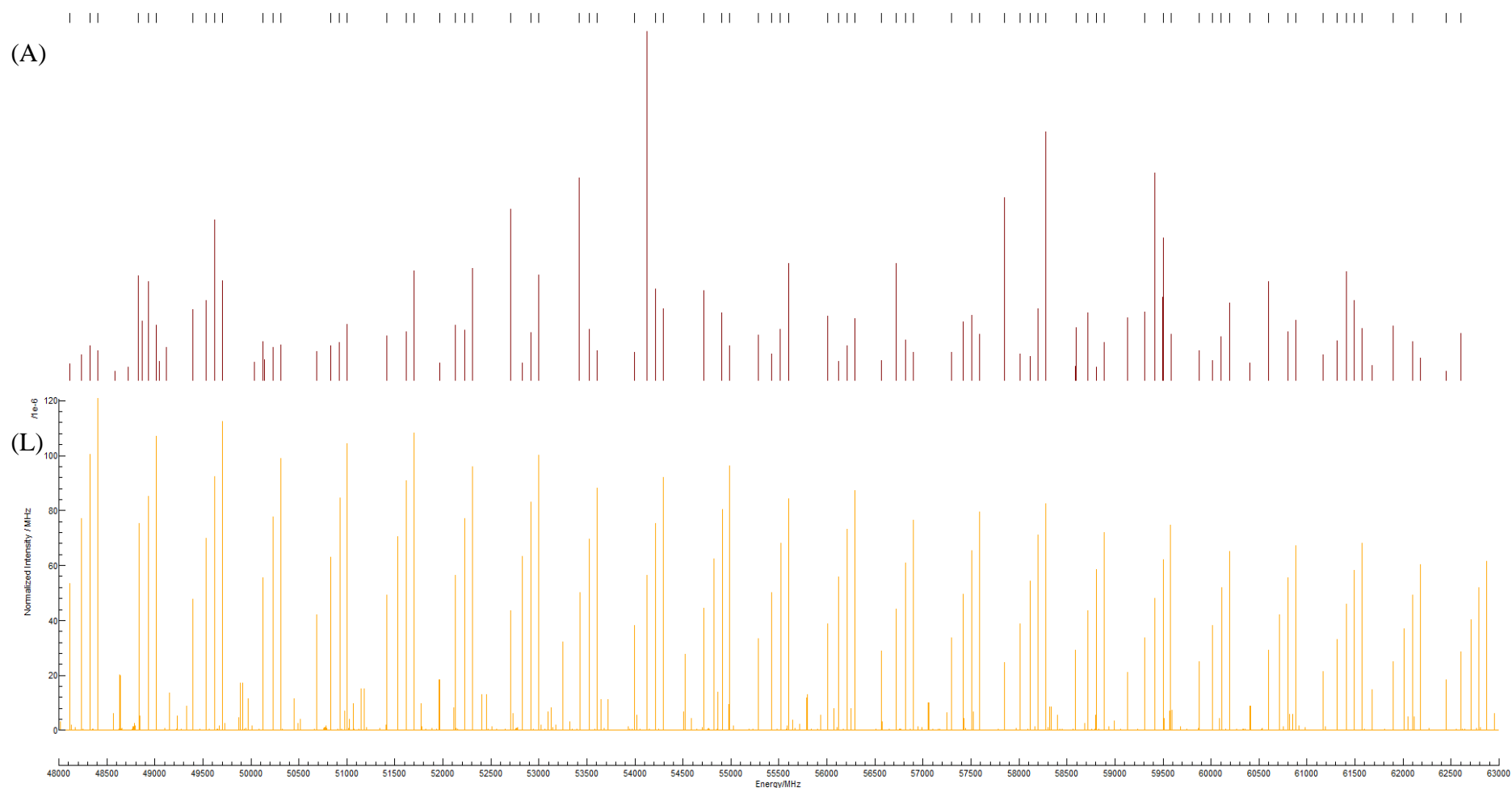
Figure 5.6: Assigned *b*-type transitions, in the microwave spectrum of linalool (48-63 GHz); (L) simulation (at 10 K) based on computational calculation at the B3LYP/aug-cc-pVTZ level of theory (intensity in MHz $\times$ 10^{-6}), (A) spectrum recorded using the Stark Modulated, Continuous Jet Millimeter Wave Absorption System at Monash University
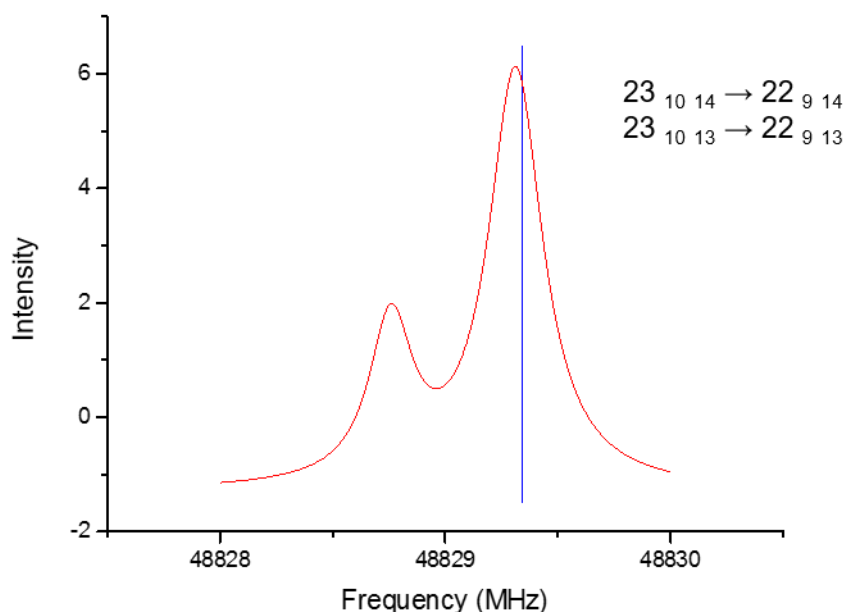
Figure 5.7: Rotational transitions of linalool at 48828.7 and 48829.3 MHz; the experimental (red) and theoretical (blue) spectra

5.3.2 Identification of the Second Set of Transitions

5.3.2.1 Contamination of the Sample

In an attempt to identify the smaller spectral feature associated with each observed transition, GC-MS analysis was used to confirm the purity of the linalool sample as 97%; the main contaminant was identified as 1,2-dihydrolinalool [3,7-dimethyl-6-octen-3-ol] which has a saturated C_1-C_2 bond in place of the unsaturated C_1=C_2 bond in linalool (Figure 5.8). 1,2-dihydrolinalool accounted for approximately 2% of the sample, an observation also made by Basketter *et al.* in 2002, whom also stated that although further purification of linalool would remove smaller constituent contaminants the species, 1,2-dihydrolinalool still remained.[46] As a recognised contaminant a conformational search on 1,2-dihydrolinalool was carried out with the structures again optimised at the B3LYP/aug-cc-pVTZ level of theory.
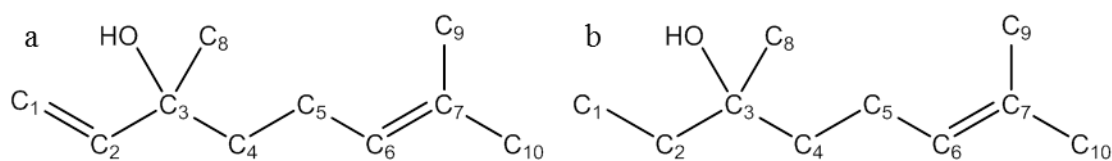
Figure 5.8: Skeletal structure of a) linalool and b) 1,2-dihydrolinalool

As can be seen in Table 5.1 the molecular parameters calculated for 1,2-dihydrolinalool were not similar to those fitted for linalool. As the assumption that the unassigned transition has similar rotational constants to the corresponding assigned transition was being employed it can be concluded that the unassigned transition in the millimetre- wave spectrum of linalool do not result from 1,2-dihydrolinalool contaminating the sample.

Table 5.1: Relative energies and rotational constants of the five lowest energy conformers of 1,2-dihydrolinalool at the B3LYP/aug-cc-pVTZ level of theory

Conformer	Relative Energy (cm⁻¹)	Rotational Constants (GHz)		
		A	B	C
I	0.00	2.5959	0.3847	0.3740
II	6.98	1.9518	0.4480	0.4172
III	11.98	2.5354	0.3908	0.3837
IV	23.29	1.9890	0.4139	0.4005
V	32.24	2.2101	0.4149	0.3861
Linalool expt.		*1.6467(10)*	*0.6823(42)*	*0.6187(36)*

5.3.2.2 Additional Conformers of Linalool

As a contamination could not account for the additional spectral lines, other low lying conformers of linalool were more closely examined. During this investigation more than 30 different conformers of linalool were identified at the B3LYP/aug-cc-pVTZ level of theory, separated by 1300 cm⁻¹; Nguyen *et al.* only described 15 conformers of linalool at the B3LYP/cc-pVTZ level of theory, again separated by 1300 cm⁻¹.[26] Both investigations agree that the lowest energy conformer of linalool is that shown in Figure 5.5, but Nguyen *et al.* did not identify conformers **V** and **VI**, suggesting that conformer **VII** is the next lowest lying conformer to **IV**. More surprisingly their investigation fails to identify linalool conformers **VIII** – **XVIII**, proposing that conformer **XIX** is the sixth lowest energy conformer of linalool, rather than the nineteenth as found in this investigation. The relative energies and rotational constants for the conformers of linalool can be seen in Table 5.2. The five lowest lying conformers identified at the B3LYP/aug-cc-pVTZ level of theory are shown in Figure 5.9.
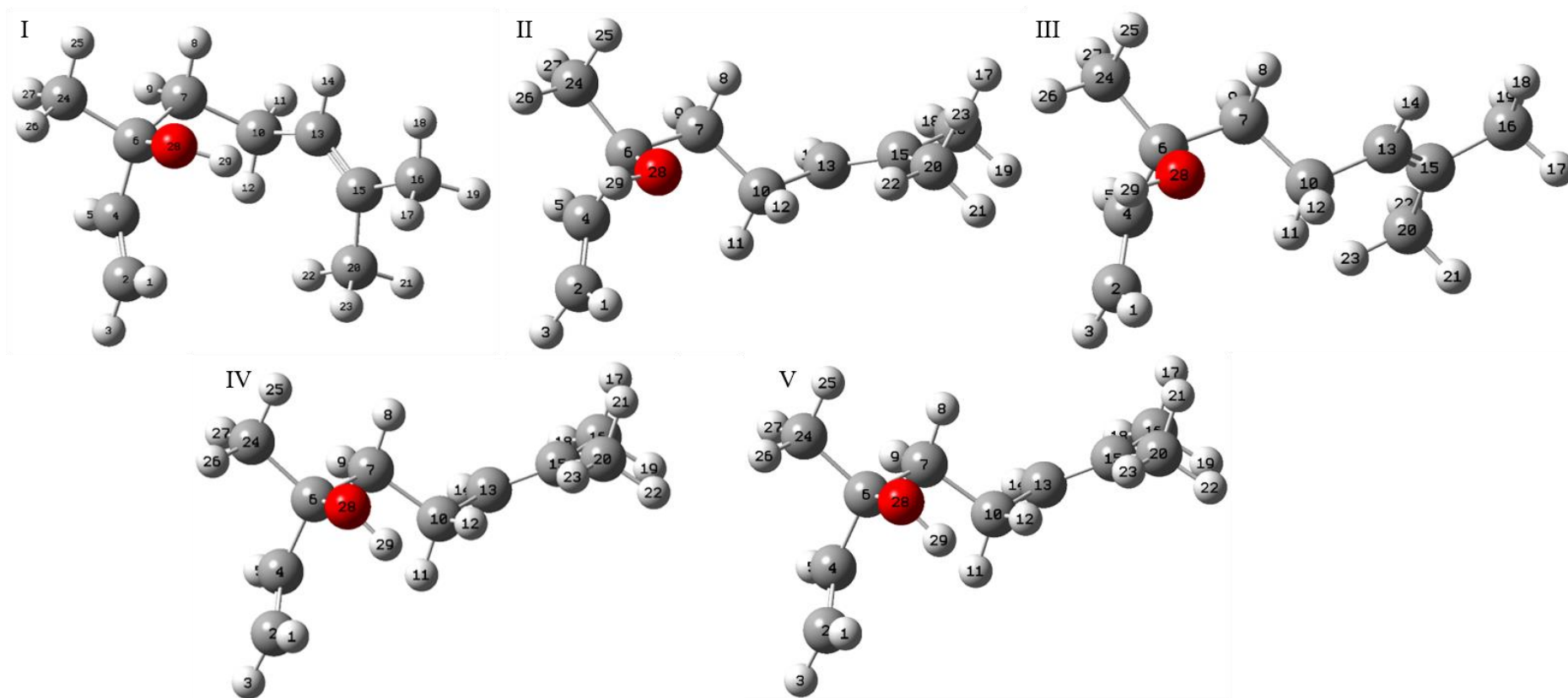
Figure 5.9: Optimised structures of linalool for the five lowest energy conformers (**I-V**) calculated at the B3LYP/aug-cc-pVTZ level of theory

Table 5.2: Relative energies and rotational constants for the 32 lowest lying energy conformers at the B3LYP/aug-cc-pVTZ, MP2/6-31++G(d,p) and MP3/6-31++G(d,p) levels of theory

Conformer	Relative Energy (cm^{-1})	Rotational Constants (GHz)		
		A	B	C
Expt.		*1.6467*	*0.6823*	*0.6187*
B3LYP/aug-cc-pVTZ				
I	0.00	1.6606	0.6466	0.5892
II	43.91	2.0938	0.4401	0.4333
III	58.95	2.0084	0.4648	0.4236
IV	90.45	2.1554	0.4294	0.4245
V	123.93	2.0417	0.4568	0.4167
VI	222.35	2.3423	0.4172	0.3969
VII	229.18	2.1715	0.4261	0.4197
VIII	243.90	2.4525	0.4085	0.3916
IX	261.64	2.2830	0.4146	0.4123
X	280.70	2.1143	0.4363	0.4291
XI	282.53	2.0369	0.4579	0.4189
XII	390.80	2.2074	0.4291	0.4070
XIII	392.92	2.2653	0.4296	0.4124
XIV	394.35	1.9940	0.4562	0.4160
XV	397.31	2.0420	0.4503	0.4108
XVI	398.02	1.9931	0.5477	0.5262
XVII	420.58	2.0634	0.4432	0.4067
XVIII	433.57	2.3096	0.4195	0.4003
XIX	495.24	1.9931	0.5477	0.5262
XX	590.74	2.2191	0.4202	0.4125
XXI	754.44	2.1654	0.4362	0.4162
XXII	769.48	1.9850	0.4765	0.4741
XXIII	821.93	1.9667	0.4812	0.4329
XXIV	838.26	1.7539	0.6197	0.5699
XXV	857.05	1.9793	0.5745	0.5524
XXVI	874.87	1.7934	0.5669	0.5380

Conformer	Relative Energy (cm⁻¹)	Rotational Constants (GHz)		
		A	B	C
XXVII	897.80	2.2731	0.4199	0.4050
XXVIII	902.08	1.7005	0.697	0.5749
XXIX	984.12	1.7317	0.5973	0.5554
XXX	1001.11	1.7338	0.6256	0.5712
XXXI	1015.31	2.0827	0.4687	0.4495
XXXII	1224.67	2.2562	0.4582	0.4394
MP2/6-31++G**				
I	0.00	1.6369	0.6961	0.6303
XIX	402.06	1.7387	0.6058	0.5577
XVI	706.42	1.9556	0.5753	0.5544
II	758.53	2.0791	0.4720	0.4552
III	784.29	1.9767	0.4862	0.4533
XXVIII	839.71	1.6256	0.7433	0.6548
V	907.04	2.0201	0.4780	0.4398
IV	927.41	2.1752	0.4564	0.4381
VII	1008.09	2.0161	0.4845	0.4546
XXIX	1109.95	1.7390	0.6681	0.6285
MP3/6-31++G**				
I	0.00	1.6381	0.6817	0.6167
XIX	427.21	1.6820	0.6473	0.5933
II	488.73	2.0769	0.4534	0.4440
III	517.28	1.9854	0.4769	0.4401
XVI	607.97	1.9723	0.5638	0.5442
V	621.57	2.0272	0.4667	0.4292
IV	647.12	2.1746	0.4497	0.4335
VII	714.06	2.0351	0.4730	0.4466
XXVIII	873.55	1.6302	0.7198	0.6369
XXIX	1032.08	1.7324	0.6532	0.6125

Optimisation of the preliminary structures at both HF/6-31G(d) and MP2/6-31G(d) hinted that the relative energies of the conformers of linalool are completely dependent upon the level of theory used, a pattern also noted by the Nguyen *et al.* FTMW investigation[26]. In order to explore this observation further, the geometries of the conformers were optimised at the MP2/6-31++G(d,p) level of theory; the ten lowest energy conformers are listed in Table 5.2.

These calculations further support the aforementioned observation; conformer **XIX**, which was the nineteenth lowest energy conformer using B3LYP, becomes the second lowest energy conformer at the MP2/6-31++G(d,p) level of theory. **XVI** (a conformer Nguyen *et al.* failed to identify) is promoted from the sixteenth lowest energy conformer to the third. Other conformers that find their relative position greatly altered from the B3LYP/aug-cc-pVTZ calculations include **XXVIII** and **XXIX**, which were promoted from 28th and 29th lowest energy conformers to the sixth and tenth respectively.

To further expand this investigation additional quantum chemical calculations at the MP3/6-31++G(d,p) level of theory were conducted. These calculations revealed the same ten lowest energy conformers as seen in the MP2 calculations, yet the relative energies are again different; for example conformer **XVI** goes from the third lowest energy conformer to the fifth. No comparisons can be made to Nguyen *et al.* as MP3 calculations were not undertaken.

Conformer **XIX** (Figure 5.10) was the second lowest lying conformer of linalool at both MP2 and MP3/6-31++G(d,p) levels of theory and had the most similar molecular parameters to conformer **I**. However, these were still not appropriate for the fitting of the unassigned spectral lines. Retaining the assumption that the unassigned transitions have similar rotational constants to the corresponding assigned transition, it can be concluded that the unassigned transitions in the millimetre wave spectrum of linalool are not caused by a second conformer of linalool.
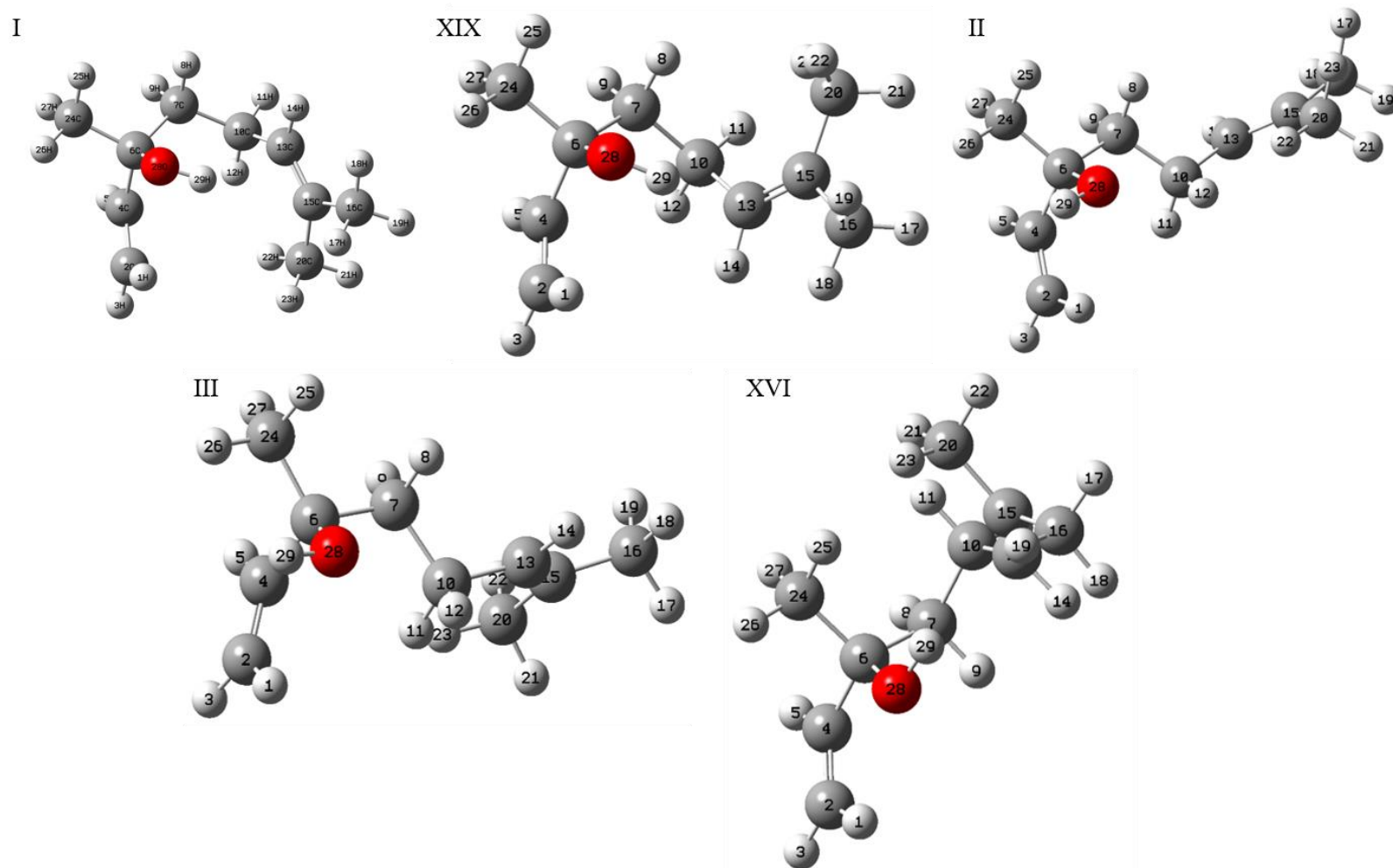
Figure 5.10: Optimised structures of linalool for the five lowest energy conformers (**I, XIX, II, III** and **XVI**) calculated at the MP3/6-31++G(d,p) level of theory

5.3.2.3 Internal Rotors within Linalool

As both contamination and additional conformers could not account for the additional spectral line associated with each transition, internal rotation within conformer **I** was explored. If a methyl group is able to rotate about a single bond via a sufficiently low barrier then it is known that the rotational levels possessed by a given molecule would be split, as described in Chapter 2. Analysis of the microwave spectrum allows for the determination of the barrier for this internal rotation.
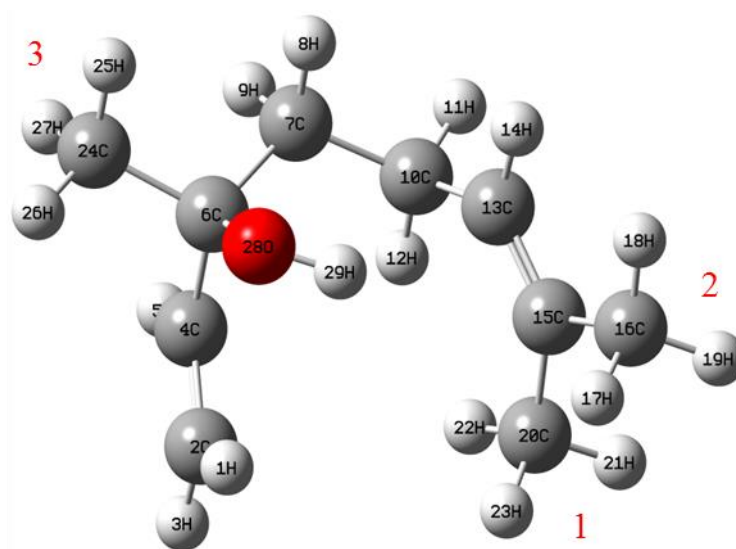
Figure 5.11: Optimised structure of linalool calculated at the MP3/6-31++G(d,p) level of theory, which contains three methyl rotors (labelled 1, 2 and 3)

Each of the three methyl rotors ((1) H_{22}-C_{20}-C_{15}-C_{13}, (2) H_{18}-C_{16}-C_{15}-C_{13} and (3) H_{27}-C_{24}-C_6-C_4 as given in Figure 5.11), were individually varied at the B3LYP/6-31G(d,p) level of theory using two methodologies:

    (i)   All other geometry parameters were fixed to the optimised structure as calculated at the MP3/6-31++G(d,p) level of theory

    (ii)   All other geometry parameters were allowed to relax.

The OH rotor (H_{29}-O_{28}-C_6-C_{24}) and terminal $C(H)=C(CH_3)_2$ unit (H_{14}-C_{13}-C_{10}-H_{11}) were also varied at the B3LYP/6-31G(d,p) level of theory, while all other geometry parameters were allowed to relax. Rotation about H_{29}-O_{28}-C_6-C_{24} and H_{14}-C_{13}-C_{10}-H_{11} connects conformers **XIX** and **XXIX** (Figure 5.12) to conformer **I**, via barriers of 427.21 cm^{-1} and 1032.08 cm^{-1} respectively, which are sufficiently large that splitting of the spectral lines

would be unexpected. Elimination of conformer **XIX** as the cause of the unassigned spectral lines had already taken place after the previously mentioned study of its spectral parameters.
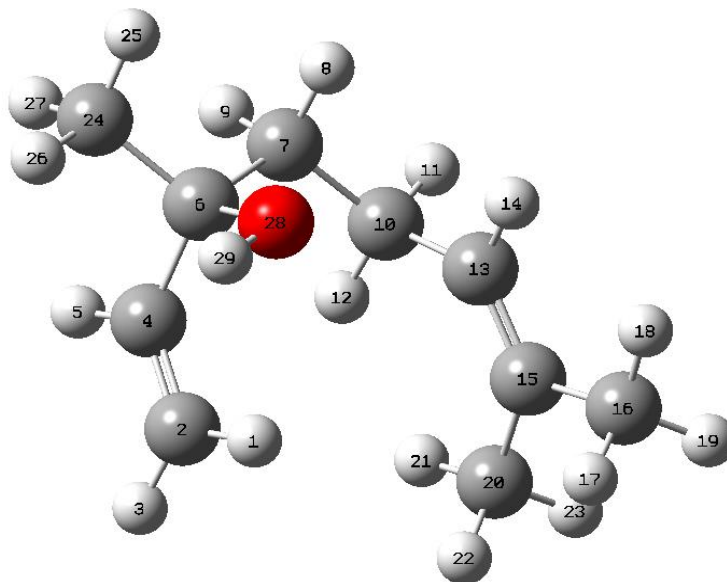
Figure 5.12: Optimised structure of linalool conformer **XXIX** calculated at the MP3/6-31++G(d,p) level of theory

Calculating the energy barrier for the methyl group rotations emphasised the importance of using a relaxed system; when fixing all other geometry parameters the barrier heights for each of the methyl rotors, H_{22}-C_{20}-C_{15}-C_{13}, H_{18}-C_{16}-C_{15}-C_{13} and H_{27}-C_{24}-C_6-C_4, were 910, 2014 and 5649 cm^{-1}, respectively. Rotational barriers of this magnitude would be too high to produce the splitting observed in the microwave spectrum of linalool. When all other geometry parameters were allowed to relax, a geometry optimisation of each structure along the potential energy surface was carried out; the rotational barriers for the three methyl rotor decreased to 305, 792 and 1163 cm^{-1} respectively.

Torsion about the H_{22}-C_{20}-C_{15}-C_{13} dihedral angle resulted in the lowest V_3 barrier of 299 cm^{-1}; this is in comparison to 761 and 1145 cm^{-1} for H_{18}-C_{16}-C_{15}-C_{13} and H_{27}-C_{20}-C_{15}-C_{13}, dihedral angles respectively (Figure 5.17). The rotational barrier for the methyl rotor H_{22}-C_{20}-C_{15}-C_{13} was small enough that the splitting in the spectral lines in the microwave spectrum of linalool would be expected. As previously mentioned the lower the internal rotation barrier the larger the splitting observed in the microwave spectrum. In this investigation a barrier for internal rotation of 300 cm^{-1} has resulted in splitting of ~ 400 kHz.
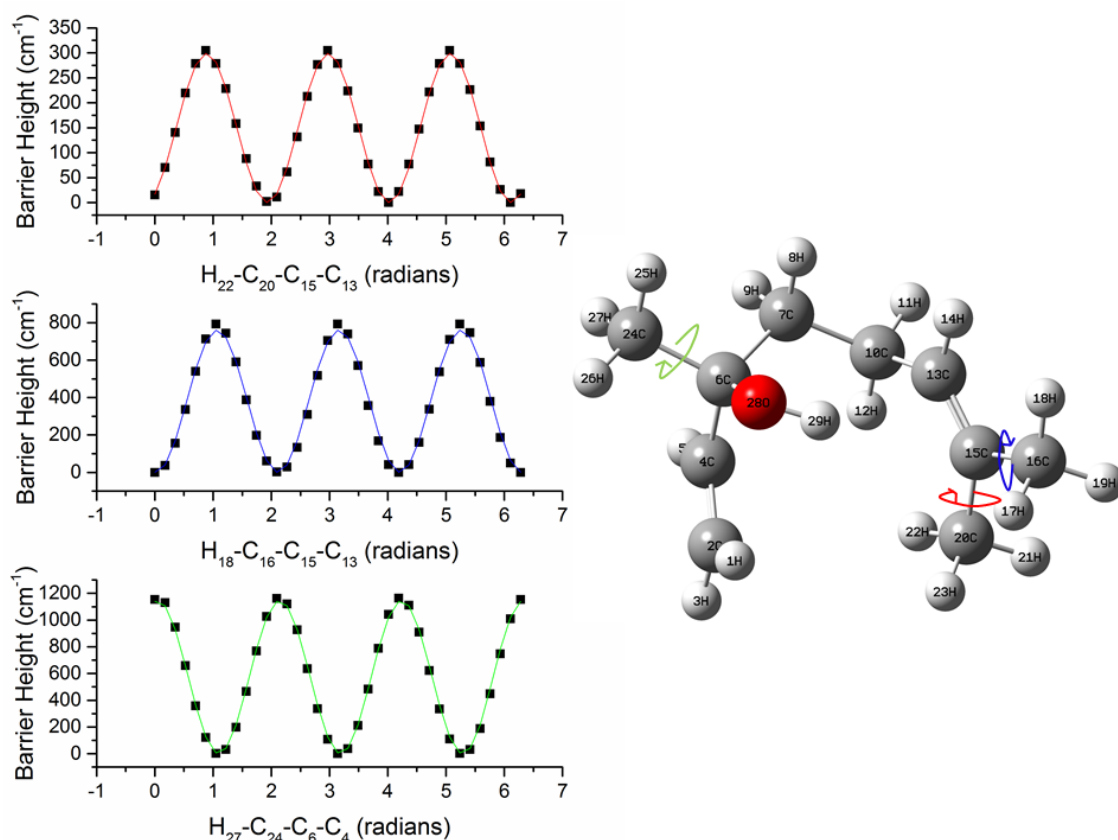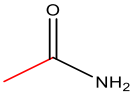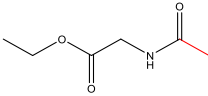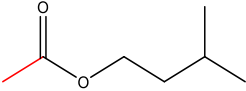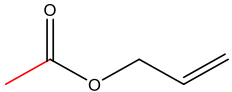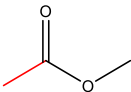
Figure 5.13: Result of the relaxed potential energy surface scans for each of the three methyl groups associated with linalool. PES scans were carried out using the B3LYP/6-31G(d,p) level of theory
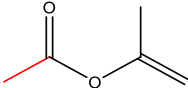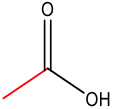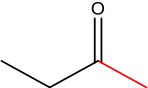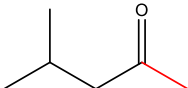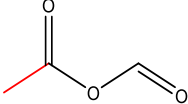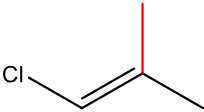
It seems that internal rotation is the cause of the unassigned spectral lines, it is important to consider the accuracy of these potential energy surface scan calculations using the B3LYP/6-31G(d,p) level of theory. A literature search produced more than 20 papers in which the barrier for internal methyl rotation was measured experimentally for a variety of different organic molecules. The barriers for internal methyl rotation for each of these molecules were calculated at the B3LYP/6-31G(d,p) level of theory. Additional calculations with the 6-31++G(d,p) basis set were undertaken to assess the importance of the diffuse functions in such calculations, see Table 5.3. The methyl rotor with the lowest rotation barrier can be seen highlighted in Table 5.3.

Table 5.3: Comparison of experimental and calculated barriers for methyl rotation

Molecule	Skeletal Structure[a]	Experimental Barrier (cm⁻¹)	Calculated Barrier[b] (cm⁻¹)	Experimental – Calculated (%)	Calculated Barrier[c] (cm⁻¹)	(Expt.–Calc.) /Expt. (%)
m-toluidine		1.97[47]	10	407.6	11	458
Acetamide		24.34[48]	31	27.5	70	188.0
Ethyl Acetamidoacetate		63.695[28]	89	39.7	133	108.8
Isoamyl Acetate		93.953[49]	72	23.4	48	48.9
Allyl Acetate		98.093[50]	76	22.5	57	41.9
Methyl Acetate		101.74[51]	74	27.3	60	41
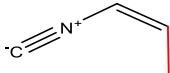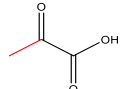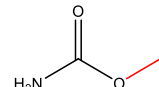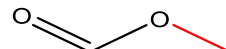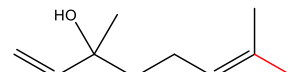
[a]Methyl rotor with the lowest barrier of internal rotation highlighted in red, [b]Barrier calculated at the B3LYP/6-31G(d,p) level of theory, [c]Barrier calculated at the B3LYP/6-31++G(d,p) level of theory

Table 5.3: Cont.

Molecule	Skeletal Structure[a]	Experimental Barrier (cm^{-1})	Calculated Barrier[b] (cm^{-1})	Experimental – Calculated (%)	Calculated Barrier[c] (cm^{-1})	(Expt.–Calc.) /Expt. (%)
Isopropenyl Acetate		135.3498[52]	116	14.3	85	37.2
Acetic Acid		170.178[53]	134	21.3	125	26.5
Ethyl Methyl Ketone		181.17[54] 183[55]	176	2.9 3.8	112	38.2 38.8
Methyl Isobutyl Ketone		250.3[56]	240	4.1	140	44.1
Formic Acetic Anhydride		254.711[57]	231	9.3	210	17.6
1-chloro-2-methylpropene		304.34[58]	310	1.9	274	9.9
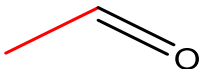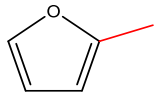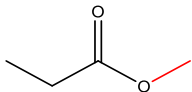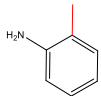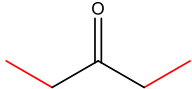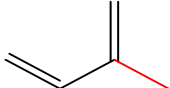
[a]Methyl rotor with the lowest barrier of internal rotation highlighted in red, [b]Barrier calculated at the B3LYP/6-31G(d,p) level of theory, [c]Barrier calculated at the B3LYP/6-31++G(d,p) level of theory

Table 5.3: Cont.

Molecule	Skeletal Structure[a]	Experimental Barrier (cm^{-1})	Calculated Barrier[b] (cm^{-1})	Experimental – Calculated (%)	Calculated Barrier[c] (cm^{-1})	(Expt.–Calc.) /Expt. (%)
Z-1-Propenyl Isocyanide		335.409[59]	425	26.7	366	9.1
Pyruvic Acid		336.368[60]	228	32.2	300	10.8
Methyl Carbamate		359.141[61]	162	54.9	223	37.9
Methyl Formate		370.924[62]		77.1		82.4
		372.672[63]	85	77.2	65	82.5
		370.7398[64]		77.1		82.6
Methanol		373.594[65]	474	26.9	401	7.3
Linalool		400.2[26]	305	23.8	351	12.3
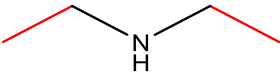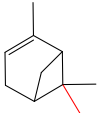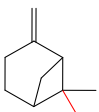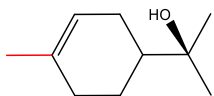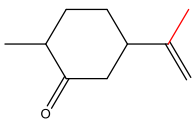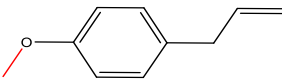
[a]Methyl rotor with the lowest barrier of internal rotation highlighted in red, [b]Barrier calculated at the B3LYP/6-31G(d,p) level of theory, [c]Barrier calculated at the B3LYP/6-31++G(d,p) level of theory

Table 5.3: Cont.

Molecule	Skeletal Structure[a]	Experimental Barrier (cm⁻¹)	Calculated Barrier[b] (cm⁻¹)	Experimental − Calculated (%)	Calculated Barrier[c] (cm⁻¹)	(Expt.−Calc.) /Expt. (%)
Acetaldehyde		407.716[65] 407.947[68]	395	3.1	367	1.8
2-methylfuran		412.873[69]	333	19.3	367	11.1
Methyl Propionate		429.324[70]	224	47.8	283	34.1
o-toluidine		531[49]	701	32.0	698	31.4
Diethyl Ketone		771.93[69]	686	11.1	733	5.0
Isoprene		916[70]	855	6.7	807	11.9
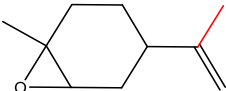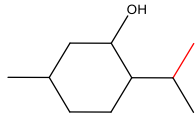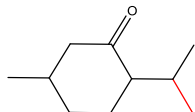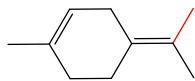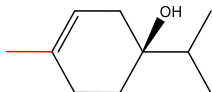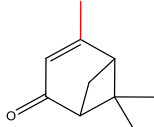
[a]Methyl rotor with the lowest barrier of internal rotation highlighted in red, [b]Barrier calculated at the B3LYP/6-31G(d,p) level of theory, [c]Barrier calculated at the B3LYP/6-31++G(d,p) level of theory

Table 5.3: Cont.

Molecule	Skeletal Structure[a]	Experimental Barrier (cm⁻¹)	Calculated Barrier[b] (cm⁻¹)	Experimental – Calculated (%)	Calculated Barrier[c] (cm⁻¹)	(Expt.–Calc.) /Expt. (%)
Diethyl Amine		1051.74[71]	1122	6.7	1077	2.4
α-pinene		-	820		783	
β-pinene		-	874		849	
α-terpineol		-	783		768	
Dihydrocarvone		-	599		564	
Estragole		-	1157		1115	

[a]Methyl rotor with the lowest barrier of internal rotation highlighted in red, [b]Barrier calculated at the B3LYP/6-31G(d,p) level of theory, [c]Barrier calculated at the B3LYP/6-31++G(d,p) level of theory

Table 5.3: Cont.

Molecule	Skeletal Structure[a]	Experimental Barrier (cm^{-1})	Calculated Barrier[b] (cm^{-1})	Experimental – Calculated (%)	Calculated Barrier[c] (cm^{-1})	(Expt.–Calc.) /Expt. (%)
Limonene Oxide		-	585		540	
Menthol		-	998		974	
Menthone		-	1042		1022	
Terpinolene		-	208		191	
Terpinen-4-ol		-	759		744	
Verbenone		-	741		808	

[a]Methyl rotor with the lowest barrier of internal rotation highlighted in red, [b]Barrier calculated at the B3LYP/6-31G(d,p) level of theory, [c]Barrier calculated at the B3LYP/6-31++G(d,p) level of theory

117

Generally, using the 6-31G(d,p) basis set, the calculated methyl rotors with the greatest accuracy in comparison to those measured experimentally, are those generally bound to an unsaturated bond, whereas those with the worst accuracy are bound either to an oxygen atom or are substituents on an aromatic system. No such trend is apparent when using the 6-31++G(d,p) basis set.

The comparison between the two basis sets yielded no definite answer when questioning the importance of the diffuse functions for calculating internal rotation barriers. The majority of the tested molecules suggest that to calculate the internal rotational barrier for a methyl group bound to either a C=C or C=O unsaturated bond, such as in acetamide and isoprene, the 6-31G(d,p) basis set yields the more accurate results. However, this observation is not categorical as methyl acetate, linalool and others, which have methyl rotors bound to an unsaturated bond, have their methyl rotational barrier more accurately calculated using the 6-31++G(d,p) basis set. There seems to be no overall pattern as to which of the methyl rotational barriers tested are more accurately determined using the 6-31++G(d,p) basis set, meaning that it cannot be concluded that the inclusion of diffuse functions is beneficial to such calculations.

It is interesting that for toluidine the barrier for methyl rotation is calculated with a greater degree of accuracy with the methyl and amine substituents in the *ortho-* rather than the *meta-*position. The barrier for internal rotation for *o*-toluidine was calculated as 698 cm^{-1} at the B3LYP/6-31++G(d,p), compared to 531 cm^{-1} recorded by Bird and Pratt [48] a difference of 31.4%. This difference is significantly smaller than that observed for *m*-toluidine, the internal barrier was calculated as 11 cm^{-1} compared to 1.97 cm^{-1} recorded by Bird and Pratt [48], a difference of 458%. It can be postulated that the structural stability considerations that accompany electrophilic substituent reactions that would have led to the creation of these di-substituted aromatic systems, could also be used to comment on the accuracy of the computational calculations.

During electrophilic substituent reactions methyl substituents are *ortho-* and *para-* directing activators as they possess an electron-donating inductive effect. Alkyl substituents donate electrons via an σ-bond due to the difference in electronegativity between the alkyl substituent and the aromatic ring. In the *ortho-* and *para-* positions, a resonance form places the positive charge directly on the methyl substituted carbon, this

forms a tertiary carbocation which is best stabilized by the inductive electron-donation of the alkyl group.[17]

Similarly, during electrophilic substituent reactions amine substituents are *ortho-* and *para*-directing activators as they possess a strong electron-donating resonance effect, which outweighs the weaker electron-withdrawing inductive effect. Amine substituents donate electrons via a π-bond due to the overlap of the lone pair of the amine group and a *p*-orbital on the aromatic ring, the lone pair move from the substituent to the aromatic ring placing a negative charge on the ring. In the *ortho-* and *para-* positions, the most stable resonance form is created where the positive charge can directly stabilised by donation from the lone pair on the nitrogen.[17]

As both methyl and amine groups are *ortho-* and *para*-directing, due to greater resonance stability, it stands to reason that *o*-toluidine is a more stable structure than *m*-toluidine. Due to its reduced stability it could be argued that the ability of Gaussian 03 to accurately calculate the optimised structure and internal methyl rotational barrier for *m*-toluidine, would be reduced, in comparison to *o*-toluidine, resulting in the extremely large discrepancy between the theoretical and experimental rotation barriers.

Table 5.3 does show a comparison between the theoretical and experimental rotation barrier for linalool, which results from the FTMW study by Nguyen *et al.*[26] The authors also completed their own internal rotation computational calculations at the MP2/6-311++G(d,p) level of theory and calculated the barriers for each of the methyl rotors H_{22}-C_{20}-C_{15}-C_{13}, H_{18}-C_{16}-C_{15}-C_{13} and H_{27}-C_{24}-C_6-C_4 as 324, 776 and 1327 cm^{-1} respectively. Considering their lowest barrier of rotation at 324 cm^{-1}, the discrepancy between the theoretical and experimental barrier was reduced to 19% for the MP2 calculation in comparison to 24% for B3LYP/6-31G(d,p) calculation as listed in Table 5.3. With the inclusion of diffuse functions (B3LYP/6-31++G(d,p)) the discrepancy between the theoretical and experimental barrier was further reduced to 12%, as listed in Table 5.3.

5.3.2.4 Fitting of the Internal Rotation Barrier

In the initial fit which accounts for the splitting of the spectral lines, resultant from the torsional motion of the dihedral angle H_{22}-C_{20}-C_{15}-C_{13}, the rotational constants from 274 *b*-type transitions could be obtained from XIAM[27], which uses the internal axis method to accommodate for internal rotation whilst fitting asymmetric top molecules. Preliminary

fits using this programme offered unacceptably high errors with regards to the observed transitions; the average Obs.-Calc. of 0.1 MHz.

In attempts to overcome this issue the molecular parameters from the Nguyen *et al.* FTMW study were analysed. A minor alteration involves the molecular parameters fitted for each data set; Nguyen *et al.* were unable to fit the centrifugal distortion constant ΔK due to large correlation to B-(A+C)/2, an issue not experienced during the analysis of the data from this investigation. More importantly Nguyen *et al.* fitted 78 transitions (63 *a*-type transitions with the selection rule $\Delta J = \pm 1$, $\Delta K_a = 0$ and $\Delta K_c = \pm 1$, ± 3 and 15 *c*-type transitions $\Delta J = \pm 1$, $\Delta K_a = \pm 1$, ± 3 and $\Delta K_c = 0$) with a standard deviation of 4.6 kHz, whereas this investigation has 241 *b*-type transitions. Nguyen *et al.* state that there are no *b*-type transitions due to the negligible dipole moment in the B direction. This suggests that the initial fit in this investigation was undertaken using the incorrect prediction of the dipole moment. Changing the axis system fitted 241 *c*-type transitions which had a greatly reduced error with regards to the observed transitions; the average Obs.-Calc. was now 0.05 MHz.

The rotational transitions from the FTMW[26] paper as well as those recorded in this investigation were fitted using the molecular parameters published by Nguyen *et al.* as an initial guess. These parameters allowed the *A*-state transitions from the Stark modulated microwave spectrum of linalool to be fitted with minimal error yet the overall standard deviation of the fit seemed comparatively large. Closer inspection of the individual transitions showed that whilst the *A*-state transitions were fitting well the *E*-states were not, in fact these fits suggested that there was additional splitting on the *E*-state transitions thus we would expect to see three peaks at each frequency in the recorded spectrum of linalool.

Nguyen *et al.* suggest that the rotation about H_{18}-C_{16}-C_{15}-C_{13}, with a barrier of 776 cm^{-1}, would result in additional splitting of the *A*- and *E*-species, however only some transitions displayed additional splitting, which was in the order of 10 kHz.[26] Ordinarily only broadened lines were found so the authors concluded that even with their spectrometer in high resolution mode they are unable to pick up the splitting due to the internal rotation about the angle H_{18}-C_{16}-C_{15}-C_{13}.

The Stark modulated, continuous jet millimetre wave absorption system used in this investigation produced 2 lines at each rotational frequency, an *A*- and *E*-state caused by

splitting due to the internal torsion about H_{22}-C_{20}-C_{15}-C_{13}; however, the XIAM fits suggest that there should be in fact 3 lines, with additional splitting of the *E*-state. These fits suggest that the *E*-state transitions are split by around 100 kHz with the *A*-state transition positioned between them. It was theorised that using a 2000 V Stark voltage was too large in order to see this additional splitting.

5.3.3 Investigating the Stark Effect of the Microwave Spectrum of Linalool

In order to investigate whether altering the voltage of the Stark field would result in the additional splitting predicted by initial fits, rotational transitions of linalool were recorded with 500, 200, 100, 75, 50, 25 and 15 V between the plates which were separated by 3.5 cm. Unfortunately there was little consistency with the observed splitting patterns across these voltages; of the sampled frequencies the use of Stark fields of 500 and 100 V cm^{-1} (Figure 5.14) only produced two transitions as previously seen in the original investigation with a Stark field of 2000 V cm^{-1}.
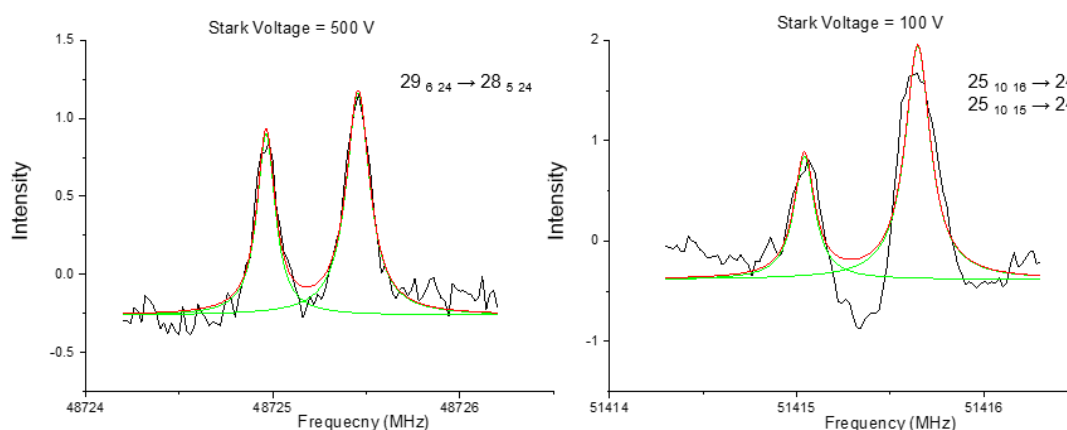
Figure 5.14: Rotational transitions fitted using a Lorentzian line shape function, using a 500 and 100 V Stark field

For practical reasons not every rotational frequency could be recorded with each of the sample Stark fields so there is no way to categorically conclude that Stark fields of 500 and 100 V would always result in only two transitions, but this was the result from this investigation.

However, as can be seen from Figure 5.15 there was less regularity using Stark voltages of 200, 75, 50 and 25 V; for each of these Stark fields rotational frequencies were recorded with a combination of two and three transitions therefore there is no way to emphatically

conclude that a particular Stark field will yield the desired splitting resulting in the three transitions predicted by the initial fits. Having said this Figure 5.15 seems to show that using a Stark voltage of either 200 V or 25 V gives the clearest depiction of the third peak; whilst a third peak is still visible when using a Stark voltage of 75 V and 50 V, they are more reminiscent of a shoulder on the larger central peak rather than a separate peak.

For each of the Stark voltages tested, all transitions were fitted using the XIAM[27] program to ascertain which, if any, Stark field offered an improvement on the overall fit in comparison to the experiment carried out using a 2000 V cm^{-1} Stark field. The fits from the Stark fields of 50 and 25 V cm^{-1} produced overall standard deviations of 150 and 169 kHz respectively, rather large especially in comparison to the 4.6 kHz recorded by Nguyen *et al.* [26].
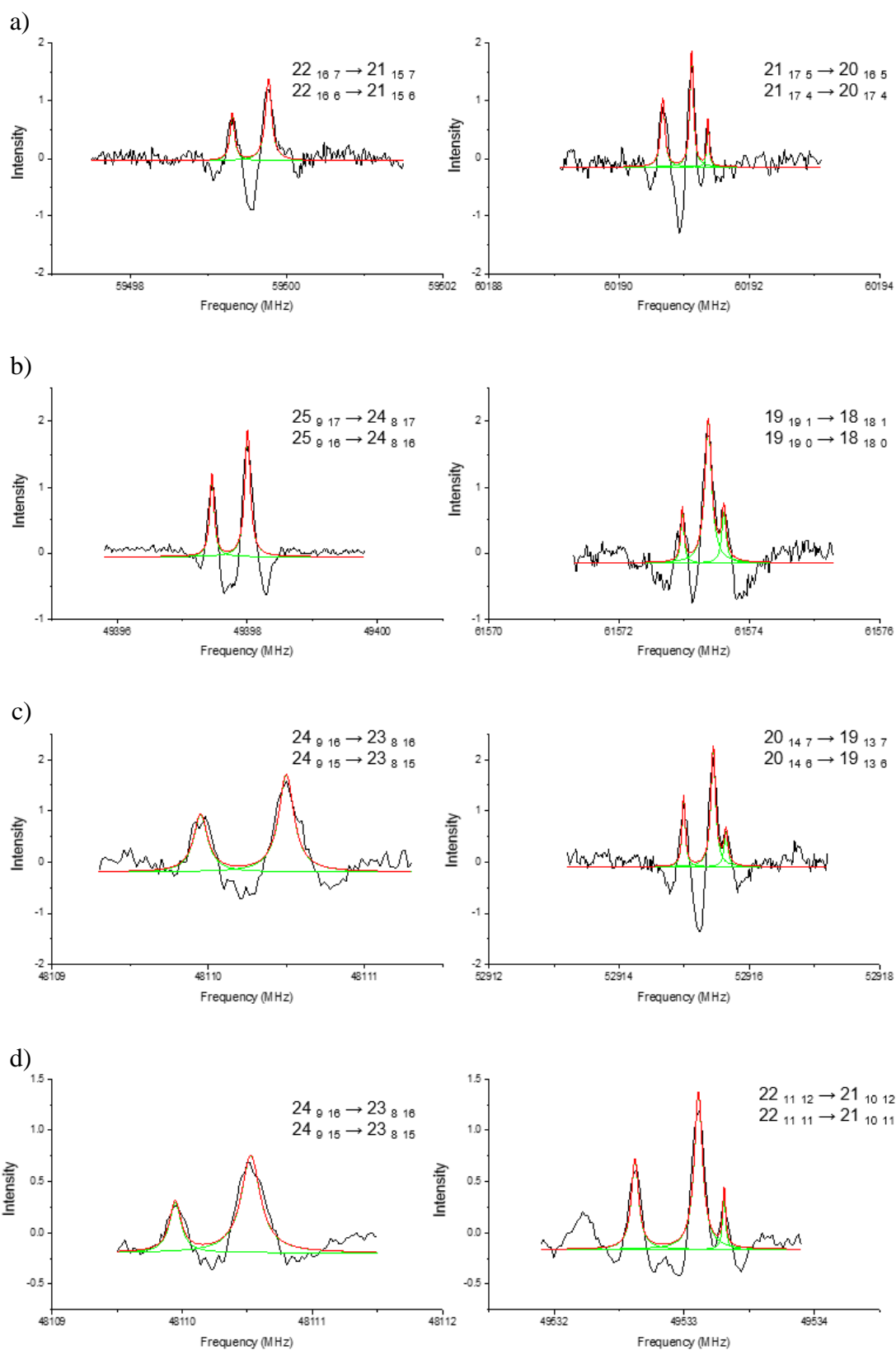
Figure 5.15: Rotational transitions fitted using a Lorentzian line shape function, using a) 200 V, b) 75 V, c) 50 V or d) 25 V Stark voltages

The use of a 15 V Stark voltage showed the most reproducibility for the observed splitting patterns, with the vast majority of transitions being split into three distinct peaks (Figure 5.16). This suggested that the Stark field used to conduct the original experiment was too large to observe the splitting of the spectral lines.
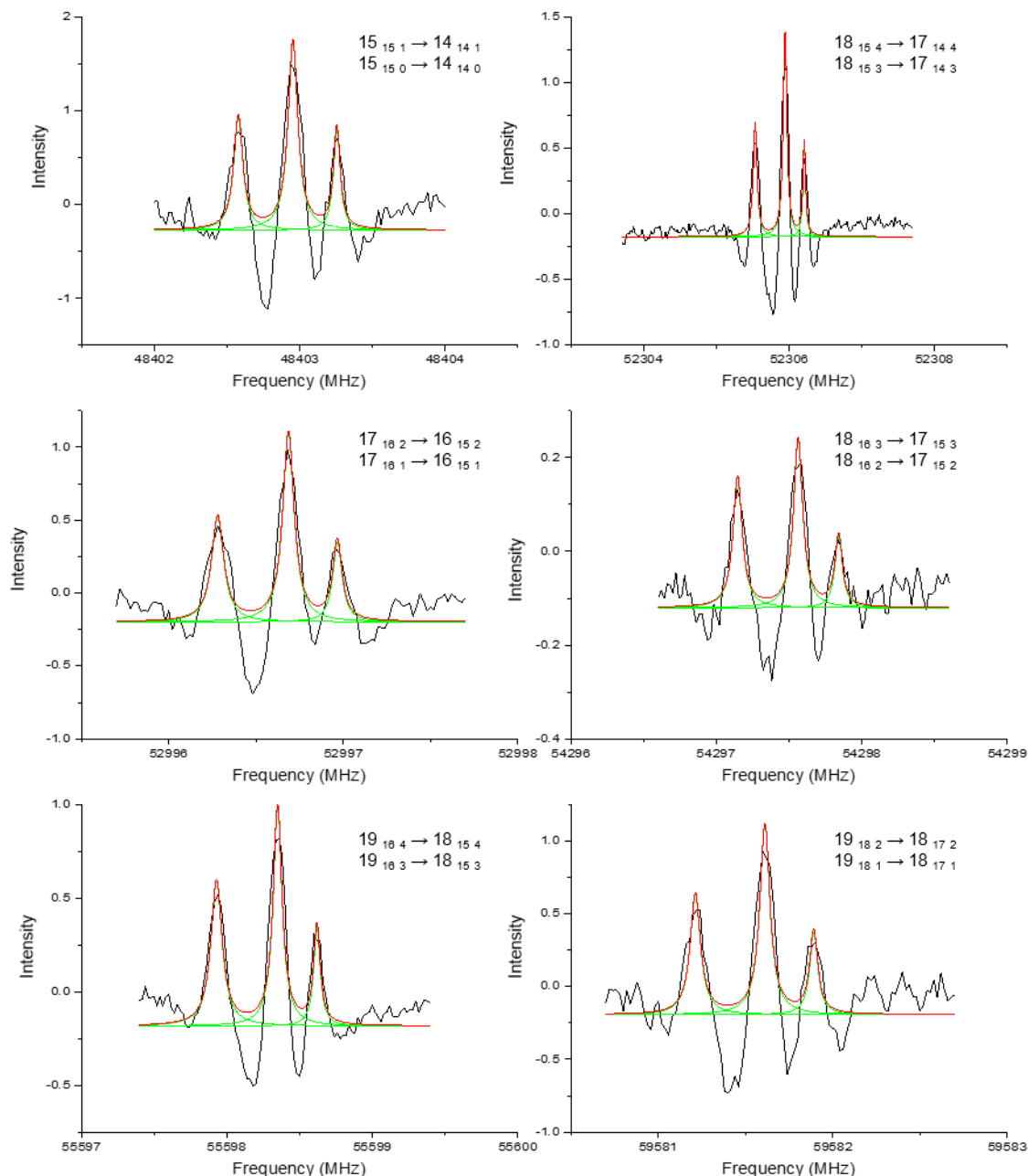
Figure 5.16: Rotational transitions fitted using a Lorentzian line shape function, using 15 V Stark voltages

Each of the rotational frequencies shown in Figure 5.16 have many commonalities; all of the examples have relatively low intensities, show the presence of three transitions and the majority have a similar line width of around 70 kHz, the only exception to this are the

transitions at 52306 MHz where the line width is around 55 kHz. Whilst a 15 V Stark field seemingly produces the additional splitting to yield the predicted three transitions and initial fits calculated an extremely low standard deviation of 9.6 kHz, it should be noted that the use of this voltage was not perfect; the use of a 15 V Stark field still produced rotational frequencies with only two transitions present.

As can be seen in Figure 5.17, not only are there two transitions present but the scan is extremely noisy, resulting in an average line width of 106 kHz.
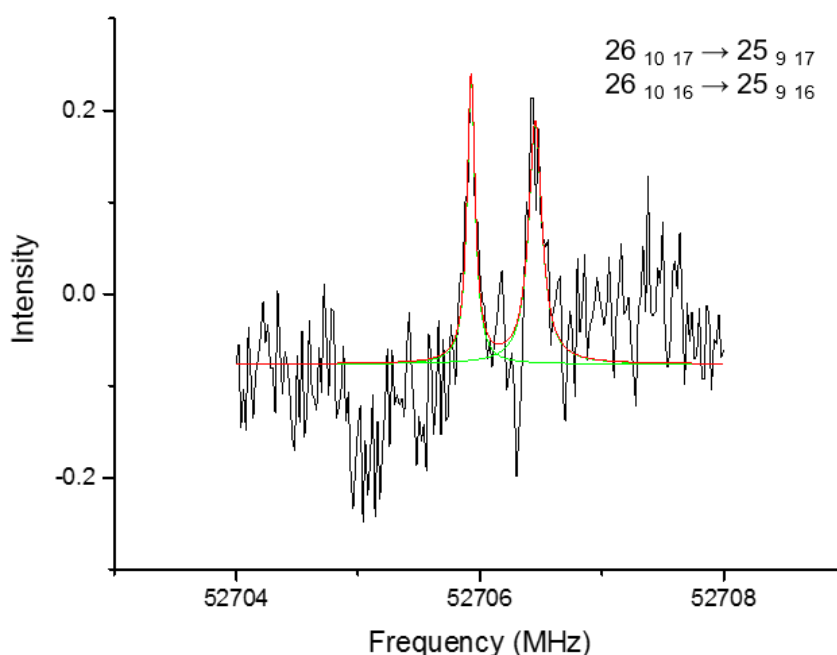
Figure 5.17: Rotational transition at 52706 MHz fitted using a Lorentzian line shape function, using 15 V Stark voltage

In order to truly observe the effect that altering the Stark field had on the observable splitting of the spectral lines, single rotational frequencies were observed at a variety of different Stark fields ranging from 1600 – 12.5 V. Figures 5.18 and 5.19 show transitions present at 58280 and 49398 MHz respectively; they show that as the Stark field applied is decreased the noise present in the spectrum increases and the recorded intensities of the observed transitions decreases.

The rotational transitions at 58280 MHz possessed the desired behaviour with regards to the splitting of the spectral lines; with Stark fields between 1600 – 400 V the "third" peak is only present at a slight shoulder on the larger central peak. Between 200 – 50 V this shoulder becomes more defined until the use of the low Stark field voltages of 25 and

12.5 V reveal this transition as a separate peak. However, the rotational transitions at 49398 MHz did not display the desired behaviour with respect to the observed splitting pattern. Regardless of the Stark field used only two transitions were detected at this rotational frequency. While far from conclusive, the transitions observed in Figures 5.17 and 5.19 suggested that re-recording the microwave spectrum of linalool using a lower Stark field would be ill advised as there would no guarantee that three peaks would be observed, which would be the primary objective of this experiment.
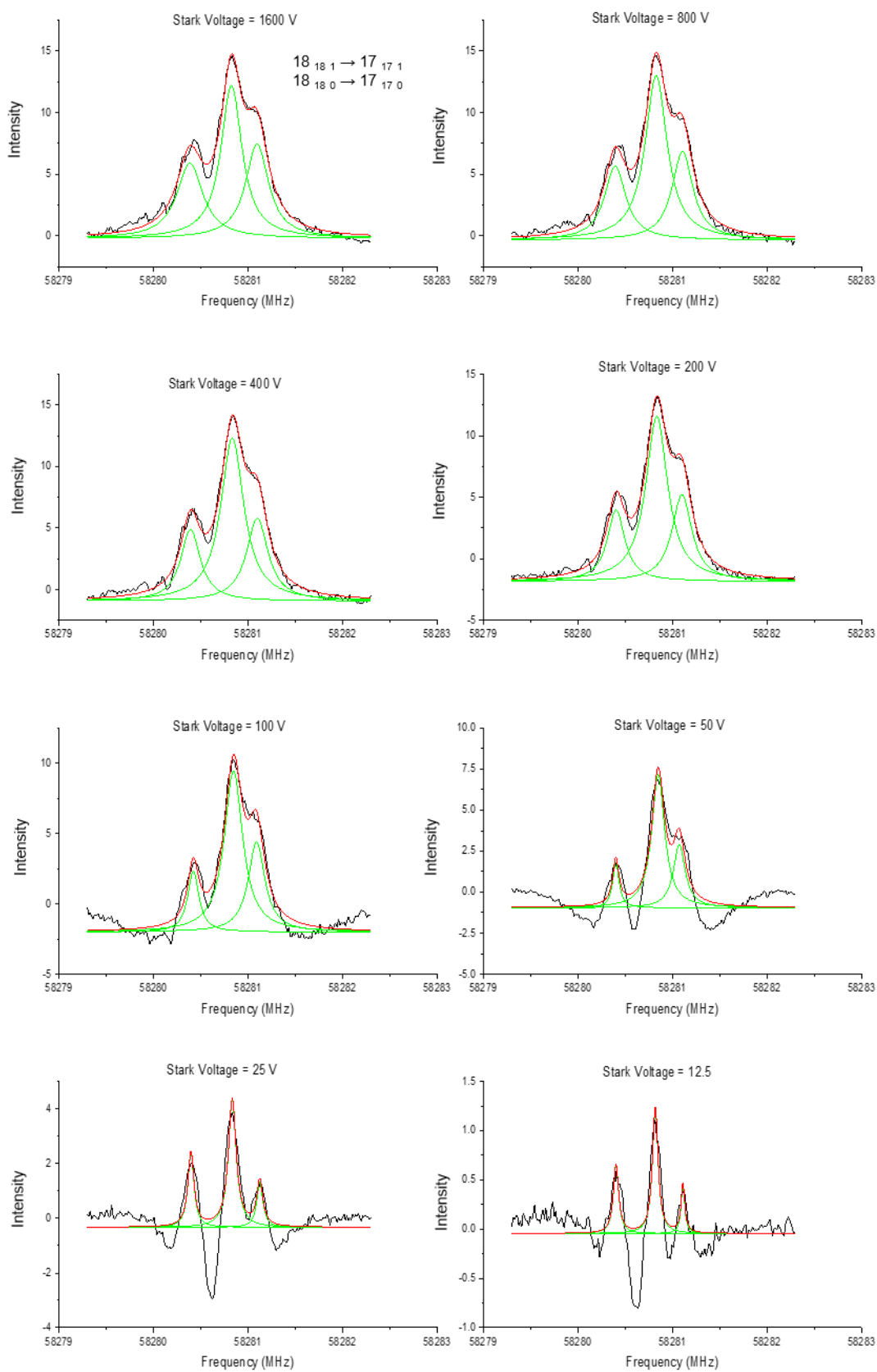
Figure 5.18: Rotational transition at 58280.9 MHz, fitted using a Lorentzian line shape function, at Stark voltages ranging from 1600 – 12.5 V
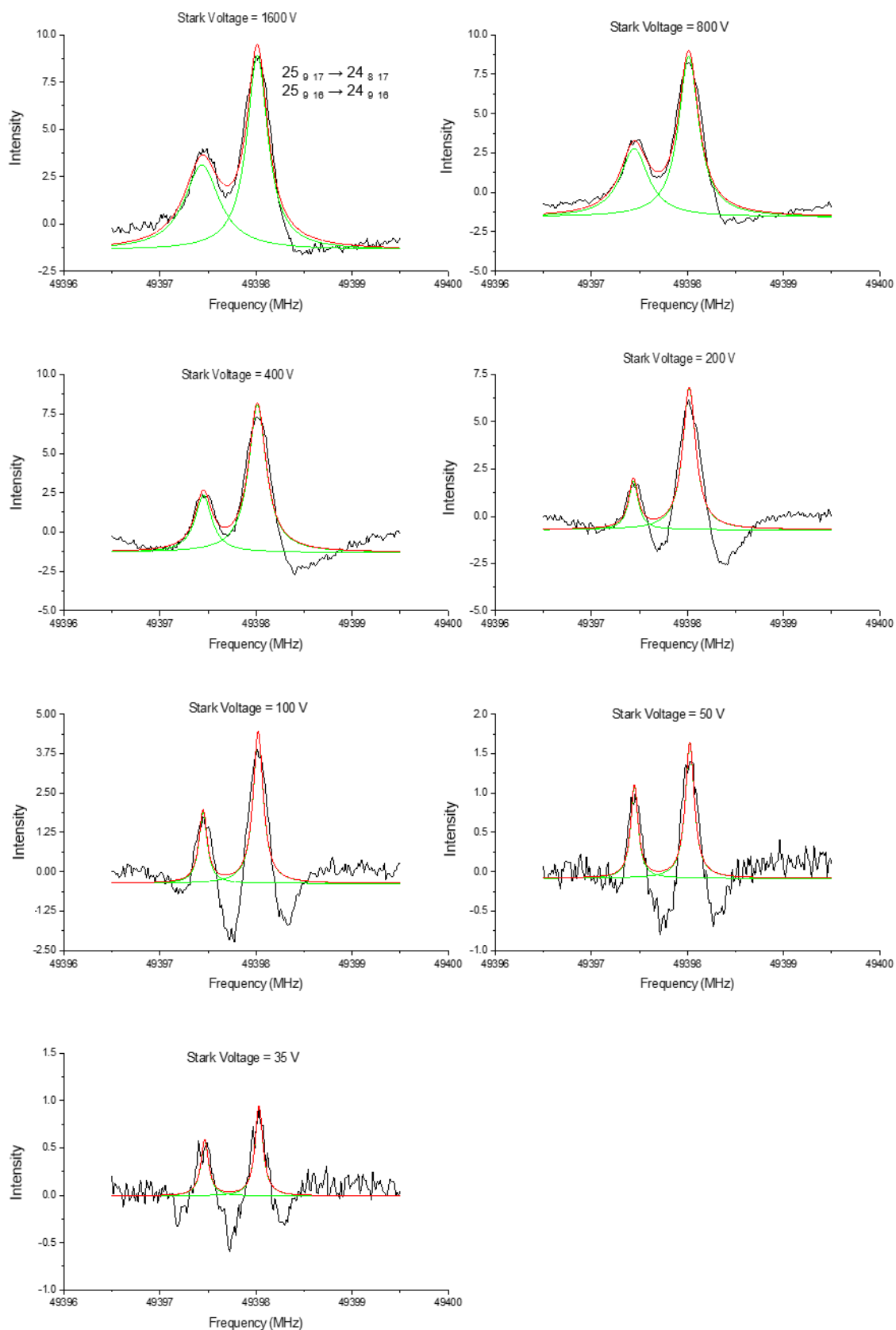
Figure 5.19: Rotational transition at 49398 MHz, fitted using a Lorentzian line shape function, at Stark voltages ranging from 1600 – 35 V

5.3.4 Final Fitting of Microwave Spectrum of Linalool

The rotational constants from the 63 a-type (with the selection rule $\Delta J = \pm 1$, $\Delta K_a = 0$ and $\Delta K_c = \pm 1, \pm 3$) and 332 c-type transitions (with the selection rule $\Delta J = \pm 1$, $\Delta K_a = \pm 1, \pm 3$ and $\Delta K_c = 0$), which are listed in Table 5.4, were fitted in good agreement with the MP3/6-31++G(d,p) values (Table 5.5).

Table 5.4: Fitted a- and c-type transition frequencies (MHz) from the millimetre-wave spectrum of linalool

Transition $(J'_{K_aK_c} - J''_{K_aK_c})$		Observed	Calculated	Obs-Calc	Standard deviation[a]
$6_{24} - 5_{14}$	E	10520.8709	10520.8121	0.0588	0.0046
$7_{16} - 6_{15}$	E	9282.9370	9282.8717	0.0653	0.0046
$7_{16} - 6_{15}$	A	9283.0431	9283.0925	-0.0494	0.0046
$7_{25} - 6_{15}$	E	11785.3089	11785.2534	0.0555	0.0046
$7_{25} - 6_{15}$	A	11785.3567	11785.3557	0.0010	0.0046
$7_{25} - 6_{24}$	E	9233.5150	9233.6774	0.0520	0.0046
$7_{25} - 6_{24}$	A	9233.6206	9233.6774	-0.0568	0.0046
$7_{26} - 6_{25}$	E	9082.9959	9082.9627	0.0332	0.0046
$7_{34} - 6_{33}$	E	9137.3078	9137.3423	-0.0345	0.0046
$7_{34} - 6_{33}$	A	9137.4690	9137.5205	-0.0515	0.0046
$7_{34} - 6_{24}$	A	13977.6961	13977.6569	0.0392	0.0046
$7_{35} - 6_{25}$	E	14161.4660	14161.4182	0.0478	0.0046
$7_{35} - 6_{25}$	A	14161.5788	14161.5616	0.0172	0.0046
$7_{35} - 6_{34}$	A	9126.2905	9126.3454	-0.0549	0.0046
$7_{35} - 6_{34}$	E	9126.2975	9126.1763	0.1212	0.0046
$7_{52} - 6_{25}$	A	9083.0642	9083.1093	-0.0451	0.0046
$7_{52} - 6_{51}$	E	9117.0816	9117.0496	0.0320	0.0046
$7_{52} - 6_{51}$	A	9117.1612	9117.2174	-0.0562	0.0046
$8_{08} - 7_{07}$	E	10195.9366	10195.9153	0.0213	0.0046
$8_{08} - 7_{07}$	A	10196.0218	10196.0484	-0.0266	0.0046
$8_{17} - 7_{16}$	E	10588.9827	10588.9106	0.0721	0.0046
$8_{17} - 7_{16}$	A	10589.1019	10589.1527	-0.0508	0.0046

Table 5.4: Cont.

$8_{18} - 7_{17}$	E	10103.5341	10103.5570	-0.0229	0.0046
$8_{18} - 7_{17}$	A	10103.5602	10103.5806	-0.0204	0.0046
$8_{26} - 7_{25}$	E	10581.2135	10581.1436	0.0699	0.0046
$8_{26} - 7_{25}$	A	10581.3368	10581.3987	-0.0619	0.0046
$8_{26} - 7_{16}$	A	13083.6554	13083.6619	-0.0065	0.0046
$8_{26} - 7_{16}$	E	13083.5602	13082.5253	0.0349	0.0046
$8_{27} - 7_{17}$	A	14277.7137	14277.7830	-0.0693	0.0046
$8_{27} - 7_{26}$	E	10370.5938	10370.5576	0.0362	0.0046
$8_{27} - 7_{26}$	A	10370.6706	10370.7193	-0.0487	0.0046
$8_{35} - 7_{34}$	E	10455.0938	10455.0602	0.0336	0.0046
$8_{35} - 7_{34}$	A	10455.2164	10455.2716	-0.0552	0.0046
$8_{35} - 7_{25}$	E	15090.6923	15199.1907	-0.0433	0.0046
$8_{35} - 7_{25}$	A	15124.2128	15124.2506	-0.0378	0.0046
$8_{36} - 7_{35}$	E	10433.1366	10433.0582	0.0784	0.0046
$8_{36} - 7_{35}$	A	10433.1989	10433.2527	-0.0538	0.0046
$9_{18} - 8_{26}$	E	9390.8315	9390.7327	0.0988	0.0046
$9_{18} - 8_{26}$	A	9390.9964	9391.0910	-0.0946	0.0046
$9_{09} - 8_{08}$	E	11430.3747	11430.3467	0.0280	0.0046
$9_{09} - 8_{08}$	A	11430.4905	11430.5215	-0.0310	0.0046
$9_{18} - 8_{17}$	E	11885.4284	11885.3474	0.0810	0.0046
$9_{18} - 8_{17}$	A	11885.6002	11885.5474	-0.0528	0.0046
$9_{19} - 8_{18}$	A	11354.0406	11354.0746	-0.0340	0.0046
$9_{27} - 8_{17}$	E	14424.9375	14424.8650	0.0725	0.0046
$9_{27} - 8_{17}$	A	14425.0363	14425.0548	-0.0185	0.0046
$9_{27} - 9_{26}$	E	11930.3406	11930.2503	0.0903	0.0046
$9_{27} - 9_{26}$	A	11930.4811	11930.5457	-0.0646	0.0046
$9_{28} - 8_{27}$	E	11654.3614	11654.3230	0.0384	0.0046
$9_{28} - 8_{27}$	A	11654.4445	11654.4966	-0.0521	0.0046
$9_{36} - 8_{35}$	E	11779.3516	11779.2927	0.0589	0.0046
$9_{36} - 8_{35}$	A	11779.4825	11779.5415	-0.0590	0.0046
$9_{63} - 8_{62}$	A	11723.0944	11723.1656	-0.0712	0.0046
$9_{37} - 8_{36}$	E	11739.9110	11739.8457	0.0653	0.0046

Table 5.4: Cont.

$9_{3\,7} - 8_{3\,6}$	A	11740.0067	11740.0648	-0.0581	0.0046
$9_{6\,3} - 8_{6\,2}$	E	11722.9970	11722.9504	0.0466	0.0046
$10_{0\,10} - 9_{0\,9}$	E	12661.8902	12661.8474	0.0428	0.0046
$10_{0\,10} - 9_{0\,9}$	A	12662.0681	12662.0999	-0.0318	0.0046
$10_{1\,9} - 9_{1\,8}$	E	13170.5266	13170.4433	0.0833	0.0046
$10_{1\,9} - 9_{1\,8}$	A	13170.6451	13170.6957	-0.0506	0.0046
$10_{1\,9} - 9_{2\,7}$	A	10631.1577	10631.2410	-0.0833	0.0046
$10_{1\,9} - 9_{2\,7}$	E	10631.0162	10630.9257	0.0905	0.0046
$10_{1\,10} - 9_{1\,9}$	A	12601.8192	12601.8571	-0.0379	0.0046
$10_{2\,8} - 9_{1\,8}$	A	15816.8379	15816.8659	-0.0280	0.0046
$10_{2\,8} - 9_{1\,8}$	E	15816.6976	15816.5945	0.1031	0.0046
$10_{2\,8} - 9_{2\,7}$	E	13277.1876	13277.0769	0.1107	0.0046
$10_{2\,8} - 9_{2\,7}$	A	13277.3533	13277.4113	-0.0580	0.0046
$10_{2\,9} - 9_{2\,8}$	A	12934.0579	12934.1143	-0.0564	0.0046
$10_{3\,7} - 9_{3\,6}$	E	13111.4579	13111.3747	0.0832	0.0046
$10_{3\,7} - 9_{3\,6}$	A	13111.6061	13111.6655	-0.0594	0.0046
$10_{6\,4} - 9_{6\,3}$	E	13028.2138	13028.1596	0.0542	0.0046
$10_{6\,4} - 9_{6\,3}$	A	13028.3255	13028.4008	-0.0753	0.0046
$11_{1\,10} - 10_{1\,9}$	E	14442.9312	14442.8574	0.0738	0.0046
$11_{1\,10} - 10_{1\,9}$	A	14443.0520	14443.1006	-0.0486	0.0046
$11_{2\,9} - 10_{2\,8}$	E	14618.7017	14918.5679	0.1338	0.0046
$11_{2\,9} - 10_{2\,8}$	A	14618.8844	14618.9385	-0.0541	0.0046
$11_{2\,10} - 10_{10\,9}$	A	14209.2751	14209.3341	-0.0590	0.0046
$11_{3\,8} - 10_{3\,7}$	E	14452.3357	14452.2259	0.1098	0.0046
$11_{3\,8} - 10_{3\,7}$	A	14452.5050	14452.5629	-0.0579	0.0046
$11_{4\,8} - 10_{4\,7}$	A	14357.0538	14357.1187	-0.0649	0.0046
$12_{0\,12} - 11_{0\,11}$	A	15124.2128	15124.2506	-0.0378	0.0046
$12_{1\,12} - 11_{1\,11}$	A	15090.6490	15090.6923	-0.0433	0.0046
$15_{15\,1} - 14_{14\,1}$	E	48402.5732	48402.5820	-0.0087	0.0164
$15_{15\,0} - 14_{14\,0}$	E	48402.5732	48402.6135	-0.0403	0.0164
$15_{15\,1} - 14_{14\,1}$	A	48402.9754	48402.6095	0.3658	0.0677
$15_{15\,0} - 14_{14\,0}$	A	48402.9754	48402.6095	0.3658	0.0677

Table 5.4: Cont.

16 $_{3\,13}$ − 15 $_{4\,11}$	A	15199.2951	15199.3589	-0.0638	0.0046
16 $_{15\,2}$ − 15 $_{14\,2}$	E	49703.6305	49703.6758	-0.0452	0.0058
16 $_{15\,1}$ − 15 $_{14\,1}$	E	49703.6305	49703.7073	-0.0767	0.0058
16 $_{15\,2}$ − 15 $_{14\,2}$	A	49704.0744	49703.7268	0.3475	0.0719
16 $_{15\,1}$ − 15 $_{14\,1}$	A	49704.0744	49703.7268	0.3475	0.0719
16 $_{16\,1}$ − 15 $_{15\,1}$	E	51695.2955	51695.3032	-0.0076	0.0065
16 $_{16\,0}$ − 15 $_{15\,0}$	E	51695.2955	51695.3347	-0.0392	0.0065
16 $_{16\,1}$ − 15 $_{15\,1}$	A	51695.7000	51695.3307	0.3692	0.0606
16 $_{16\,0}$ − 15 $_{15\,0}$	A	51695.7000	51695.3307	0.3692	0.0606
17 $_{14\,4}$ − 16 $_{13\,4}$	E	49012.8966	49013.0692	-0.1726	0.0071
17 $_{14\,3}$ − 16 $_{13\,3}$	E	49012.8966	49013.1006	-0.2041	0.0571
17 $_{14\,4}$ − 16 $_{13\,4}$	A	49013.4843	49013.1672	0.3171	0.0720
17 $_{14\,3}$ − 16 $_{13\,3}$	A	49013.4843	49013.1672	0.3171	0.0720
17 $_{15\,3}$ − 16 $_{14\,3}$	E	51004.6448	51004.6771	-0.0323	0.0074
17 $_{15\,2}$ − 16 $_{14\,2}$	E	51004.6448	51004.7086	-0.0637	0.0074
17 $_{15\,3}$ − 16 $_{14\,3}$	A	51005.0560	51004.7517	0.3044	0.0574
17 $_{15\,2}$ − 16 $_{14\,2}$	A	51005.0560	510057517	0.3044	0.0574
17 $_{16\,2}$ − 16 $_{15\,2}$	E	52996.2944	52996.2826	0.0119	0.0080
17 $_{16\,1}$ − 16 $_{15\,1}$	E	52996.2944	52996.3141	-0.0196	0.0080
17 $_{16\,2}$ − 16 $_{15\,2}$	A	52996.6949	52996.3336	0.3612	0.0588
17 $_{16\,1}$ − 16 $_{15\,1}$	A	52996.6949	52996.3336	0.3612	0.0588
17 $_{17\,1}$ − 16 $_{16\,1}$	E	54987.9126	54987.9275	-0.0148	0.0043
17 $_{17\,0}$ − 16 $_{16\,0}$	E	54987.9126	54987.9590	-0.0463	0.0043
17 $_{17\,1}$ − 16 $_{16\,1}$	A	54988.3735	54987.9550	0.4184	0.0655
17 $_{17\,0}$ − 16 $_{16\,0}$	A	54988.3735	54987.9550	0.4184	0.0655
18 $_{13\,6}$ − 17 $_{12\,6}$	E	48322.0270	48322.1283	-0.1013	0.0188
18 $_{13\,5}$ − 17 $_{12\,5}$	E	48322.0270	48322.1596	-0.1326	0.0188
18 $_{13\,6}$ − 17 $_{12\,6}$	A	48322.4710	48322.2730	0.1980	0.0195
18 $_{13\,5}$ − 17 $_{12\,5}$	A	48322.4710	48322.2730	0.1980	0.0195
18 $_{14\,5}$ − 17 $_{13\,5}$	E	50313.8480	50313.9157	-0.0677	0.0064
18 $_{14\,4}$ − 17 $_{13\,4}$	E	50313.8480	50313.9471	-0.0991	0.0064
18 $_{14\,5}$ − 17 $_{13\,5}$	A	50314.3362	60314.0371	0.2991	0.0663

$18_{14\,4} - 17_{13\,4}$	A	50314.3362	60314.0371	0.2991	0.0663
$18_{15\,4} - 17_{14\,4}$	E	52305.5319	52305.5645	-0.0326	0.0062
$18_{15\,3} - 17_{14\,3}$	E	52305.5319	52305.5959	-0.0640	0.0062
$18_{15\,4} - 17_{14\,4}$	A	52305.9438	52305.6625	0.2813	0.0562
$18_{15\,3} - 17_{14\,3}$	A	52305.9438	52305.6625	0.2813	0.0562
$18_{16\,3} - 17_{15\,3}$	E	54297.1455	54297.1686	-0.0231	0.0076
$18_{16\,2} - 17_{15\,2}$	E	54297.1455	54297.2000	-0.0545	0.0076
$18_{16\,3} - 17_{15\,3}$	A	54297.5619	54297.2431	0.3188	0.0576
$18_{16\,2} - 17_{15\,2}$	A	54297.5619	54297.2431	0.3188	0.0576
$18_{17\,2} - 17_{16\,2}$	E	56288.8207	56288.7848	0.0359	0.0075
$18_{17\,1} - 17_{16\,1}$	E	56288.8207	56288.8163	0.0045	0.0075
$18_{17\,2} - 17_{16\,2}$	A	56289.2559	56288.8359	0.4200	0.0615
$18_{17\,1} - 17_{16\,1}$	A	56289.2559	56288.8359	0.4200	0.0615
$18_{18\,1} - 17_{17\,1}$	A	58280.9175	58280.4764	0.4411	0.1813
$18_{18\,0} - 17_{17\,0}$	A	58280.9175	58280.4764	0.4411	0.1813
$19_{13\,7} - 18_{12\,7}$	E	49622.5342	49622.6386	-0.1044	0.0087
$19_{13\,6} - 18_{12\,6}$	E	49622.5342	49622.6700	-0.1357	0.0087
$19_{13\,7} - 18_{12\,7}$	A	49623.0029	49622.8065	0.1964	0.0088
$19_{13\,6} - 18_{12\,6}$	A	49623.0029	49622.8065	0.1964	0.0088
$19_{14\,6} - 18_{13\,6}$	E	51614.5306	51614.5880	-0.0574	0.0063
$19_{13\,5} - 18_{13\,5}$	E	51614.5306	51614.6194	-0.0888	0.0063
$19_{14\,6} - 18_{13\,6}$	A	51614.9695	51614.7328	0.2368	0.0082
$19_{14\,5} - 18_{13\,5}$	A	51614.9695	51614.7328	0.2368	0.0082
$19_{15\,5} - 18_{14\,5}$	E	53606.2282	53606.3144	-0.0862	0.0583
$19_{15\,4} - 18_{14\,4}$	E	53606.2282	5360.3458	-0.1176	0.0583
$19_{15\,5} - 18_{14\,5}$	A	53606.7073	53606.4359	0.2714	0.0142
$19_{15\,4} - 18_{14\,4}$	A	53606.7073	53606.4359	0.2714	0.0142
$19_{16\,4} - 18_{15\,4}$	E	55597.9279	55597.9423	-0.0144	0.0093
$19_{16\,3} - 18_{15\,3}$	E	55597.9279	55597.9737	-0.0458	0.0093
$19_{16\,4} - 18_{15\,4}$	A	55598.3482	55598.0403	0.3079	0.0576
$19_{16\,3} - 18_{15\,3}$	A	55598.3482	55598.0403	0.3079	0.0576
$19_{17\,3} - 18_{16\,3}$	A	57589.8495	57589.6217	0.2278	0.0899

Table 5.4: Cont.

$19_{17\,3} - 18_{16\,3}$	A	57589.8495	57589.6217	0.2278	0.0899
$19_{18\,2} - 18_{17\,2}$	E	59581.2879	59581.1765	0.1114	0.0567
$19_{18\,1} - 18_{17\,1}$	E	59581.2879	59581.2080	0.0799	0.0567
$19_{18\,2} - 18_{17\,2}$	A	59581.2276	59581.6819	0.4543	0.0561
$19_{18\,2} - 18_{17\,2}$	A	59581.2276	59581.6819	0.4543	0.0561
$19_{19\,1} - 18_{18\,1}$	E	61572.9725	61572.8614	0.1111	0.0060
$19_{19\,0} - 18_{18\,0}$	E	61572.9725	61572.8930	0.0796	0.0060
$19_{19\,1} - 18_{18\,1}$	A	61572.3967	61572.8890	-0.5193	0.1127
$19_{19\,0} - 18_{18\,0}$	A	61572.3967	61572.8890	-0.5193	0.1127
$20_{12\,9} - 19_{11\,9}$	E	48930.0180	48930.1017	-0.0837	0.0117
$20_{12\,8} - 19_{11\,8}$	E	48930.0180	48930.1330	-0.1150	0.0117
$20_{12\,9} - 19_{11\,9}$	A	48930.4800	48930.3153	0.1647	0.0134
$20_{12\,8} - 19_{11\,8}$	A	48930.4800	48930.3153	0.1647	0.0134
$20_{13\,8} - 19_{12\,8}$	E	50922.8090	50922.8787	-0.0697	0.0212
$20_{13\,7} - 19_{12\,7}$	E	50922.8090	50922.9100	-0.1010	0.0212
$20_{13\,8} - 19_{12\,8}$	A	50923.2860	50923.0697	0.2163	0.0272
$20_{13\,7} - 19_{12\,7}$	A	50923.2860	50923.0697	0.2163	0.0272
$20_{14\,7} - 19_{13\,7}$	E	52914.9820	52915.0538	-0.0717	0.0071
$20_{14\,6} - 19_{13\,6}$	E	52914.9820	52915.0851	-0.1030	0.0071
$20_{14\,7} - 19_{13\,7}$	A	52915.4301	52915.2217	0.2084	0.0078
$20_{14\,6} - 19_{13\,6}$	A	52915.4301	52915.2217	0.2084	0.0078
$20_{15\,6} - 19_{14\,6}$	E	54906.7813	54906.9014	-0.1200	0.0079
$20_{15\,5} - 19_{14\,5}$	E	54906.7813	54906.9327	-0.1514	0.0079
$20_{15\,6} - 19_{14\,6}$	A	54907.3157	54907.0461	0.2696	0.0668
$20_{15\,5} - 19_{14\,5}$	A	54907.3157	54907.0461	0.2696	0.0668
$20_{16\,5} - 19_{15\,5}$	E	56898.5584	56898.5832	-0.0248	0.0074
$20_{16\,4} - 19_{15\,4}$	E	56898.5584	56898.6145	-0.0561	0.0074
$20_{16\,5} - 19_{15\,5}$	A	56898.0459	56797.7046	-0.6586	0.1129
$20_{16\,4} - 19_{15\,4}$	A	56898.0459	56797.7046	-0.6586	0.1129
$21_{11\,11} - 20_{10\,11}$	E	48234.6740	48234.8254	-0.1514	0.0159
$21_{11\,10} - 20_{10\,10}$	E	48234.6740	48234.8567	-0.1827	0.0159
$21_{11\,11} - 20_{10\,11}$	A	48235.1630	48235.0830	0.0800	0.0150

Table 5.4: Cont.

$21_{11\,10} - 20_{10\,10}$	A	48235.1630	48235.0830	0.0800	0.0150
$21_{12\,10} - 20_{11\,10}$	E	50229.5903	50229.5244	0.0659	0.0049
$21_{12\,9} - 20_{11\,9}$	E	50229.5903	50229.5556	0.0346	0.0049
$21_{12\,10} - 20_{11\,10}$	A	50229.7400	50229.7605	-0.0205	0.0122
$21_{12\,9} - 20_{11\,9}$	A	50229.7400	50229.7605	-0.0205	0.0122
$21_{13\,9} - 20_{12\,9}$	E	52222.7066	52222.8034	-0.0968	0.0079
$21_{13\,8} - 20_{12\,8}$	E	52222.7066	52222.8347	-0.1280	0.0079
$21_{13\,9} - 20_{12\,9}$	A	52223.1774	52223.0172	0.1602	0.0091
$21_{13\,8} - 20_{12\,8}$	A	52223.1774	52223.0172	0.1602	0.0091
$21_{14\,8} - 20_{13\,8}$	E	54215.1657	54215.2780	-0.1123	0.0074
$21_{14\,7} - 20_{13\,7}$	E	54215.1657	54215.3093	-0.1436	0.0074
$21_{14\,8} - 20_{13\,8}$	A	54215.6317	54215.4691	0.1626	0.0088
$21_{14\,7} - 20_{13\,7}$	A	54215.6317	54215.4691	0.1626	0.0088
$21_{15\,7} - 20_{14\,7}$	E	56207.1867	56207.2977	-0.1110	0.0429
$21_{15\,6} - 20_{14\,6}$	E	56207.2867	56207.3290	-0.0423	0.0429
$21_{15\,7} - 20_{14\,7}$	A	56207.7328	56207.4657	0.2672	0.0937
$21_{15\,6} - 20_{14\,6}$	A	56207.7328	56207.4657	0.2672	0.0937
$21_{16\,6} - 20_{15\,6}$	E	58199.0289	58199.0690	-0.0401	0.0072
$21_{16\,5} - 20_{15\,5}$	E	58199.0289	58199.1003	-0.0714	0.0072
$21_{16\,6} - 20_{15\,6}$	A	58199.4637	58199.2137	0.2500	0.0069
$21_{16\,5} - 20_{15\,5}$	A	58199.4637	58199.2137	0.2500	0.0069
$21_{17\,5} - 20_{16\,5}$	E	60190.6701	60190.7183	-0.0481	0.0078
$21_{17\,4} - 20_{16\,4}$	E	60190.6701	60190.7496	-0.0795	0.0078
$21_{17\,5} - 20_{16\,5}$	A	60191.1142	60190.8397	0.2745	0.0567
$21_{17\,4} - 20_{16\,4}$	A	60191.1142	60190.8397	0.2745	0.0567
$21_{18\,4} - 20_{17\,4}$	E	62182.3463	62182.3255	0.0208	0.0062
$21_{18\,3} - 20_{17\,3}$	E	62182.3463	62182.3569	-0.0106	0.0062
$21_{18\,4} - 20_{17\,4}$	A	62182.7658	62182.4235	0.3423	0.0586
$21_{18\,3} - 20_{17\,3}$	A	62182.7658	62182.4235	0.3423	0.0586
$22_{11\,12} - 21_{10\,12}$	E	49532.6230	49532.7339	-0.1109	0.0068
$22_{11\,11} - 21_{10\,11}$	E	49532.6230	49532.7651	-0.1421	0.0068
$22_{11\,12} - 21_{10\,12}$	A	49533.1090	49533.0131	0.0959	0.0078

$22_{11\,11} - 21_{10\,11}$	A	49533.1090	49533.0131	0.0959	0.0078
$22_{13\,10} - 21_{12\,10}$	E	53522.2952	53522.3643	-0.0691	0.0972
$22_{13\,9} - 21_{12\,9}$	E	53522.2952	53522.3955	-0.1003	0.0972
$22_{13\,10} - 21_{12\,10}$	A	53522.8541	53522.6008	0.2533	0.0559
$22_{13\,9} - 21_{12\,9}$	A	53522.5841	53522.6008	0.2533	0.0559
$22_{14\,9} - 21_{13\,9}$	E	55515.1672	55515.2233	-0.0561	0.0060
$22_{14\,8} - 21_{13\,8}$	E	55515.1672	55515.2545	-0.0874	0.0060
$22_{14\,9} - 21_{13\,9}$	A	55515.6237	55515.4373	0.1865	0.0065
$22_{14\,8} - 21_{13\,8}$	A	55515.6237	55515.4373	0.1865	0.0065
$22_{16\,7} - 21_{15\,7}$	E	59499.3070	59499.3758	-0.0688	0.0071
$22_{16\,6} - 21_{15\,6}$	E	59499.3070	59499.4071	-0.1001	0.0071
$22_{16\,7} - 21_{15\,7}$	A	59499.7714	59499.5438	0.2276	0.0096
$22_{16\,6} - 21_{15\,6}$	A	59499.7714	59499.5438	0.2276	0.0096
$22_{17\,6} - 21_{16\,6}$	E	61491.0656	61491.0893	-0.0237	0.0065
$22_{17\,5} - 21_{16\,5}$	E	61491.0656	61491.1206	-0.0550	0.0065
$22_{17\,6} - 21_{16\,6}$	A	61491.5171	61491.2341	0.2831	0.0596
$22_{17\,5} - 21_{16\,5}$	A	61491.5171	61491.2341	0.2831	0.0596
$23_{10\,14} - 22_{9\,14}$	E	48828.7933	48828.8601	-0.0668	0.0086
$23_{10\,13} - 22_{9\,13}$	E	48828.7933	48828.8914	-0.0981	0.0086
$23_{10\,14} - 22_{9\,14}$	A	48829.3446	48829.1789	0.1657	0.0140
$23_{10\,13} - 22_{9\,13}$	A	48829.3446	48829.1774	0.1672	0.0140
$23_{11\,13} - 22_{10\,13}$	E	50829.7950	50829.8687	-0.0737	0.0133
$23_{11\,12} - 22_{11\,12}$	E	520829.7950	50829.9000	-0.1050	0.0133
$23_{11\,13} - 22_{10\,13}$	A	50830.3050	50830.1691	0.1359	0.0144
$23_{11\,12} - 22_{11\,12}$	A	50830.3050	50830.1691	0.1359	0.0144
$23_{12\,12} - 22_{11\,12}$	A	52827.0986	52827.1139	-0.0153	0.0114
$23_{12\,11} - 22_{11\,11}$	A	52827.0986	52827.1139	-0.0153	0.0114
$23_{14\,10} - 22_{10\,13}$	E	56814.7653	56814.8494	-0.0841	0.0069
$23_{14\,9} - 22_{13\,9}$	E	56814.7653	56814.8806	-0.1153	0.0069
$23_{14\,10} - 22_{10\,13}$	A	56815.2497	56815.0862	0.1636	0.0124
$23_{14\,9} - 22_{13\,9}$	A	56815.2497	56815.0862	0.1636	0.0124
$23_{15\,9} - 22_{14\,9}$	E	58807.2636	58807.3977	-0.1342	0.0120

Table 5.4: Cont.

$23_{15\,8} - 22_{14\,8}$	E	58807.2636	58807.4289	-0.1654	0.0120
$23_{15\,9} - 22_{14\,9}$	A	58807.8125	58807.6118	0.2007	0.0114
$23_{15\,8} - 22_{14\,8}$	A	58807.8125	58807.6118	0.2007	0.0114
$23_{16\,8} - 22_{15\,8}$	E	60799.3810	60799.4781	-0.0971	0.0087
$23_{16\,7} - 22_{15\,7}$	E	60799.3810	60799.5094	-0.1283	0.0087
$23_{16\,8} - 22_{15\,8}$	A	60799.9578	60799.6693	0.2885	0.0653
$23_{16\,7} - 22_{15\,7}$	A	60799.9578	60799.6693	0.2885	0.0653
$24_{9\,16} - 23_{8\,16}$	E	48109.9860	48110.0437	-0.0577	0.0055
$24_{9\,15} - 23_{8\,15}$	E	48109.9860	48110.0488	-0.0628	0.0055
$24_{9\,16} - 23_{8\,16}$	A	48110.4993	48110.4335	0.0659	0.0120
$24_{9\,15} - 23_{8\,15}$	A	48110.4993	48110.3234	0.1759	0.0120
$24_{10\,15} - 23_{9\,15}$	E	50122.6130	50122.6895	-0.0765	0.0123
$24_{10\,14} - 23_{9\,14}$	E	50122.6130	50122.7208	-0.1078	0.0123
$24_{10\,15} - 23_{9\,15}$	A	50123.1790	50123.0284	0.1506	0.0219
$24_{10\,14} - 23_{9\,14}$	A	50123.1790	50123.0251	0.1539	0.0219
$24_{11\,14} - 23_{10\,14}$	E	52126.0683	52126.1296	-0.0613	0.0060
$24_{11\,13} - 23_{10\,13}$	E	52126.0683	52126.1608	-0.0925	0.0060
$24_{11\,14} - 23_{10\,14}$	A	52126.5869	52126.4507	0.1362	0.0091
$24_{11\,13} - 23_{10\,13}$	A	52126.5869	52126.4506	0.1363	0.0091
$24_{12\,13} - 23_{11\,13}$	E	54124.9015	54124.5781	0.3234	0.0639
$24_{12\,12} - 23_{11\,12}$	E	54124.9015	54124.6093	0.2922	0.0639
$24_{12\,13} - 23_{11\,13}$	A	54125.0715	54124.8801	0.1914	0.0597
$24_{12\,12} - 23_{11\,12}$	A	54125.0715	54124.8801	0.1914	0.0597
$24_{13\,12} - 23_{12\,12}$	A	56120.6316	56120.4648	0.1668	0.0236
$24_{13\,11} - 23_{12\,11}$	A	56120.6316	56120.4648	0.1668	0.0236
$24_{14\,11} - 23_{13\,11}$	E	58114.1050	58114.1136	-0.0086	0.0565
$24_{14\,10} - 23_{13\,10}$	E	58114.1050	58114.1447	-0.0397	0.0565
$24_{14\,11} - 23_{13\,11}$	A	58114.6038	58114.3729	0.2308	0.0407
$24_{14\,10} - 23_{13\,10}$	A	58114.6038	58114.3729	0.2308	0.0407
$24_{15\,10} - 23_{14\,10}$	E	60106.9024	60107.0359	-0.1335	0.0092
$24_{15\,9} - 23_{14\,9}$	E	60106.9024	60107.0670	-0.1647	0.0092
$24_{15\,10} - 23_{14\,10}$	A	60107.4113	60107.2728	0.1385	0.0102

Table 5.4: Cont.

$24_{15\,9} - 23_{14\,9}$	A	60107.4113	60107.2728	0.1385	0.0102
$24_{16\,9} - 23_{15\,9}$	E	62099.2833	62099.3487	-0.0654	0.0073
$24_{16\,8} - 23_{15\,8}$	E	62099.2833	62099.3798	-0.0966	0.0073
$24_{16\,9} - 23_{15\,9}$	A	62099.7598	62099.5629	0.1969	0.0102
$24_{16\,8} - 23_{15\,8}$	A	62099.7598	62099.5629	0.1969	0.0102
$25_{9\,17} - 24_{8\,17}$	E	49397.4566	49397.6012	-0.1446	0.0081
$25_{9\,16} - 24_{8\,16}$	E	49397.4566	49397.5406	-0.0840	0.0081
$25_{9\,17} - 24_{8\,17}$	A	49398.0036	49398.0269	-0.0233	0.0102
$25_{9\,16} - 24_{8\,16}$	A	49398.0036	49397.8098	0.1938	0.0102
$25_{10\,16} - 24_{9\,16}$	E	51415.0645	51415.1057	-0.0412	0.0081
$25_{10\,15} - 24_{9\,15}$	E	51415.0645	51415.1369	-0.0724	0.0081
$25_{10\,16} - 24_{9\,16}$	A	51415.6162	51415.4649	0.1513	0.0101
$25_{10\,15} - 24_{9\,15}$	A	51415.6162	51415.4575	0.1587	0.0101
$25_{11\,15} - 24_{10\,15}$	E	53421.7575	53421.4090	0.3485	0.1099
$25_{11\,14} - 24_{10\,14}$	E	53421.7575	53421.4402	0.3173	0.1099
$25_{11\,15} - 24_{10\,15}$	A	53421.9426	53421.7502	0.1924	0.0217
$25_{11\,14} - 24_{10\,14}$	A	53421.9426	53421.7500	0.1926	0.0217
$25_{12\,14} - 24_{11\,14}$	E	55421.5373	55421.6134	-0.0762	0.0140
$25_{12\,13} - 24_{11\,13}$	E	55421.5373	55421.6446	-0.1073	0.0140
$25_{12\,14} - 24_{11\,14}$	A	55422.1107	55421.9366	0.1741	0.0250
$25_{12\,13} - 24_{11\,13}$	A	55422.1107	55421.9366	0.1742	0.0250
$25_{14\,12} - 24_{13\,12}$	E	59412.7699	59412.9704	-0.2005	0.0113
$25_{14\,11} - 24_{13\,11}$	E	59412.7699	59413.0015	-0.2316	0.0113
$25_{14\,12} - 24_{13\,12}$	A	59413.4537	59413.2521	0.2016	0.0265
$25_{14\,11} - 24_{13\,11}$	A	59413.4537	59413.2521	0.2016	0.0265
$25_{15\,11} - 24_{14\,11}$	E	61406.2759	61406.3522	-0.0764	0.0074
$25_{15\,10} - 24_{14\,10}$	E	61406.2759	61406.3833	-0.1075	0.0074
$25_{15\,11} - 24_{14\,11}$	A	61406.7722	61406.6119	0.1604	0.0090
$25_{15\,10} - 24_{14\,10}$	A	61406.7722	61406.6119	0.1604	0.0090
$26_{9\,18} - 25_{8\,18}$	E	50682.6822	50682.8047	-0.1225	0.0111
$26_{9\,17} - 25_{8\,17}$	E	50682.6822	50682.5736	0.1086	0.0111
$26_{9\,18} - 25_{8\,18}$	A	50683.2098	50683.2579	-0.0481	0.0052

$26_{9\ 17} - 25_{8\ 17}$	A	50683.2098	50682.8428	0.3669	0.0052
$26_{10\ 17} - 25_{9\ 17}$	E	52705.9277	52705.9423	-0.0147	0.0080
$26_{10\ 16} - 25_{9\ 16}$	E	52705.9277	52705.9732	-0.0455	0.0080
$26_{10\ 17} - 25_{9\ 17}$	A	52706.4545	52706.3228	0.1318	0.0132
$26_{10\ 16} - 25_{9\ 16}$	A	52706.4545	52706.3073	0.1472	0.0132
$26_{10\ 17} - 25_{9\ 17}$	E	54715.5486	54715.5924	-0.0437	0.0179
$26_{10\ 16} - 25_{9\ 16}$	E	54715.5486	54715.6236	-0.0749	0.0179
$26_{10\ 17} - 25_{9\ 17}$	A	54716.1215	54715.9532	0.1683	0.0311
$26_{10\ 16} - 25_{9\ 16}$	A	54716.1215	54715.9528	0.1687	0.0311
$26_{10\ 17} - 25_{9\ 17}$	E	56717.7490	56717.8565	-0.1075	0.0180
$26_{10\ 16} - 25_{9\ 16}$	E	56717.7490	56717.8876	-0.1386	0.0180
$26_{10\ 17} - 25_{9\ 17}$	A	56718.3602	56718.2003	0.1599	0.0367
$26_{10\ 16} - 25_{9\ 16}$	A	56718.3602	56718.2003	0.1599	0.0367
$26_{13\ 14} - 25_{12\ 14}$	E	58715.6446	58715.8803	-0.2357	0.0069
$26_{13\ 13} - 25_{12\ 13}$	E	58715.6446	58715.9114	-0.2668	0.0569
$26_{13\ 14} - 25_{12\ 14}$	A	58716.1889	58716.2049	-0.0160	0.0050
$26_{13\ 13} - 25_{12\ 13}$	A	58716.1889	58716.2049	-0.0160	0.0050
$27_{9\ 19} - 26_{8\ 19}$	E	51965.1405	51965.4086	-0.2681	0.0602
$27_{9\ 18} - 26_{8\ 18}$	E	51965.1405	51964.8225	0.3180	0.0602
$27_{9\ 19} - 26_{8\ 19}$	A	51965.2968	51965.8742	-0.5773	0.1083
$27_{9\ 18} - 26_{8\ 18}$	A	51965.2968	51965.1033	0.1935	0.0083
$27_{11\ 17} - 26_{10\ 17}$	E	56008.5031	56008.5575	-0.0544	0.0328
$27_{11\ 16} - 26_{10\ 16}$	E	56008.5031	56008.5887	-0.0586	0.0328
$27_{11\ 17} - 26_{10\ 17}$	A	56009.1065	56008.9373	0.1692	0.0419
$27_{11\ 16} - 26_{10\ 16}$	A	56009.1065	56008.9364	0.1702	0.0419
$27_{12\ 16} - 26_{11\ 15}$	E	58013.1427	58013.2190	-0.0763	0.0064
$27_{12\ 15} - 26_{11\ 15}$	E	58013.1427	58013.2501	-0.1074	0.0064
$27_{12\ 16} - 26_{11\ 15}$	A	58013.6691	58013.5831	0.0260	0.0105
$27_{12\ 15} - 26_{11\ 15}$	A	58013.6691	58013.5831	0.0861	0.0105
$27_{13\ 15} - 26_{12\ 15}$	E	60012.5092	60012.7743	-0.2651	0.0608
$27_{13\ 14} - 26_{12\ 14}$	E	60012.5092	60012.8054	-0.2962	0.0608
$27_{13\ 15} - 26_{12\ 15}$	A	60013.4234	60013.1201	0.1233	0.0576

Table 5.4: Cont.

$27_{13\ 14} - 26_{12\ 14}$	A	60013.2334	60013.1201	0.1233	0.0576
$28_{10\ 19} - 27_{9\ 19}$	E	55282.0954	55282.1506	-0.0552	0.0091
$28_{10\ 18} - 27_{9\ 18}$	E	55282.0954	55282.1742	-0.0788	0.0091
$28_{10\ 19} - 27_{9\ 19}$	A	55282.7144	55282.5820	0.1325	0.0128
$28_{10\ 18} - 27_{9\ 18}$	A	55282.7144	55282.5200	0.1944	0.0128
$28_{11\ 18} - 27_{10\ 18}$	E	57300.1510	57300.1740	-0.0230	0.0074
$28_{11\ 17} - 27_{10\ 17}$	E	57300.1510	57300.2052	-0.0542	0.0074
$28_{11\ 18} - 27_{10\ 18}$	A	57300.7159	57300.5723	0.1436	0.0085
$28_{11\ 17} - 27_{10\ 17}$	A	57600.7159	57300.5702	0.1457	0.0085
$28_{12\ 17} - 27_{11\ 17}$	E	59307.5457	59307.6075	-0.0617	0.0305
$28_{12\ 16} - 27_{11\ 16}$	E	59307.5457	59307.6386	-0.0928	0.0305
$28_{12\ 17} - 27_{11\ 17}$	A	59308.1471	59307.9912	0.1559	0.0338
$28_{12\ 16} - 27_{11\ 16}$	A	59308.1471	59307.9912	0.1559	0.0338
$28_{13\ 16} - 27_{12\ 16}$	E	61308.9092	61308.9401	-0.0309	0.0048
$28_{13\ 15} - 27_{12\ 15}$	E	61308.9092	61309.9711	-0.0619	0.0048
$28_{13\ 16} - 27_{12\ 16}$	A	61309.4913	61309.3067	0.1846	0.0134
$28_{13\ 15} - 27_{12\ 15}$	A	61309.4913	61309.3067	0.1846	0.0134
$29_{11\ 19} - 28_{10\ 19}$	E	58590.2253	58590.3026	-0.0773	0.0212
$29_{11\ 18} - 28_{10\ 18}$	E	58590.2253	58590.3338	-0.1085	0.0212
$29_{11\ 19} - 28_{10\ 19}$	A	58590.8472	58590.7191	0.1281	0.0182
$29_{11\ 18} - 28_{10\ 18}$	A	58590.8472	58590.7147	0.1325	0.0182
$29_{12\ 18} - 28_{11\ 18}$	E	60600.8907	60600.9227	-0.0320	0.0069
$29_{12\ 17} - 28_{11\ 17}$	E	60600.8907	60600.9537	-0.0631	0.0069
$29_{12\ 18} - 28_{11\ 18}$	A	60601.4818	60601.3255	0.1563	0.0097
$29_{12\ 17} - 28_{11\ 17}$	A	60601.4818	60601.3254	0.1565	0.0097
$29_{13\ 17} - 28_{12\ 17}$	E	62604.2884	62604.3038	-0.0154	0.0074
$29_{13\ 16} - 28_{12\ 16}$	E	62604.2884	62604.3348	-0.0464	0.0074
$29_{13\ 17} - 28_{12\ 17}$	A	62604.8555	62604.6907	0.1647	0.0104
$29_{13\ 16} - 28_{12\ 16}$	A	62604.8555	62604.6907	0.1647	0.0104
$30_{11\ 20} - 29_{10\ 20}$	E	59878.7724	59878.7950	-0.0226	0.0098
$30_{11\ 19} - 29_{10\ 19}$	E	59878.7724	59878.8261	-0.0537	0.0098
$30_{11\ 20} - 29_{10\ 20}$	A	59879.3848	59879.2296	0.1552	0.0130

$30_{11\ 19} - 29_{10\ 19}$	A	59879.3848	59879.2208	0.1640	0.0130
$30_{12\ 19} - 29_{11\ 19}$	E	61893.0120	61893.0594	-0.0473	0.0121
$30_{12\ 18} - 29_{11\ 18}$	E	61893.0120	61893.0904	-0.0784	0.0121
$30_{12\ 19} - 29_{11\ 19}$	A	61893.6199	61893.4806	0.1393	0.0190
$30_{12\ 18} - 29_{11\ 18}$	A	61893.6199	61893.4803	0.1393	0.0190
$31_{10\ 22} - 30_{9\ 22}$	E	59129.6606	59129.7744	-0.1138	0.0164
$31_{10\ 21} - 30_{9\ 21}$	E	59129.6606	59129.5627	0.0979	0.0164
$31_{10\ 22} - 30_{9\ 22}$	A	59130.2307	59130.2966	-0.0659	0.0638
$31_{10\ 21} - 30_{9\ 21}$	A	59130.2307	59129.8904	0.3404	0.0638
$31_{10\ 22} - 30_{9\ 22}$	E	61165.5494	61165.4923	0.0571	0.0093
$31_{10\ 21} - 30_{9\ 21}$	E	61165.5494	61165.5230	0.0264	0.0093
$31_{10\ 22} - 30_{9\ 22}$	A	61166.1295	61165.9460	0.1836	0.0110
$31_{10\ 21} - 30_{9\ 21}$	A	61166.1295	61165.9285	0.2010	0.0110
$32_{10\ 23} - 31_{9\ 23}$	E	60406.7672	60406.9929	-0.2257	0.0614
$32_{10\ 22} - 31_{9\ 22}$	E	60406.7672	60406.4680	0.2992	0.0614
$32_{10\ 23} - 31_{9\ 23}$	A	60407.4012	60407.5264	-0.1253	0.0065
$32_{10\ 22} - 31_{9\ 22}$	A	60407.4012	60406.8014	0.5998	0.0065
$33_{10\ 24} - 32_{9\ 24}$	E	61680.6947	61681.1523	-0.4576	0.0922
$33_{10\ 23} - 32_{9\ 23}$	E	61680.6947	61680.0653	0.6293	0.0922
$33_{10\ 24} - 32_{9\ 24}$	A	61681.2280	61681.6820	-0.4540	0.0956
$33_{10\ 23} - 32_{9\ 23}$	A	61681.2280	61680.4154	0.8126	0.0956

With the decision not to repeat the experiment using a reduced Stark field, a variety of datasets were fitted in an attempt to assign the microwave spectrum of linalool; the transitions assigned by Nguyen *et al.*[26] from their Fourier Transform experiment, the transitions recorded using the Stark Modulated, Continuous Jet System during this investigation and finally a combination of the two datasets.

For each of the three datasets two different rotational fitting programs were used; XIAM treats the internal rotation in an asymmetric top molecule utilising the *principal axis method* (PAM) where the axis labels *a*, *b*, *c* in the molecule are defined by traditional spectroscopic moment-of-inertia ordering $I_a < I_b < I_c$.[72] The BELGI-C1[28, 29] program utilises the *rho axis method* (RAM) devised to describe rotational-interaction-rotational

motion of molecules. Certain coupling terms have been eliminated, resulting in a Hamiltonian operator with only $\Delta K = 0$ matrix elements[72], to fit a single internal rotor of C_{3v} symmetry, such as a methyl rotor, which can rotate relative to the rest of the molecule, which does not possess a plane of symmetry (C_1). Due to the different axis systems employed in these two programs the molecular parameters must first undergo a transformation from RAM to PAM before they can be directly compared.

As can be seen from Table 5.5 the inclusion of the Stark modulated data greatly increases the overall standard deviation from 4.6 kHz (fitted for 83 transitions) as observed by Nguyen *et al.* to 90 kHz (fitted for 312 transitions) when using the XIAM fitting program. This is an unsurprising observation due to the better resolution of Fourier transform system giving more accurate transition frequencies. For the same reason it was foreseeable that combining the Fourier transform dataset with the Stark modulated dataset, for 395 transitions, would reduce the overall standard deviation to 90 kHz in comparison to 105.8 kHz for only the Stark modulated dataset, as shown in Table 5.5.

It is important to mention the great variation in the constants δ_J and δ_K; for the calculated and Fourier transform datasets δ_J has a magnitude 10^{-3} kHz; however, the introduction of the Stark modulated dataset increases this to 10^{-2} kHz. The Stark modulated data shows high correlation between δ_J and all the other constants which accounts for the fourfold increase in δ_J from the Fourier transform dataset. When the two datasets are combined there is a low correlation between δ_J and all other constants, with the exception of $B-$, explaining why the magnitude of δ_J is greater than the Fourier transform dataset yet less than half that from the Stark modulated data. Although at the same order of magnitude the value of δ_K from the combination dataset is twice that of the Fourier transform data. This is attributed to the large correlation (~0.9) between δ_K and Δ_J, Δ_{JK} and Δ_K.

Due to the limitations of the BELGI-C_1 program, where 30 is the maximum J value that can be fitted, 16 transitions from the Stark modulated dataset had to be removed as the J quantum number are beyond the limitations of the programs. Interestingly Nguyen *et al.* had to remove 6 E species transitions to obtain the BELGI-C_1 fit, that had been previously been included in the XIAM fit, although no reason for this has been supplied. Besides the transitional omissions already mentioned an additional 21 $E-$ species transitions had to be excluded (that had been in the corresponding XIAM fits) as the BELGI-C_1 was incapable of producing the correct quantum numbers in these transitions causing large errors in the

fit. Of the 6 of the *E* species that Nguyen *et al.* were unable to fit, three could be included upon combination of the Fourier transform and Stark modulated datasets.

As can be seen from Table 5.5 the inclusion of the Stark modulated data greatly increases the overall standard deviation, from 6.6 kHz for 83 transitions recorded by Nguyen *et al.* to 194.9 kHz when all 354 transitions were considered, using the BELGI-C$_1$ fitting program. This observation agrees with the analysis from the XIAM program. Combining the Fourier transform dataset with the Stark modulated dataset the overall standard deviation reduces to 194.9 kHz from 218.5 kHz, fitted with the BELGI-C$_1$ program, when considering only the 275 transitions in the Stark modulated dataset (see Table 5.5).

The final column in Table 5.5, *'BELGI-C1 transformed'* shows the manipulated BELGI-C1 parameters so that they can be directly compared to the XIAM parameters. As these two programs utilise different axis systems, A, B, C, D_{ab}, D_{ac} and D_{bc} from BELGI (RAM quantities) must be converted into the corresponding PAM quantities (as used in XIAM); this conversion is completed using the abc executable file, available as part of the BELGI package.

Table 5.5: Molecular parameters fitted using the XIAM and BELGI-C$_1$ programs, from the Fourier Transform Microwave System, the Stark Modulated Continuous Jet Millimeter Wave Absorption System and a combination of both data sets

Parameters[a]	Calculated	XIAM			BELGI-C$_1$			BELGI-C$_1$ (transformed)		
		FTMW[b,c]	Stark Modulated	Combination	FTMW[b]	Stark Modulated	Combination	FTMW[b]	Stark Modulated	Combination
A (GHz)	1.6381[d]	1.64674	1.64672	1.64673	1.5884	1.5938(23)	1.5938(13)	1.6414	1.6417	1.6417
B (GHz)	0.6817[d]	0.68220	0.68220	0.68220	0.7274	0.7213(23)	0.7212(71)	0.6834	0.6825	0.6824
C (GHz)	0.6167[d]	0.61885	0.61875	0.61875	0.6256	0.6251(19)	0.6254(30)	0.6166	0.6160	0.6163
Δ_J (kHz)	0.10165[e]	0.11550	0.11888	0.12371	0.0952	0.0826(12)	0.0918(77)			
Δ_{JK} (kHz)	0.46003[e]	0.38430	0.36660	0.33876	0.4428	0.5682(47)	0.4541(14)			
Δ_K (kHz)	-0.32346[e]		-0.24502	-0.21214		-0.5248(69)	-0.3097(20)			
δ_J (kHz)	0.00497[e]	0.00735	0.02943	0.01179		0.1490(19)	-0.0187(35)			
δ_K (kHz)	0.26001[e]	0.234	0.26001	0.55174	0.0779		-0.3360(83)			
V_3 (cm^{-1})	305.07[f]	400.20	300.46	346.20	399.40	283.9(16)	300.6(27)	399.40	283.9(16)	300.6(12)
D_{ab} (GHz)					0.1995	0.1884	0.1884			
D_{aci} (GHz)					-0.0930	-0.093	-0.093			
D_{bci} (GHz)					-0.0224	-0.02238	-0.02238			
F (GHz)					157.93097	157.93097	157.93097			
F_0 (GHz)	157.931	160	157.931	157.931						
ρ					0.010236	7.849×10^{-6}	7.849×10^{-6}			
F_v (GHz)					0.01213	0.01213	0.01213			

Table 5.5: Cont.

Parameters[a]	*Calculated*	XIAM			BELGI-C$_1$			BELGI-C$_1$ (transformed)		
		FTMW[b,c]	Stark Modulated	Combination	FTMW[b]	Stark Modulated	Combination	FTMW[b]	Stark Modulated	Combination
Δ_{ab} (GHz)					0.001285	0.001285	0.001285			
$I_\alpha{}^g$ (u Å^2)		3.15862	3.19999	3.19999						
$< (i,a)$ (°)		85.04	90.07	89.87				78(4)	116	116
$< (i,b)$ (°)		30.01	36.14	17.68				30(4)	29	29
$< (i,c)$ (°)		60.49	53.86	72.32				62(4)	101	101
σ^h (kHz)		4.6	105.8	90.0	6.6	218.5	194.9	6.6	218.5	194.9
$N_A/N_E{}^i$		46/37	160/152	206/189	46/31	152/123	197/157	46/31	152/123	197/157

[a]Fitted using an *A*-reduced Hamiltonian in the I^r representation

[b]Molecular parameters taken from Nguyen *et al.* 2013

[c]The centrifugal distortion constant Δ_K was not included in the fit due the high correlation to A - (B+C)/2

[d]MP3/6-31++G(d,p)

[e]MP2/6-31++G(d,p)

[f]B3LYP/6-31G(d,p)

[g]Moment of inertia I_α of the internal rotor, fixed to the value corresponding to a rotational constant of F_0

[h]Standard deviation of the fit

[i]Number of fitted A/E transitions

Table 5.5 shows worse results using the BELGI-C$_1$ fitting program than for XIAM. Whilst there is little discrepancy for the Fourier transform dataset, the overall standard deviation dramatically increases for the Stark modulated dataset rising from 105.8 kHz to 218.5 kHz and the combination of the two datasets rising from 90.0 kHz to 194.9 kHz and as previously mentioned the BELGI-C$_1$ code seems to struggle with the fitting a number of E-species lines. Nguyen *et al.* identifies this difficulty as arising from the small coupling constant between rotation and global rotation (ρ parameter) and the intermediate height of the torsional barrier (V_3), which is fitted as 0.010236 and 399.4 cm^{-1} respectively in Nguyen *et al.* study. For the Stark modulated and combination datasets the ρ parameter is even smaller at 7.849×10^{-6}, while V_3 remains at an intermediate height of 280-300 cm^{-1}, possibly exacerbating the fitting difficulties. In the ground state of linalool the internal rotation splitting are small (~400 kHz) which induces high correlation between various parameters ρ, V_3, F, D_{ab}, D_{aci} and D_{bci}, which all control the internal rotation splitting. In the BELGI-C1 code the parameters ρ and F are fixed whilst V_3 and D_{ab} are fitted; a small value of D_{ab} (a measure of the angle between the ρ vector and principle axis system) results in internal rotation splittings carrying little information. Alternatively XIAM derives the ρ and F parameters from the fitted angles of the methyl group relative to the principle axis system as well as fitting the angles of the methyl group within the molecule. This method combines a restricted data set from the torsional ground state and an intermediate internal rotation splitting, giving more accurate information and thus making it a far more effective tool.[26]

5.4 Conclusions

The microwave spectrum of linalool has been recorded and assigned over the 48-63 GHz region. Overall 312 transitions were recorded using a Stark modulated, continuous jet millimetre wave absorption system with an overall standard deviation of 105.8 kHz. These transitions were merged with those recorded by Nguyen *et al.* using a Fourier transform microwave spectrometer; combined 395 transitions were observed with an overall standard deviation of 90.0 kHz.

The observed spectrum suggests the presence of two species, so computational chemistry calculations investigating the structure and barrier heights associated with the three methyl groups of linalool have been carried out. Structural analysis predicts many conformer of linalool; whilst the lowest energy conformer has been assigned to half of the recorded transitions, all remaining transitions failed to be assigned by any of the other

identified conformers. Further analysis of the computational chemistry calculations confirmed that the rotational transitions of linalool are split into corresponding *A*- and *E*-species due to the presence of a low barrier for internal methyl rotation, which agrees with the observed spectrum.

5.5 References

1.	C. Backtorp, J. R. T. J. Wass, I. Panas, M. Skold, A. Borje and G. Nyman, *Journal of Physical Chemistry A*, 2006, **110**, 12204-12212.

2.	J. Nilsson, J. Carlberg, P. Abrahamsson, G. Hulthe, B. A. Persson and A. T. Karlberg, *Rapid Communications in Mass Spectrometry*, 2008, **22**, 3593-3598.

3.	Y. T. Padrayuttawat. A., Tamura. H., Tokunaga. T., *Food Science and Technology International, Tokyo*, 1997, **3**, 402-408.

4.	M. Skold, A. Borje, E. Harambasic and A. T. Karlberg, *Chemical Research in Toxicology*, 2004, **17**, 1697-1705.

5.	F. Gandara, A. Garcia-Cortes, C. Cascales, B. Gomez-Lor, E. Gutierrez-Puebla, M. Iglesias, A. Monge and N. Snejko, *Inorganic Chemistry*, 2007, **46**, 3475-3484.

6.	S. C. Rastogi, S. Heydorn, J. D. Johansen and D. A. Basketter, *Contact Dermatitis*, 2001, **45**, 221-225.

7.	A. Calogirou, D. Kotzias and A. Kettrup, *Naturwissenschaften*, 1995, **82**, 288-289.

8.	C. Amelynck, N. Schoon, T. Kuppens, P. Bultinck and E. Arijs, *International Journal of Mass Spectrometry*, 2005, **247**, 1-9.

9.	Y. H. Shu, E. S. C. Kwok, E. C. Tuazon, R. Atkinson and J. Arey, *Environmental Science and Technology*, 1997, **31**, 896-904.

10.	C. D. Geron and R. R. Arnts, *Atmospheric Environment*, 2010, **44**, 4240-4251.

11.	P. Dominguez-Taylor, L. G. Ruiz-Suarez, I. Rosas-Perez, J. M. Hernandez-Solis and R. Steinbrecher, *Atmospheric Environment*, 2007, **41**, 2780-2790.

12.	V. Simon, L. Dumergues, G. Solignac and L. Torres, *Atmospheric Research*, 2005, **74**, 37-48.

13.	E. Joo, J. Dewulf, M. Demarcke, C. Amelynck, N. Schoon, J. F. Muller, M. Simpraga, K. Steppe and H. Van Langenhove, *I International Journal of Mass Spectrometry,* 2010, **291**, 90-95.

14.	A. K. BorgKarlson, C. R. Unelius, I. Valterova and L. A. Nilsson, *Phytochemistry*, 1996, **41**, 1477-1483.

15.	T. L. Sun, Y. D. Wang, C. X. Zhang, X. M. Sun and J. T. Hu, *Acta Chimica Sinica*, 2011, **69**, 1965-1972.

16.	A. Lee, A. H. Goldstein, J. H. Kroll, N. L. Ng, V. Varutbangkul, R. C. Flagan and J. H. Seinfeld, *Journal Geophysical Research-Atmospheres,* 2006, **111**.

17. J. McMurray, *Organic Chemistry*, Brooks/Cole, London, 2007.

18. E. Grosjean and D. Grosjean, *International Journal of Chemical Kinetics*, 1998, **30**, 21-29.

19. A. Calogirou, B. R. Larsen and D. Kotzias, *Atmospheric Environment*, 1999, **33**, 1423-1439.

20. X. Chen and P. K. Hopke, *Atmospheric Environment*, 2009, **43**, 3935-3940.

21. J. F. Bacon and J. H. Vandermaas, *Canadian Journal of Chemistry-Revue Canadienne De Chimie*, 1989, **67**, 250-256.

22. H. Schulz, B. Schrader, R. Quilitzsch, S. Pfeffer and H. Kruger, *Journal of Agriculture and Food Chemistry*, 2003, **51**, 2475-2481.

23. M. Sandasi, G. P. P. Kamatou, C. Gavaghan, M. Baranska and A. M. Viljoen, *Vibrational Spectroscopy*, 2011, **57**, 242-247.

24. T. L. Nguyen, J. Peeters and L. Vereecken, *Physical Chemistry Chemical Physics,* 2009, **11**, 5643-5656.

25. T. L. Nguyen, R. Winterhalter, G. Moortgat, B. Kanawati, J. Peeters and L. Vereecken, *Physical Chemistry Chemical Physics*, 2009, **11**, 4173-4183.

26. H. V. L. Nguyen, H. Mouhib, S. Klahm, W. Stahl and I. Kleiner, *Physical Chemistry Chemical Physics*, 2013, **15**, 10012-10018.

27. H. Hartwig and H. Dreizler, *Zeitschrift Fur Naturforschung Section A -A Journal of Physical Sciences*, 1996, **51**, 923-932.

28. R. J. Lavrich, A. R. H. Walker, D. F. Plusquellic, I. Kleiner, R. D. Suenram, J. T. Hougen and G. T. Fraser, *Journal of Chemical Physics*, 2003, **119**, 5497-5504.

29. I. Kleiner and J. T. Hougen, *Journal of Chemical Physics*, 2003, **119**, 5505-5509.

30. J. K. G. Watson, *Vibrational Spectra and Structure: A Series of Advances, ed J.R. During, Elsevier, Amsterdam*, Elsevier, Oxford, 1977.

31. PGOPHER, a Program for Simulating Rotational, Vibrational and Electronic Structure, C. M. Western, University of Bristol, http://pgopher.chm.bris.ac.uk

32. J. A. Pople and R. K. Nesbet, *Journal of Chemical Physics*, 1954, **22**, 571-572.

33. R. McWeeny and G. Diercksen, *Journal of Chemical Physics*, 1968, **49**, 4852-4857.

34. W. J. Hehre, R. F. Stewart and J. A. Pople, *Journal of Chemical Physics*, 1969, **51**, 2657-2664.

35. I. Wavefunction, Irvine, CA, 2008.

36. http://www.chemcraftprog.com.

37. A. D. Becke, *Journal of Chemical Physics*, 1993, **98**, 5648-5652.

38. P. J. Stephens, F. J. Devlin, C. F. Chabalowski and M. J. Frisch, *Journal of Physical Chemistry*, 1994, **98**, 11623-11627.

39. T. H. Dunning, *Journal of Chemical Physics*, 1989, **90**, 1007-1023.

40. J. A. Pople, R. Seeger and R. Krishnan, *International Journal of Quantum Chemistry*, 1977, **11**, 149-161.

41. J. A. Pople, J. S. Binkley and R. Seeger, *International Journal of Quantum Chemistry*, 1976, 1-19.

42. Harihara.Pc and J. A. Pople, *Theoretica Chimica Acta*, 1973, **28**, 213-222.

43. M. J. Frisch, G. W. Trucks, H. B. Schlegel, G. E. Scuseria, M. A. Robb, J. R. Cheeseman, J. A. M. Jr., T. Vreven, K. N. Kudin, J. C. Burant, J. M. Millam, S. S. Iyengar, J. Tomasi, V. Barone, B. Mennucci, M. Cossi, G. Scalmani, N. Rega, G. A. Petersson, H. Nakatsuji, M. Hada, M. Ehara, K. Toyota, R. Fukuda, J. Hasegawa, M. Ishida, T. Nakajima, Y. Honda, O. Kitao, H. Nakai, M. Klene, X. Li, J. E. Knox, H. P. Hratchian, J. B. Cross, V. Bakken, C. Adamo, J. Jaramillo, R. Gomperts, R. E. Stratmann, O. Yazyev, A. J. Austin, R. Cammi, C. Pomelli, J. W. Ochterski, P. Y. Ayala, K. Morokuma, G. A. Voth, P. Salvador, J. J. Dannenberg, V. G. Zakrzewski, S. Dapprich, A. D. Daniels, M. C. Strain, O. Farkas, D. K. Malick, A. D. Rabuck, K. Raghavachari, J. B. Foresman, J. V. Ortiz, Q. Cui, A. G. Baboul, S. Clifford, J. Cioslowski, B. B. Stefanov, G. Liu, A. Liashenko, P. Piskorz, I. Komaromi, R. L. Martin, D. J. Fox, T. Keith, M. A. Al-Laham, C. Y. Peng, A. Nanayakkara, M. Challacombe, P. M. W. Gill, B. Johnson, W. Chen, M. W. Wong, C. Gonzalez and J. A. Pople, Gaussian, Inc., Wallingford CT, 2004, vol. Revision E.01.

44. G. Schaftenaar and J. H. Noordik, *Journal of Computer-Aided Molecular Design*, 2000, **14**, 123-134.

45. GaussView, Version 5, R. Dennington, T. Keith, and J. Millam, *Semichem Inc*., Shawnee Mission, KS, 2009.

46. D. A. Basketter, Z. M. Wright, N. R. Colson, G. Y. Patlewicz and C. K. S. Pease, *Contact Dermatitis*, 2002, **47**, 161-164.

47. R. G. Bird and D. W. Pratt, *Journal of Molecular Spectroscopy*, 2011, **266**, 81-85.

48. V. V. Ilyushin, E. A. Alekseev, S. F. Dyubko, I. Kleiner and J. T. Hougen, *Journal of Molecular Spectroscopy*, 2004, **227**, 115-139.

49.   L. W. Sutikdja, D. Jelisavac, W. Stahl and I. Kleiner, *Molecular Physics*, 2012, **110**, 2883-2893.

50.   H. V. L. Nguyen, H. Mouhib, W. Stahl and I. Kleiner, *Molecular Physics*, 2010, **108**, 763-770.

51.   M. Tudorie, I. Kleiner, J. T. Hougen, S. Melandri, L. W. Sutikdja and W. Stahl, *Journal of Molecular Spectroscopy*, 2011, **269**, 211-225.

52.   H. V. L. Nguyen and W. Stahl, *Journal of Molecular Spectroscopy*, 2010, **264**, 120-124.

53.   V. V. Ilyushin, C. P. Endres, F. Lewen, S. Schlemmer and B. J. Drouin, *Journal of Molecular Spectroscopy*, 2013, **290**, 31-41.

54.   H. V. L. Nguyen, V. Van, W. Stahl and I. Kleiner, *Journal of Chemical Physics*, 2014, **140**.

55.   J. A. Kroll, S. T. Shipman and S. L. W. Weaver, *Journal of Molecular Spectroscopy*, 2014, **295**, 52-57.

56.   Y. Y. Zhao, W. Stahl and V. L. N. Ha, *Chemical Physics Letters*, 2012, **545**, 9-13.

57.   A. Bauder, *Molecular Physics*, 2013, **111**, 1999-2002.

58.   T. Bruhn and W. Stahl, *Journal of Molecular Spectroscopy*, 2000, **202**, 272-280.

59.   S. Samdal, H. Mollendal and J. C. Guillemin, *Journal of Physical Chemistry A*, 2012, **116**, 8833-8839.

60.   Z. Kisiel, L. Pszczolkowski, E. Bialkowska-Jaworska and S. B. Charnley, *Journal of Molecular Spectroscopy*, 2007, **241**, 220-229.

61.   V. Ilyushin, E. Alekseev, J. Demaison and I. Kleiner, *Journal of Molecular Spectroscopy*, 2006, **240**, 127-132.

62.   M. Carvajal, F. Willaert, J. Demaison and I. Kleiner, *Journal of Molecular Spectroscopy*, 2007, **246**, 158-166.

63.   V. Ilyushin, A. Kryvda and E. Alekseev, *Journal of Molecular Spectroscopy*, 2009, **255**, 32-38.

64.   M. Tudorie, V. Ilyushin, J. Vander Auwera, O. Pirali, P. Roy and T. R. Huet, *Journal of Chemical Physics*, 2012, **137**.

65.   L. H. Xu, R. M. Lees and J. T. Hougen, *Journal of Chemical Physics*, 1999, **110**, 3835-3841.

66.   I. Kleiner, J. T. Hougen, J. U. Grabow, S. P. Belov, M. Y. Tretyakov and J. Cosleou, *Journal of Molecular Spectroscopy*, 1996, **179**, 41-60.

67. I. A. Finneran, S. T. Shipman and S. L. Widicus Weaver, *Journal of Molecular Spectroscopy*, 2012, **280**, 27-33.

68. V. L. N. Ha, W. Stahl and I. Kleiner, *Molecular Physics*, 2012, **110**, 2035-2042.

69. V. L. N. Ha and W. Stahl, ChemPhysChem: A European Journal of Chemical Physics and Physical Chemistry, 2011, **12**, 1900-1905.

70. S. L. Hsu, M. K. Kemp, J. M. Pochan, R. C. Benson and W. H. Flygare, *Journal of Chemical Physics*, 1969, **50**, 1482-1483.

71. V. L. M. Ha and W. Stahl, *Journal of Chemical Physics*, 2011, **135**.

72. J. T. Hougen, I. Kleiner and M. Godefroid, *Journal of Molecular Spectroscopy*, 1994, **163**, 559-586.

Chapter Six

Microwave Spectroscopy of Verbenone

6.1 Introduction

6.1.1 Emission of Verbenone

Verbenone ($C_{10}H_{14}O$) is a monoterpene bicyclic ketone[1, 2], thus has a conformationally locked structure for which only one conformer can be identified (Figure 6.1).
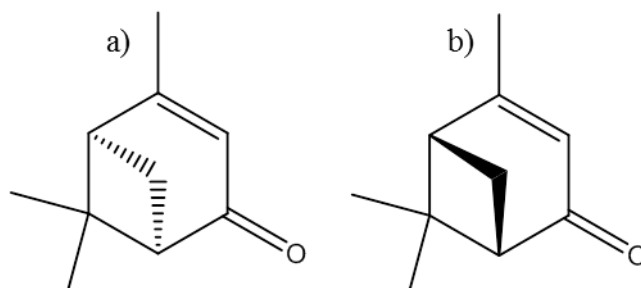
Figure 6.1: Skeletal structures of the enantiomers (a) *(1R)(+)*-verbenone and (b) *(1S)(-)*-verbenone

(1R)(+)-Verbenone occurs in *Verbena triphylla* L. (Spanish verbena – from where verbenone is named), Spanish *Eucalyptus globulus* (Blum Gum) oils[1-3], *Verbena triphylla* (lemon verbena)[2] and is also a major constituent in Spanish *Rosmarinus officinalis* (Rosemary) oils.[1-3] Verbenone is widely reported to possess an odour similar to that of camphor, but it has also been likened to scents of celery and menthol.[2, 3] Whilst natural *(1S)(-)*-verbenone has yet to be to found in the plant kingdom[3], it is used as a major constituent in strawberry, raspberry, dill, rosmarinus and spearmint flavour mixtures which are in high demand in the food industry.[4] Due to its spicy and camphoraceous fragrance *(1S)(-)*-verbenone can also be used in herbal tea, spices and perfumes.[2]

With regards to atmospheric chemistry, verbenone [4,6,6-trimethylbicyclo[3.1.1]-hept-3-en-2-one] is classified as an oxygenated terpene, and has emission rates of 5.5 ng C g^{-1} $h^{-1\dagger}$ and 4.0 ng C g^{-1} h^{-1} from *Pinus taeda* (Lob lolly pine) and *Pinus Virginia* (Virginia pine) respectively; such emission rates are significantly lower compared to the emission rate of α-pinene which has emissions rates of 1289 ng C g^{-1} h^{-1} from *Pinus taeda* and 233 ng C g^{-1} h^{-1} from and *Pinus Virginia.*[5] Whilst oxidation reaction of verbenone result in a high amount of formaldehyde (32%) the yield of secondary organic aerosol (SOA) has been recorded at 19%. Lee *et al.* described this SOA yield in the gas phase as unexpectedly low due to the presence of an endocyclic carbon-carbon double bond and a

---

†ng C g^{-1} h^{-1} – nanograms of carbon per gram of air per year

low carbon mass balance ($79 \pm 17\%$) compare to other C_{10} terpenes.[6] The authors describe the carbon balance (%) as the carbon arising from identified gas phase products such as formaldehyde and formic acid, in addition to the yield of unidentified compounds, of which SOA are assumed to constitute 60%.

6.1.2 Role in Insect Pheromones

Whilst verbenone plays a small role in atmospheric chemistry is it is renowned for its use as an alternative to traditional insecticides and can be produced in a variety of different ways. Predominately verbenone is produced through the auto-oxidation of α-pinene (in absence of beetles) via *cis*- and *trans*-verbenol (Figure 6.2).[1, 7-10]
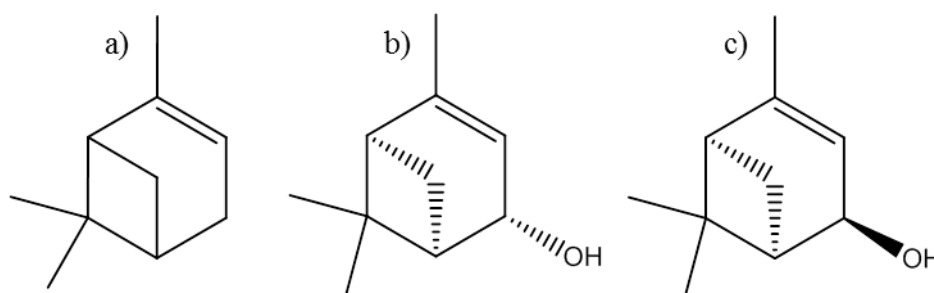
Figure 6.2: Skeletal structures of (a) α-pinene, (b) *trans*-verbenol and (c) *cis*- verbenol

First discovered in *Dendroctonus ponderosae* Hopkins (mountain pine beetle)[7, 11, 12] and later in *Dendroctonus frontalis* (southern pine beetle)[13], *Dendroctonus brevicomis* (western pine beetle)[8, 13-15] and *Ips typographus* (spruce bark beetle)[11] verbenone is naturally produced by a variety of beetles as an anti-aggregation pheromone making it a highly important compound with regards to plant-insect interactions and insect pheromones.[7] Anti-aggregation pheromones, are excreted chemicals that are used by beetles to reduce the attractiveness of a given location, lessening the mass gathering of beetles.[11] Mountain pine beetle (MPB) are the most damaging insect pest towards several pine species and more recently have become even more widespread and persistent in their attack on *Pinus albicaulis* Engelm (whitebark pine). It has been suggested that a warming climate would favour MPB at higher elevation alpine areas, where whitebark pine predominate.[12]

There are continuous calls for the whitebark pine to be listed as an endangered species as beetle-caused tree mortality continues to grow; in 2005 the greatest beetle-caused tree mortality was recorded for the Greater Yellowstone area of the western U.S.A. In 2013 Macfarlane *et al.* estimated moderate to severe mortality within 82% of the whitebark

pine distribution in the Greater Yellowstone area based on aerial surveys,[16] corresponding to the findings of Haroldson and Podruzny that 73% of mature trees have died between 2002 and 2012.[17]

Mountain pine beetles colonise and kill their pine host in order to reproduce[18] and while female beetles initiate the attack on a given tree[19] it is the male beetles that during the latter stages of attack, release verbenone to reduce the attractive response of other beetles. This prevents the aggregation of further beetles, thus shifting the focus of attack to another target and preventing over-colonisation of the first tree. This suggests that rather than being responsible for the termination of mass beetle attack, verbenone in fact regulates the density of a beetle attack within a close range of the infected tree.[14, 15]

Whilst verbenone may predominately be formed in the absence of beetles it is clear that beetles themselves are also capable of producing the pheromone verbenone, within specialised cells of their abdomens. More specifically the mid-gut is thought to be the location of verbenone production based on the location of the pheromone in the hindgut and the known histology and anatomy of the beetles' gut tissues.[10]

Within the gut, microorganisms and yeast facilitate the metabolic conversion of *trans*-verbenol into verbenone.[7, 11] Whilst the production of verbenone acts as anti-aggregation pheromone between beetles, this only remains the case as long as no further oxidation of verbenone occurs. Studies by Brand *et al.* in 1976[13] and more recently Lindgren *et al.* in 1996[11] have shown that in fully colonised trees there is an increase in the concentration of verbenone, confirming that no further oxidation occurs.

Neither study explains the lack of verbenone oxidation; however, if we examine the oxidation process of *α*-pinene (another terpene with an endocyclic double bond) a potential explanation becomes apparent.
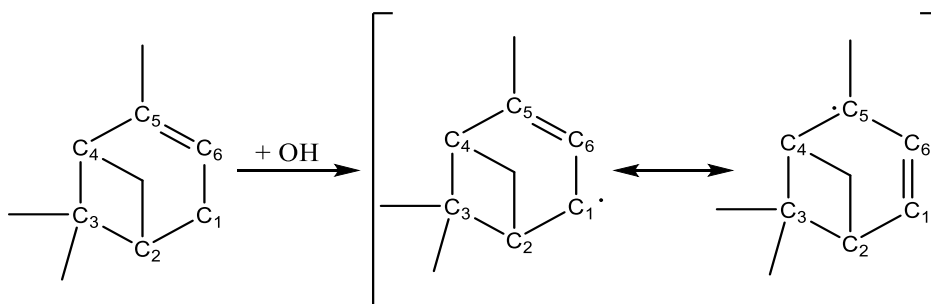
Figure 6.3: First step for *α*-pinene oxidation as proposed by Peeters *et al.*[20]

The first resonance structure shown in Figure 6.3, shows a radical at C_1, where a H-atom has been abstracted and H_2O formed. Due to the C=O bond at C_1, there is no H-atom to be abstracted preventing the formation of this structure. The second resonance structure shows a radical at C_5 and an unsaturated C=C bond between C_1 and C_6. Again due to the C=O bond at C_1 a second unsaturated bond $C_1=C_6$ could not be formed as carbon is only capable of forming four bonds. The only examples of verbenone oxidation occur under extreme laboratory conditions: a reaction between verbenone and CH_3CN in an excess of ozone (~2 mmol) at -40 °C[21] or the reaction between verbenone and potassium permanganate dissolved in a mixture of acetic acid and water (volume ratio 10:1)[22], neither of which resemble atmospheric conditions.

As well as the oxidation of verbenone there is also a potential photochemical fate for verbenone. In the presence of direct sunlight verbenone may isomerize to chrysanthenone, a terpene with no behavioural effects on bark beetles.[8] This photochemcical conversion is one of a few examples of an ultimate 1,3-alkyl shift of an α,β-unsaturated ketone; a process that can either occur via an overall 1,3-alkyl migration (Path a, see Figure 6.4) which is faster than the cleavage of verbenone into a ketene (an optically inactive species formed by Path b) followed by a intramolecular thermal or photolytic cyclization forming chrysanthenone (Path c, see Figure 6.4).[23]
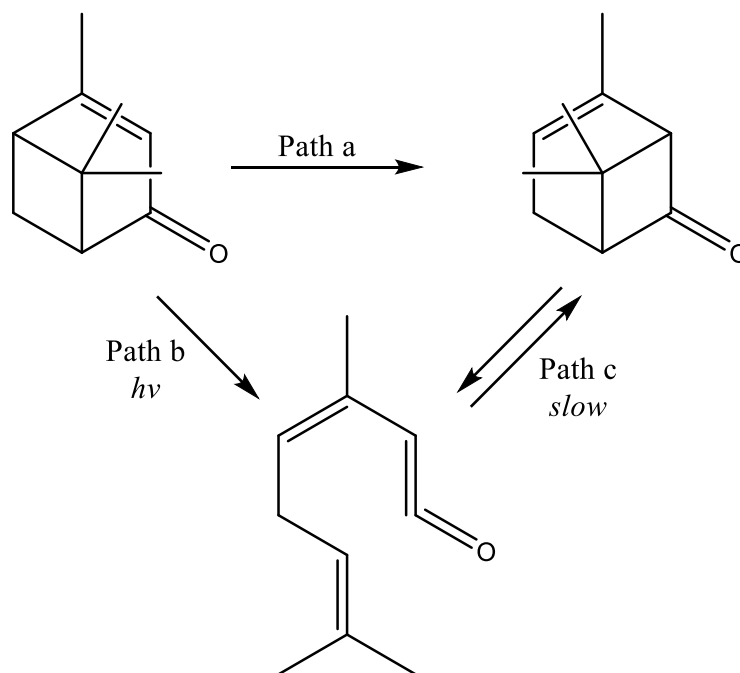
Figure 6.4: Two possible pathways through which chrysanthenone is formed form verbenone

6.1.3 Uses of Verbenone

As a pheromone proven to play a vital role in insect-interactions, verbenone is being used and developed as an effective alternative to common pesticides. It is currently unclear over the precise role verbenone plays in host colonisation; presently it is uncertain whether application of verbenone onto a living tree prevents initial attack or decreases the attack rate so that the host's resistance could overcome the initial attack, thus preventing mass attack of beetles and thereby saving the tree.[15]

Recently verbenone pouches, contain 7.5 g of the active ingredient, are being used to combat the colonisation of various pine species by mountain pine beetles. The verbenone is dispersed via evaporation from these slow release pouches which are attached at a height of approximately 3 meters, to the trunks of trees vulnerable to beetle colonisation. Although these pouches have proven remarkably effective against the *Dendroctonus* genus (bark beetles), which in particular has reduced the loss of lodgepole and white bark pine (a previously mentioned candidate for the endangered species list) it doesn't appear effective against *Conophthorus ponderosae* (white pine cone beetle).[12]

Whilst verbenone pouches have proved effective as an insecticide, they are by no means perfect; testing has shown that new release devices are required in order to develop greater ease of application particularly over rugged terrain.[12] This development builds upon the knowledge gained from the past 20 years where verbenone has been used as a deterrent against not only bark beetle attack but also against the feeding of adult weevils.[24]

Alternatively the United States Department of Agriculture (USDA) Forest Service has successfully been using pheromone-releasing laminated flakes for decades. These 3.2 × 3.2 mm square flakes are comprised of three layers of laminate plastics; a pheromone releasing inner layer containing approximately 15% verbenone is sandwiched between two semi-permeable outer layers. The release rate of verbenone from these flakes is known to be dependent on temperature and humidity. Lab tests suggest that these flakes are capable of releasing biologically significant quantities of verbenone for up to 42 days at a constant temperature of 30 °C; however, field tests suggest this time could be increased to up to 10 weeks due to the diurnal temperature and shading of the flakes by other vegetation. Similarly to the slow release pouches, verbenone releasing flakes have proved extremely effective at protecting lodgepole pine from mountain pine beetle attack; in both the Washington and Wyoming study sites application of verbenone flakes resulted

in the trapping of approximately 50% fewer beetles in comparison to their respective control sites.[12]

Whilst it has been stated that (*1S*)-(-)-verbenone could not be found in the plant kingdom, Ju *et al.* described its production via the animal kingdom, *"(1S)-(-)-verbenone is a naturally occurring anti-aggregation pheromone generated by bark beetles"*.[25] As previously mentioned verbenone is believed to be an oxidation product of *trans*-verbenol, whose anti-ischemic and anti-inflammatory effects have already been identified. The majority of investigations involving verbenone focus on the (*R*) enantiomer, Ju *et al.* attention is on the (*S*) enantiomer – hoping to discover whether it possesses anti-ischemic as well as the antibacterial, acaricidal and anti-inflammatory properties, already known to be characteristics of essential oils containing (*1S*)-(-)-verbenone.[25] This was not the first study looking into the medicinal uses of verbenone, in 2005 whilst probing the antimicrobial effects of the essential oil of *Rosmarinus officinalis L* (of which verbenone is a major constituent[1-3]) Santoyo *et al.* found that verbenone was most effective against the gram-positive *Staphylococcus aureus* bacteria (i.e. it takes up the crystal violet stain in the Gram stain test and appears purple coloured under a microscope) and that the fungus *Aspergillus niger* was the least susceptible. Generally the gram-positive bacteria (*Staphylococcus aureus* and *Bacillus subtilis*) are more sensitive than the gram-negative bacteria (*Escherichia coli* and *Pseudomonas aeruginosa*) to the antimicrobial activity of verbenone which in turn is more sensitive than the yeast (*Candida albicans*) and the fungus (*Aspergillus niger*).[26]

6.1.4 Previous Spectroscopic and Theoretical Works

To date little work has been carried out on the spectroscopy of verbenone; a study in 2010 by Ureña *et al.* examined the vibrational circular dichroism patterns of verbenone along with two other bicyclic terpenes.[1] This study is the first and only report carried out on the infrared spectrum of verbenone, and whilst it states verbenone has 69 vibrational normal modes is pays particular attention to the vibrational stretches of the >C=C< bond at 1618 cm^{-1} and –C=O bond at 1680 cm^{-1}. To aid with the interpretation of their recorded infrared spectra, computational chemistry calculations were carried out at the B3LYP/cc-pVDZ level of theory to evaluate not only the optimised structure of the system but also the harmonic vibrational frequencies. To date no microwave spectroscopy investigation has been carried out on verbenone.

6.2 Experimental

6.2.1 Microwave Spectroscopy

Full details of the experiment are discussed in Chapter 2, but briefly the recording of the microwave spectrum (48-69 GHz) of verbenone on the Monash system is discussed here. Verbenone was purchased from Sigma-Aldrich (98%) and used without further purification. A sample of verbenone was vaporised at a temperature of 80 $^{\circ}$C, in a stream of argon at a pressure of 0.3 bar, in the presence of a 2000 V cm^{-1} Stark field.

A low resolution search spectrum was first recorded over a wide frequency range (48-69 GHz) using a strip chart, before the individual lines were recorded and digitally averaged before a Lorentzian line shape fitted (see Figure 6.5) giving typical full width half height (FWHH) for transitions of 200-400 kHz.
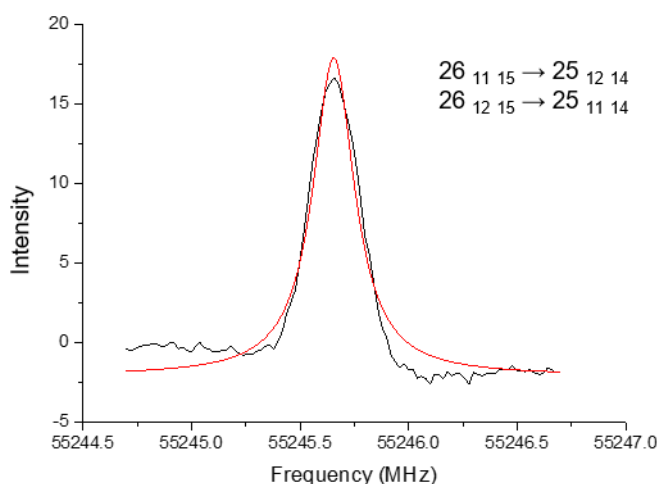
Figure 6.5: Rotation transition of verbenone at 56255.7 MHz, fitted using a Lorentzian line shape function

Lines were fitted using Watson's *A*-reduced Hamiltonian with an *II^l* representation[27] using the PGopher simulation and fitting program written by C.M. Western.[28]

Full details of the experiment are discussed in Chapter 2, but briefly the recording of the microwave spectrum (9-22 GHz) of verbenone on the Hannover system is discussed here. In order to obtain sufficient vapour pressure, verbenone was heated in a 1.5 mm orifice reservoir nozzle situated at the rear of the Fabry-Pérot resonator reflectors. The spectra was recorded with a nozzle temperature of 80 $^{\circ}$C, with a backing pressure of

approximately 1 bar and a pulse repetition rate of 20 kHz with neon carrier gas. Under these conditions the rotational temperature of the molecular beam was <2 K. A Lorentzian line-shape function was fitted to each of the line profiles, giving typical full width half height (FWHH) for transitions of 10-50 kHz.

6.2.2 Computational Details

A crude conformational search at the Hartree-Fock (HF)[29, 30] level of theory with a STO-3G basis set[31], using the Spartan Pro program[32] confirmed the presence of only one conformer of verbenone. This preliminary structure was systematically optimised via HF and second-order Møller-Plesset perturbation theory (MP2)[33] with the 6-31G(d,p) basis set[34] and visualised using Chemcraft.[35] This initial structure was utilised in geometry optimisation and harmonic frequency calculations using either the B3LYP[36, 37] functional with the aug-cc-pVTZ basis set[38] or MP2 with the 6-31++G(d,p) basis set[34], using the Gaussian 03 software package.[39] Due to the complexity of the molecule, utilising the MP2/aug-cc-pVTZ would have been computationally too expensive to have undertaken. Tight optimizations and SCF convergence criteria were used for each of these calculations in addition to an ultrafine pruning grid for the B3LYP calculations. The centrifugal distortion constants of verbenone, were also calculated at using Gaussian 03 at both levels of theory.

Potential energy surface (PES) scans were carried out to investigate the potential for internal rotation of verbenone's three methyl rotors. Relaxed potential energy surface scans were created in Molden.[35] Rotation around the dihedral angles associated (see Figure 6.6) with each of the methyl rotors, H_{11}- C_9- C_8- C_1, H_{16}- C_{13}- C_8- C_1 and H_{23}- C_{20}-C_{17}- C_1 were analysed at the B3LYP/6-31G(d,p) level of theory. To generate the potential energy surface each dihedral angle was rotated from 0° to 360° with a step size of 10°, whilst carrying out a geometry optimisation at each step. All potential energy surface scans and final optimised structures were visualised using GaussView 5.0 graphical interface.[40]

6.3 Results and Discussions

6.3.1 Initial Assignment of the Microwave Spectrum of Verbenone

The assignment of the microwave spectrum obtained of verbenone on the Monash system (48-69 GHz) was straightforward. Due to the rigidity of its structure, only a single

conformer (Figure 6.6) was identified. Gas-Chromatography Mass Spectrometry (GC-MS) also refuted the presence of a contamination in the sample
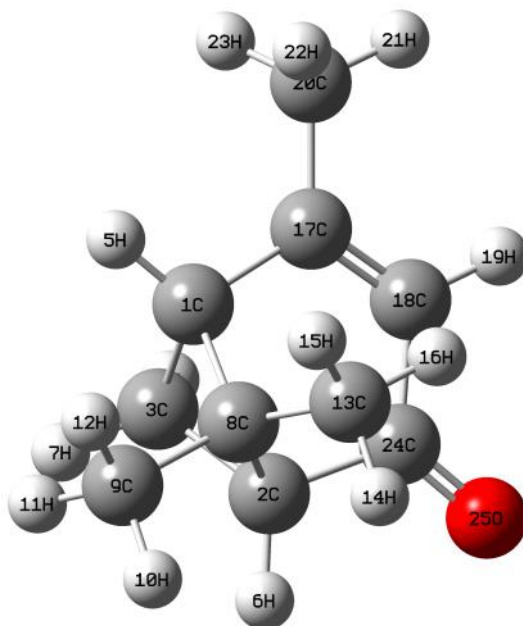
Figure 6.6: Optimised structure of verbenone calculated at the B3LYP/aug-cc-pVTZ level of theory

Table 6.1: Structure parameters of verbenone (numbering is based on Figure 6.6). Bond lengths in pm and angles in degrees

Parameters	This Work		Ureña *et al.*
	B3LYP	**MP2**	**(Ref 1)**[a]
R(C1-C3)	155.7	155.5	156.1
R(C2-C3)	155.6	155.4	156.0
R(C2-C8)	157.7	156.9	158.1
R(C1-C8)	158.2	157.2	158.6
R(C8-C13)	153.1	152.3	153.5
R(C8-C9)	152.5	152.8	153.0
R(C17-C18)	134.2	135.6	135.2
R(C17-20C)	149.3	149.6	149.8
R(24C-25O)	121.7	123.8	-
∠(C1-C3-C2)	85.9°	85.9°	85.9°
∠(C3-C2-C8)	87.5°	87.4°	87.6°
∠(C2-C8-C1)	84.3°	84.8°	84.3°
∠(C8-C1-C3)	87.2°	87.3°	87.3°
∠(C2-C8-9C)	112.1°	111.9°	111.9°
∠(C1-C8-C13)	119.9°	119.6°	118.9°
∠(C9-8C-C13)	108.1°	108.3°	108.1°
∠(C1-C8-C9)	112.0°	111.9°	112.2°
∠(C2-C8-C13)	119.0°	118.7°	119.8°
∠(C17-C1-C8)	110.6°	110.4°	110.6°
∠(C17-C1-C3)	107.1°	107.0°	107.2°
∠(C24-C2-C8)	109.9°	109.5°	110.0°
∠(C24-C2-C3)	107.5°	107.6°	107.5°

[a]Calculated at the B3LYP/cc-pVDZ level of theory

Verbenone can be classed as an oblate near-symmetric rotor as it possesses one principal moment of inertia significantly larger than the other two. As verbenone has an asymmetric parameter (κ) of +0.428, a Watson's A reduced Hamiltonian using an II^l representation was used to fit the spectroscopic parameters (including the dipole moments $x = 0.4690$, $y = -4.4609$, $z = -0.6450$) of the spectrum obtained using the Monash spectrometer using the PGopher program[28] (Figure 6.7).
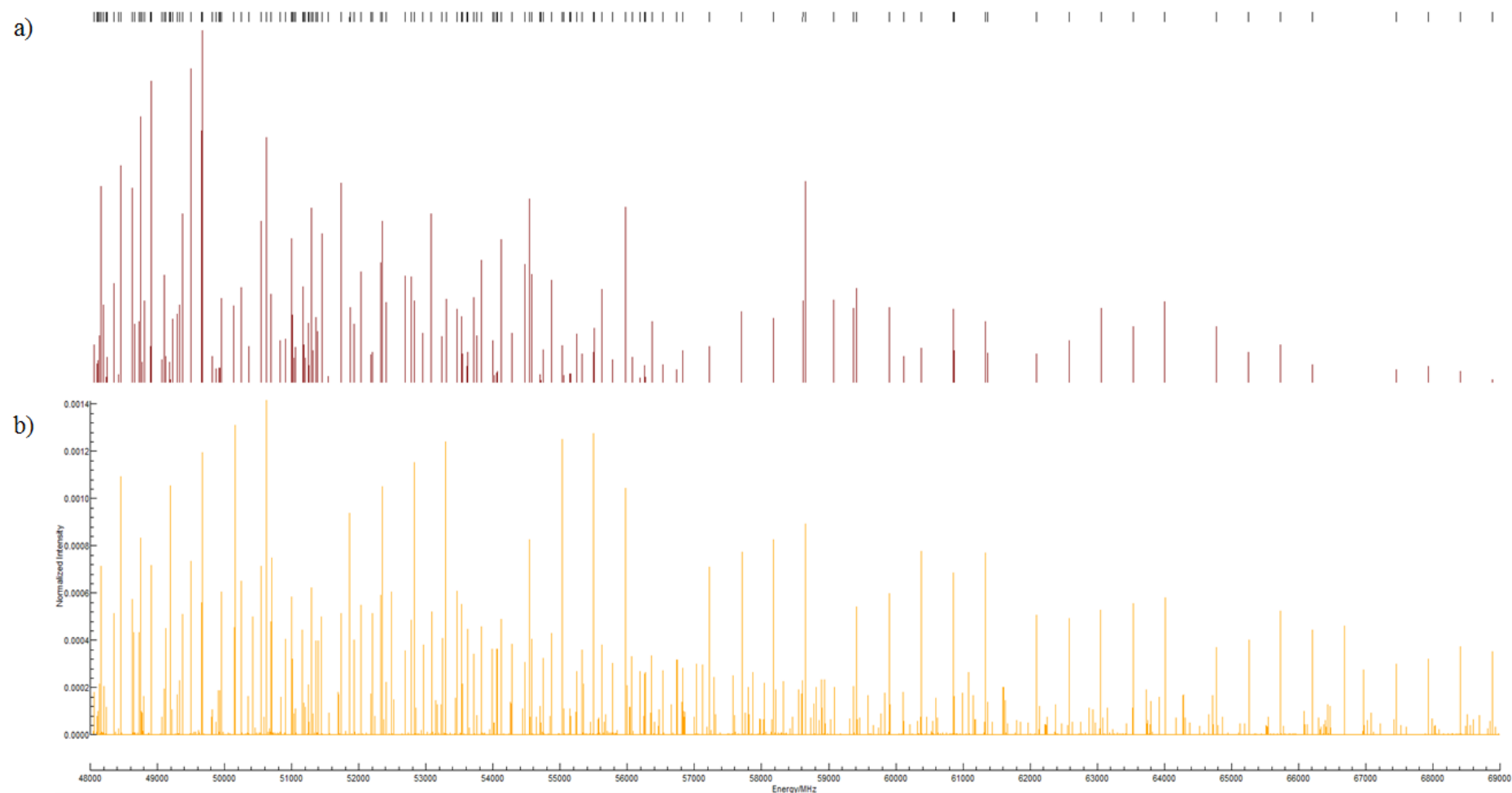
Figure 6.7: Fitted microwave spectrum of verbenone (48-69 GHz); a) lines observed using the Monash spectrometer, b) a simulation based on computational calculation at the B3LYP/aug-cc-pVTZ level of theory, simulated at 10 K

The rotational constants from the 1 *a*-type (with the selection rule $\Delta J = \pm 1$, $\Delta K_a = 0$ and $\Delta K_c = \pm 1, \pm 3$) and 252 *b*-type transitions (with the selection rule $\Delta J = +1$, $\Delta K_a = \pm 1, \pm 3$ and $\Delta K_c = \pm 1, \pm 3$), which are listed in Table 6.2, were fitted in good agreement with both the B3LYP/aug-cc-pVTZ and MP2/6-31++G(d,p) values (Table 6.3).

Table 6.2: Fitted *a*- and *b*-type transition frequencies (MHz) from the millimeter-wave spectrum of verbenone

Transition $(J'_{K_a K_c} - J''_{K_a K_c})$	Observed	Calculated	Obs-Calc	Standard deviation[a]
$5_{0\,5} - 4_{1\,4}$	9332.6782	9332.6939	-0.0157	0.0015
$5_{2\,3} - 4_{3\,2}$	10575.4698	10575.4825	-0.0127	0.0032
$5_{2\,4} - 4_{1\,3}$	10104.5809	10104.4944	0.0865	0.0018
$5_{3\,3} - 4_{2\,2}$	11079.7396	11079.7494	-0.0098	0.0031
$5_{5\,1} - 4_{4\,0}$	13101.6263	13101.6213	-0.0051	0.0025
$6_{1\,5} - 5_{2\,4}$	11871.5307	11871.5307	-0.0178	0.0017
$6_{2\,5} - 5_{1\,4}$	11878.0028	11878.0196	-0.0168	0.0019
$6_{6\,1} - 5_{5\,0}$	15804.2418	15804.2457	-0.0039	0.0030
$7_{7\,0} - 6_{6\,1}$	18508.1732	18508.1783	-0.0051	0.0027
$7_{7\,1} - 6_{6\,0}$	18492.9677	18492.9676	0.0000[b]	0.0014
$7_{7\,1} - 6_{6\,0}$	18492.9871	18492.9839	0.0032	0.0015
$8_{8\,0} - 7_{7\,1}$	21180.6635	21180.6650	-0.0015	0.0013
$16_{4\,12} - 15_{3\,13}$	49873.7250	49873.7568	-0.0318	0.029831
$16_{5\,11} - 15_{4\,12}$	49069.8870	49069.8832	0.0038	0.036975
$16_{5\,12} - 15_{2\,13}$	49873.7250	49873.757	-0.0320	0.029831
$16_{6\,10} - 15_{5\,11}$	48245.1977	48245.1233	0.0744	1
$16_{6\,11} - 15_{3\,12}$	49069.8870	49069.8897	-0.0027	0.036975
$16_{7\,10} - 15_{4\,11}$	48245.1977	48245.3064	-0.1087	1
$17_{6\,11} - 16_{5\,12}$	51548.0079	51547.8149	0.1930	1
$17_{7\,11} - 16_{4\,12}$	51548.0079	51547.8443	0.1636	1
$17_{9\,8} - 16_{8\,9}$	48777.8100	48777.8708	-0.0609	1
$17_{10\,8} - 16_{7\,9}$	48902.3212	48902.2856	0.0356	0.026504
$17_{11\,7} - 16_{8\,8}$	48115.5834	48115.5979	-0.0146	0.015668
$17_{12\,6} - 16_{9\,7}$	48106.9421	48106.9474	-0.0053	0.01497

Table 6.2: Cont.

$17_{13\,5} - 16_{10\,6}$	49813.6417	49813.6333	0.0084	0.01395
$18_{7\,11} - 17_{6\,12}$	54014.2235	54014.1718	0.0517	0.044617
$18_{8\,11} - 17_{5\,12}$	54014.2235	54014.2892	-0.0656	1
$18_{10\,8} - 17_{9\,9}$	51031.6344	51031.6525	-0.0180	0.023493
$18_{11\,7} - 17_{10\,8}$	49221.8058	49221.8287	-0.0228	0.016677
$18_{11\,8} - 17_{8\,9}$	51315.6738	51315.6386	0.0352	0.018413
$18_{13\,6} - 17_{10\,7}$	51261.7572	51261.731	0.0263	0.016874
$19_{12\,7} - 18_{11\,8}$	51058.6190	51058.5891	0.0299	0.015795
$19_{12\,8} - 18_{9\,9}$	53753.0846	53753.0752	0.0094	0.01656
$19_{13\,6} - 18_{12\,7}$	49106.0054	49106.0124	-0.0070	0.017803
$19_{14\,6} - 18_{13\,6}$	48243.7232	48243.7008	0.0224	0.017553
$19_{14\,6} - 18_{11\,7}$	54711.6305	54711.6351	-0.0046	0.015027
$19_{15\,4} - 18_{14\,5}$	48723.1348	48723.0853	0.0496	0.03366
$19_{15\,5} - 18_{14\,4}$	48655.6116	48655.6866	-0.0750	1
$19_{16\,3} - 18_{15\,4}$	49191.2999	49191.2176	0.0823	1
$19_{16\,4} - 18_{15\,3}$	49186.6500	49186.7012	-0.0512	1
$19_{17\,2} - 18_{16\,3}$	49672.1293	49672.2872	-0.1580	0.030847
$19_{17\,3} - 18_{16\,2}$	49672.1293	49672.0987	0.0306	1
$19_{19\,0} - 18_{18\,1}$	50622.8905	50622.8610	0.0295	0.025724
$19_{19\,1} - 18_{18\,0}$	50622.8905	50622.8609	0.0296	0.025724
$20_{12\,8} - 19_{11\,9}$	55149.9640	55149.9558	0.0082	0.022123
$20_{14\,6} - 19_{13\,7}$	51244.8692	51244.8374	0.0318	0.016389
$20_{14\,7} - 19_{13\,6}$	49333.5872	49333.6232	-0.0360	0.017504
$20_{15\,5} - 19_{14\,6}$	51005.8313	51005.7643	0.0670	1
$20_{15\,6} - 19_{14\,5}$	50686.7277	50686.7415	-0.0138	0.017635
$20_{16\,4} - 19_{15\,5}$	51388.3747	51388.2888	0.0859	1
$20_{16\,5} - 19_{15\,4}$	51357.8999	51357.9551	-0.0552	1
$20_{17\,3} - 19_{16\,4}$	51867.7539	51868.6030	-0.8491	1
$20_{17\,4} - 19_{16\,3}$	51867.7539	51866.7650	0.9888	1
$20_{18\,2} - 19_{17\,3}$	52349.3617	52349.4239	-0.0622	1
$20_{18\,3} - 19_{17\,2}$	52349.3617	52349.3531	0.0086	0.021777
$20_{19\,1} - 19_{18\,2}$	52825.5700	52825.5800	-0.0100	0.022172

Table 6.2: Cont.

$20_{19\,2} - 19_{18\,1}$	52825.5700	52825.5784	-0.0084	0.022172
$20_{20\,0} - 19_{19\,1}$	53299.5242	53299.5279	-0.0037	0.022057
$20_{20\,1} - 19_{19\,0}$	53299.5242	53299.5279	-0.0037	0.022057
$21_{13\,9} - 20_{12\,8}$	48056.6734	48056.6967	-0.0233	0.016519
$21_{14\,7} - 20_{13\,8}$	54698.9777	54698.9851	-0.0074	0.015203
$21_{14\,8} - 20_{13\,7}$	50358.4286	50358.4232	0.0055	0.014996
$21_{15\,6} - 20_{14\,7}$	53548.0944	53548.1273	-0.0329	0.017062
$21_{15\,7} - 20_{14\,6}$	52401.8799	52401.9167	-0.0368	0.016013
$21_{16\,5} - 20_{15\,6}$	53618.0838	53618.0859	-0.0021	0.017365
$21_{16\,6} - 20_{15\,5}$	53460.5566	53460.6169	-0.0603	1
$21_{17\,4} - 20_{16\,5}$	54061.7184	54061.6696	0.0487	0.042187
$21_{17\,5} - 20_{16\,4}$	54048.3255	54048.4089	-0.0834	1
$21_{18\,3} - 20_{17\,4}$	54545.9417	54546.3106	-0.3689	1
$21_{18\,4} - 20_{17\,3}$	54545.9417	54545.5765	0.3652	1
$21_{19\,2} - 20_{18\,3}$	55026.4515	55026.4688	-0.0174	0.034334
$21_{19\,3} - 20_{18\,2}$	55026.4515	55026.4426	0.0089	0.034334
$21_{20\,1} - 20_{19\,2}$	55502.3179	55502.2899	0.0280	0.032346
$21_{20\,2} - 20_{19\,1}$	55502.3179	55502.2893	0.0286	0.032346
$21_{21\,0} - 20_{20\,1}$	55976.1530	55976.1694	-0.0164	0.023517
$21_{21\,1} - 20_{20\,0}$	55976.1530	55976.1694	-0.0164	0.023517
$22_{11\,11} - 21_{12\,10}$	48136.1124	48136.1219	-0.0095	0.01844
$22_{12\,10} - 21_{13\,9}$	48803.4187	48803.4119	0.0068	0.017185
$22_{12\,11} - 21_{11\,10}$	48195.1608	48195.1497	0.0111	0.019131
$22_{13\,9} - 21_{14\,8}$	48753.5154	48753.5332	-0.0177	0.016035
$22_{13\,10} - 21_{12\,9}$	49296.0370	49296.0330	0.0040	0.017092
$22_{14\,9} - 21_{13\,8}$	51185.3505	51185.3313	0.0192	0.016176
$22_{15\,8} - 21_{14\,7}$	53615.6980	53615.7047	-0.0067	0.015766
$22_{17\,5} - 21_{16\,6}$	56265.6981	56265.6406	0.0576	1
$22_{18\,5} - 21_{17\,4}$	56732.7852	56732.8738	-0.0886	1
$22_{19\,3} - 21_{18\,4}$	57223.9380	57223.9985	-0.0605	1
$22_{19\,4} - 21_{18\,3}$	57223.7392	57223.71	0.0291	0.023413
$22_{20\,2} - 21_{19\,3}$	57703.4235	57703.4221	0.0015	0.021678

$22_{20,3} - 21_{19,2}$	57703.4235	57703.4124	0.0111	0.021678
$22_{21,1} - 21_{20,2}$	58178.9971	58178.9597	0.0374	0.032371
$22_{21,2} - 21_{20,1}$	58178.9971	58178.9595	0.0376	0.032371
$22_{22,0} - 21_{21,1}$	58652.7263	58652.7844	-0.0581	1
$22_{22,1} - 21_{21,0}$	58652.7263	58652.7844	-0.0581	1
$23_{9,14} - 22_{10,13}$	48352.5872	48352.5559	0.0314	0.01315
$23_{10,13} - 22_{11,12}$	49126.9641	49127.0381	-0.074	0.083761
$23_{10,14} - 22_{9,13}$	48352.5872	48352.6088	-0.0215	0.01315
$23_{11,12} - 22_{12,11}$	49916.0860	49916.1442	-0.0582	1
$23_{12,11} - 22_{13,10}$	50690.8357	50690.8421	-0.0064	0.016955
$23_{12,12} - 22_{11,11}$	49929.9721	49929.9255	0.0466	0.026804
$23_{13,10} - 22_{14,9}$	51199.0460	51199.0232	0.0228	0.02259
$23_{13,11} - 22_{12,10}$	50833.4787	50833.4588	0.0199	0.029761
$23_{14,10} - 22_{13,9}$	52184.9060	52184.8582	0.0478	0.020368
$23_{15,8} - 22_{16,7}$	48414.9779	48414.9734	0.0045	0.015517
$23_{19,4} - 22_{18,5}$	59415.5266	59416.6534	-1.1268	1
$23_{19,5} - 22_{18,4}$	59415.5266	59414.2912	1.2354	1
$23_{20,3} - 22_{19,4}$	59901.4859	59901.5503	-0.0643	1
$23_{20,4} - 22_{19,3}$	59901.4859	59901.4386	0.0474	0.027089
$23_{21,2} - 22_{20,3}$	60380.3181	60380.2909	0.0273	0.043791
$23_{21,3} - 22_{20,2}$	60380.3181	60380.2874	0.0308	0.043791
$23_{22,2} - 22_{21,1}$	60855.5933	60855.5910	0.0023	0.021111
$23_{22,1} - 22_{21,2}$	60855.5933	60855.5910	0.0022	0.021111
$23_{23,0} - 22_{22,1}$	61329.4365	61329.3720	0.0645	1
$23_{23,1} - 22_{22,0}$	61329.4365	61329.3720	0.0645	1
$24_{7,17} - 23_{8,16}$	48620.9427	48620.9660	-0.0232	0.022848
$24_{8,16} - 23_{9,15}$	49376.9417	49376.9204	0.0213	0.024361
$24_{8,17} - 23_{7,16}$	48620.9427	48620.9660	-0.0232	0.022848
$24_{9,15} - 23_{10,14}$	50137.9872	50137.9359	0.0514	0.01853
$24_{9,16} - 23_{8,15}$	49376.9417	49376.9208	0.0209	0.024361
$24_{10,14} - 23_{11,13}$	50907.3251	50907.2816	0.0435	1
$24_{10,15} - 23_{9,14}$	50137.9872	50137.9447	0.0425	1

Table 6.2: Cont.

$24_{11\ 14} - 23_{10\ 13}$	50907.3251	50907.4646	-0.1395	0.031584
$24_{15\ 9} - 23_{16\ 8}$	52177.9446	52177.9542	-0.0096	0.021495
$24_{20\ 4} - 23_{19\ 5}$	62094.5937	62095.0684	-0.4747	1
$24_{20\ 5} - 23_{19\ 4}$	62094.5937	62094.0999	0.4937	1
$24_{21\ 3} - 23_{20\ 4}$	62578.9254	62578.9400	-0.0146	0.041807
$24_{21\ 4} - 23_{20\ 3}$	62578.9254	62578.8973	0.0281	0.041807
$24_{22\ 2} - 23_{21\ 3}$	63057.0883	63057.0835	0.0048	0.022689
$24_{22\ 3} - 23_{21\ 2}$	63057.0883	63057.0822	0.0061	0.022689
$24_{23\ 1} - 23_{22\ 2}$	63532.1810	63532.1847	-0.0037	0.035335
$24_{23\ 2} - 23_{22\ 1}$	63532.1810	63532.1847	-0.0037	0.035335
$24_{24\ 0} - 23_{23\ 1}$	64005.9332	64005.9313	0.0020	0.027915
$24_{24\ 1} - 23_{23\ 0}$	64005.9332	64005.9313	0.0020	0.027915
$25_{4\ 21} - 24_{5\ 20}$	48159.0535	48159.0515	0.0020	0.019647
$25_{5\ 20} - 24_{6\ 19}$	48908.379	48908.4257	-0.0467	0.021776
$25_{5\ 21} - 24_{4\ 20}$	48159.0535	48159.0515	0.0020	0.019647
$25_{6\ 19} - 24_{7\ 18}$	49658.8555	49658.8835	-0.0280	0.021331
$25_{6\ 20} - 24_{5\ 19}$	48908.379	48908.4257	-0.0467	0.021776
$25_{7\ 19} - 24_{6\ 18}$	49658.8555	49658.8835	-0.0280	0.021331
$25_{8\ 17} - 24_{9\ 16}$	51165.8161	51165.7719	0.0442	0.020753
$25_{9\ 16} - 24_{10\ 15}$	51924.6601	51924.6241	0.0360	0.025007
$25_{9\ 17} - 24_{8\ 16}$	51165.8161	51165.7719	0.0442	0.020753
$25_{10\ 15} - 24_{11\ 14}$	52690.0324	52690.0525	-0.0201	1
$25_{10\ 16} - 24_{9\ 15}$	51924.6601	51924.6255	0.0346	0.025007
$25_{11\ 14} - 24_{12\ 13}$	53466.4620	53466.2041	0.2579	1
$25_{11\ 15} - 24_{10\ 14}$	52690.0324	52690.0849	-0.0525	0.016957
$25_{12\ 14} - 24_{11\ 13}$	53466.4620	53466.7916	-0.3296	1
$25_{13\ 12} - 24_{14\ 11}$	55052.7274	55052.7463	-0.0188	0.030993
$25_{14\ 11} - 24_{14\ 10}$	56190.3542	56190.3355	0.0187	1
$25_{14\ 12} - 24_{13\ 11}$	55141.4072	55141.3582	0.0489	0.025087
$25_{21\ 4} - 24_{20\ 5}$	64773.1849	64773.3893	-0.2044	1
$25_{21\ 5} - 24_{20\ 4}$	64773.1849	64772.9987	0.1863	1
$25_{22\ 3} - 24_{21\ 4}$	65256.1184	65256.1742	-0.0558	0.032154

Table 6.2: Cont.

$25_{22\,4} - 24_{21\,3}$	65256.1184	65256.1581	-0.0396	1
$25_{23\,3} - 24_{22\,2}$	65733.8129	65733.8066	0.0063	0.028426
$25_{23\,2} - 24_{22\,3}$	65733.8129	65733.8071	0.0058	0.028426
$25_{24\,1} - 24_{23\,2}$	66208.7809	66208.7413	0.0397	0.034171
$25_{24\,2} - 24_{23\,1}$	66208.7809	66208.7412	0.0397	0.034171
$26_{2\,24} - 25_{3\,23}$	48453.6473	48453.6104	0.0369	0.02284
$26_{3\,24} - 25_{2\,23}$	48453.6473	48453.6104	0.0369	0.02284
$26_{4\,22} - 25_{5\,21}$	49950.3760	49950.3765	-0.0005	0.018948
$26_{5\,22} - 25_{4\,21}$	49950.3760	49950.3765	-0.0005	0.018948
$26_{6\,20} - 25_{7\,19}$	51449.7205	51449.7109	0.0096	0.02502
$26_{7\,19} - 25_{8\,18}$	52201.3054	52201.2968	0.0085	0.017468
$26_{7\,20} - 25_{6\,19}$	51449.7205	51449.7109	0.0096	0.02502
$26_{8\,18} - 25_{9\,17}$	52955.0790	52955.0855	-0.0066	0.017985
$26_{8\,19} - 25_{7\,18}$	52201.3054	52201.2968	0.0085	0.017468
$26_{9\,17} - 25_{10\,16}$	53712.2692	53712.2583	0.0110	0.017181
$26_{9\,18} - 25_{8\,17}$	52955.079	52955.0855	-0.0066	0.017985
$26_{10\,16} - 25_{11\,15}$	54474.6986	54474.7151	-0.0166	0.02301
$26_{10\,17} - 25_{9\,16}$	53712.2692	53712.2585	0.0107	0.017181
$26_{11\,15} - 25_{12\,14}$	55245.655	55245.6155	0.0396	1
$26_{11\,16} - 25_{10\,15}$	54474.6986	54474.7206	-0.0220	0.02301
$26_{12\,15} - 25_{11\,14}$	55245.655	55245.7258	-0.0707	0.025011
$26_{22\,4} - 25_{21\,5}$	67451.3583	67451.4878	-0.1294	1
$26_{22\,5} - 25_{21\,4}$	67451.3583	67451.3325	0.0258	0.043997
$26_{23\,3} - 25_{22\,4}$	67933.2416	67933.2684	-0.0268	0.032211
$26_{23\,4} - 25_{22\,3}$	67933.2416	67933.2624	-0.0208	0.032211
$26_{24\,2} - 25_{23\,3}$	68410.4584	68410.4673	-0.0089	0.035902
$26_{24\,3} - 25_{23\,2}$	68410.4584	68410.4672	-0.0087	0.035902
$26_{25\,1} - 25_{24\,2}$	68885.2382	68885.2608	-0.0226	0.041219
$26_{25\,2} - 25_{24\,1}$	68885.2382	68885.2608	-0.0226	0.041219
$27_{0\,27} - 26_{1\,26}$	48749.3435	48749.3858	-0.0423	0.021269
$27_{1\,26} - 26_{2\,25}$	49497.1242	49497.1724	-0.0482	0.026556
$27_{1\,27} - 26_{0\,26}$	48749.3435	48749.3858	-0.0423	0.021269

Table 6.2: Cont.

Transition				
$27_{2\,25} - 26_{3\,24}$	50245.1385	50245.0843	0.0542	1
$27_{2\,26} - 26_{1\,25}$	49497.1242	49497.1724	-0.0482	0.026556
$27_{3\,24} - 26_{4\,23}$	50993.2584	50993.2153	0.0431	0.026023
$27_{3\,25} - 26_{2\,24}$	50245.1385	50245.0843	0.0542	1
$27_{4\,23} - 26_{5\,22}$	51741.7199	51741.7009	0.0190	0.031181
$27_{4\,24} - 26_{3\,23}$	50993.2584	50993.2153	0.0431	0.026023
$27_{5\,23} - 26_{4\,22}$	51741.7199	51741.7009	0.0190	0.031181
$27_{6\,21} - 26_{7\,20}$	53240.6023	53240.6089	-0.0065	0.017744
$27_{7\,20} - 26_{8\,19}$	53991.7002	53991.7362	-0.0360	0.022413
$27_{7\,21} - 26_{6\,20}$	53240.6023	53240.6089	-0.0065	0.017744
$27_{8\,19} - 26_{9\,18}$	54744.7422	54744.7449	-0.0027	0.017315
$27_{8\,20} - 26_{7\,19}$	53991.7002	53991.7362	-0.0360	0.022413
$27_{9\,18} - 26_{10\,17}$	55500.5870	55500.5876	-0.0006	0.031513
$27_{9\,19} - 26_{8\,18}$	54744.7422	54744.7449	-0.0027	0.017315
$27_{10\,17} - 26_{11\,16}$	56260.7684	56260.7535	0.0149	0.038958
$27_{10\,18} - 26_{9\,17}$	55500.5870	55500.5876	-0.0006	0.031513
$27_{11\,17} - 26_{10\,16}$	56260.7684	56260.7544	0.0140	0.038958
$28_{0\,28} - 27_{1\,27}$	50540.9234	50540.9131	0.0103	0.020131
$28_{1\,27} - 27_{2\,26}$	51288.7116	51288.6684	0.0432	0.021557
$28_{1\,28} - 27_{0\,27}$	50540.9234	50540.9131	0.0103	0.020131
$28_{2\,26} - 27_{3\,25}$	52036.5451	52036.5423	0.0028	0.022198
$28_{2\,27} - 27_{1\,26}$	51288.7116	51288.6684	0.0432	0.021557
$28_{3\,25} - 27_{4\,24}$	52784.5906	52784.6196	-0.0289	0.018884
$28_{3\,26} - 27_{2\,25}$	52036.5451	52036.5423	0.0028	0.022198
$28_{4\,24} - 27_{5\,23}$	53533.0237	53533.0207	0.0030	0.018795
$28_{4\,25} - 27_{3\,24}$	52784.5906	52784.6196	-0.0289	0.018884
$28_{5\,23} - 27_{6\,22}$	54281.8862	54281.9181	-0.0319	0.021802
$28_{5\,24} - 27_{4\,23}$	53533.0237	53533.0207	0.0030	0.018795
$28_{6\,22} - 27_{7\,21}$	55031.5719	55031.5587	0.0132	0.023053
$28_{6\,23} - 27_{5\,22}$	54281.8862	54281.9181	-0.0319	0.021802
$28_{7\,21} - 27_{8\,20}$	55782.2905	55782.3001	-0.0096	0.020865
$28_{7\,22} - 27_{6\,21}$	55031.5719	55031.5587	0.0132	0.023053

Table 6.2: Cont.

$28_{8\,20} - 27_{9\,19}$	56534.6627	56534.666	-0.0033	0.026637
$28_{8\,21} - 27_{7\,20}$	55782.2905	55782.3001	-0.0096	0.020865
$28_{9\,20} - 27_{8\,19}$	56534.6627	56534.6660	-0.0033	0.026637
$29_{0\,29} - 28_{1\,28}$	52332.4118	52332.4243	-0.0125	0.018889
$29_{1\,28} - 28_{2\,27}$	53080.1564	53080.1475	0.0089	0.019923
$29_{1\,29} - 28_{0\,28}$	52332.4118	52332.4243	-0.0125	0.018889
$29_{2\,27} - 28_{3\,26}$	53827.9373	53827.9836	-0.0463	0.021157
$29_{2\,28} - 28_{1\,27}$	53080.1564	53080.1475	0.0089	0.019923
$29_{3\,26} - 28_{4\,25}$	54575.9901	54576.0093	-0.0193	0.018736
$29_{3\,27} - 28_{2\,26}$	53827.9373	53827.9836	-0.0463	0.021157
$29_{4\,25} - 28_{5\,24}$	55324.3513	55324.3329	0.0184	0.02747
$29_{\,4\,26} - 28_{3\,25}$	54575.9901	54576.0093	-0.0193	0.018736
$29_{5\,24} - 28_{6\,23}$	56073.1081	56073.1065	0.0016	0.025443
$29_{5\,25} - 28_{4\,24}$	55324.3513	55324.3329	0.0184	0.02747
$29_{6\,23} - 28_{7\,22}$	56822.5459	56822.5459	0.0000	0.019965
$29_{6\,24} - 28_{5\,23}$	56073.1081	56073.1065	0.0016	0.025443
$29_{7\,23} - 28_{6\,22}$	56822.5459	56822.5459	0.0000	0.019965
$29_{9\,20} - 28_{10\,19}$	59078.7181	59078.6807	0.0374	0.02595
$29_{10\,20} - 28_{9\,19}$	59078.7181	59078.6807	0.0374	0.02595
$29_{12\,17} - 28_{13\,16}$	61365.2769	61365.3067	-0.0298	0.029369
$29_{13\,17} - 28_{12\,16}$	61365.2769	61365.3185	-0.0416	0.029369
$30_{0\,30} - 29_{1\,29}$	54123.9665	54123.9188	0.0478	0.031731
$30_{1\,29} - 29_{2\,28}$	54871.6077	54871.6090	-0.0013	0.019051
$30_{1\,30} - 29_{0\,29}$	54123.9665	54123.9188	0.0478	0.031731
$30_{2\,28} - 29_{3\,27}$	55619.4142	55619.4072	0.0070	0.019614
$30_{2\,29} - 29_{1\,28}$	54871.6077	54871.6090	-0.0013	0.019051
$30_{3\,27} - 29_{4\,26}$	56367.4257	56367.3834	0.0423	0.032501
$30_{3\,28} - 29_{2\,27}$	55619.4142	55619.4072	0.0070	0.019614
$30_{4\,27} - 29_{3\,26}$	56367.4257	56367.3834	0.0423	0.032501
$30_{6\,24} - 29_{7\,23}$	58613.5890	58613.5591	0.0300	0.026243
$30_{7\,23} - 29_{8\,22}$	59363.6729	59363.6884	-0.0155	0.022877
$30_{7\,24} - 29_{6\,23}$	58613.5890	58613.5591	0.0300	0.026243

Table 6.2: Cont.

30 $_{8\ 22}$ − 29 $_{9\ 21}$	60115.0784	60115.0633	0.0151	0.026935
30 $_{8\ 23}$ − 29 $_{7\ 22}$	59363.6729	59363.6884	-0.0155	0.022877
30 $_{9\ 21}$ − 29 $_{10\ 20}$	60868.2300	60868.2280	0.0020	0.020797
30 $_{9\ 22}$ − 29 $_{8\ 21}$	60115.0784	60115.0633	0.0151	0.026935
30 $_{10\ 21}$ − 29 $_{9\ 20}$	60868.2300	60868.2280	0.0020	0.020797

[a]Original weighting was 10 % FWHH; however, in cases where Obs-Calc ≥ 0.05 the standard deviation applied to the transition was increased to 1.

[b]Obs-Calc = 0.0000 as this is the sole *E*-species transition identified by the FTMW experiment

Table 6.3: Microwave molecular parameters and calculated rotational constants for verbenone

Molecular Parameters[a]	Unit	Stark modulated continuous jet[b]	FTMW[b]	Combination[b]	Combination[b,c]	B3LYP[e]	MP2[e]
A	MHz	1338.44480(27)	1338.44367(13)	1338.44533(15)	1338.44533(15)	1341.82	1336.47
B	MHz	1212.02804(30)	1212.02586(43)	1212.02854(21)	1212.02854(21)	1206.24	1217.88
C	MHz	895.87687(32)	895.88068(17)	895.87751(18)	895.87751(18)	892.91	895.85
Δ_J	kHz	0.04125(27)	0.04125[d]	0.04169(18)	0.04169(18)	0.0415	0.0427
Δ_{JK}	kHz	0.09003(72)	0.09003[d]	0.09055(63)	0.09055(63)	0.0559	0.0576
Δ_K	kHz	-0.08205(59)	-0.08205[d]	-0.08262(54)	-0.08262(54)	-0.0398	-0.0395
δ_J	kHz	-0.00896(41)	-0.00896[d]	-0.00902(79)	0.00902(79)	0.00975	0.0101
δ_K	kHz	0.02752(41)	0.02752[d]	0.02715(33)	-0.02715(33)	-0.0300	-0.0338
No of Lines		241	12	253	253		
σ	MHz	0.98	4.58	0.94	0.94		

[a]Fitted using an *A*-reduced Hamiltonian in the *II^l* representation

[b]Fitted using the PGopher program

[c]Fitted using an *A*-reduced Hamiltonian in the *I^r* representation

[d]Constants fixed to those obtained from the Stark modulated fit

[e]This work. Calculated at the B3LYP/aug-cc-pVTZ and MP2/6-31++G(d,p) levels of theory using a *I^r* representation

Verbenone was originally fitted with a Watson's *A* reduced Hamiltonian using an II^l representation however this caused issues with the centrifugal distortion constants; whilst experimentally δ_J takes a negative value and δ_K a positive, theoretically δ_J takes the positive value and δ_K a negative. This difference can be attributed to the representation being used; whilst verbenone was fitted using an II^l representation, the default for Gaussian 03 calculations is an I^r representation (a prolate near-symmetric top). The consequence of this is a difference in the symmetry of the axis system used, resulting in experimental values of δ_J and δ_K with the reversed sign of those calculated.[41] To eliminate this conflict in axis systems, the constants noted in Table 6.3 were fitted with the I^r representation so that the theoretical and experimental centrifugal constants could be compared; however, the constants from the II^l representation are the ones that should be trusted.

The experimental values of Δ_{JK} and Δ_K are significantly different to those obtained theoretically. Correlation between parameters is usually accountable for such a difference, however, a correlation of 0.919 (see Table 6.4) suggests that parameter correlation is not responsible for the discrepancy between the theoretical and experimentally determined parameters. Instead it appears that the discrepancy is another consequence of the differing axis representations used; Gaussian 03 uses an I^r representation, whilst the fits in Table 6.3 were completed with an II^l representation for an oblate near-symmetric rotor.

Table 6.4: Correlation matrix for the experimental data seen in Table 6.3

A	1.000							
B	0.244	1.000						
C	-0.048	0.259	1.000					
Δ_K	-0.227	0.543	-0.078	1.000				
Δ_{JK}	0.339	-0.682	-0.050	-0.919	1.000			
Δ_J	0.113	0.932	0.411	0.534	-0.730	1.000		
δ_K	-0.490	-0.286	0.311	-0.001	0.089	-0.325	1.000	
δ_J	-0.140	-0.850	0.163	-0.538	0.666	-0.771	0.368	1.000

6.3.2 Investigating the Internal Rotation within Verbenone

Whilst the overall fit of the spectrum was straightforward, there were around 10 instances where the spectral lines appeared split in the predicted spectrum (red trace in Figure 6.8), yet they were not observed this way in the recorded spectrum (blue trace in Figure 6.8).
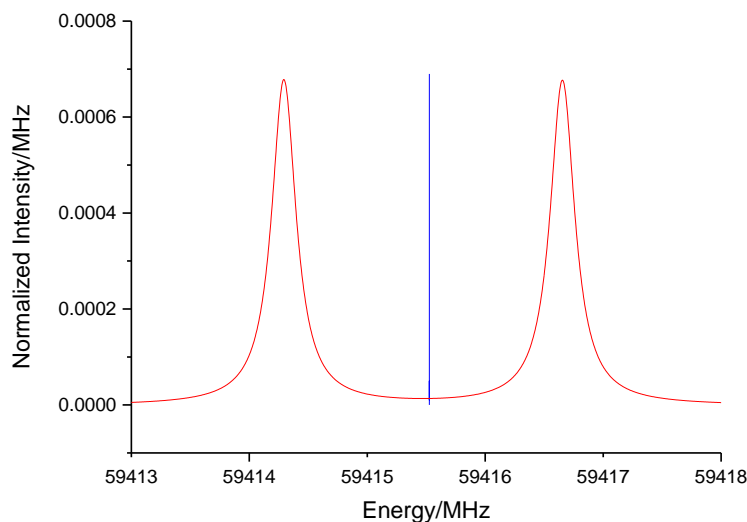
Figure 6.8: Rotational transitions of verbenone at 59414 and 59416 MHz, comparing the theoretical (red) and experimental (blue) spectra.

The observed peak at 59415 MHz has a peak width of 0.5 MHz which is approximately double that of the average peak width of the spectrum. This additional peak width is attributed to the presence of *C*-type transitions underneath the more intense *B*-type transitions; coupled with the Stark effect has resulted in only a single peak being observed.

As methyl rotation splitting was observed in the linalool investigation, an investigation into the potential splitting of verbenone's spectral lines was undertaken; the dihedral angles H_{11}- C_9- C_8- C_1, H_{16}- C_{13}- C_8- C_1 and H_{23}- C_{20}- C_{17}- C_1 were rotated through 360° at 10° intervals in order to obtain PES scans. Potential energy functions for each of the three methyl rotors in verbenone were fitted using the general expression of potential function for torsional motion via Equation 2.27.

Torsion about the H_{23}- C_{20}- C_{17}- C_1 dihedral angle resulted in the lowest V_3 barrier of 741 cm^{-1}; this is in comparison to 844 and 831 cm^{-1} for φ = H_{11}- C_9- C_8- C_1 and H_{16}- C_{13}- C_8- C_1, dihedral angles, respectively, as seen in Figure 6.9.
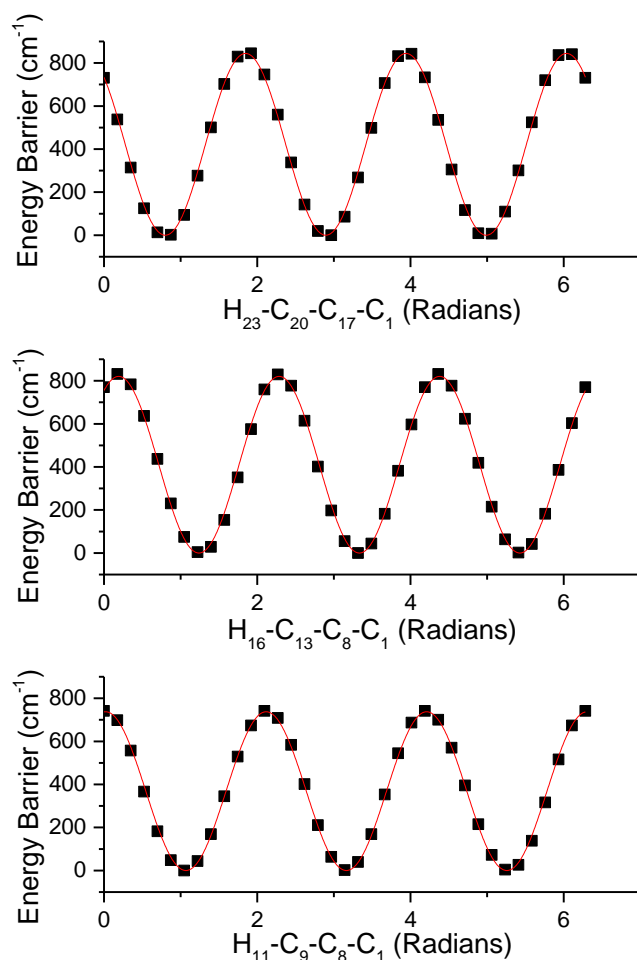
Figure 6.9: Result of the relaxed potential energy surface scans for each of the three methyl groups associated with verbenone. PES scan were carried out using the B3LYP/6-31G(d,p) level of theory

Unfortunately these rotation barriers cannot be fitted using the XIAM program, without any split rotational transitions included. The resolution of the Monash spectrometer only enables a single transition to be observed (as in Figure 6.8); without any split rotational transitions the V_3 parameter must remained fixed during the fitting process.

Previously a study by Nguyen *et al.* measuring the microwave spectrum of linalool, postulated that whilst the lowest barrier of internal methyl rotation (324 cm^{-1} calculated at the MP2/6-31++G(d,p) level of theory) was the source of the observed splitting of their spectral lines, the second lowest internal barrier (776 cm^{-1} calculated at the MP2/6-31++G(d,p) level of theory) would also give rise to additional splitting of the spectral lines[42]. However Nguyen *et al.* was unable to detect this additional splitting due to the

resolution limitations of the spectrometer; 2 kHz for isolated lines but worsen when lines are broadened by overlapping transitions.

The findings from this linalool investigation poses an interesting question, if an internal barrier of 776 cm^{-1}, results in the splitting of the spectral lines, then why is there little to no observed splitting of the verbenone spectral lines when it possesses a lower internal barrier of 741 cm^{-1}? The resolution of the Stark modulated system was incapable of detecting splitting which is predicted to be of the order of ~100-150 kHz, therefore additional transitions were investigated using a Fourier transform microwave system between 9-21 GHz, which has a resolution of ~5 kHz.

Figure 6.10: Rotational transitions of verbenone at 18492.98 MHz, showing the splitting between the *A*-state (red) and *E*-state (green) as measured by Fourier transform microwave spectroscopy.

Of the 12 transitions recorded using the FTMW spectrometer in Hannover, only a single transition appeared to show the splitting postulated in the Nguyen *et al.* paper. Due to running the spectrometer in parallel mode, two peaks for each of the *A*- and *E*-states appear due to the Doppler shift in each direction, so four peaks would be expected if splitting had occurred. In order to obtain the transition frequency for the *A*- and *E*-states (seen as the red and green traces respectively in Figure 6.10) the mean of the observed

178

frequencies is taken. The only transition to exhibit splitting using the Fourier transform spectrometer was at 18492.98 MHz (Figure 6.10); the observed splitting was 20 kHz, much lower than the XIAM predictions conducted using the original Stark Modulated data, which suggested splitting of 80 kHz.

As the experimental splitting present between the two states was narrower than predicted; the transition at 21180.66 MHz was examined as the splitting was predicted to be twice that of the 18492.98 MHz transition. Whilst the splitting of the *A*- and *E*-states of the 21180.66 MHz transition was predicted to be 160 kHz, as can be seen from Figure 6.11, experimetally no splitting is recorded. The splitting of 160 kHz was obtained from a predictive calculation, therefore full confidence in the result cannot be achieved, suggesting that the splitting of verbenone was not as the calculations seemed. This seems to suggest that the Fourier transform system does not have the resolution to observe the splitting caused by the internal rotation of the methyl rotor centred on C_9. As only a single split peak has been experimentally observed, it could be suggested that the additional peak is representative of an excited vibrational state rather than internal rotation. The use of neon as a carrier gas also gives credence to this theory.
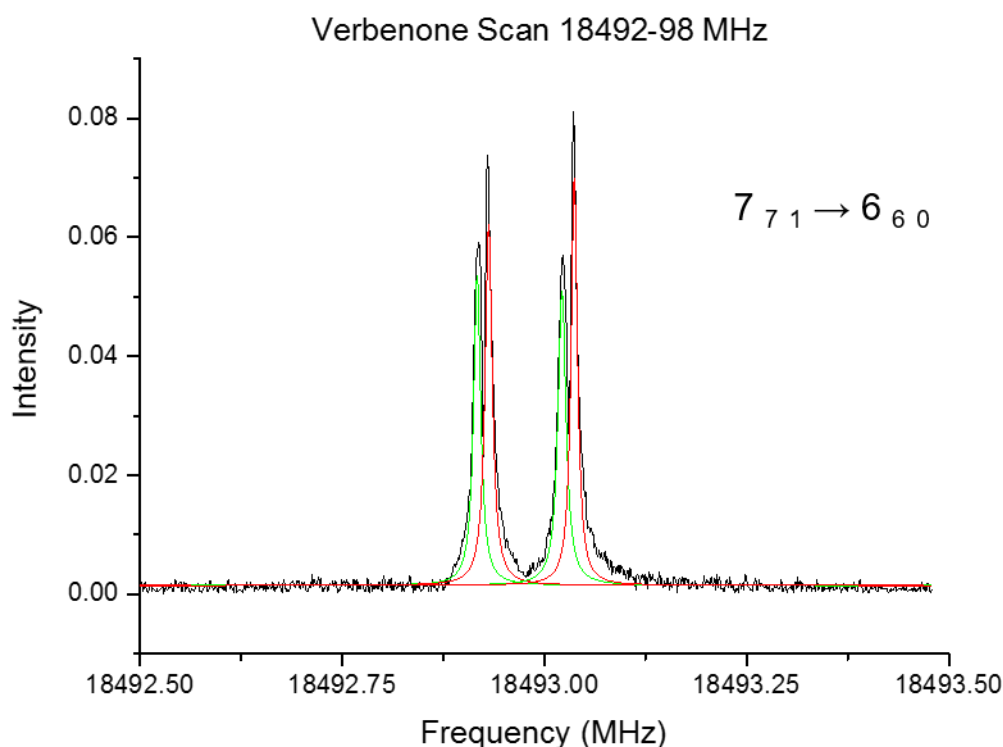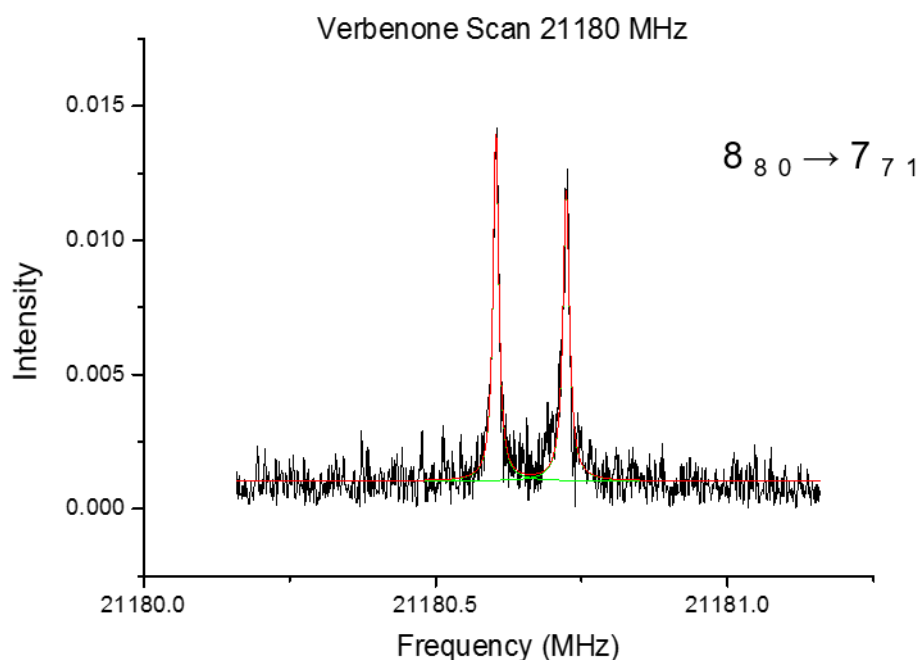

Figure 6.11: Rotational transitions of verbenone at 21180.66 MHz, showing the lack of splitting between the *A*-state and *E*-state as measured by Fourier transform microwave spectroscopy. The predicted splitting was 160 kHz

Table 6.5: Microwave molecular parameters and calculated rotational constants for verbenone

Molecular Parameters[a]	Unit	Stark modulated continuous jet	FTMW[b,c]	Combination[c]	B3LYP[d,e]	MP2[f]
A	GHz	1.33844(55)	1.33844(96)	1.33846(76)	1341.82	1336.47
B	GHz	1.21203(33)	1.21213(50)	1.21203(65)	1206.24	1217.88
C	GHz	0.89588(35)	0.89590(66)	0.89588(34)	892.91	895.85
Δ_J	kHz	0.04122(29)	2.02341(18)	0.04244(56)	0.0415	0.0427
Δ_{JK}	kHz	0.09028(78)	-5.72143(37)	0.09056(21)	0.0559	0.0576
Δ_K	kHz	-0.08221(64)	3.61007(37)	-0.08287(19)	-0.0398	-0.0395
δ_J	kHz	-0.00899(95)	-0.69342	-0.00902(28)	0.00975	0.0101
δ_K	kHz	0.02739(44)	-1.47824(54)	0.02713(10)	-0.0300	-0.0338
V_3	cm^{-1}	737.00	794.75(29)	828.28(22)	741	
F_0	GHz	157.878	157.878	157.878		
$I_a{}^g$	(u Å^2)	3.20108	3.20108	3.20108		
$<(i,a)$	º	31.25	31.25	31.25		
$<(i,b)$	º	103.57	103.57	103.57		
$<(i,c)$	º	62.44	62.44	62.44		
No of Lines		241	12	253		
σ^h	kHz	25.8	14.9	28.4		

[a]Fitted using an A-reduced Hamiltonian in the I^r representation

[b]The centrifugal distortion constant δ_J remained fixed

[c]Fits include 1 E-species transition

[d]Calculated at the B3LYP/aug-cc-pVTZ level of theory using a I^r representation

[e]V_3 calculated at the B3LYP/6-31G(d,p) level of theory

[f]Calculated at the MP2/6-31++G(d,p) level of theory using a I^r representation

[g]Moment of inertia I_a of the internal rotor, fixed to the value corresponding to a rotational constant of F_0

[h]Standard deviation of the fit

The Stark modulated continuous jet and the Fourier transform data were analysed in three fits using the program XIAM, two fitting each experimental data set separately and a third combining both data sets, as seen in Table 6.5. Of the 12 Fourier transform transitions fitted only one showed a splitting of the spectral line (that seen in Figure 6.10), suggesting a suitable low rotational barrier height. With only one possible *E*-state any fits containing this transition cannot be deemed an accurate account of microwave spectrum of verbenone.

The absence of splitting of the spectral lines suggests that the internal methyl rotational barrier is actually higher than the 741 cm^{-1} calculated at the B3LYP/6-31G(d,p) level of theory, otherwise splitting would be expected to be observed experimentally. Inclusion of diffuse functions into the basis set (see investigation in Chapter 5, Table 5.3) results in a calculated barrier of 808 cm^{-1}; this barrier would then be greater than the second barrier of linalool, as recorded by Nguyen *et al.*, and therefore we would not expect to detect any splitting of the energy levels. The Fourier transform data matches this revised expectation.

6.4 Conclusion

The microwave spectrum of verbenone has been recorded using the Stark modulated, continuous jet millimetre wave absorption spectrometer, located at Monash University, Victoria, Australia and assigned over the 48-69 GHz region; 241 transitions were observed with a standard deviation of 25.8 kHz. A further 12 transitions were recorded using the Pulsed-supersonic jet, Fabry-Pérot type resonator high resolution Fourier Transform Microwave System located at Gottfried-Wilhelm-Leibniz-Universität in Hannover, Germany and assigned over the 9-22 GHz region with a standard deviation of 14.9. The overall investigation fitted 253 transitions over the 9-69 GHz region with an overall standard deviation of 28.4 kHz. This assignment was supported by computational chemistry calculations which investigated the structure and barrier heights associated with the three methyl groups of verbenone.

The structural analysis predicts only a single conformer of verbenone which agrees with the observed spectrum. Initial evaluation of the barrier height of the methyl groups, calculated with at the B3LYP/6-31G(d,p) level of theory, suggests that no splitting from internal rotation would be expected; however, a study by Nguyen *et al.* on the terpene linalool at the MP2/6-31++G(d,p) level of theory proposes the opposite to be true. A higher resolution experiment using a FTMW was conducted to ascertain whether splitting

of the spectral lines could be observable. Further analysis of the of the methyl rotor, calculated at the B3LYP/6-31++G(d,p) level of theory, suggest that the rotational barrier was much higher than originally determined, accounting for the lack of splitting observed in the rotational spectrum of verbenone.

6.5 References

1. F. P. Ureña, J. R. A. Moreno and J. J. L. Gonzalez, *Chirality*, 2010, **22**, E123-E129.

2. M. Miyazawa, A. Sugie and T. Shimada, *Drug Metabolism and Disposition*, 2003, **31**, 1049-1053.

3. U. Ravid, E. Putievsky, I. Katzir, E. Lewinsohn and N. Dudai, *Flavour and Fragrance Journal*, 1997, **12**, 109-112.

4. R. P. Limberger, A. M. Aleixo, A. G. Fett-Neto and A. T. Henriques, *Electronic Journal of Biotechnology*, 2007, **10**, 500-507.

5. C. D. Geron and R. R. Arnts, *Atmospheric Environment*, 2010, **44**, 4240-4251.

6. A. Lee, A. H. Goldstein, J. H. Kroll, N. L. Ng, V. Varutbangkul, R. C. Flagan and J. H. Seinfeld, *Journal of Geophysical Research-Atmospheres*, 2006, **111**.

7. I. Etxebeste and J. A. Pajares, *Journal of Applied Entomology*, 2011, **135**, 258-268.

8. C. J. Fettig, S. R. McKelvey, R. R. Borys, C. P. Dabney, S. M. Hamud, L. J. Nelson and S. J. Seybold, *Journal of Economic Entomology*, 2009, **102**, 1846-1858.

9. D. W. A. Hunt, J. H. Borden, B. S. Lindgren and G. Gries, *Canadian Journal of Forest Research-Revue Canadienne De Recherche Forestiere*, 1989, **19**, 1275-1282.

10. G. J. Blomquist, R. Figueroa-Teran, M. Aw, M. M. Song, A. Gorzalski, N. L. Abbott, E. Chang and C. Tittiger, *Insect Biochemistry and Molecular Biology*, 2010, **40**, 699-712.

11. B. S. Lindgren, G. Nordlander and G. Birgersson, *Journal of Applied Entomology-Zeitschrift Fur Angewandte Entomologie*, 1996, **120**, 397-403.

12. N. E. Gillette, E. M. Hansen, C. J. Mehmel, S. R. Mori, J. N. Webster, N. Erbilgin and D. L. Wood, *Agricultural and Forest Entomology*, 2012, **14**, 367-375.

13. J. M. Brand, J. W. Bracke, L. N. Britton, A. J. Markovetz and S. J. Barras, *Journal of Chemical Ecology*, 1976, **2**, 195-199.

14. J. A. Byers, D. L. Wood, J. Craig and L. B. Hendry, *Journal of Chemical Ecology*, 1984, **10**, 861-877.

15. P. E. Tilden and W. D. Bedard, *Journal of Chemical Ecology*, 1988, **14**, 113-122.

16. W. W. Macfarlane, J. A. Logan and W. R. Kern, *Ecological Applications*, 2013, 40**23**, 421-437.

17. M. A. Haroldson and S. Podruzny, ed. U. S. G. Survey, Bozeman, MT, 2013.

18. C. M. Costello, F. T. van Manen, M. A. Haroldson, M. R. Ebinger, S. L. Cain, K. A. Gunther and D. D. Bjornlie, *Ecology and Evolution*, 2014, **4**, 2004-2018.

19. L. Zhang, J. Sun and S. R. Clarke, *Environmental Entomology*, 2006, **35**, 655-660.

20. J. Peeters, L. Vereecken and G. Fantechi, *Physical Chemistry Chemical Physics*, 2001, **3**, 5489-5504.

21. O. S. Kukovinets, T. I. Zvereva, V. G. Kasradze, F. Z. Galin, L. L. Frolova, A. V. Kuchin, L. V. Spirikhin and M. I. Abdullin, *Chemistry of Natural Compounds*, 2006, **42**, 216-218.

22. X.-L. Sun and R. Wang, *Chemistry and Industry of Forest Products*, 2011, **31**, 95-99.

23. W. F. Erman, *Journal of the American Chemical Society*, 1967, **89**, 3828-3841.

24. B. S. Lindgren and D. R. Miller, *Environmental Entomology*, 2002, **31**, 759-765.

25. C. Ju, S. Song, S. Hwang, C. Kim, M. Kim, J. Gu, Y. K. Oh, K. Lee, J. Kwon, K. Lee, W. K. Kim and Y. Choi, *Bioorganic & Medicinal Chemistry Letters*, 2013, **23**, 5421-5425.

26. S. Santoyo, S. Cavero, L. Jaime, E. Ibanez, F. J. Senorans and G. Reglero, *Journal of Food Protection*, 2005, **68**, 790-795.

27. J. K. G. Watson, *Vibrational Spectra and Structure : A Series of Advances, ed J.R. During, Elsevier, Amsterdam*, Elsevier, Oxford, 1977.

28. PGOPHER, a Program for Simulating Rotational, Vibrational and Electronic Structure, C. M. Western, University of Bristol, http://pgopher.chm.bris.ac.uk

29. J. A. Pople and R. K. Nesbet, *Journal of Chemical Physics*, 1954, **22**, 571-572.

30. R. McWeeny and G. Diercksen, *Journal of Chemical Physics*, 1968, **49**, 4852-4857.

31. W. J. Hehre, R. F. Stewart and J. A. Pople, *Journal of Chemical Physics*, 1969, **51**, 2657-2664.

32. I. Wavefunction, Irvine, CA, 2008.

33. C. Møller and M. S. Plesset, *Physical Review*, 1934, **46**, 618-622.

34. Harihara.Pc and J. A. Pople, *Theoretica Chimica Acta*, 1973, **28**, 213-222.

35. http://www.chemcraftprog.com.

36.   A. D. Becke, *Journal of Chemical Physics*, 1993, **98**, 5648-5652.

37.   P. J. Stephens, F. J. Devlin, C. F. Chabalowski and M. J. Frisch, *Journal of Physical Chemistry*, 1994, **98**, 11623-11627.

38.   T. H. Dunning, *Journal of Chemical Physics*, 1989, **90**, 1007-1023.

39.   M. J. Frisch, G. W. Trucks, H. B. Schlegel, G. E. Scuseria, M. A. Robb, J. R. Cheeseman, J. A. M. Jr., T. Vreven, K. N. Kudin, J. C. Burant, J. M. Millam, S. S. Iyengar, J. Tomasi, V. Barone, B. Mennucci, M. Cossi, G. Scalmani, N. Rega, G. A. Petersson, H. Nakatsuji, M. Hada, M. Ehara, K. Toyota, R. Fukuda, J. Hasegawa, M. Ishida, T. Nakajima, Y. Honda, O. Kitao, H. Nakai, M. Klene, X. Li, J. E. Knox, H. P. Hratchian, J. B. Cross, V. Bakken, C. Adamo, J. Jaramillo, R. Gomperts, R. E. Stratmann, O. Yazyev, A. J. Austin, R. Cammi, C. Pomelli, J. W. Ochterski, P. Y. Ayala, K. Morokuma, G. A. Voth, P. Salvador, J. J. Dannenberg, V. G. Zakrzewski, S. Dapprich, A. D. Daniels, M. C. Strain, O. Farkas, D. K. Malick, A. D. Rabuck, K. Raghavachari, J. B. Foresman, J. V. Ortiz, Q. Cui, A. G. Baboul, S. Clifford, J. Cioslowski, B. B. Stefanov, G. Liu, A. Liashenko, P. Piskorz, I. Komaromi, R. L. Martin, D. J. Fox, T. Keith, M. A. Al-Laham, C. Y. Peng, A. Nanayakkara, M. Challacombe, P. M. W. Gill, B. Johnson, W. Chen, M. W. Wong, C. Gonzalez and J. A. Pople, Gaussian, Inc., Wallingford CT, 2004, vol. Revision E.01.

40.   GaussView, Version 5, R. Dennington, T. Keith, and J. Millam, *Semichem Inc.*, Shawnee Mission, KS, 2009.

41.   G. W. King, R. M. Hainer and P. C. Cross, *Journal of Chemical Physics*, 1943, **11**, 27-42.

42.   H. V. L. Nguyen, H. Mouhib, S. Klahm, W. Stahl and I. Kleiner, *Physical Chemistry Chemical Physics*, 2013, **15**, 10012-10018.

Chapter Seven

Theoretical Investigation of Terpinolene Ozonolysis: Proof of Concept

7.1 Introduction

Whilst the ozonolysis mechanism of terpinolene has been experimentally hypothesised, the establishment of a mechanism through quantum chemical calculations has yet to be elucidated. Before attempting to generate such a mechanism, quantum chemical calculations were carried out on two well documented systems, isoprene and pinene ozonolysis, in order to test both the feasibility of such calculations and their accuracy.

7.2 Pinene Ozonolysis

7.2.1 Structure and Reactivity of α- and β-pinene

Pinene ($C_{10}H_{16}$) is an unsaturated cyclic monoterpene[1] for which two isomers can be identified, α-pinene (the most abundant isomer)[2-7] and β-pinene (Figure 7.1 a and b respectively). α- and β-pinene are the two most abundant terpenes in the troposphere, accounting for ~35% and ~23% respectively of the total terpene emission of 10^{14} g yr^{-1}.[8] The presence of the carbon bridge is common to both structures and results in a lack of symmetry; the only structural difference is the positioning of the unsaturated C=C bond: α-pinene [(1S,5S)-2,6,6-Trimethylbicyclo[3.1.1]hept-2-ene] possesses an endocyclic double bond and β-pinene [6,6-Dimethyl-2-methylenebicyclo[3.1.1]heptane] possesses an exocyclic double bond. As terpinolene (Figure 7.1c) contains both an endo- and exocyclic double bond it is important to examine both isomers.
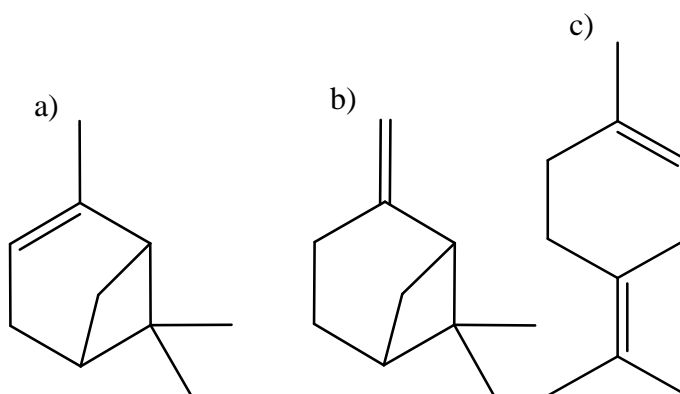
Figure 7.1: Skeletal structure of the cyclic monoterpenes a) α-pinene, b) β-pinene and c) terpinolene

It has been stated that the ozonolysis of α-pinene is slower due to the presence of an endocyclic double bond. The presence of an unsaturated C=C bond flattening the cyclohexane conformation and the addition of a methyl substituent to an sp^2 hybridised carbon atom both increase the steric hindrance of the system compromising the overlap

of the ozone and double bond orbitals. The addition of a bridgehead, which is out of plane in comparison to the six-membered ring, adds extra steric effects so the face of the cyclohexene ring on which ozone reacts must now be considered.[1]

A common source of both α- and β-pinene is *Pinus sylvestris L* (Scots pine),[9] the emission of α-pinene has been measured at 1.3 – 19.8 μg^{-1} h^{-1} from *Pinus halepensis* Mill. (Mediterranean evergreen conifer) and 0.11 – 14.7 μg^{-1} h^{-1} from *Quercus ilex L.* (Mediterranean evergreen broad-leaved species).[10]

A number of studies have sought to measure the rate constants for the reactions of α- and β-pinene with common atmospheric oxidants; as can be seen in Table 7.1 the reactivity's of both structural isomers are similar with respect to each of the atmospheric oxidants. Both isomers have the greatest reactivity towards ozone; however, α-pinene is substantially more reactive than β-pinene. For NO_3 α-pinene is more reactive, while for OH radicals β-pinene is more reactive.

Table 7.1: Comparison of rate constants of the three main atmospheric oxidants with both α- and β-pinene

	Rate constants (cm³ molecule⁻¹ s⁻¹)	Atkinson 1997[11]	Calogirou *et al.* 1999[2]	Atkinson and Arey 2003[12]
α-pinene	k_{OH}	53.7×10^{-12}	54×10^{-12}	52.3×10^{-12}
	k_{O_3}	86.6×10^{-18}	86.6×10^{-18}	84×10^{-18}
	k_{NO_3}	61.6×10^{-13}	61.6×10^{-13}	61.6×10^{-13}
β-pinene	k_{OH}	78.9×10^{-12}	79×10^{-12}	74.3×10^{-12}
	k_{O_3}	15×10^{-18}	15×10^{-18}	15×10^{-18}
	k_{NO_3}	25.1×10^{-13}	25.1×10^{-13}	25.1×10^{-13}

7.2.2 Previous Theoretical Works on Pinene

β-pinene ozonolysis has been studied at the B3LYP/6-311G(d,p) level of theory by Nguyen *et al.*[13] and poses a possible template for terpinolene ozonolysis due the presence of an external double C=C bond. An ozonolysis reaction by definition is "*the process of treating an organic compound with ozone to form an ozonide*". So the widely recognised defect of the B3LYP functional,[13,14] its inability to model ozone as a singlet open-shell biradical,[15] therefore makes modelling this reaction problematic. In the reaction scheme

of *β*-pinene reacting with ozone the energy of the entrance channel transition state is underestimated by ~10 kcal mol^{-1}; the authors proposed solution is to optimise the O_3 addition channel at the MPW1B95/6-31+G(d,p) level of theory, due to its good performance when calculating weak interactions. However, the MPW1B95 functional was solely used on the entrance channel as use of this functional across the entire potential energy surface would result in the height of subsequent transition states being over estimated by ~5 kcal mol^{-1}.[13] Although the B3LYP functional generally performs better than the MPW1B95 functional for the majority of the reaction process, the initial flaw for ozone addition would be expected during the theoretical investigation into the ozonolysis of terpinolene.

Prior to this investigation Zhang and Zhang carried out computational chemistry calculations in order to determine the ozonolysis process of *α*- and *β*-pinene.[8] This study stated the importance of the inclusion of polarisation functions and electron correlation effects in quantum-chemical methods that aim to obtain accurate energetics of primary ozonides and carbonyl oxides , so the B3LYP/6-31G(d,p) level of theory was used. The study shows structures and energy barriers for the ozonolysis of pinene to form the primary ozonide (POZ) which through bond breakage form a Criegee intermediate and finally the formation of hydroperoxide intermediates or dioxiranes from the Criegee intermediate.

The B3LYP/6-31G(d,p) optimised structures were then employed in single point calculations using both the MP2 and CCSD(T) levels of theory with a variety of basis sets. Table 7.2 compares the activation energies of the entrance channel for the ozonolysis of pinene at each of the different levels of theory. The activation energies of the B3LYP and MP2 methods were deemed inaccurate as they produce negative activation energies, as the addition of ozone is sensitive to electron correlation and the basis set used. The CCSD(T) single point energy calculations results in positive activation energies and the authors had already disregarded completing the entire potential energy surface with this method due to the greater expense of using CCSD(T) for the O_3-pinene system.[8]

The comparison between the theoretical and experimental values for the activation energy of the ozonolysis of pinene seen in Table 7.2 shows a better match for *β*-pinene rather than *α*-pinene. This suggests that the theoretical calculations are more able to accurately determine the activation energy for the ozonolysis process for an exo-cyclic double bond.

This result is encouraging as the ozonolysis of terpinolene preferentially occurs at the exo-cyclic C=C double bond.

Table 7.2: Zero point corrected (ZPE) corrected activation energies (in kcal mol^{-1}) for the entrance channel for the ozonolysis of *α*- and *β*-pinene as recorded by Zhang and Zhang[8], compared to the experimental activation energy recorded by Khamaganov and Hites[16]

Level of Theory	*α*-pinene	*β*-pinene
B3LYP/6-31G(d,p)	-2.5	-3.1
MP2/6-31G(d)	-8.7	-7.2
MP2/6-311++G(d,p)	-8.8	-6.3
CCSD(T)/6-31G(d)	0.4	1.1
CCSD(T) + CF[a]	0.3	2.0
Experimental	*1.05*	*2.58*

[a]Correction factor was determined from the energy difference between the MP2/6-31G(d) and MP2/6-311++G(d,p) levels. The CCSD(T)/6-31G(d) level was then corrected by this MP2 level correction factor

7.2.3 Current Theoretical Investigation into *α*-pinene Ozonolysis

7.2.3.1 Computational Details

Attempts to model the ozonolysis of *α*-pinene in the study by Zhang and Zhang were carried out to confirm that such a process was feasible for the analysis of the ozonolysis of terpinolene. In this proof of concept work, geometry optimisation and the harmonic vibrational frequency calculations were carried out using the B3LYP[17,18] functional with the 6-31++G(d,p)[19] basis set; tight optimisation and SCF convergence as well as an ultrafine pruning grid were used with the Gaussian 03 software package.[20] Transition states were searched for by using the QST3 method; which uses the optimised structures of the reactant and products for a given step as well as an initial guess of the transition state structure; for the entrance channel the reactants were ozone and *α*-pinene with the POZ as the product. Frequency calculations enabled the confirmation of a transition state structure, due to the presence of a single imaginary frequency occurring at the location at which the bond is being formed or broken. All optimised structures were visualised using GaussView 5.0.[21]

7.2.3.2 Results and Discussion

As can be seen in Figure 7.2, a potential energy surface for the ozonolysis of α-pinene could successfully be recreated. This schematic diagram also emphasises the fact that quantum-chemical calculations are highly dependent upon the basis set used; in this work the addition of diffuse functions has caused slight differences in the relative energies of these structures. The discrepancy in energy between the two levels of theory ranges from 0.1 to 6.3 kcal mol^{-1}. The inclusion of diffuse functions in the basis set has resulted in a negative activation energy for the entrance channel; however, it offers an improvement on Zhang and Zhang's findings. As the activation energy remains negative with this new basis set, it confirms that the B3LYP functional fails in the case of van der Waals complexes and loose transition states.
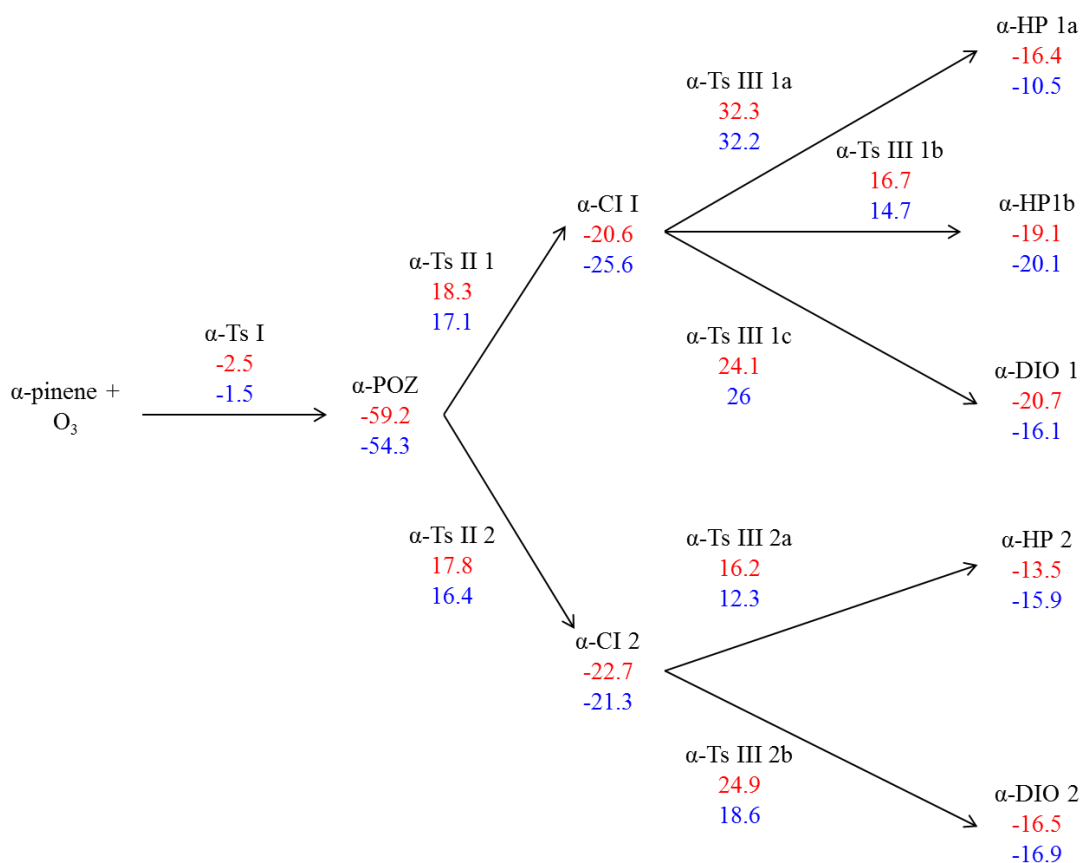

Figure 7.2: Schematic diagram for the ozonolysis of α-pinene, relative energies (in kcal mol^{-1}) shown in red are calculated by Zhang and Zhang at the B3LYP/6-31G(d,p) level of theory,[8] those shown in blue are from this work using the B3LYP/6-31++G(d,p) level of theory

More important than the similarity in the relative energies, is comparability of the optimised structures; Figure 7.3 shows the optimised structure of α-Ts I along with the important bond lengths and dihedral angles. The authors define α-Ts I as the transition state for the addition of ozone to α-pinene.

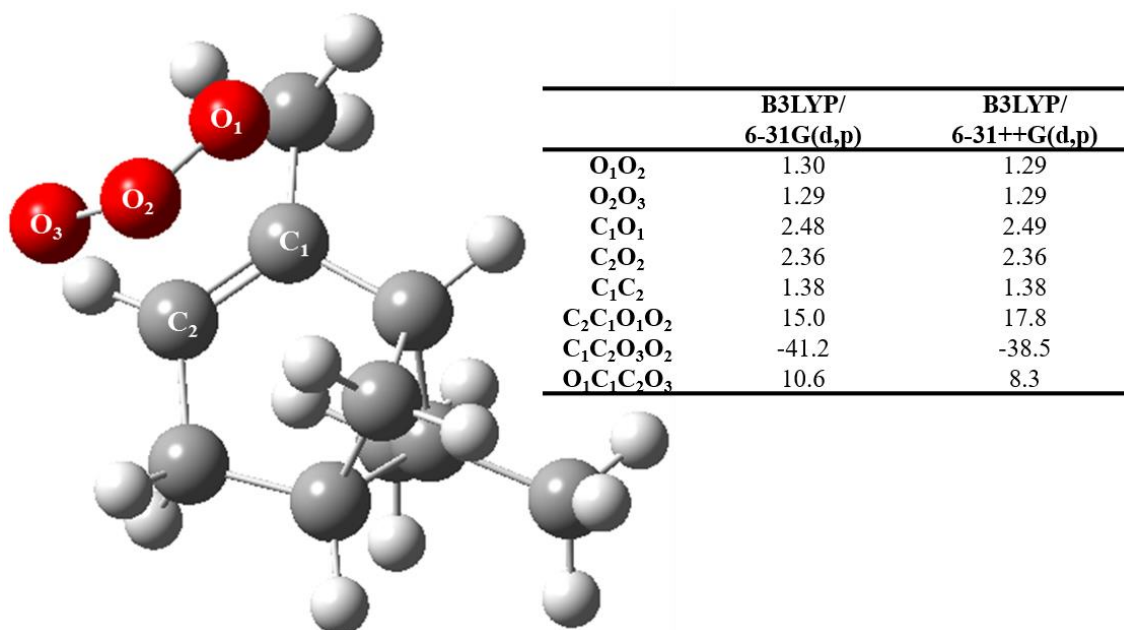|	B3LYP/ 6-31G(d,p)	B3LYP/ 6-31++G(d,p)
O_1O_2	1.30	1.29
O_2O_3	1.29	1.29
C_1O_1	2.48	2.49
C_2O_2	2.36	2.36
C_1C_2	1.38	1.38
$C_2C_1O_1O_2$	15.0	17.8
$C_1C_2O_3O_2$	-41.2	-38.5
$O_1C_1C_2O_3$	10.6	8.3

Figure 7.3: Optimised geometry of α-Ts I optimised at the B3LYP/6-31++G(d,p) level of theory, including comparison of the bond lengths (Å) and dihedral angles (°) at the B3LYP/6-31G(d,p)[8] and B3LYP/6-31++G(d,p) levels of theory

The bond lengths are almost identical between the two calculations while the dihedral angles differ by no more that ~3°, which shows that the ozonolysis of α-pinene has been successfully recreated using the B3LYP/6-31++G(d,p) level of theory. This confirms that in principle such a theoretical investigation would be suitable in order to establish the ozonolysis mechanism of terpinolene; however, further analysis of the level of theory employed is required in an attempt to improve the accuracy of the entrance channel activation energy. The study of a simpler system would assist with the ambition of calculating a more truthful activation energy.

7.3 Isoprene Ozonolysis

7.3.1 Structure and Reactivity of Isoprene

Isoprene (C_5H_8) is a doubly unsaturated terpene for which two conformers have been identified; the $\alpha\alpha$conformer and the more dominant (due to greater stability) *trans-*

conformer[22] (Figure 7.4). Isoprene has been identified as one of the most abundant hydrocarbons emitted by the terrestrial biosphere, with an emission rate of between 450 – 500 Tg yr^{-1}.[7, 22-24] As the simplest terpene structure, isoprene is the ideal system to attempt to find an appropriate level of theory that yields a more accurate activation energy for the ozonolysis entrance channel.
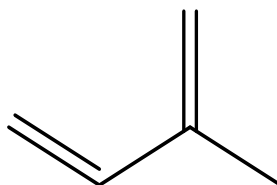

Figure 7.4: Skeletal structure of *cis*-isoprene

As isoprene [2-methyl-1,3-butadiene] is only emitted from vegetation during the day the reaction between isoprene and OH radicals is anticipated to dominate over reactions with ozone and NO_3 radicals.[7] This expectation is supported by a study that measured the rate constants for the reaction of isoprene with each of these common atmospheric oxidants; Hao *et al.* detailed the rate constants in 2009 for the reaction with OH radicals as 100×10^{-12} cm^3 molecule^{-1} s^{-1} and with ozone as 1.27×10^{-17} cm^3 molecule^{-1} s^{-1}.[9] It is unsurprising that isoprene appears least reactive towards NO_3 radicals which dominate night-time chemistry; that is not to say that isoprene is completely unreactive during night-time hours as isoprene ozonolysis is believed to provide an important source of night-time OH radicals.[24]

7.3.2 Previous Theoretical Works on Isoprene

Two previous studies have been completed investigating the ozonolysis of isoprene, both from the perspective of examining the mechanism of OH formation from this reaction. In 1997 Gutbrod *et al.* propose that the ozonolysis of isoprene proceeded via the accepted Criegee mechanism[25]; cycloaddition of the ozone to one of the unsaturated C=C bonds to form a 1,2,3-trioxolane, also referred to as the primary ozonide (POZ). The POZ then decomposes into an aldehyde and a carbonyl oxide, also known as a Criegee intermediate (Figure 7.5).[26]
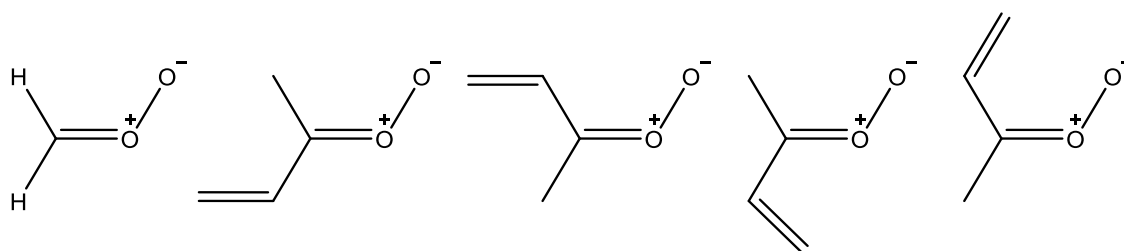
Figure 7.5: Criegee intermediates for the ozonolysis of isoprene as proposed by Gutbrod *et al.*[26]

The group identify that the most critical geometric feature of this intermediate as the ratio between the C=O and O-O bond lengths; Hartree-Fock and semi-empirical molecular orbital methods overestimate this ratio, while methods renowned for poor electron correlation underestimate the ratio. The authors of this study used the MP2/6-31G(d,p) level of theory, which they determine only yields reasonable geometrical parameters, so these are used as starting values for density functional theory (DFT) calculations. Gutbrod *et al.* used B3LYP/6-31G(d,p) as it has the ability to adequately reproduce the most reliable geometrical parameters for carbonyl oxides from CCSD(T)/TZ+2P calculations and it is a cheaper computational alternative.[26]

In 2003 Zhang and Zhang offered the same mechanism for isoprene ozonolysis, whilst calculating the activation energies required for each subsequent reaction step to proceed. The authors expand upon this mechanism by discussing the mechanics of the initial ozone addition; the two molecules must approach in a parallel plane allowing for maximal overlay between the π-HOMO orbital of isoprene and the π*-LUMO of ozone, in order to form an oxygen envelope conformation for the POZ.

As the presence of polarization functions is vital to the calculations of accurate energetics for the POZ, the authors used the B3LYP/6-31G(d,p) level of theory in order to optimise the structures of the reactants, products and transition states. Harmonic vibrational frequency calculations were also conducted at this level of theory in order to confirm the presence of energy minima and maxima. Additionally single point energy calculations were carried out using second order Møller–Plesset perturbation theory (MP2) and coupled-cluster theory with single and double excitations including perturbative corrections for triple excitations (CCSD(T)) with a variety of basis sets, as listed in Table 7.3. The authors highlight the extreme computational demands of using the larger 6-311++G(d,p) basis set in conjunction with the CCSD(T) calculation as the reason for not completing such a calculation.[24]

195

Table 7.3: Zero point energy (ZPE) corrected activation energies for the entrance channel for the ozonolysis of isoprene as recorded by Zhang and Zhang[24], compared to the experimental activation energy recorded by Khamaganov and Hites[16]

Level of Theory	Activation Energy (kcal mol^{-1})
B3LYP/6-31G(d,p)[a]	-1.6
MP2/6-31G(d)	-5.5
MP2/6-311++G(d,p)	-4.8
CCSD(T)/6-31G(d)	2.6
CCSD(T)/6-31G(d) + CF[b]	3.3
Experimental	*3.97*

[a]Geometry optimisation carried out at B3LYP/6-31G(d,p) level of theory, all other calculations carried out based on this structure, [b]Correction factor was determined from the energy difference between the MP2/6-31G(d) and MP2/6-311++G(d,p) levels. The CCSD(T)/6-31G(d) level was then corrected by this MP2 level correction factor

Table 7.3 depicts the activation energy for the entrance channel of isoprene ozonolysis at various levels of theory. The most prevalent observation is that CCSD(T) calculations yield the most accurate activation energies for O_3-isoprene addition as both MP2 and B3LYP produce negative activation energies for this process. These findings match the corresponding calculations for the ozonolysis of *α*- and *β*-pinene (Table 7.2). The comparison between the theoretical and experimental values for the activation energy of the ozonolysis of isoprene seen in Table 7.3 shows a good match for the CCSD(T) calculations and a poor match for the MP2 calculations.

7.3.3 Current Theoretical Investigation into Isoprene Ozonolysis

7.3.3.1 The Problem with the B3LYP Functional

There is a blatantly obvious question facing computational chemists: if the defect of the B3LYP functional for the calculation of ozone is so well known,[13, 22, 24] then why is it still being used? It also appears that the shortcomings of B3LYP are not restricted to ozone, with it also described as: yielding the greatest error for bond lengths[48], underestimating barrier heights[27, 28] and giving a poor description of the energetics for van der Waals and H-bonded systems.[15, 29] B3LYP is the most popular method for synthetic/mechanistic

concepts as organic chemists believe it accurately describes their systems[29, 30]. However, Grimme *et al.* comment on the huge, chemically relevant errors that B3LYP produces for organic processes such as dissociation reactions and enthalpies of formation (errors increasing with increasing size of the molecule).[49, 50]

7.3.3.2 The Proposed Solution

An array of review articles discuss the benefits and drawbacks of a wide variety of density functional theory methods in comparison to each other and to second order Møller–Plesset perturbation theory (MP2), a full discussion of which can be found in Chapter 3. The most commonly recommended functional is MPW1K (modified Perdew-Wang 1-parameter-method for kinetics)[31] which offers improved performance in calculations of bond distances and energies, while maintaining a low computational cost.[27, 28] The MPW1K functional has been specifically recommended as an alternative to B3LYP for locating transition state structures.[28] Based on the findings of the review articles the ozonolysis of isoprene will also be calculated using the MPW1K functional, to ascertain whether this yields a more accurate activation energy for the addition O_3- to isoprene.

7.3.3.3 Computational Details

Firstly, attempts to recreate the O_3-isoprene addition step in the study by Zhang and Zhang [24] were carried out to confirm that such a process could be conducted to produce accurate activation energies for the addition of ozone to terpenes. In this proof of concept work, geometry optimisation and harmonic vibrational frequency calculations were carried out using the B3LYP[17, 18] functional with the 6-31G(d,p)[19] basis set, using tight optimisation and SCF convergence with an ultrafine pruning grid. The B3LYP structures then underwent single point energy calculations using MP2[32] and CCSD(T)[33] with the 6-31G(d)[19] or 6-311G++(d,p)[34] basis sets, using the Gaussian 03 software package.[20]

To expand upon Zhang and Zhang's investigation geometry optimisation and harmonic vibrational frequency calculations were carried out at the MP2/6-31G(d), MP2/6-311G++(d,p)and CCSD/6-31G(d) levels of theory, rather than just single point energy calculations. It should be noted that CCSD[35-38] was used rather than CCSD(T) (used by Zhang and Zhang) due to the reduced computational cost. Additionally to these, further geometry optimisation and harmonic vibrational frequency calculations were conducted with the B3LYP and MPW1K[31] functionals and with MP3[39, 40] with the 6-31++G(d,p)[19]

and 6-31G(d) basis sets (geometry optimisation of ozone was performed using unrestricted B3LYP and MPW1K). Frequency calculations enabled the confirmation of a transition state structure, due to the presence of a suitable single imaginary frequency. All optimised structures were visualised using GaussView 5.0.[21]

7.3.4 Results and Discussion

The entrance channel for the ozonolysis of isoprene as supplied by Zhang and Zhang[24] was successfully recreated; however, the expanded investigation generated differing success.

Table 7.4: Zero point energy (ZPE) corrected activation energies for the entrance channel for the ozonolysis of isoprene, compared to the experimental activation energy recorded by Khamaganov and Hites[16]

Level of Theory	Activation Energy (kcal mol^{-1})
B3LYP/6-31(d,p)	-1.57
B3LYP/6-31++G(d,p)[a]	1.91
MP2/6-31G(d)	-[b]
MP2/6-311++G(d,p)	-[b]
MP3/6-31G(d)	-[b]
CCSD/6-31G(d)	-[b]
MPW1K/6-31++G(d,p)	1.90
Experimental	*3.97(5)*

[a]Optmisation of ozone carried out using UB3LYP/6-31++G(d,p) level of theory

[b]No transition state structure located

As previously mentioned B3LYP offers a poor description of ozone, resulting in inaccurate activation energies; however, as can be seen in Table 7.4, calculation of ozone using UB3LYP/6-31++G(d,p), vastly improves the accuracy of the activation energy, yielding a positive rather than negative activation energy. The stability of the wavefunction was also checked to ascertain whether the given conformer of ozone was in a local minimum after relaxing certain constraints. The original optimisation of ozone was carried out using a restricted wavefunction which was deemed to be unstable; this indicated that an unrestricted wavefunction was required. The resulting orbitals were used

to re-optimise the structure of ozone. Inclusion of the 'unrestricted' command allows electrons of unlike spins to use different spatial orbitals, allowing a more truthful description of the singlet open-shell biradical structure of ozone.

Unfortunately geometry optimisation calculations conducted using MP2, MP3 and CCSD failed to locate a transition state structure, confirmed by the lack of an imaginary vibrational frequency. Whilst the use of UB3LYP offers improvement of the theoretical activation energy in comparison to that determined experimentally, it appears equally as accurate as the MPW1K functional, suggesting that these maybe the most suitable functionals to determine the ozonolysis reaction path of terpinolene.

Calculation	C_1O_1	C_2O_3
B3LYP/6-31G(d)	2.21	2.48
B3LYP/6-31++G(d,p)	2.20	2.50
MP2/6-31G(d)[a]	-	-
MP2/6-311++G(d,p)[a]	-	-
CCSD/6-31G(d)[a]	-	-
MPW1K/6-31++G(d,p)	2.22	2.40

[a]No transition state structure found
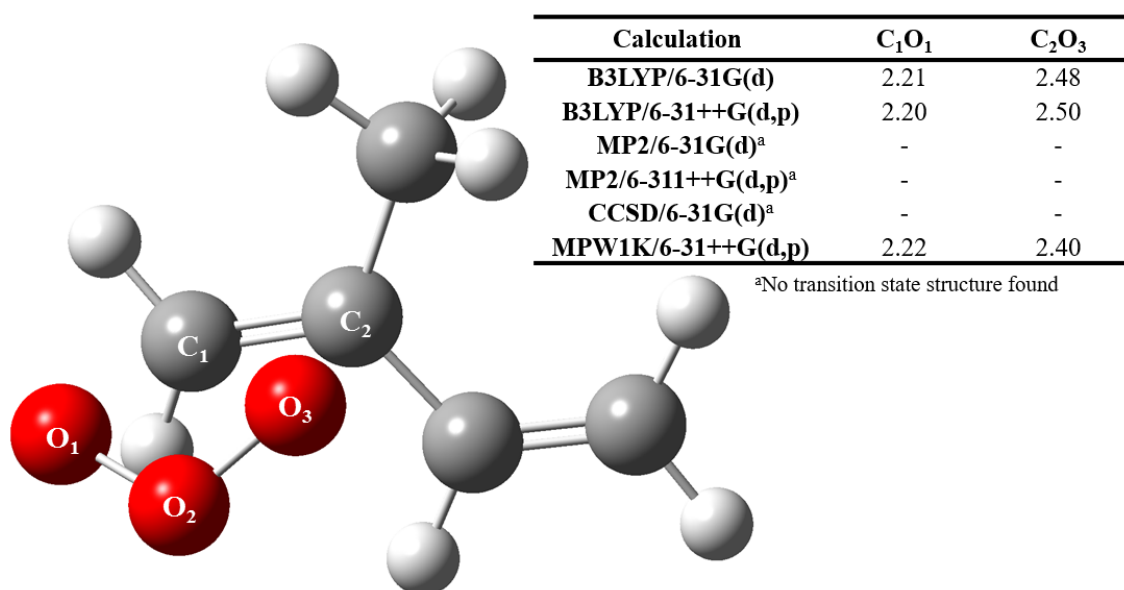
Figure 7.6: Optimised geometry of the O_3-isoprene addition transition state at the B3LYP/6-31++G(d,p) level of theory, including comparison of the C-O bond lengths (Å) at each of the levels of theory tested

Location of transition state structures using MP2 (frozen core) and CCSD calculations were unsuccessful (Table 7.4); the C-O bond distances supplied in Figure 7.6 may hold the key to explaining this. Whilst the C_2O_3 bond length (see Figure 7.6) calculated with MP2 remains comparable to those determined using density functional theory, the C_1O_1 bond length has increased by ~0.2 Å. The increase in bond length is more extreme for the CCSD calculation: the C_1-O_1 bond length has increased by ~0.9 Å and C_2O_3 bond length has increased by ~0.6 Å. This increase is significant as these new MP2 and CCSD structures are not transition states, a statement confirmed by the absence of imaginary frequencies.

The bond lengths for the MP3/6-31G(d) structure have been omitted from Figure 7.6 as the optimised structure differs greatly from that shown above. Whilst the other calculations all yielded the same structure (besides the expected slight variation in bond lengths, angles etc.) the MP3 optimised structure saw the O_3 unit rotated through ~90°, so that it sits perpendicularly across the $C_1=C_2$ bond (Figure 7.7). The lack of an imaginary frequency confirms that this is not a transition state structure.
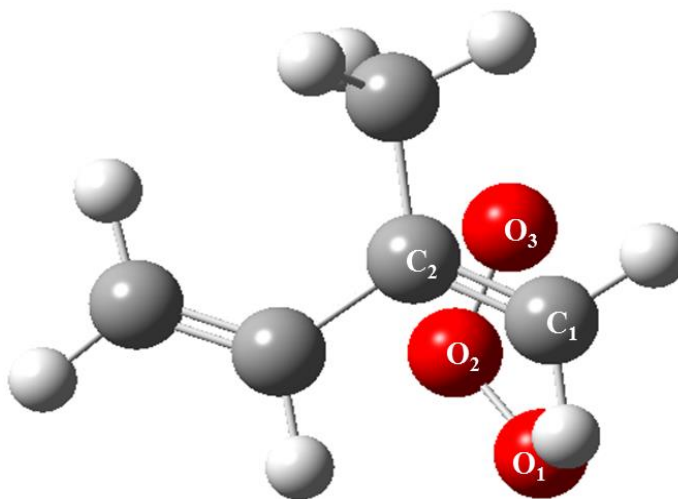
Figure 7.7: Geometry of the failed attempt to locate the O_3-isoprene addition transition state at the MP3/6-31G(d) level of theory

The recommendation of Lynch *et al.* in 2001 and Xu *et al.* in 2011 for the use of the MPW1K functional as an alternative to B3LYP to locate transition state structures appears well founded.[28, 31] Testing the stability of the wavefunction when using the MPW1K functional confirmed this recommendation to be true. Table 7.4 shows that MPW1K yields a positive activation energy for the addition of ozone to isoprene, without the need for unrestricted geometry optimisation calculations for ozone, making this a far more accurate calculation than B3LYP. It also shows that the difference between the use of the MPW1K functional and the unrestricted B3LYP functional for the addition of ozone is negligible.

7.4 Terpinolene Ozonolysis

7.4.1 Structure and Reactivity of Terpinolene

Terpinolene ($C_{10}H_{16}$) is a doubly unsaturated cyclic monoterpene[41] for which only a single conformer can be identified (Figure 7.8). By considering the structure of cyclohexene, the basic foundation of the terpinolene (also known as δ-terpinene) structure

is a half-chair conformation in order to reduce the steric hindrance of the methylene H.[42] It is therefore of little surprise to discover that there is no symmetry in the terpinolene structure. The internal double bond, results in the 6-membered ring forming the chair (rather than boat) conformation, causing the external double bond of terpinolene to bend out of the plane of the ring (Figure 7.8).
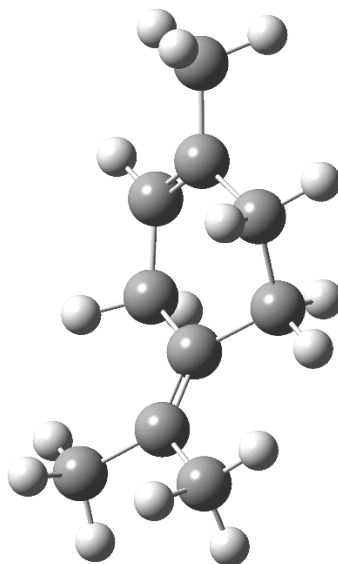

Figure 7.8: Optimised structure of the cyclic monoterpene terpinolene at the B3LYP/6-31++G(d,p) level of theory

With the ambition to study the mechanism for the ozonolysis of terpinolene [1-methyl-4-(1-methylethylidene)-cyclohexene] it is important to decipher at which of the two unsaturated bonds the initial attack of O_3 is more likely to occur. It is widely agreed that the more substituted exocyclic $C_1=C_2$ double bond is more reactive than the endocyclic $C_3=C_4$ double bond.[1, 12, 43-48] By comparing the ozonolysis rate constants of the two double bonds Harrison and Wells[46] were able to support this consensus, citing the rate constant for reaction at the $C_1=C_2$ bond as 120×10^{-17} cm^3 molecule^{-1} s^{-1}, which is about triple that of 43×10^{-17} cm^3 molecule^{-1} s^{-1} calculated for the $C_3=C_4$ bond.

The unreactivity of the endocyclic double bond in all cyclic monoterpenes is subject to the conformational constraints due to the two sp^2 hybridised carbons present in the six-membered ring. By adding a solitary C=C double bond into a cyclohexane ring, the chair conformation becomes flattened resulting in a half-chair conformation of cyclohexene. Further addition of a methyl substituent onto one of these sp^2 hybridised carbon atoms, as in terpinolene, induces further steric hindrance or an alteration of the frontier orbitals such that the overlap with ozone orbitals is compromised.[1] Ideally for the successful

addition of ozone to a double bond the lowest unoccupied molecular orbital (LUMO) of ozone must overlap with the highest occupied molecular orbital (HOMO) of terpinolene.[43] Vereecken and Francisco offered an additional insight into the reduced reactivity of the endocyclic double bond; ozonolysis of the endocyclic double bond does not yield a stabilised Criegee intermediate as the carbonyl product and Criegee intermediate remain joined together.[51]

Of the three main atmospheric oxidants terpinolene shows a higher reactivity towards ozone[5], with rate constants measured as: 190×10^{-17} cm^3 molecules^{-1} s^{-1},[9, 52] $1290 \pm 360 \times 10^{-18}$ cm^3 molecules^{-1} s^{-1} [1] and 1880×10^{-18} cm^3 molecule^{-1} s^{-1}.[2, 51] These ozonolysis rate constants are orders of magnitude lower than those stated for reaction with OH radicals (225×10^{-12} cm^3 molecules^{-1} s^{-1} [9, 11, 12] and 22.5×10^{-11} cm^3 molecules^{-1} s^{-1} [2]) and with NO$_3$ radicals (9.7×10^{-11} cm^3 molecules^{-1} s^{-1} [7, 16] and 9620×10^{-14} cm^3 molecules^{-1} s^{-1}).[2]

The shorter lifetime of terpinolene of around 0.26 hours (with respect to ozone),[1, 23] is thought to be partially attributed to the fact that acetone is directly formed through the oxidation of the exocyclic double bond.[23, 44] Along with acetone the unsaturated ketone 4-methyl-3-cyclohexenen-1-one is also produced.[2, 23, 43] Due to the unsaturated nature of this product, there is the potential for a further oxidation process to occur; the ozonolysis of the endocyclic double bond present in 4-methyl-3-cyclohexene-1-one has a measured rate constant of 7×10^{-17} cm^3 molecule^{-1} s^{-1}, causing a rapid reaction that could result in some unexpected products for the terpinolene system.[23, 46]

With respect to clarifying the mechanism for terpinolene ozonolysis it has been suggested that the addition of ozone to the exocyclic double bond should produce a mechanism that resembles that constructed Nguyen *et al.* in 2009 whilst investigating *β*-pinene ozonolysis.[13] Alternatively, ozonolysis at the endocyclic double bond, believed to only contribute ~1% of the ozonolysis reaction[1] should produce a mechanism that resembles that constructed by Zhang and Zhang in 2005 whilst investigating the ozonolysis of *α*-pinene.[8]

7.4.2 Biogenic Emissions of Terpinolene

Global emissions of volatile C$_{10}$ monoterpenes have been estimated at approximately 140 MT yr^{-1},[3] and whilst terpinolene emissions may not be the most prominent in the

atmosphere,[23] when compared to other C_{10} terpenes such as *α*- and *β*-pinene and 3-carene,[45] due to its multiple biogenic sources it is still considered an important compound in relation to atmospheric chemistry. Biogenic sources, in which terpinolene emissions are at their greatest (> 5% of the total emission) include *Liriodendron tulipifera* (tulip tree) the *Carya* species (Hickory), and *Cornus florida* (flowering dogwood). Terpinolene is emitted to a lesser extent (< 2% of the total emission) from *Pseudot-suga menziesii* (Douglas fir) and a few *Pinus* species, such as *Pinus banksiana* (Jack pine), *P. sylvestris* (Scots pine)[54] and *Dacrydium colensoi* (New Zealand silver pine).[55] Emission rates of terpinolene have been recorded from *Pinus taeda* (lob lolly pine) and *Pinus Virginia* (Virginia pine) as 8.5 ng C g^{-1} h^{-1} and 21 ng C g^{-1} h^{-1} respectively.[56]

As well as direct emission, terpinolene can also be found in the essential oils of North American *Picea* species,[54] *melaleuca alternifolia* (narrow-leaved paperbark), *melaleuca trichostachya* (small tree myrtaceae family), *manila elemi* (manila elemi gum) and *Nectranda elaiophora*.[55] Terpinolene is also the main active component in *Microtoena patchoulii* (*Labiatae*, perennial herb).[41]

7.4.3 Uses of Terpinolene

As with many other terpenes that are extracted from plants, vegetables, herbs, spices and fruits, terpinolene is used in a variety of domestic products, to flavour food and beverages, to enhance perfumes,[55] air fresheners and cleaners.[45, 46] Besides these domestic uses the broad spectrum of biological activity of terpinolene is being exploited; due to its antioxidant properties[57] the medical sector use of terpinolene as an anticancer[58] treatment is being thoroughly investigated. As well as a conventional medicine, terpinolene is used in aromatic traditional medicines – whilst terpinolene itself has yet to be fully investigated it is believed the evaporability of the constituents maybe important to its pharmacological activity,[41] particularly with respect to how the constituents interact with nasal receptors. Not only useful for the treatment of humans, terpinolene's antifungal[59] and larvacidal[60] properties could be useful in the plant kingdom and is an avenue yet to be fully explored.

7.4.4 Previous Works on Terpinolene

7.4.4.1 Spectroscopic Investigations

Varieties of experimental studies have been carried out and published probing the oxidation of terpinolene. The majority of these works use similar, if not the same,

analytical techniques to monitor the ozonolysis products. Proton-transfer-reaction mass spectrometry (PTR-MS) has been used by Herrmann *et al.* to measure OH yields from the ozonolysis of both of terpinolene's double bonds[44] whilst Lee *et al.*'s chamber study uses the same technique to focus on the secondary organic aerosol (SOA) yields from gas-phase products of terpinolene photooxidation.[23]

Other studies incorporate an element of chromatography into their product analysis, the most popular being gas chromatography-mass spectrometry (GC-MS). Ma and Marston uses this technique to follow the Criegee mechanism[25] and analyse the organic acid formation from the ozonolysis reaction with gas chromatography with a flame ionization detection (GC-FID).[45] The GC-MS results enabled the creating of a potential mechanism for the formation of the carboxylic acid products from the ozonolysis of terpinolene as seen in Figure 7.9. This study became the building block for Stewart *et al.* investigation, which using the same setup monitored the kinetics of the gas phase reaction between monoterpenes and both O_3 and NO_3 radicals.[1]

Accompanying these techniques other groups have chosen Fourier transform infrared spectroscopy (FTIR) to assist with the analysis of their investigations. Koch *et al.* explored the formation of new particles in monoterpene ozonolysis,[47] whilst Hakola *et al.* aimed to quantify the gas-phase product formation when terpinolene was oxidised with O_3 and OH radicals.[48] Harrison and Well, however, decided to take an altogether different approach; rather than the more common techniques mentioned above this investigation utilised a denuder and filter apparatus, enabling the group to separate the aerosols from the gases, to investigate the reaction between terpinolene with both O_3 and NO_3.[46]
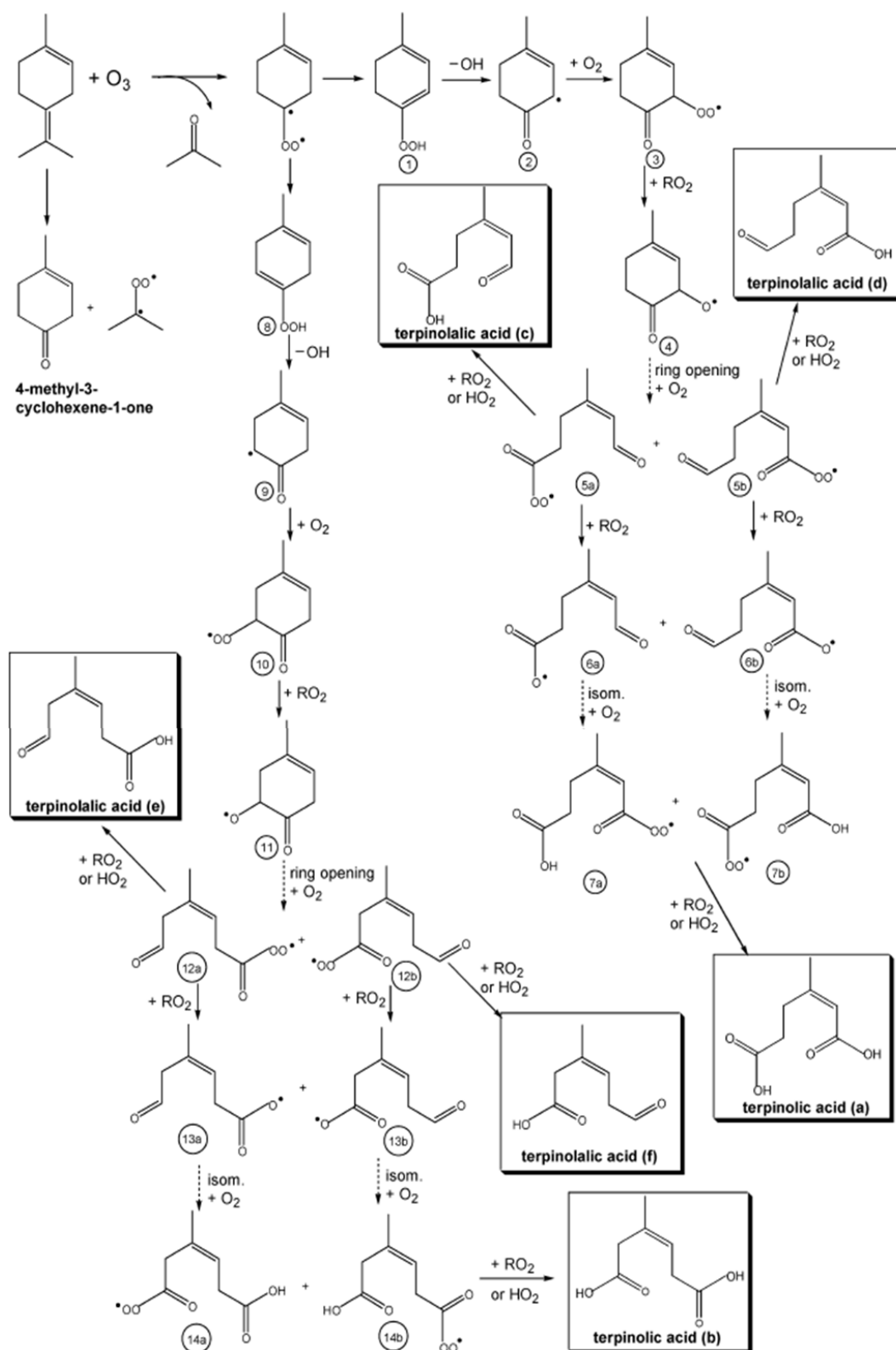
Figure 7.9: Scheme 4 taken from Ma and Marston 2009 depicting the possible mechanism for the formation of carboxylic acids identified from the ozonolysis of terpinolene[45]

7.4.4.2. Theoretical Investigations

Terpinolene ozonolysis has briefly been studied at the BPW91/6-31G(d) and B3LYP/6-31G(d) levels of theory; rather than examining the full ozonolysis mechanism as is the ambition of this investigation the study by Ayadi and Abderrabba was focusing on the reactivity of the two double bonds present in three different terpenes, which included terpinolene.[43] This investigation solely focuses on the initial oxidation process and so did not go further than the production of 4-methyl-3-cyclohexene-1-one for the ozonolysis of the exocyclic unsaturated carbon bond.
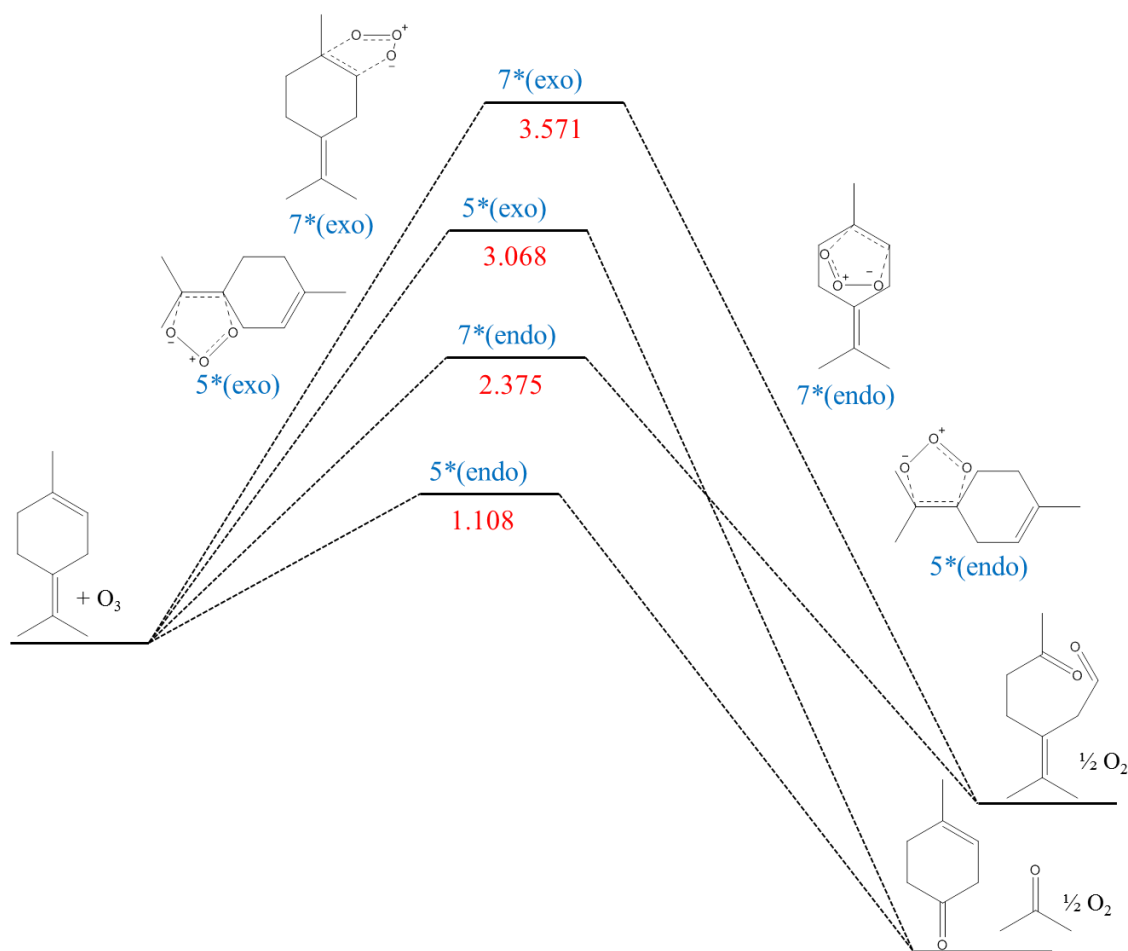
Figure 7.10: Figure 4 taken from Ayadi and Abderrabba 2011, the energetic profile of terpinolene ozonolysis, calculated at the B3LYP/6-31G(*d*) level of theory (energy in kcal mol^{-1})[43]

As Figure 7.10 shows besides bypassing the primary ozonide (POZ) and the transition states that lead on from this, the authors state the products expected from ozonolysis of the external double bond are 4-methyl-3-cyclohexene-1-one, acetone and ½O$_2$. Other literature investigating the ozonolysis of isoprene,[26] camphene,[61] sabinene[62] and β-

caryophyllene;[14, 63] however, do not agree with this outcome and instead propose two different reaction pathways: the first producing a Criegee intermediate and a ketone, whilst the second results in a carbonyl and a radical (Figure 7.11). For terpinolene ozonolysis this carbonyl is the aforementioned 4-methyl-3-cyclohexene-1-one, which was not only observed in Ma and Marston's GC-MS study[45] but also in the chamber study conducted by Lee *et al.* with recorded yields of $53 \pm 9\%$.[64] Ayadi and Abderrabba provide no explanation as to why their study should yield different results from the perceived norm, so the aim of this investigation is to pursue both avenues in order to establish the correct pathway.
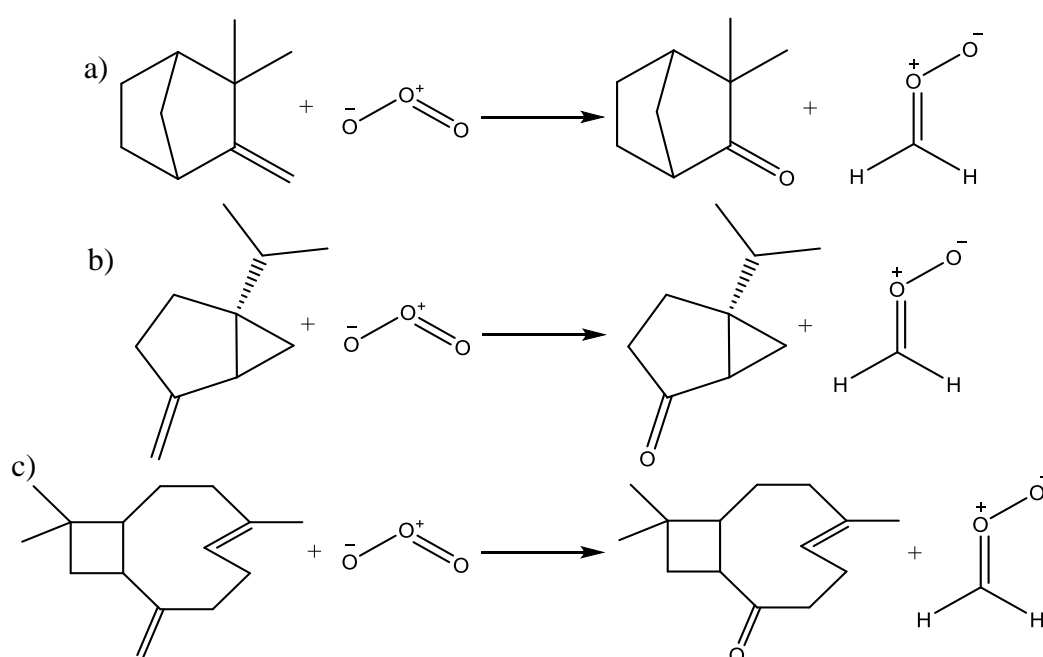
Figure 7.11: Ozonolysis process producing a ketone product and a Criegee intermediate for a) camphene, b) sabinene and c) β-caryophyllene

7.5 Conclusions

Recreation of the ozonolysis of α-pinene mechanism at the B3LYP/6-31++G(d,p) level of theory confirmed that such computational calculations would be suitable to investigate the ozonolysis of terpinolene. This examination highlighted the well documented flaw in the use of B3LYP for such an investigation; its inability to describe ozone as a singlet open-shell biradical leads to inaccurate determination of the entrance channel activation energy. Optimisation of the simpler O_3-isoprene system using various levels of theory showed that in order to accurately use B3LYP for such mechanistic investigations an unrestricted direction was required for the optimisation of ozone. The recommended

MPW1K functional provides an equally accurate activation barrier for O_3-isoprene addition, suggesting that MPW1K/6-31++G(d,p) is a suitable method to analyse the ozonolysis of terpinolene.

7.6 References

1.   D. J. Stewart, S. H. Almabrok, J. P. Lockhart, O. M. Mohamed, D. R. Nutt, C. Pfrang and G. Marston, *Atmospheric Environment*, 2013, **70**, 227-235.

2.   A. Calogirou, B. R. Larsen and D. Kotzias, *Atmospheric Environment*, 1999, **33**, 1423-1439.

3.   J. Peeters, L. Vereecken and G. Fantechi, *Physical Chemistry Chemical Physics*, 2001, **3**, 5489-5504.

4.   K. Kowalewski and T. Gierczak, *Journal of Chromatography A*, 2011, **1218**, 7264-7274.

5.   R. Winterhalter, R. Van Dingenen, B. R. Larsen, N. R. Jensen and J. Hjorth, *Atmospheric Chemistry and Physics Discussions*, 2003, **3**, 1-39.

6.   Y. Ma, A. T. Russell and G. Marston, *Physical Chemistry Chemical Physics*, 2008, **10**, 4294-4312.

7.   J. Zhao and R. Zhang, in *Advances in Quantum Chemistry, Vol 55: Applications of Theoretical Methods to Atmospheric Science*, eds. J. R. Sabin and E. Brandas, 2008, vol. 55, pp. 177-213.

8.   D. Zhang and R. Zhang, *Journal of Chemical Physics*, 2005, **122**, 114308

9.   L. Q. Hao, P. Yli-Pirila, P. Tiitta, S. Romakkaniemi, P. Vaattovaara, M. K. Kajos, J. Rinne, J. Heijari, A. Kortelainen, P. Miettinen, J. H. Kroll, J. K. Holopainen, J. N. Smith, J. Joutsensaari, M. Kulmala, D. R. Worsnop and A. Laaksonen, *Atmospheric Chemistry and Physysics*, 2009, **9**, 8121-8137.

10.   J. S. Blanch, J. Llusia, U. Niinemets, S. M. Noe and J. Penuelas, *Journal of Environmental Biology*, 2011, **32**, 1-6.

11.   R. Atkinson, *Journal of Physical and Chemical Reference Data*, 1997, **26**, 215-290.

12.   R. Atkinson and J. Arey, *Chemical Reviews*, 2003, **103**, 4605-4638.

13.   T. L. Nguyen, J. Peeters and L. Vereecken, *Physical Chemistry Chemical Physics*, 2009, **11**, 5643-5656.

14.   T. L. Nguyen, R. Winterhalter, G. Moortgat, B. Kanawati, J. Peeters and L. Vereecken, *Physical Chemistry Chemical Physics*, 2009, **11**, 4173-4183.

15.   S. E. Wheeler, D. H. Ess and K. N. Houk, *Journal of Physical Chemistry A*, 2008, **112**, 1798-1807.

16. V.G. Khamaganov and R.A. Hites, *Journal of Physical Chemistry A*, 2001, **105**, 815-822

17. A. D. Becke, *Journal of Chemical Physics*, 1993, **98**, 5648-5652.

18. P. J. Stephens, F. J. Devlin, C. F. Chabalowski and M. J. Frisch, *Journal of Physical Chemistry*, 1994, **98**, 11623-11627.

19. Harihara.Pc and J. A. Pople, *Theoretica Chimica Acta*, 1973, **28**, 213-222.

20. M. J. Frisch, G. W. Trucks, H. B. Schlegel, G. E. Scuseria, M. A. Robb, J. R. Cheeseman, J. A. M. Jr., T. Vreven, K. N. Kudin, J. C. Burant, J. M. Millam, S. S. Iyengar, J. Tomasi, V. Barone, B. Mennucci, M. Cossi, G. Scalmani, N. Rega, G. A. Petersson, H. Nakatsuji, M. Hada, M. Ehara, K. Toyota, R. Fukuda, J. Hasegawa, M. Ishida, T. Nakajima, Y. Honda, O. Kitao, H. Nakai, M. Klene, X. Li, J. E. Knox, H. P. Hratchian, J. B. Cross, V. Bakken, C. Adamo, J. Jaramillo, R. Gomperts, R. E. Stratmann, O. Yazyev, A. J. Austin, R. Cammi, C. Pomelli, J. W. Ochterski, P. Y. Ayala, K. Morokuma, G. A. Voth, P. Salvador, J. J. Dannenberg, V. G. Zakrzewski, S. Dapprich, A. D. Daniels, M. C. Strain, O. Farkas, D. K. Malick, A. D. Rabuck, K. Raghavachari, J. B. Foresman, J. V. Ortiz, Q. Cui, A. G. Baboul, S. Clifford, J. Cioslowski, B. B. Stefanov, G. Liu, A. Liashenko, P. Piskorz, I. Komaromi, R. L. Martin, D. J. Fox, T. Keith, M. A. Al-Laham, C. Y. Peng, A. Nanayakkara, M. Challacombe, P. M. W. Gill, B. Johnson, W. Chen, M. W. Wong, C. Gonzalez and J. A. Pople, Gaussian, Inc., Wallingford CT, 2004, vol. Revision E.01.

21. GaussView, Version 5, R. Dennington, T. Keith, and J. Millam, *Semichem Inc.*, Shawnee Mission, KS, 2009.

22. J. Peeters, T. L. Nguyen and L. Vereecken, *Physical Chemistry Chemical Physics*, 2009, **11**, 5935-5939.

23. A. Lee, A. H. Goldstein, J. H. Kroll, N. L. Ng, V. Varutbangkul, R. C. Flagan and J. H. Seinfeld, *Journal of Geophysical Research-Atmospheres*, 2006, **111**.

24. D. Zhang and R. Y. Zhang, *Journal of the American Chemical Society*, 2002, **124**, 2692-2703.

25. R. Criegee, *Angew Chemie-International Edition in English*, 1975, **14**, 745-752.

26. R. Gutbrod, E. Kraka, R. N. Schindler and D. Cremer, *Journal of the American Chemical Society*, 1997, **119**, 7330-7342.

27. B. J. Lynch and D. G. Truhlar, *Journal of Physical Chemistry A*, 2001, **105**, 2936-2941.

28. X. F. Xu, I. M. Alecu and D. G. Truhlar, *Journal of Chemical Theory and Computation*, 2011, **7**, 1667-1676.

29. C. E. Check and T. M. Gilbert, *Journal of Organic Chemistry*, 2005, **70**, 9828-9834.

30. S. Grimme, M. Steinmetz and M. Korth, *Journal of Organic Chemistry*, 2007, **72**, 2118-2126.

31. B. J. Lynch, P. L. Fast, M. Harris and D. G. Truhlar, *Journal of Physical Chemistry A*, 2000, **104**, 4811-4815.

32. C. Møller and M. S. Plesset, *Physical Review*, 1934, **46**, 618-622.

33. K. Raghavachari, G. W. Trucks, J. A. Pople and M. Headgordon, *Chemical Physics Letters*, 1989, **157**, 479-483.

34. R. Krishnan, J. S. Binkley, R. Seeger and J. A. Pople, *Journal of Chemical Physics*, 1980, **72**, 650-654.

35. J. Cizek, *Advances in Chemical Physics*, 1969, **14**, 35-88.

36. G. D. Purvis and R. J. Bartlett, *Journal of Chemical Physics*, 1982, **76**, 1910-1918.

37. G. E. Scuseria, C. L. Janssen and H. F. Schaefer, *Journal of Chemical Physics*, 1988, **89**, 7382-7387.

38. G. E. Scuseria and H. F. Schaefer, *Journal of Chemical Physics*, 1989, **90**, 3700-3703.

39. J. A. Pople, R. Seeger and R. Krishnan, *International Journal of Quantum Chemistry*, 1977, **11**, 149-161.

40. J. A. Pople, J. S. Binkley and R. Seeger, *International Journal of Quantum Chemistry*, 1976, 1-19.

41. K. Ito and M. Ito, *Journal of Natural Medicines*, 2013, **67**, 833-837.

42. S. Saebo and J. E. Boggs, *Journal of Molecular Structure*, 1981, **73**, 137-144.

43. S. Ayadi and M. Abderrabba, *Canadian Journal of Chemistry-Revue Canadienne De Chimie*, 2011, **89**, 703-708.

44. F. Herrmann, R. Winterhalter, G. K. Moortgat and J. Williams, *Atmospheric Environment*, 2010, **44**, 3458-3464.

45. Y. Ma and G. Marston, *Physical Chemistry Chemical Physics*, 2009, **11**, 4198-4209.

46. J. C. Harrison and J. R. Wells, *Atmospheric Environment*, 2013, **80**, 524-532.

47. S. Koch, R. Winterhalter, E. Uherek, A. Kolloff, P. Neeb and G. K. Moortgat, *Atmospheric Environment*, 2000, **34**, 4031-4042.

48. H. Hakola, J. Arey, S. M. Aschmann and R. Atkinson, *Journal of Atmospheric Chemistry*, 1994, **18**, 75-102.

49. S. Grimme, *Angewandte Chemie (International Edition)*, 2006, **45**, 44600-4464.

50. P. C. Redfern, P. Zapol, L. A. Curtiss, K. J. Raghavachari, *Journal of Physical Chemistry A*, 2000, **104**, 5850-5854.

51. L. Vereecken and J. S. Francisco, *Chemical Society Reviews*, 2012, **41**, 6259-6293.

52. R. Atkinson and J. Arey, *Atmospheric Environment*, 2003, **37**, S197-S219.

53. Y. H. Shu, E. S. C. Kwok, E. C. Tuazon, R. Atkinson and J. Arey, *Environmental Science and Technology*, 1997, **31**, 896-904.

54. C. Geron, R. Rasmussen, R. R. Arnts and A. Guenther, *Atmospheric Environment*, 2000, **34**, 1761-1781.

55. E. Aydin, H. Turkez and S. Tasdemir, *Arhiv Za Higijenu Rada I Toksikologiju*, 2013, **64**, 415-424.

56. C. D. Geron and R. R. Arnts, *Atmospheric Environment*, 2010, **44**, 4240-4251.

57. H. J. D. Dorman, A. C. Figueiredo, J. G. Barroso and S. G. Deans, *Flavour and Fragrance Journal*, 2000, **15**, 12-16.

58. T. Harada, E. Harada, R. Sakamoto, T. Ashitani and K. Fujita, *American Journal of Plant Science*, 2012, **3**, 268-275.

59. K. A. Hammer, C. F. Carson and T. V. Riley, *Journal of Antimicrobial Chemotherapy*, 2004, **53**, 1081-1085.

60. B. Conti, G. Benelli, G. Flamini, P. L. Cioni, R. Profeti, L. Ceccarini, M. Macchia and A. Canale, *Parasitology Research*, 2012, **110**, 2013-2021.

61. R. C. D. Oliveira and G. F. Bauerfeldt, *Journal of Chemical Physics*, 2012, **137**, 134306.

62. Y. Zhao, R. X. Zhang, H. Wang, M. X. He, X. M. Sun, Q. Z. Zhang, W. X. Wang and M. Y. Ru, *Journal of Molecular Structure:Theochem*, 2010, **942**, 32-37.

63. Y. Zhao, R. X. Zhang, X. M. Sun, M. X. He, H. Wang, Q. Z. Zhang and M. Y. Ru, *Journal of Molecular Structure:Theochem*, 2010, **947**, 68-75.

64. A. Lee, A. H. Goldstein, M. D. Keywood, S. Gao, V. Varutbangkul, R. Bahreini, N. L. Ng, R. C. Flagan and J. H. Seinfeld, *Journal of Geophysical Research-Atmospheres*, 2006, **111**.

Chapter Eight

Theoretical Investigation of Terpinolene Ozonolysis: Current Calculations

8.1 Computational Details

Due to the commonality of the method for theoretical terpene ozonolysis investigations, the DFT-B3LYP[1, 2] hybrid functional was used to portray this potential energy surface (PES). Energy minima were optimised with the 6-31++G(d,p)[3] basis set and all frequency calculations were conducted at the same level of theory, with tight optimisation and SCF convergence and an ultrafine pruning grid, using the Gaussian 03 software package.[4] Due to the common defect of the B3LYP functional, which has been described previously, the PES was also described with the hybrid Hartree-Fock-density functional MPW1K[5], used with the 6-31++G(d,p) basis set.

Transition states were searched for using either the quadratic synchronous transit (QST2)[6, 7], which uses the optimised geometries of the reactants and products in order to locate the transition state or the synchronous transit-guided quasi-Newton approach (QST3)[7, 8] which also requires an initial guess for the transition state structure. Both methods were conducted using B3LYP with the 6-31G(d,p)[3] basis set. Geometry optimisation and harmonic frequency calculations were performed using both the B3LYP and MPW1K functionals with the 6-31++G(d,p) basis set; transition state structures were identified by the presence of a single imaginary frequency. Transition state structures were confirmed through visualisation of the transitional mode, affirming that the imaginary frequency corresponds to the position within the molecule where a given reaction step is occurring, as well as intrinsic reaction coordinate (IRC)[9, 10] calculations. IRC calculations, performed here at the B3LYP/6-31++G(d,p) level of theory, are capable of validating transition state structures by producing a smooth connection between the transition state and both the reactants and products.

All energies were refined using single point energy calculations with the MPW1K functional with the extended 6-311++G(3df,3pd) basis set.[11] This basis set was chosen due to its successful use in the corresponding calculations in the theoretical investigation of the ozonolysis of β-caryophyllene.[12] All optimised structures were visualised using GaussView 5.0.[13]

8.2 Results and Discussion

8.2.1 Oxidation reaction between terpinolene and ozone

Potential energy surface (PES) scans, conducted at the B3LYP/6-31G(d,p) level of theory, were used to verify the optimised geometry of terpinolene; rotation of each of the methyl groups confirmed that the lowest energy structure had been located. The initial step for the ozonolysis of terpinolene is the addition of ozone to either of the two unsaturated C=C bonds. As mentioned in Chapter 7 the B3LYP functional struggles to show ozone as a singlet open-shell biradical, making accurate entrance channel transition state structures difficult to locate as was the case in previous studies.[14, 15] A variety of calculations were carried out with the B3LYP functional in order to ascertain the most appropriate method; whilst calculating ozone as a singlet yields greater stability than assuming it is a triplet structure, not until the unrestricted form of B3LYP was utilised was an accurate activation energy barrier established.

Whilst it has been widely agreed that the exocyclic $C_3=C_4$ double bond is more reactive[16-23] than the endocyclic $C_1=C_2$ double bond, the geometry optimisation calculations at both B3LYP and MPW1K with the 6-31++G(d,p) basis set seem to dispute this (Figure 8.1).

Initial optimisation calculations suggest that the reaction is more likely to proceed at the $C_1=C_2$ double bond due to the lower activation energy of transition state (Ts) 2 in comparison to Ts 3, which occurs via reaction at $C_3=C_4$. However, these results cannot be considered conclusive due to the slight differences in activation energy between Ts 2 and Ts 3; using B3LYP the discrepancy is 0.4 kJ mol^{-1}, whilst using MPW1K the difference is only 0.25 kJ mol^{-1}. When the energies were refined with the extended 6-311++G(3df,3pd) basis set, the calculated activation energies follow the expected trend. Extended basis set with additional polarization functions have previously been deemed essential to obtain accurate energetics for primary ozonide structures (POZ)[24-28]; the results of these initial calculations support these findings. Single point energy calculations suggest that the ozonolysis of terpinolene would progress via Ts 3, as it has the lower activation energy. As a result all other structure determined in this thesis originate from the entrance channel, progressing via Ts 3.
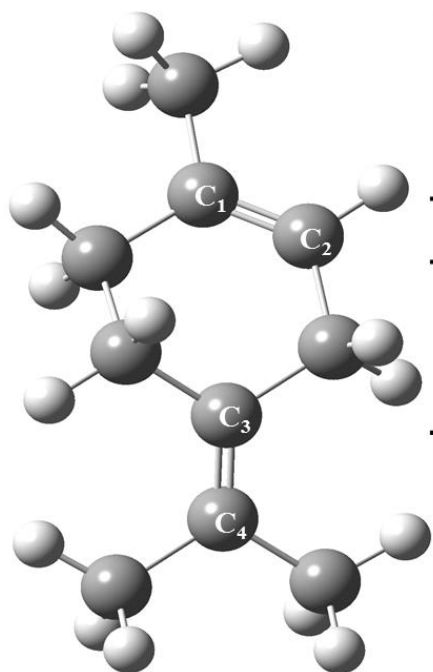
Transition State	B3LYP/ 6-31++G(*d,p*)	MPW1K/ 6-31++G(*d,p*)	MPW1K/ 6-311++G(*3df,3pd*)
Addition to $C_1=C_2$			
1	8.52	7.59	10.46
2	2.50	2.79	6.39
Addition to $C_3=C_4$			
3	2.91	3.04	5.19

Figure 8.1: Optimised geometry of terpinolene at the B3LYP/6-31++G(d,p) level of theory, including comparison of the activation energies (kJ mol^{-1}) for each of the three entrance channel transition states (Figure 8.2) at the B3LYP/6-31++G(d,p), MPW1K/6-31++G(d,p) and MPW1K/6-311++G(3df,3pd) levels of theory

Each of the transition state structures can be seen in Figure 8.2; each structure shows ozone bonding in an envelope formation, an observation previously noted during theoretical works on *α*- and *β*-pinene[15, 29] as well as isoprene[14]. The C-O distances for the endocyclic transition states are between 2.34 and 2.36 Å at the B3LYP/6-31++G(d,p) level of theory and between 2.25 and 2.34 Å at the MPW1K/6-31++G(d,p) level of theory. The C-O distances for the exocyclic transition state are between 2.57 and 2.64 Å at the B3LYP/6-31++G(d,p) level of theory and between 2.45 and 2.48 Å at the MPW1K/6-31++G(d,p) level of theory. Both Ts 1 and Ts 2 involve the reaction of O_3 at $C_1=C_2$, but Ts 1 is consistently gauged to have a much higher activation energy; the O_3-envelope formation in Ts 1 is bending back underneath the 6-membered carbon ring which would have increased steric hindrance in comparison to Ts 2 in which the O_3-envelope is pointing away from the ring.
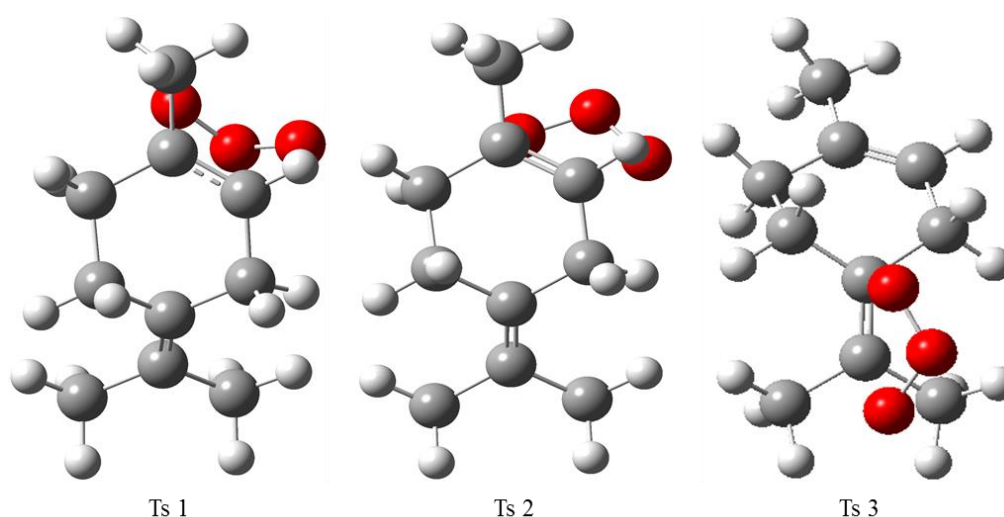
Figure 8.2: O$_3$-terpinolene addition transition state strutures, optimised at the B3LYP/6-31++G(d,p) level of theory

The POZ structures contain the same O$_3$ envelope configuration as the corresponding transition state; the O$_3$ bends back underneath the ring in both Ts 1 and the POZ 1, and away from the ring in both Ts 2 and POZ 2. The POZ decompose via the breakage of the C=C double bond and at least one of the O-O bonds. Ayadi and Abderrabba suggest that both POZ 1 and POZ 2 decompose into the same product[16]; however, Nguyen *et al.* suggests that these two POZ structures each create two different Criegee intermediates.[12] These four Criegee intermediates differ in structure depending on which O-O bond has broken, and the orientation of the remaining O-O bond and other functional groups (a methyl group in the case of terpinolene) in relation to the now broken ring.
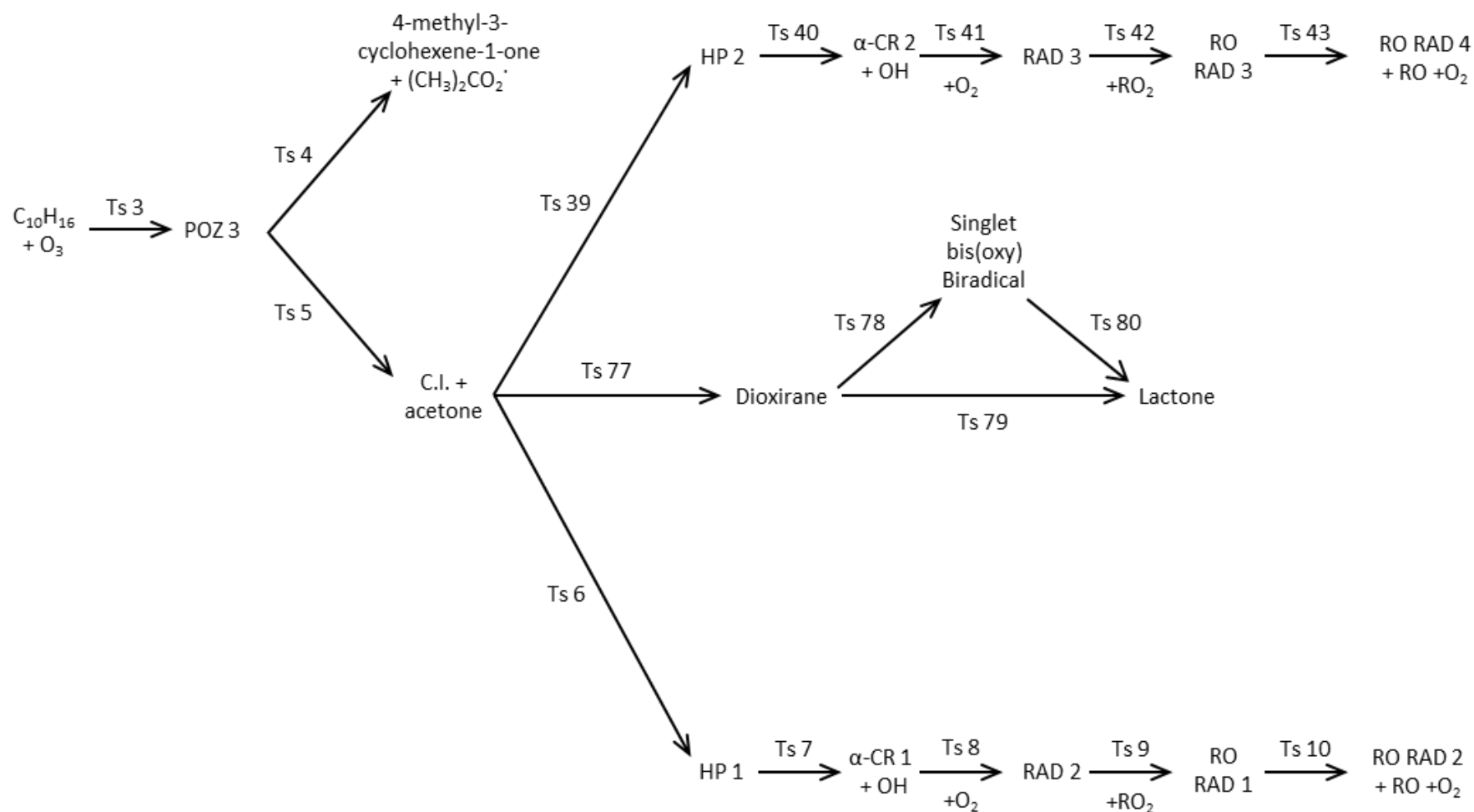
Figure 8.3: Flow chart showing the initial O_3-terpinolene addition, the subsequent decomposition of the primary ozonide and finally the hydroperoxide and ester decomposition channels of the Criegee intermediate (C.I)

Figure 8.3 shows a flow chart for the initial stages of the terpinolene ozonolysis reaction, via the lowest energy entrance channel transition state, Ts 3. After the initial ozone addition step the primary ozonide decomposes via 2 different routes: either forming 4-methyl-3-cyclohexene-1-one (Figure 8.4a) and a $(CH_3)_2CO_2 \cdot$ radical, or a Criegee intermediate (C.I.) (Figure 8.4b) and acetone. The Criegee intermediate can then either decompose via the hydroperoxide or ester channel.
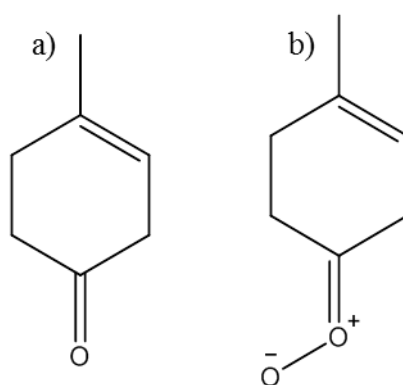
Figure 8.4: Skeletal structures of a) 4-methyl-3-cyclohexene-1-one and b) the Criegee intermediate

8.2.2 Decomposition of the Criegee intermediate

There are two equivalent hydroperoxide channels through which the Criegee intermediate can decompose, which begin via either Ts 6 or Ts 39. The slight structural difference in these channels is dependent on which side of the C=O a H is removed from the ring, during the initial decomposition step of the Criegee intermediate into either hydroperoxide (HP) 1 or 2 (Figure 8.5).
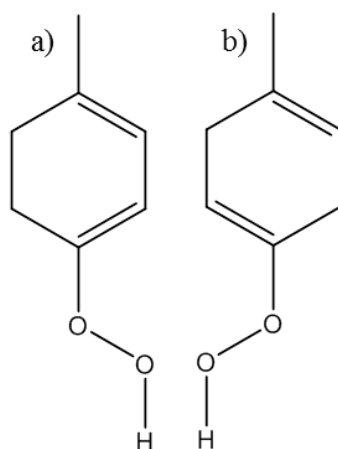
Figure 8.5: Skeletal structures of a) HP 1 (via Ts 6) and b) HP 2 (via Ts 39) for the initial decomposition step of the Criegee intermediate

The reaction via Ts 6 (Figure 8.6a) is expected to be favoured over Ts 39 due to the lower activation energy of this process using both B3LYP and MPW1K with the 6-31++G(d,p) basis set. Unfortunately this trend isn't maintained for the single point energy calculations which suggest that Ts 39 possesses the lower reaction barrier (as seen in Table 8.1 at the MPW1K/6-311++G(3df,3pd) level of theory), however, with an energy discrepancy of ~0.3 kJ mol^{-1} this opposing trend cannot be deemed conclusive.
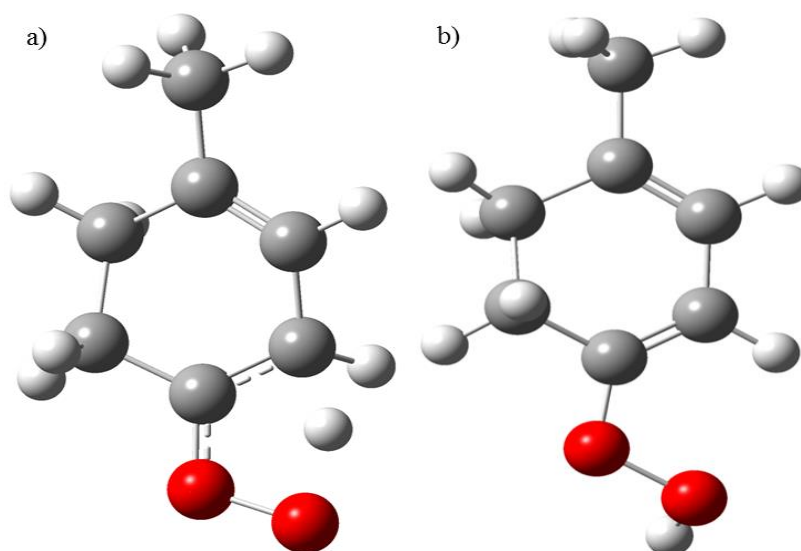
Figure 8.6: Structures of a) Ts 6 and b) HP 1, optimised at the B3LYP/6-31++G(d,p) level of theory

8.2.2.1 Hydroperoxide channel for terpinolene ozonolysis

The decomposition of hydroperoxide 1 (HP1) is shown in Figure 8.7.
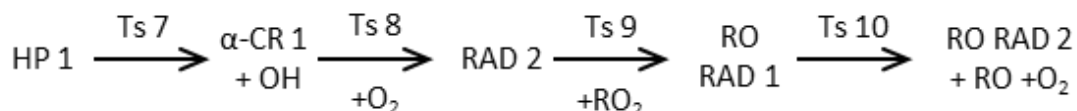
Figure 8.7: Flow chart showing the hydroperoxide channel from the hydroperoxide (HP1) to the RO radical (RO RAD 2)

This HP structure then undergoes the loss of OH, via Ts 7 yielding an α-carbonyl radical (α-CR). This loss of OH places a radical on the carbon-ring at the α-position in relation to the C=O bond (Figure 8.8). Whilst an increase is energy is indicative of reaching a transition state structure, a decrease in energy is expected between consecutive minima; α-CR 1 is ~5 kJ mol^{-1} more stable than HP 1 at the B3LYP/6-31++G(d,p) level of theory.

220

In contrast, α-CR 2 (formed in the equivalent process) is ~41 kJ mol^{-1} less stable than HP 2, a result that should not be deemed erroneous as the analogous process (HP → RAD-1) in the β-pinene ozonolysis study by Nguyen *et al.* also shows an increase in energy.[29]
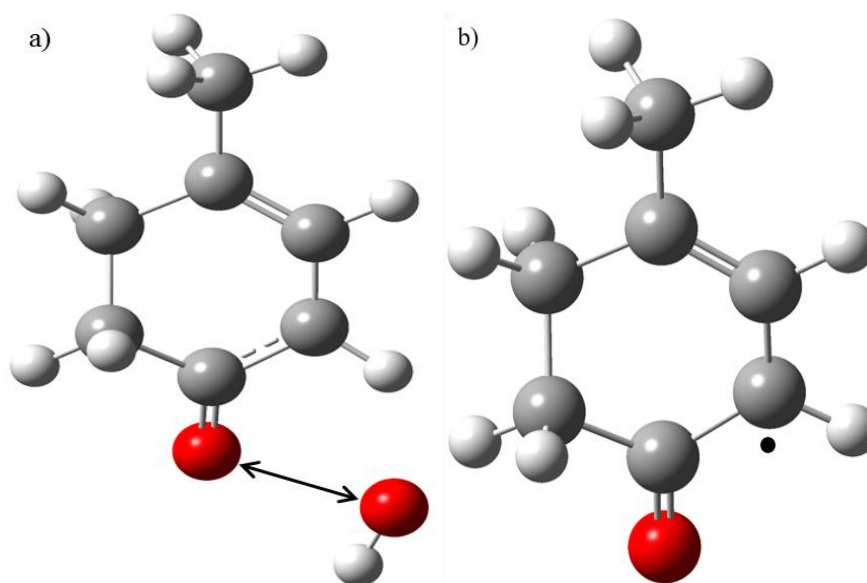

Figure 8.8: Structures of a) Ts 7 and b) α-CR 1, optimised at the B3LYP/6-31++G(d,p) level of theory. The arrow depicts the vibration of the imaginary frequency

Transition state 7 was confirmed for the OH loss process through visualisation of the imaginary transitional mode, which is portrayed by the black arrow in Figure 8.8a.
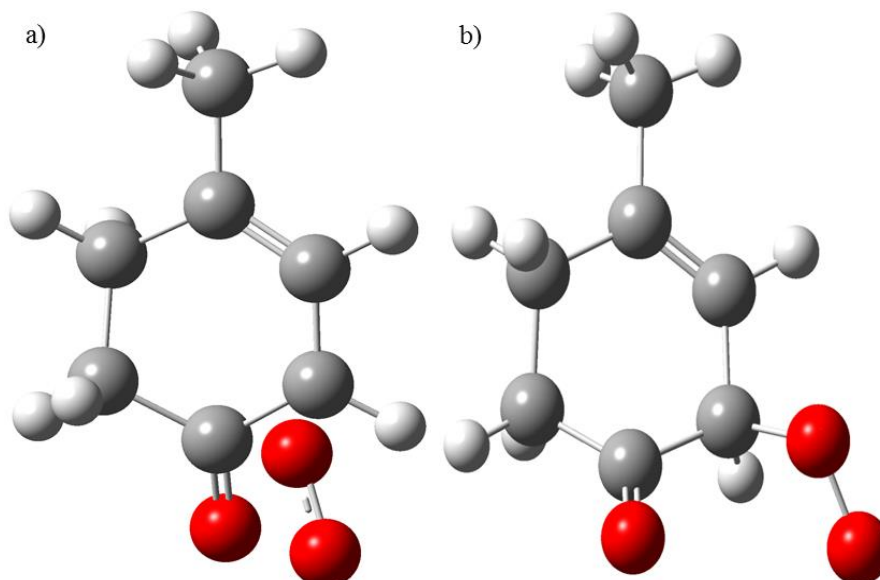
Figure 8.9: Structures of a) Ts 8 and b) RAD 2, optimised at the B3LYP/6-31++G(d,p) level of theory

The α-CR 1 structure (formed via Ts 7) subsequently undergoes the addition of O_2, via Ts 8 yielding a radical species (RAD 2) as seen in Figure 8.9. This radical structure subsequently undergoes the addition of RO_2 (where $R=CH_3$) via Ts 9 yielding a RO radical species (RO RAD 1). This RO radical then decomposes via Ts 10 to form RO RAD 2 accompanied by the loss of O_2 and RO (Figure 8.10).
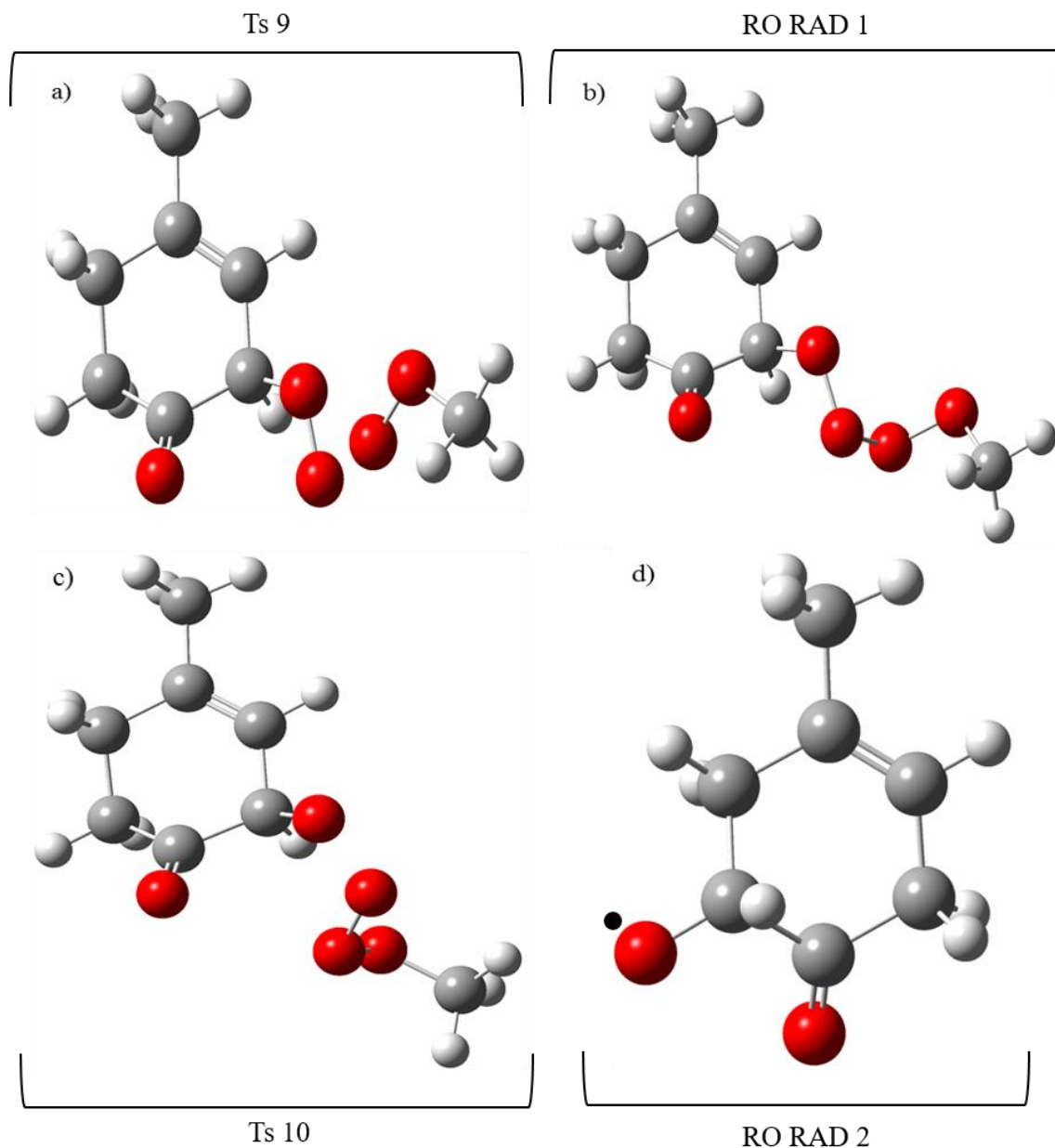
Figure 8.10: Structures of a) Ts 9, b) RO RAD 1, c) Ts 10 and d) RO RAD 2 optimised at the B3LYP/6-31++G(d,p) level of theory

The activation energies for each of the transition states 7-10 (and the corresponding transition states 40-43 from the other hydroperoxide channel) calculated at three different levels of theory are listed in Table 8.1.

Table 8.1: O$_3$-terpinolene addition and Criegee intermediate decomposition activation energies with zero-point correction included (kJ mol^{-1})

Transition State	B3LYP/ 6-31++G(d,p)	MPW1K/ 6-31++G(d,p)	MPW1K/ 6-311++G(3df,3pd)
3	2.91	3.04	5.19
4	60.41	112.67	118.66
5	56.54	108.49	114.66
6	63.86	63.51	71.79
7	89.09	126.22	146.71
8	25.09		
9	92.43	177.31	177.80
10	28.51		
39	65.21	64.52	71.51
40	145.83	221.87	244.92
41	6.84	60.93	69.77
42	10.99	183.79	182.52
43	14.63		
77	100.74	104.66	108.06
78	147.42	211.21	231.84
79	119.14	165.06	178.37
80	-126.49	-67.51	-256.72

8.2.2.2 Ester channel for terpinolene ozonolysis

The decomposition of Criegee intermediate (C.I.) via the ester channel is shown in Figure 8.11.
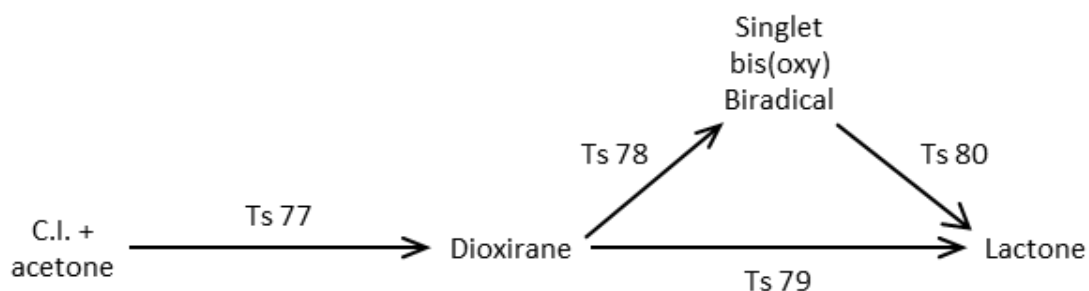
Figure 8.11: Flow chart showing the ester channel from the Criegee intermediate (C.I.) to the lactone

Whilst Ma and Marston's GC-MS study[18] grants a useful guide via the hydroperoxide channels to the carboxylic acid products, it fails to consider the ester channel as Nguyen *et al.* did for *β*-pinene[29], a terpene also possessing a exocyclic C=C double bond. The ester channel begins with the formation of a dioxirane, via Ts 77, which is ~66 kJ mol^{-1} more stable than the Criegee intermediate. The dioxirane then undergoes O-O bond cleavage via Ts 78 to form a singlet bis(oxy) biradical (SB) (Figure 8.12). The dioxirane is also more stable than the SB by ~30 kJ mol^{-1}, an observation also made by Nguyen *et al*.
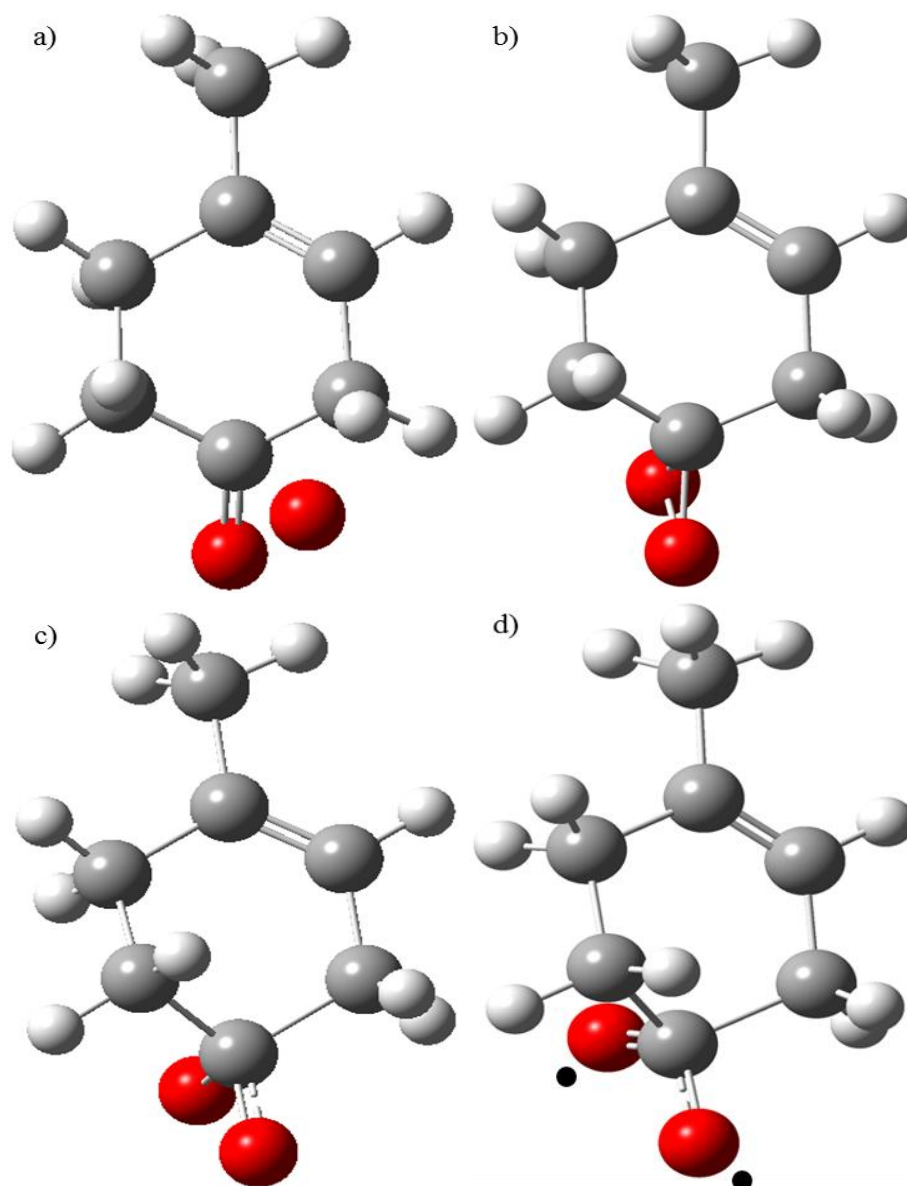
Figure 8.12: Structures of a) Ts 77, b) the dioxirane, c) Ts 78 and d) singlet bis(oxy) biradical (SB) optimised at the B3LYP/6-31++G(d,p) level of theory

Nguyen *et al*. conducted high level CASPT2//CASSCF calculations which revealed the thermal instability of the SB intermediate and the very low/negligible isomerisation barrier towards the cyclic lactone. This could explain the difficulty in locating the SB structure in this investigation; initial attempts saw the SB intermediate optimise to the lactone structure (Figure 8.13b), only by using UB3LYP (as with ozone) could the optimised geometry of the SB intermediate be obtained. Whilst the calculations by Nguyen *et al.* describe the isomerisation barrier between the SB and the lactone as low or negligible, the isomerisation barrier in this investigation (Ts 80) was determined to be highly negative (as seen in table 1), so could not be considered accurate.
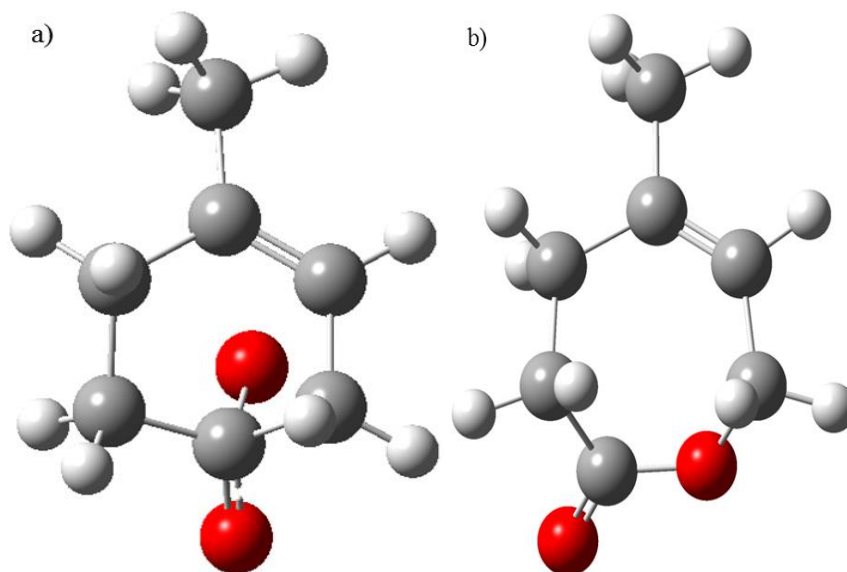
Figure 8.13: Structures of a) Ts 80 and b) the lactone optimised at the B3LYP/6-31++G(d,p) level of theory

During their theoretical investigation into the ozonolysis of β-pinene Nguyen *et al.* explored both the singlet and triplet surfaces for the ring opening process converting the dioxirane to the bis(oxy) biradical. As can be seen in Figure 8.14 (taken from the Nguyen *et al.* paper[29]) the triplet crosses the singlet surface at ~2.5 kcal mol^{-1} (~0.6 kJ mol^{-1}) below the ring breaking transition state (Ts 78) which leads to the singlet bis(oxy) biradical. As usual for singlet-triplet crossings, Nguyen *et al.* noted that the spin-orbit coupling was weak, meaning that the probability of 'hopping' onto the triplet surface was extremely small.

The authors also note that whilst chemically activated dioxiranes predominately yield singlet bis(oxy) biradicals, thermalized dioxiranes will form the triplet; the fate of which involves two successive C-C bond ruptures yielding CO_2 and a triplet biradical. The destiny of this biradical is expected to follow the traditional atmospheric degradation as other alkyl radicals.[29]

The analogous triplet surface was examined during this investigation; the triplet dioxirane was ~200 kJ mol^{-1} less stable than the Criegee intermediate, whereas the singlet dioxirane was ~65 kJ mol^{-1} more stable. As previously mentioned the singlet bis(oxy) biradical is less stable compared to the dioxirane. However, the same cannot be said for the triplet surface where a ring-breaking transition state was also not easily located, observations also supported by Figure 8.14.
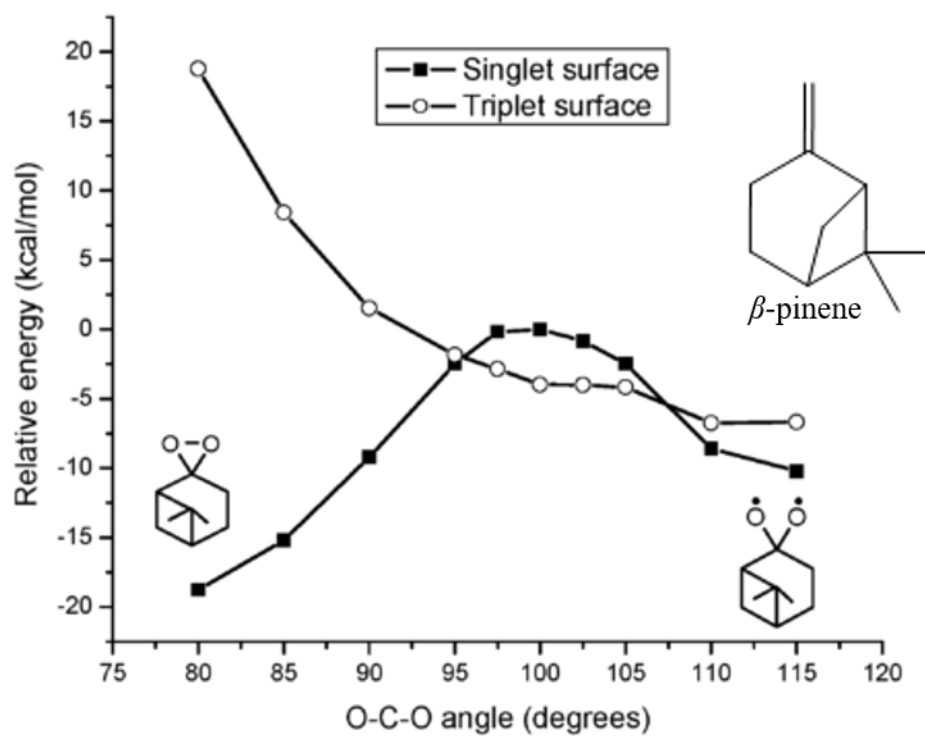
Figure 8.14: Potential energy curves for the ring opening step of the dioxirane intermediate to a bis(oxy) biradical on the singlet and triplet surfaces during the ozonolysis of *β*-pinene, derived at the CASPT2//UB3LYP level of theory[29]
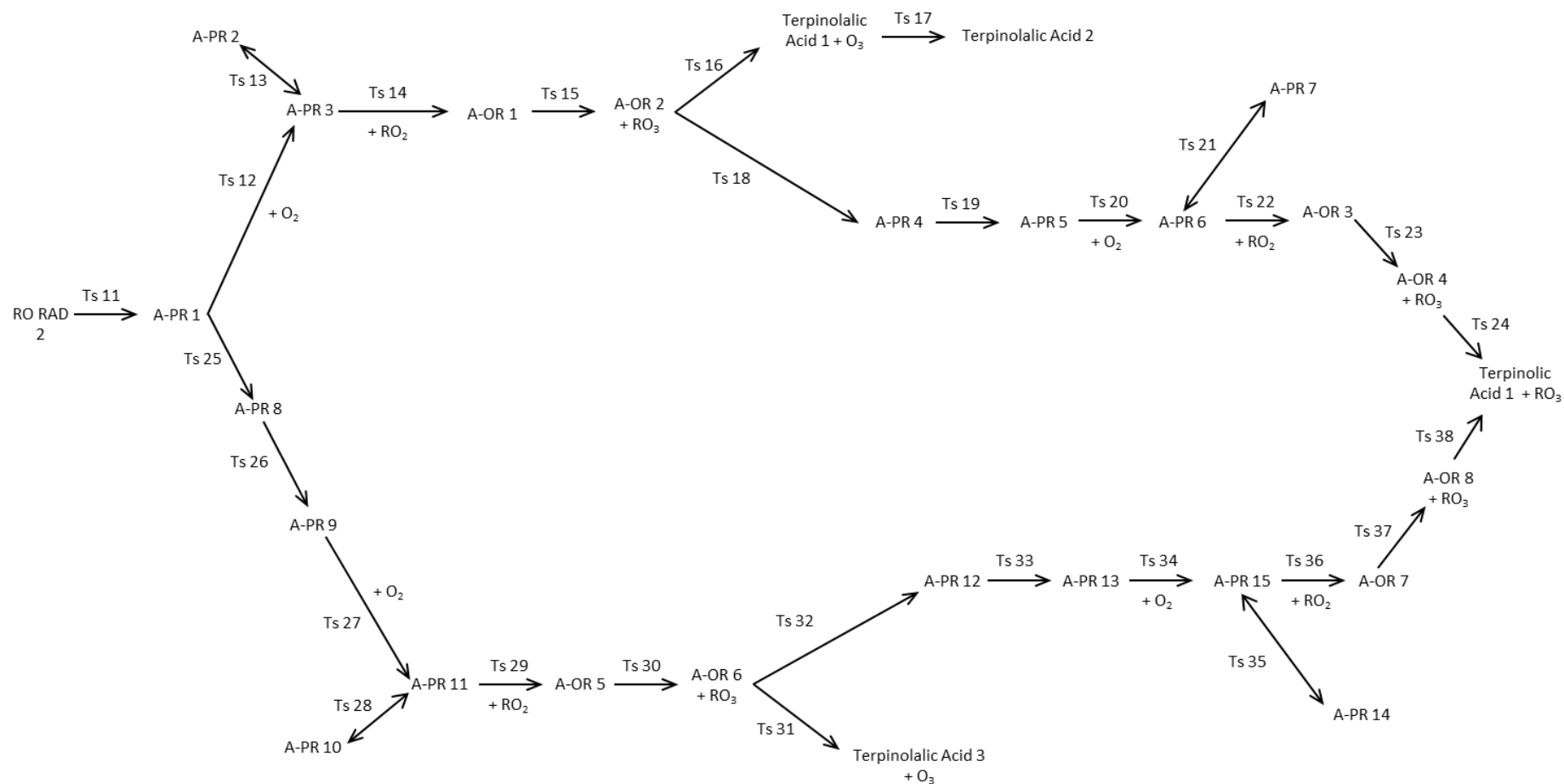
8.2.3 Decomposition of RO Radical 2

Figure 8.15: Flow chart showing the decomposition of the RO radical (RO RAD 2) via various acyl peroxy radicals (A-PR) and acyl-oxy radicals (A-OR) in order to form the products Terpinolalic and Terpinolic acids

228

The flow chart in Figure 8.15 shows a continuation of the lower energy hydroperoxide channel shown in Figure 8.3. After the initial ring opening via Ts 11 of RO RAD 2, the resultant acyl peroxy radical (A-PR 1) is oxidised via 2 similar routes.
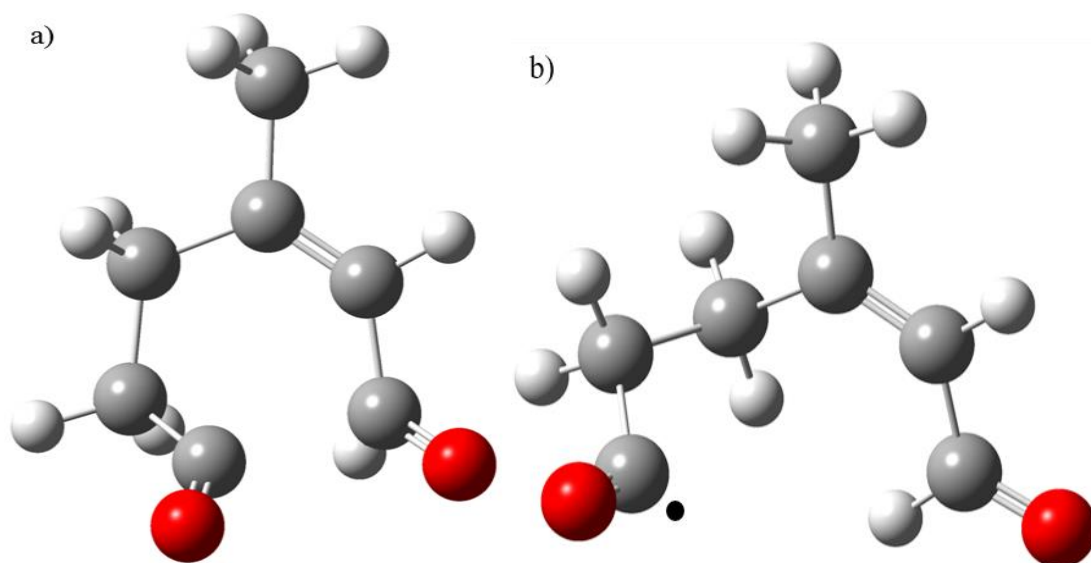
Figure 8.16: Structures of a) Ts 11 and b) A-PR 1 optimised at the B3LYP/6-31++G(d,p) level of theory

8.2.3.1 Oxidation of Acyl Peroxy Radical 1

The first of these pathways involves the direct addition of O_2 to A-PR 1 to form another acyl peroxy radical A-PR 3, whilst the second requires a H-migration and an O-flip before the addition of O_2 can occur to form A-PR 11. The H-migration process in Ts 25 occurs from C_1 to C_2 to yield A-PR 8 which is more stable than A-PR 1 by ~7 kJ mol^{-1}, before an O-flip occurs in Ts 26 resulting in the less stable A-PR 9, as shown in Figure 8.17.
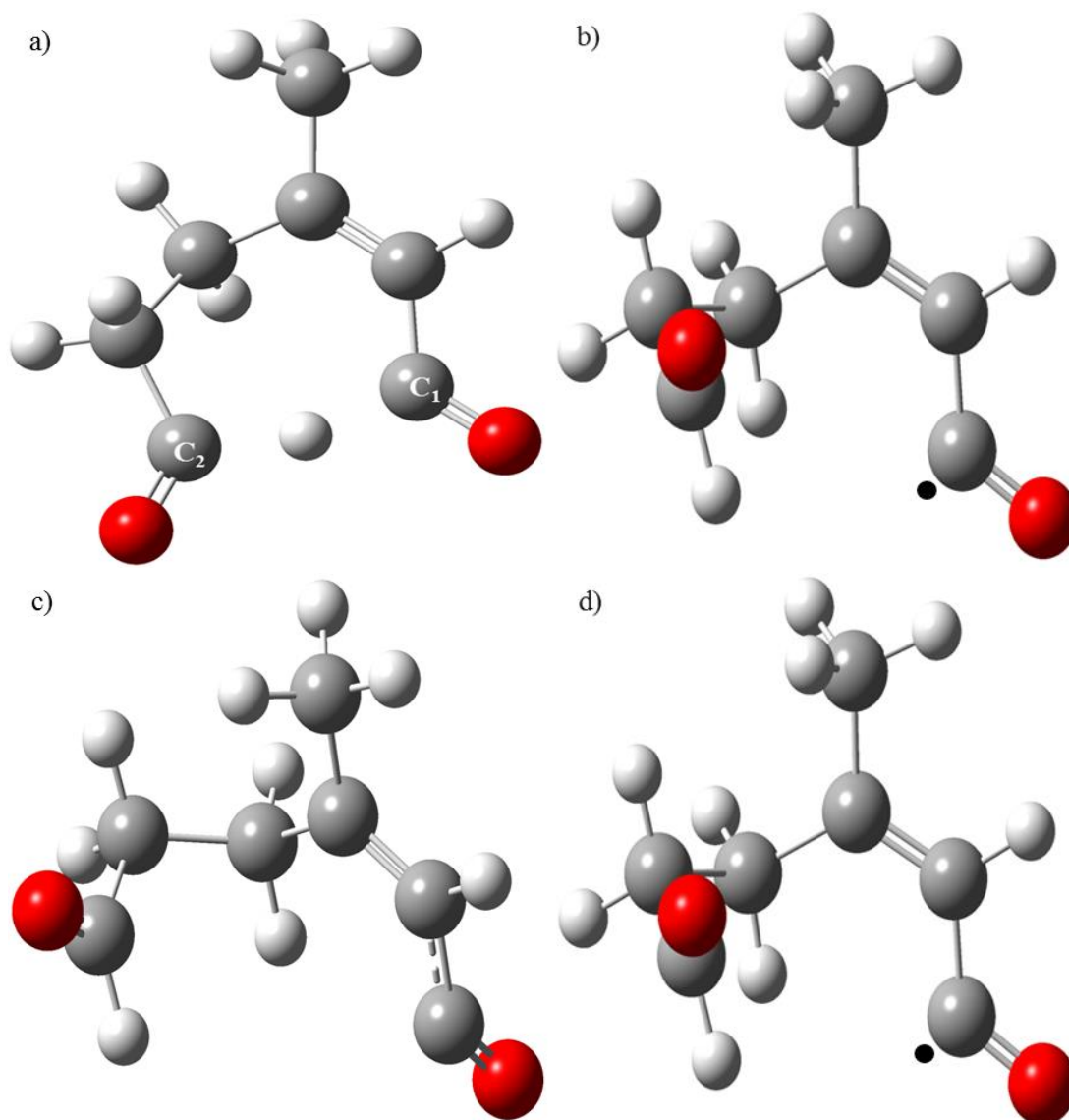
Figure 8.17: Structures of a) Ts 25, b) A-PR 8, c) Ts 26 and d) A-PR 9 optimised at the B3LYP/6-31++G(d,p) level of theory

The next step of both pathways is now the addition of O_2; location of these transition states proved problematic, on each attempt the O_2 unit moved away from the open-ring structure rather than towards which you would expect for a bonding process. Previous theoretical studies on β-Caryophyllene[30] and Sabinene[31] , do not list a transition state for this process; however, the comparability of the stated ΔH values with this investigation of ~2.5 kJ mol^{-1} implies that the A-PR3/11 structures are accurate.

Whilst attempting to resolve this issue previous works using smaller O_2-addtion systems were analysed to ascertain whether a transition state structure had been theoretically established. The authors of addition reactions between O_2 and alkyl radicals[32], ethyl

230

radicals[33] and C_3H_5 radicals[34] did not describe a transition state structure for this process. A group studying the addition of allyl radicals with O_2 indicated the presence of a transition state for this reaction with a shallow barrier of 0.99 kcal mol^{-1} [35], but show no indication of the potential structure, yielding little aid to this investigation.

Whilst the structures of O_2-addition transition states seem unsolvable, the theoretical investigation into the ozonolysis of terpinolene continued. Two potential conformations exist upon O_2 addition: with the O_2 unit pointing either away from the C-chain (A-PR 3 & 11) or bending back over the C-chain (A-PR 2 & 10). The structures in which the O_2 unit is bent back over the C-chain (shown in Figure 8.18) are more stable by ~120-130 kJ mol^{-1}.
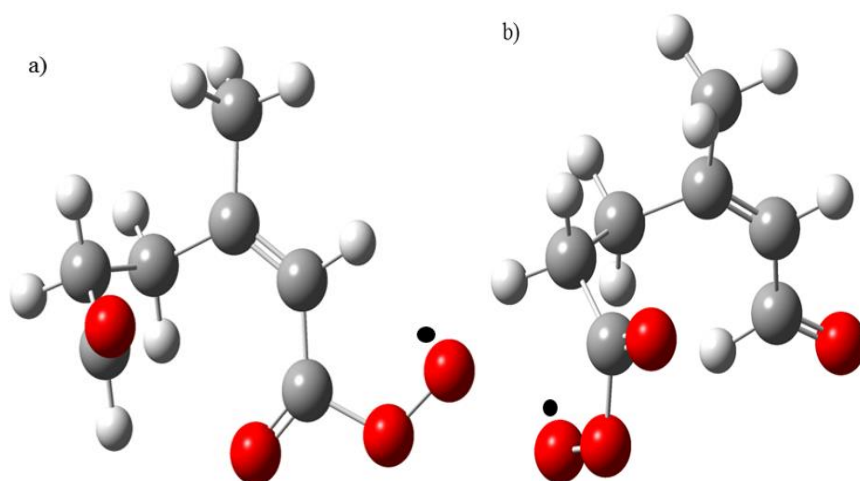

Figure 8.18: Structures of a) A-PR 10 and b) A-PR 2 optimised at the B3LYP/6-31++G(d,p) level of theory

8.2.3.2 Reaction pathways of Acyl Peroxy Radicals 3 and 11

The decomposition of the acyl peroxy radical 3 (APR 3) to acyl-oxy radical is shown in Figure 8.19. There is also an equivalent pathway for APR 11.
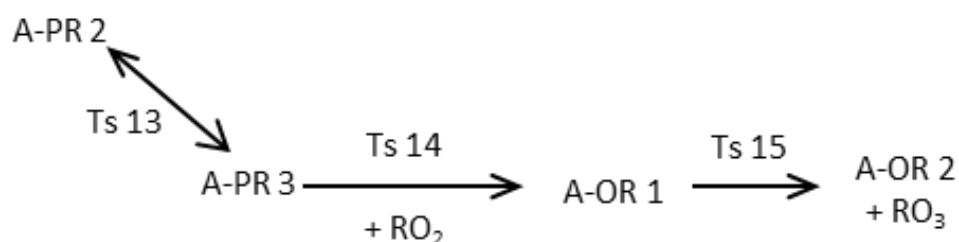

Figure 8.19: Flow chart showing the decomposition of acyl peroxy radical 3 (APR3)

The decomposition pathway of A-PR 3 requires the addition of RO_2 (where R=CH$_3$), via Ts 14 to form an acyl-oxy radical (A-OR 1). Similarly to the addition of O_2 locating the transition state structures for RO_2 addition was not simple; however, a previous flash-photolysis study on the addition of two CH_3O_2 units, shows possible intermediate and transition state structures for this process[36]. The structures from this study contain no specific details; however, it suggests a reasonable starting point for the location of these transition states structures. Unfortunately these suggestions did not lead to the simple location of the transition state structures required for this investigation. Loss of RO_3 from A-OR 1 via Ts 15, results in second acyl-oxy radical being formed (Figure 8.20). There are two possible pathways for the decomposition of A-OR 2 (& 6) leading to either terpinolalic acid, which possesses both acid and aldehyde groups, and terpinolic acid, a diacid.
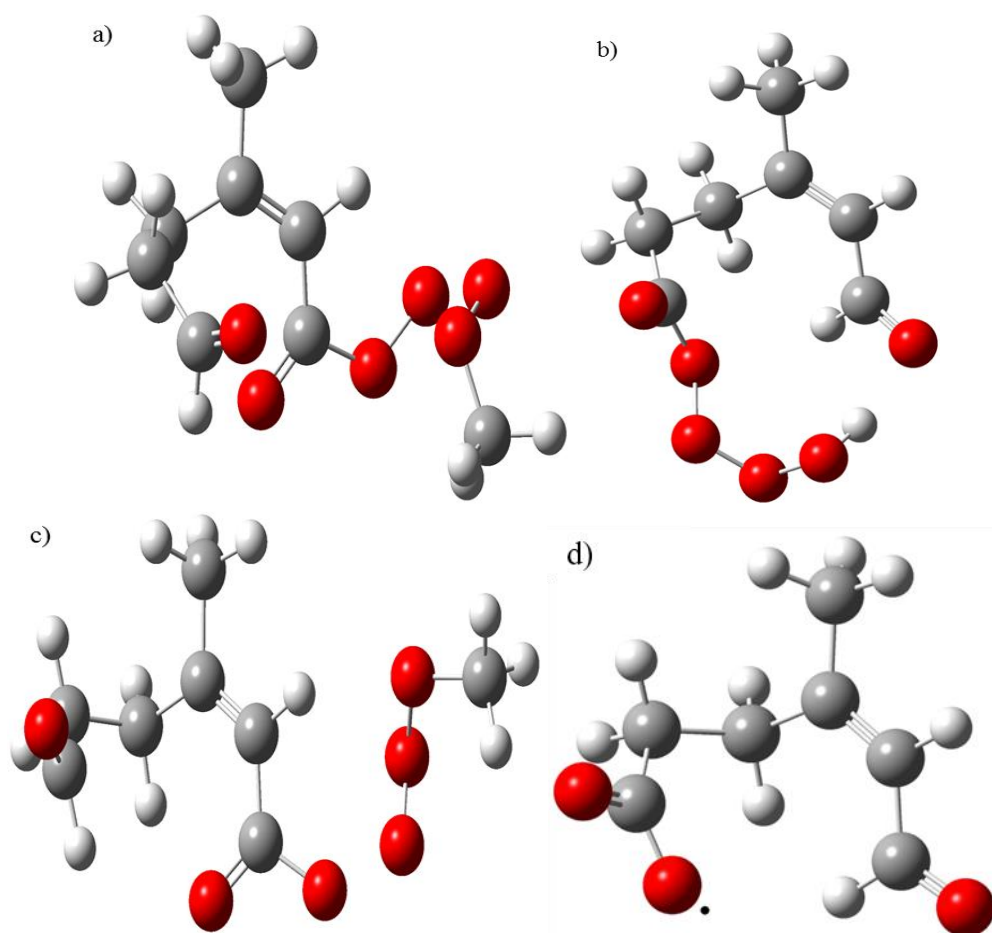

Figure 8.20: Structures of a) Ts 14, b) A-OR 1, c) Ts 15 and d) A-OR 2 optimised at the B3LYP/6-31++G(d,p) level of theory

8.2.3.3 Formation of Terpinolalic Acid

The formation of terpinolalic acid 2 is shown in Figure 8.21. There is also an equivalent pathway for Terpinolalic acid 3.
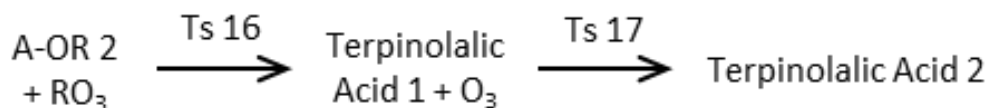
$$\text{A-OR 2} + RO_3 \xrightarrow{\text{Ts 16}} \text{Terpinolalic Acid 1} + O_3 \xrightarrow{\text{Ts 17}} \text{Terpinolalic Acid 2}$$

Figure 8.21: Flow chart showing the formation of Terpinolalic acid 2

Abstraction of a H-atom by A-OR 2 from the lost RO_3 radical (Ts 16) leads to a preliminary terpinolalic acid structure (terpinolalic acid 1) with the loss of a different RO_3 radical (where $R=CH_2$). This structure requires an O-flip to yield the 6-oxo-4-methyl-4-hexenoic acid (terpinolalic acid 2) structure suggested by Ma. The equivalent pathway originating from A-OR 6 does not require the O-flip step, so 6-oxo-3-methyl-2-hexenoic acid (terpinolalic acid 3) is formed directly with the addition of RO_3.
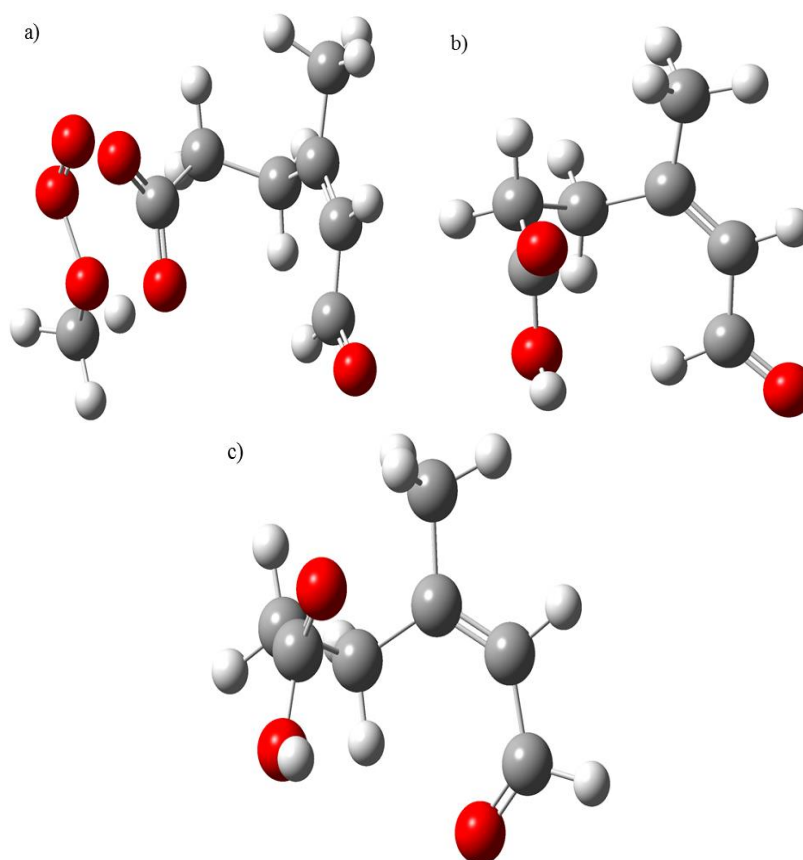

Figure 8.22: Structures of a) Ts 16, b) Terpinolalic acid 1 and c) 6-oxo-4-methyl-4-hexenoic acid optimised at the B3LYP/6-31++G(d,p) level of theory

8.2.3.4 Alterations from terpinolene ozonolysis scheme published by Ma

During their GC-MS investigation into the formation of organic acids from the ozonolysis of terpinolene, Ma *et al.* describe two different reactions pathways from acyl peroxy radicals (A-PR 3(Figure 8.23a), 11, 21 and 27): the first yielding either 3-methyl-2-hexenedoic acid or 3-methyl-3-hexenedoic acid (terpinolic acid 1 and 3) from the addition of either HO_2 or RO_2, whilst the second yields an acyl-oxy radical (A-OR 2, 6, 10 and 14 respectively) from the addition of RO_2.
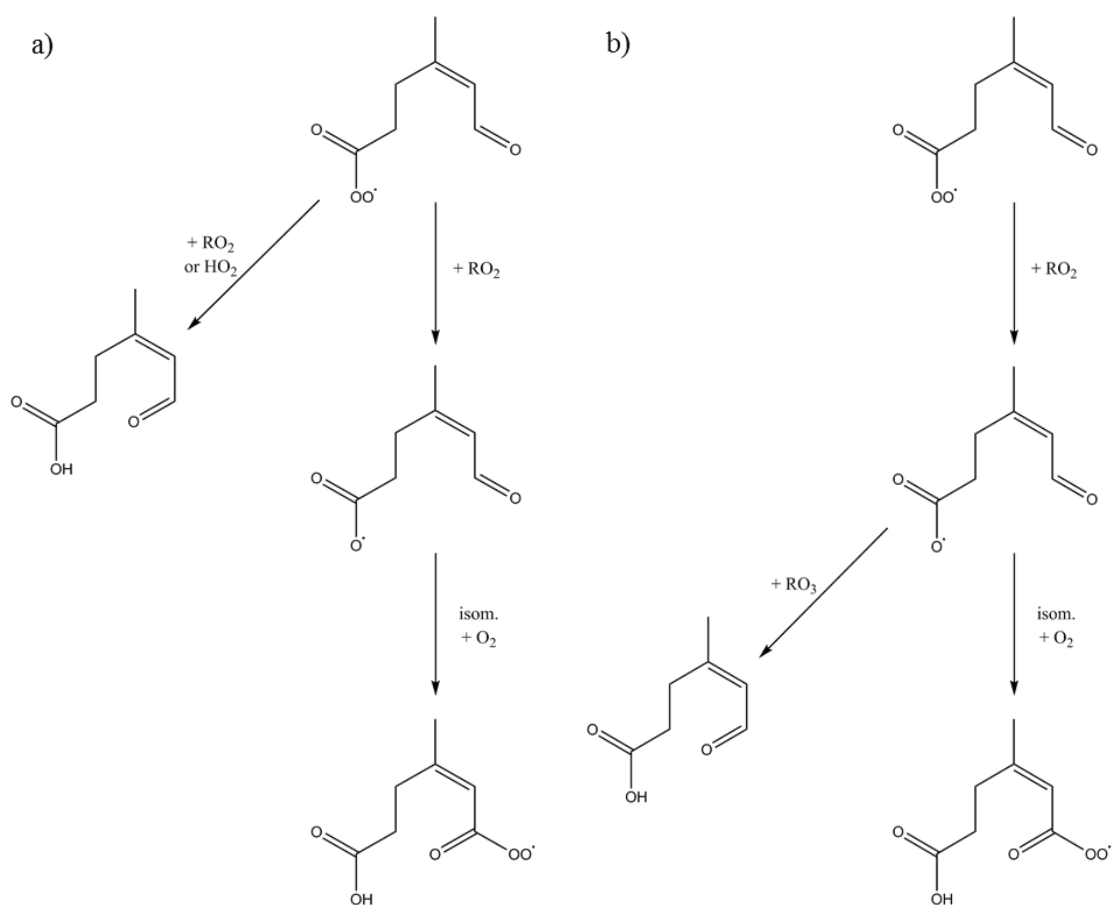

Figure 8.23: Reaction scheme for the production of Terpinolalic Acid 1 from A-PR 3 as proposed by a) Ma in 2009[18] and b) this investigation

However during the course of this theoretical investigation as both reactions involve RO_2, the formation of terpinolic acid occurred via the creation of the acyl-oxy radical. Therefore this investigation provides a slight amendment to the reaction pathway described by Ma *et al.*; terpinolic acid is a reaction product of an acyl-oxy radical (Figure 8.23b) rather than the acyl peroxy radical.

8.2.3.5 Formation of Terpinolic Acid

The formation of Terpinolic acid 1 is shown in Figure 8.24. There is also an equivalent pathway from A-OR 6.
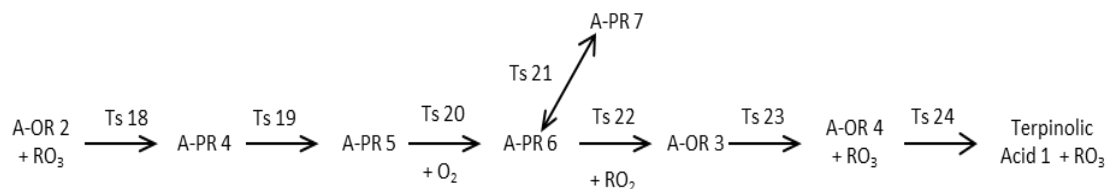

Figure 8.24: Flow chart showing the formation of Terpinolic acid 1

The second possible decomposition pathway of A-OR 2 initially proceeds via a H-migration (Ts 18, Figure 8.25a) from C_1 to O_1 to form acyl peroxy radical 4 (Figure 8.25b) before an O-flip via Ts 19 (Figure 8.25c) results in A-PR 5 (Figure 8.25d). The corresponding reaction from A-OR 6 proceeds via two H-migration steps (transition states 32 and 33).
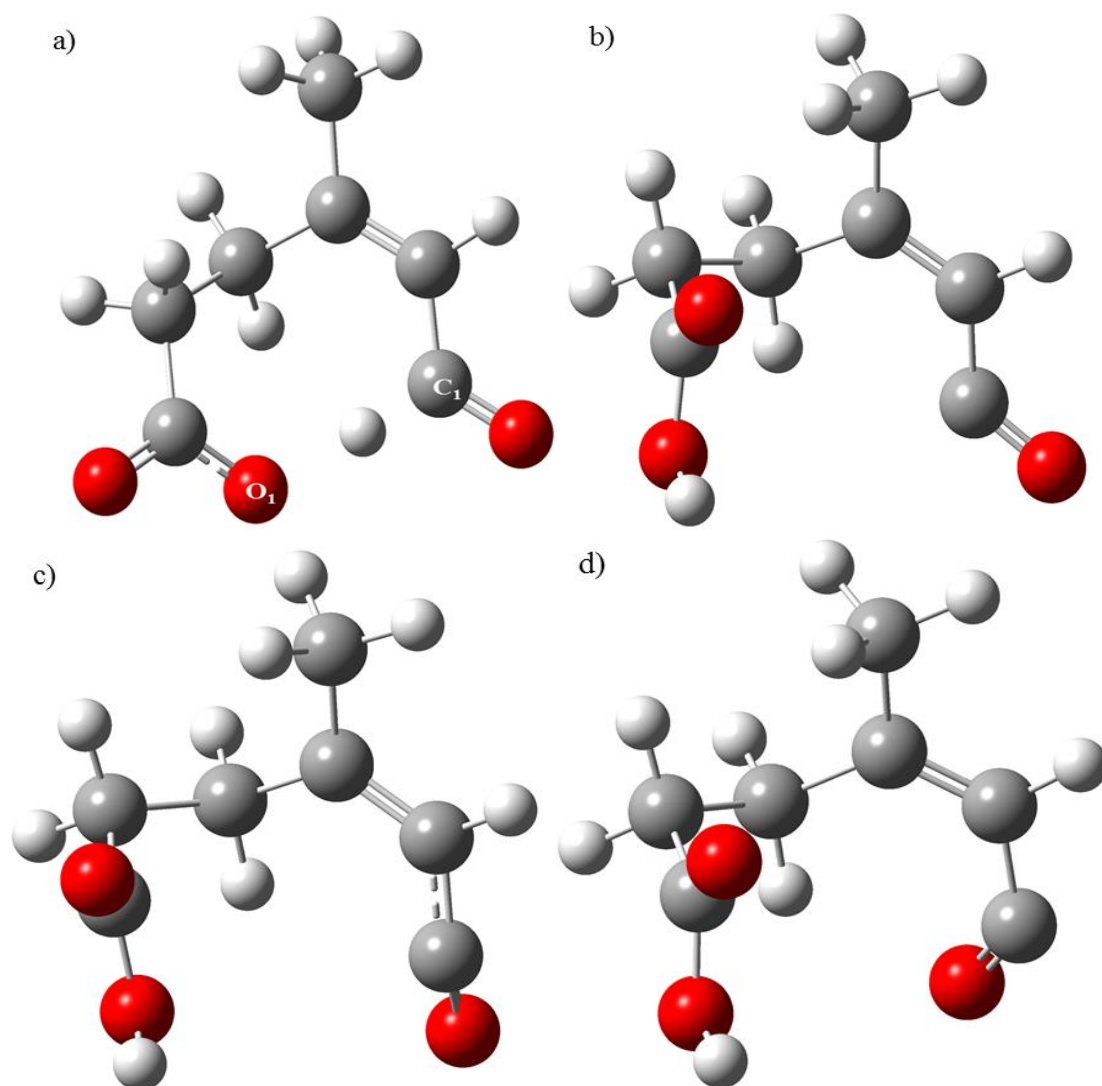
Figure 8.25: Structures of a) Ts 18, b) A-PR 4, c) Ts 19 and d) A-PR 5 optimised at the B3LYP/6-31++G(d,p) level of theory

The next step in both pathways is the addition of atmospheric O_2; as mentioned in depth earlier such transition state structures prove elusive, yet the theoretical calculations continued. Similarly to A-PR 2 and 3 (and A-PR 10 and 11) two possible conformations exist upon O_2 addition: with the O_2 unit pointing either away from the C-chain (A-PR 6 & 15) or bending back over the C-chain (A-PR 7 & 14). The structures in which the O_2 unit is bent back over the C-chain (shown in Figure 8.26) are more stable by ~125-130 kJ mol^{-1}.
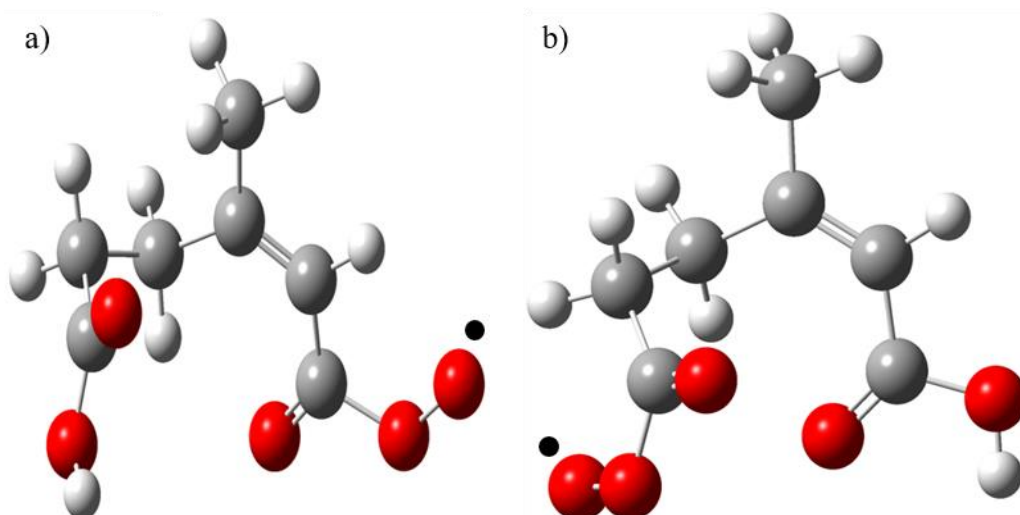
Figure 8.26: Structures of a) A-PR 6 and b) A-PR 14 optimised at the B3LYP/6-31++G(d,p) level of theory

The decomposition pathway of A-PR 6 requires the addition or RO_2 (where $R=CH_3$), via Ts 22 to form an acyl-oxy radical (A-OR 3). Loss of RO_3 from A-OR 3 via Ts 23, results in second acyl-oxy radical, A-OR 4, being formed (Figure 8.27). Abstraction of a H-atom by A-OR 4 from the lost RO_3 radical (Ts 24) yields the 3-methyl-2-hexenedoic acid (terpinolic acid 1) structure (Figure 8.27) suggested by Ma *et al.*, along with the loss of a different RO_3 (where $R=CH_2$). Abstraction of a H-atom by A-OR 8 also yields 3-methyl-2-hexenedoic acid.

The activation energies for each of the transition states 12-24 (and the corresponding transition states 25-38 from the other hydroperoxide channel) calculated at three different levels of theory are listed in Table 8.2.
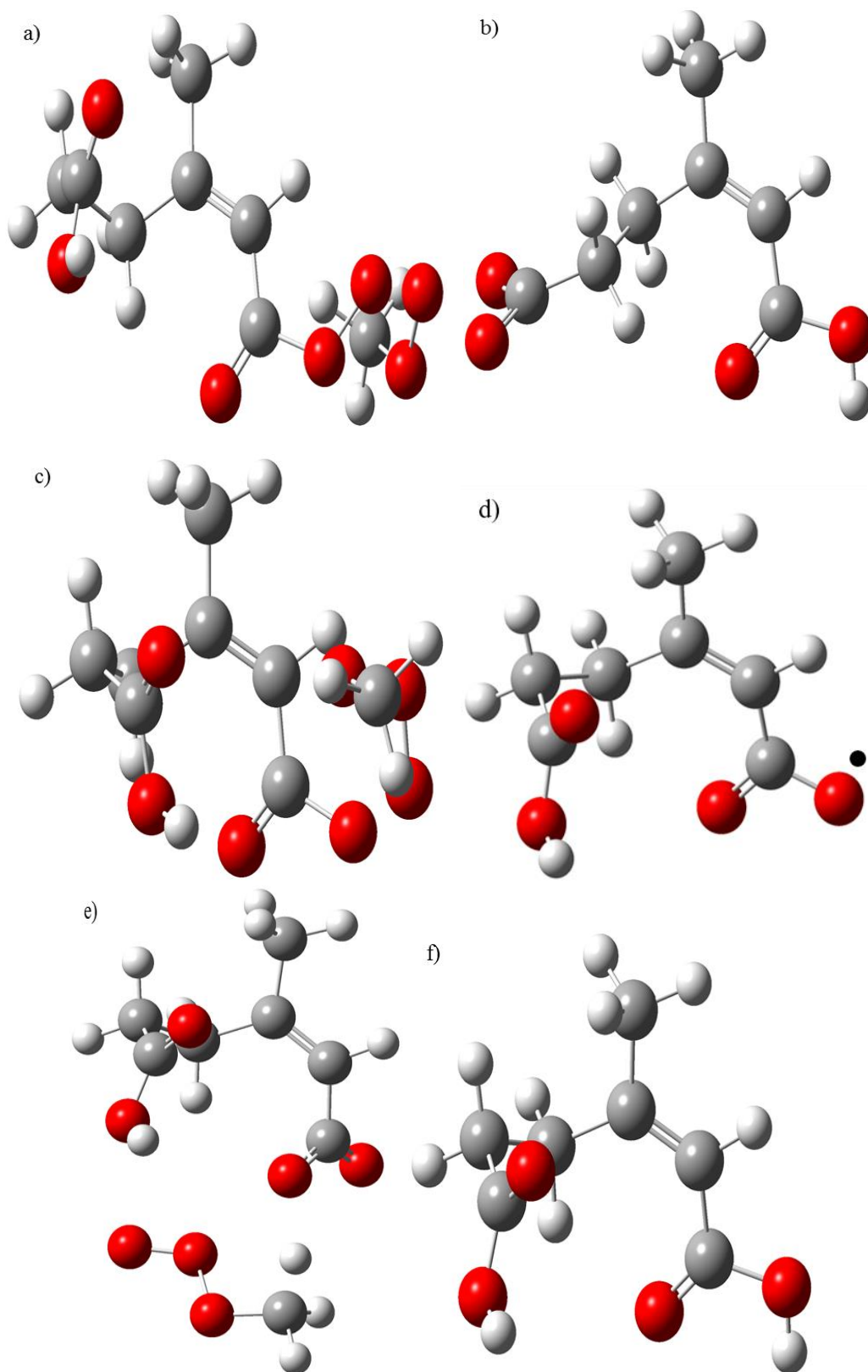
Figure 8.27: Structures of a) Ts 22, b) A-OR 3, c) Ts 23, d) A-OR 4, e) Ts 24 and f) 3-methyl-2-hexenedoic acid optimised at the B3LYP/6-31++G(d,p) level of theory

Table 8.2: Activation energies for the processes joining RO RAD 2 to the products Terpinolalic Acid and Terpinolic Acid with zero-point correction included (kJ mol^{-1})

| Transition State	B3LYP/ 6-31++G(d,p)	MPW1K/ 6-31++G(d,p)	MPW1K/ 6-311++G(3df,3pd)
11	23.89	56.66	50.43
12	-	-	-
13	22.32	24.24	27.87
14	-11.81		
15	43.3		
16	76.31		
17	30.19	28.67	30.28
18	2.45	22.91	31.34
19	11.69	11.73	13.96
20	-	-	-
21	18.81	20.69	23.20
22	11.49		
23	39.69		
24	117.37		
25	53.08	64.82	80.45
26	13.58	13.54	16.46
27	-	-	-
28	19.25	21.30	24.79
29	-6.87		
30	9.79		
31	112.57		
32	8.04	21.76	19.19
33	120.09	128.45	140.79
34	-	-	-
35	27.07	29.30	32.66
36	-9.04		
37	22.31		
38	107.14		

8.2.4 Decomposition of RO Radical 4
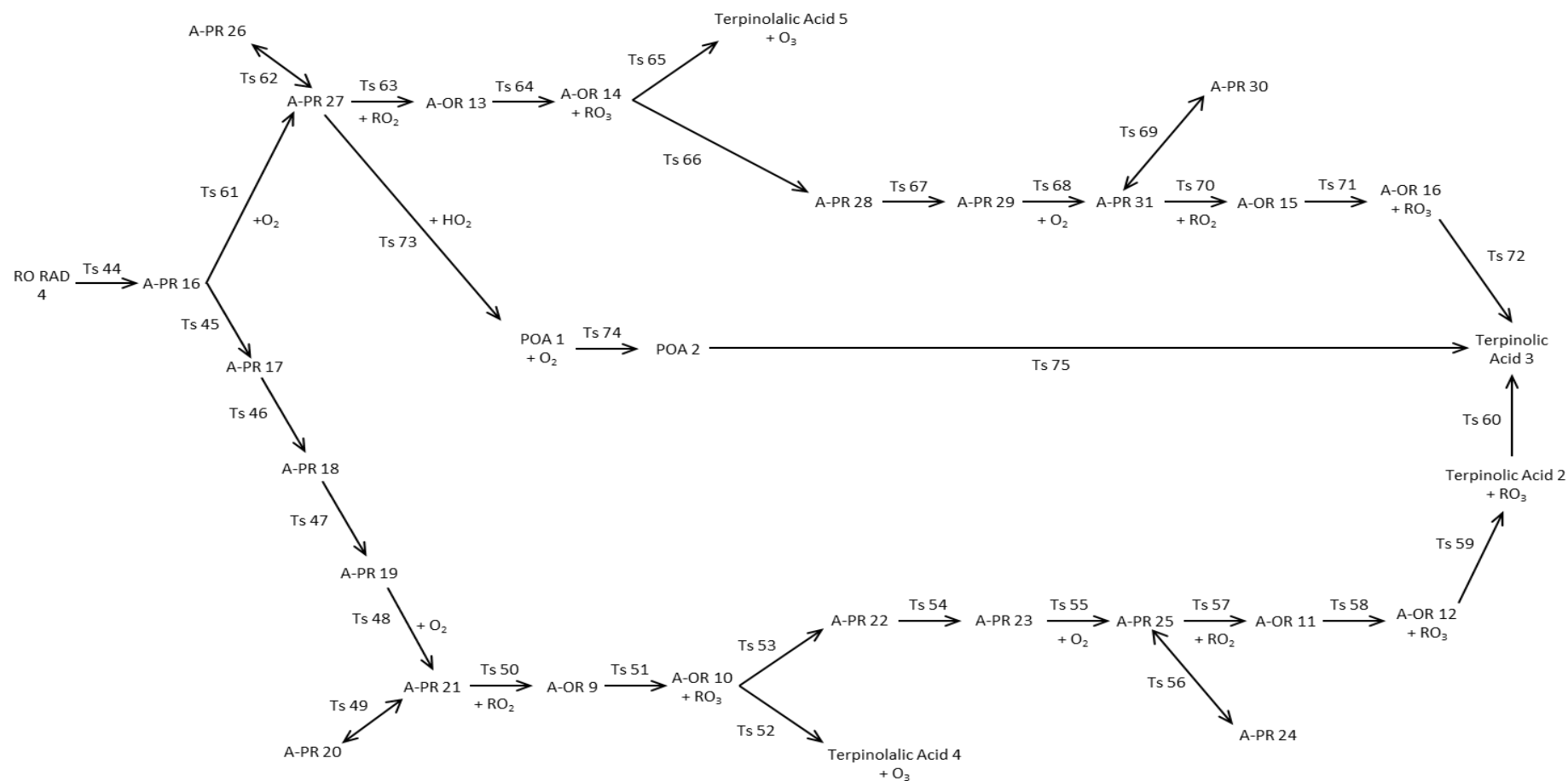
Figure 8.28: Flow chart showing the decomposition of the RO radical (RO RAD 4) via various acyl peroxy radicals (A-PR), acyl-oxy radicals (A-OR) and peroxo acids (POA) in order to form the products terpinolalic and terpinolic acids

Figure 8.28 show the analogous reaction steps to Figure 8.15, but considered the higher energy hydroperoxide channel originating from RO radical 4 (Figure 8.3). After the initial ring opening via Ts 42 of RO RAD 4 (Figure 8.29), the resultant acyl peroxy radical (A-PR 16) is oxidised via 2 routes, as A-PR 1 did. The difference between the below structures and those in Figure 8.16, originate from the differing side of the double bond from which an H atom was abstracted, from the right during the processes involving Ts 6 and the left for Ts 39.
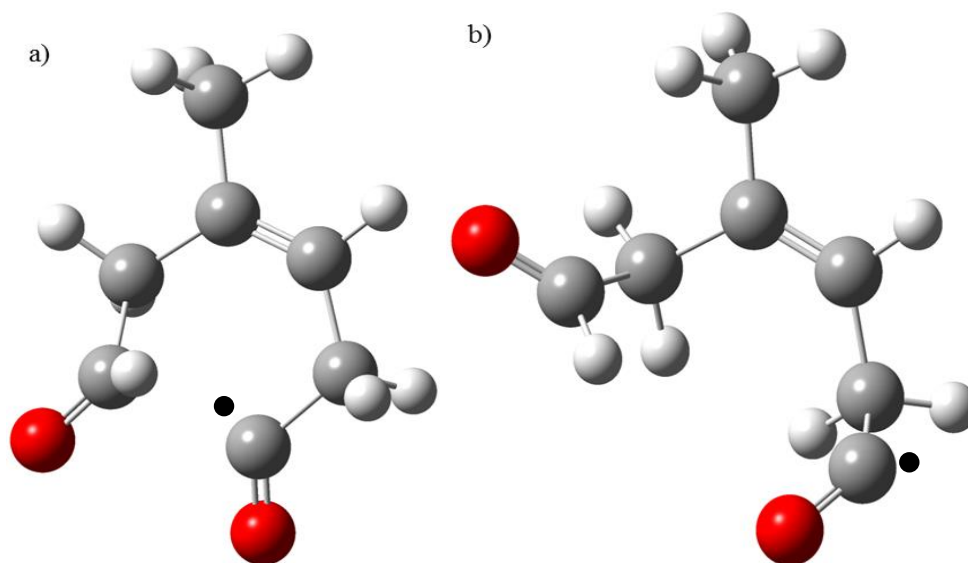

Figure 8.29: Structures of a) Ts 42 and b) A-PR 16 optimised at the B3LYP/6-31++G(d,p) level of theory

8.2.4.1 Oxidation of Acyl Peroxy Radical 16

The first of oxidation pathway involves the direct addition of O_2 to A-PR 16 to form another acyl peroxy radical A-PR 27, whilst the second requires an O-flip, followed by a H-migration and a second O-flip before the addition of O_2 can occur to form A-PR 21. The next step of both pathways is now the addition of O_2, as mentioned previously location of these transition states proved problematic. Two potential conformations also exist upon O_2 addition: with the O_2 unit pointing either away from the C-chain (A-PR 21 & 27) or bending back over the C-chain (A-PR 20 & 26). The structures in which the O_2 unit is bent back over the C-chain (shown in Figure 8.30) are more stable by ~120-125 kJ mol^{-1}.
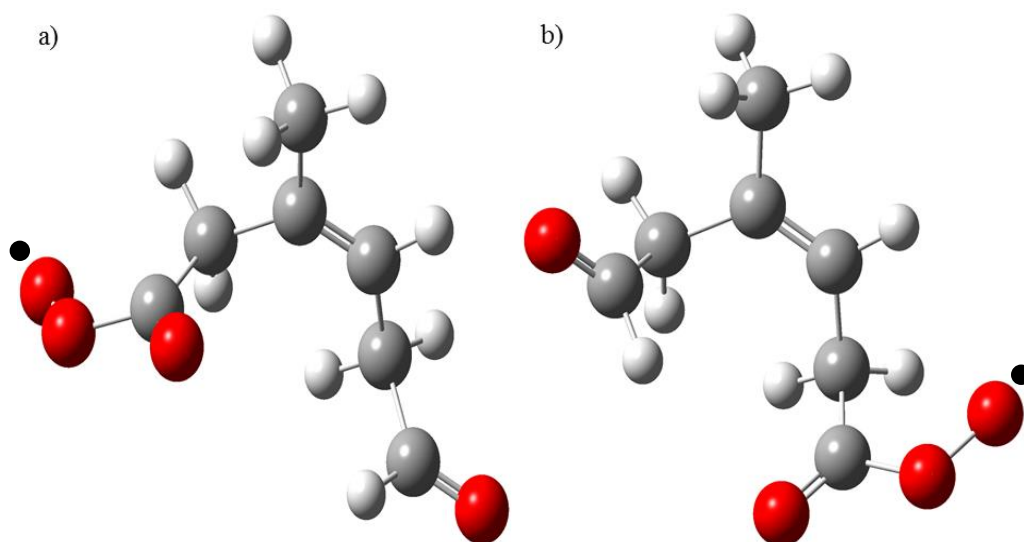
Figure 8.30: Structures of a) A-PR 20 and b) A-PR 26 optimised at the B3LYP/6-31++G(d,p) level of theory

8.2.4.2 Reaction pathways of Acyl Peroxy Radicals 21 and 27

The decomposition pathway of A-PR 21 requires the addition or RO_2 (where R=CH$_3$), via Ts 50 to form an acyl-oxy radical (A-OR 9); as mentioned previously location of these transition states proved difficult. Loss of RO_3 from A-OR 9 via Ts 51, results in second acyl-oxy radical being formed. There are two possible pathways for the decomposition of A-OR 10 (& 14) leading to either terpinolalic acid, which possesses both acid and aldehyde groups, and terpinolic acid, a diacid. There is also an additional pathway from A-PR 27 suggested by Koch *et al.*[22], which forms terpinolic acid that will be discussed later.

8.2.4.3 Formation of Terpinolalic Acid

The formation of Terpinolalic acid 5 is shown in Figure 8.31. There is also an equivalent pathway from A-OR 7.
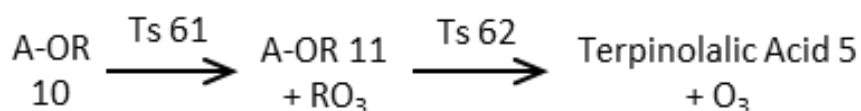

Figure 8.31: Flow chart showing the formation of Terpinolalic acid 5

Abstraction of a H-atom by A-OR 10 from the lost RO_3 yields 6-oxo-3-methyl-3-hexenoic acid (terpinolalic acid 4) (via Ts 52) suggested by Ma *et al.*[18] with the loss of a different RO_3 radical (where R=CH_2. The equivalent pathway originating from A-OR 14 yields 6-oxo-4-methyl-3-hexenoic acid (terpinolalic acid 5) via Ts 65, also seen in Figure 8.32.
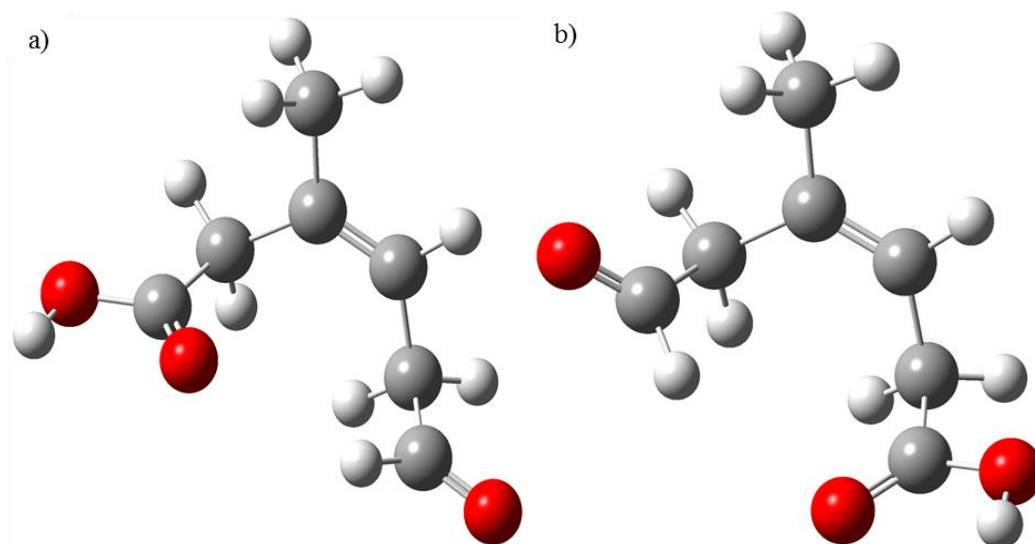

Figure 8.32: Structures of a) 6-oxo-3-methyl-3-hexenoic acid and b) 6-oxo-4-methyl-3-hexenoic acid optimised at the B3LYP/6-31++G(d,p) level of theory

8.2.4.4 Formation of Terpinolic Acid

The second possible decomposition pathway of A-OR 10 initially proceeds via a H-migration (Ts 53, Figure 8.33a) from C_1 to O_1 to form acyl peroxy radical 22 (Figure 8.33b) followed by a second H-migration via Ts 54 results in A-PR 5 (Figure 8.33c). The corresponding reaction from A-OR 14 proceeds via a H-migration before an O-flip (transition states 66 and 67).
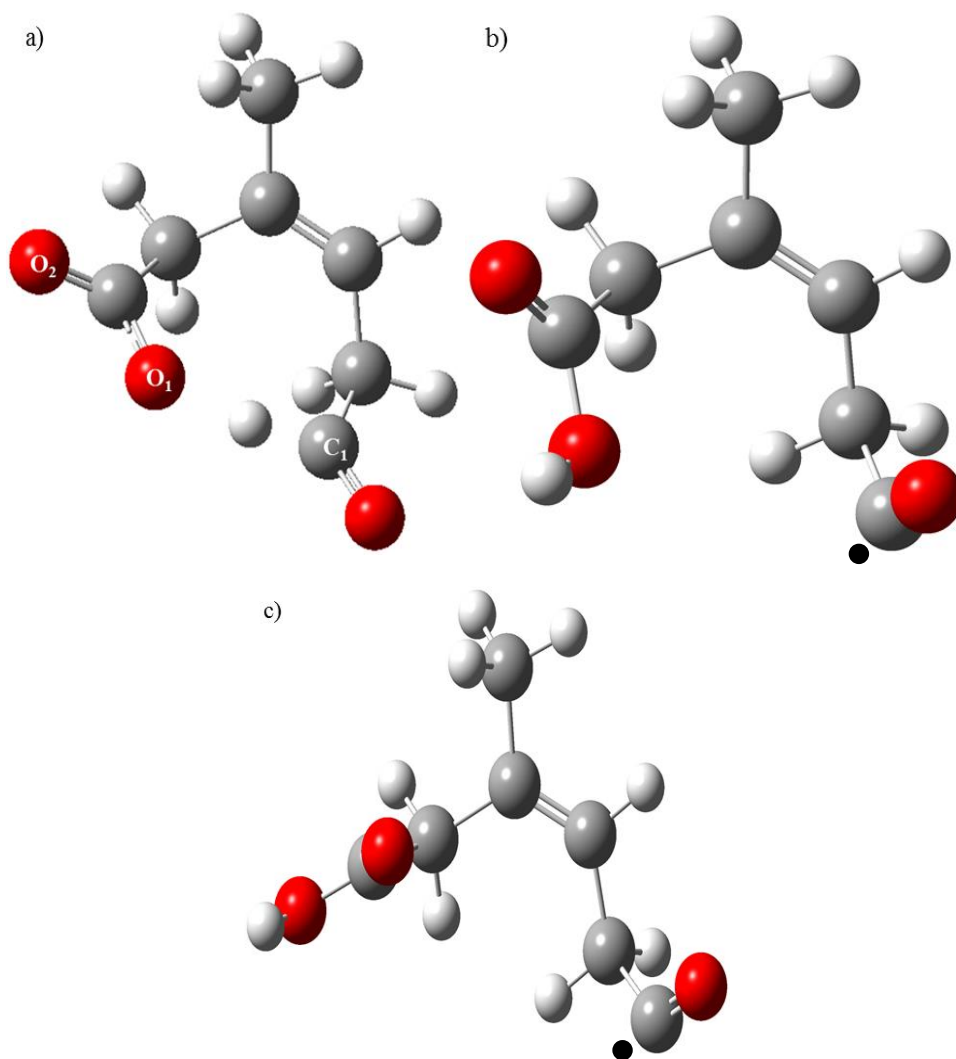
Figure 8.33: Structures of a) Ts 53, b) A-PR 22 and c) A-PR 23 optimised at the B3LYP/6-31++G(d,p) level of theory

The next step in both pathways is the addition of O_2. The transition state structures proved elusive, but the theoretical calculations continued showing two possible conformations upon O_2 addition: with the O_2 unit pointing either away from the C-chain (A-PR 25 & 31) or bending back over the C-chain (A-PR 24 & 30). The structures in which the O_2 unit is bent back over the C-chain (shown in Figure 8.34) are more stable by ~110-125 kJ mol^{-1}.
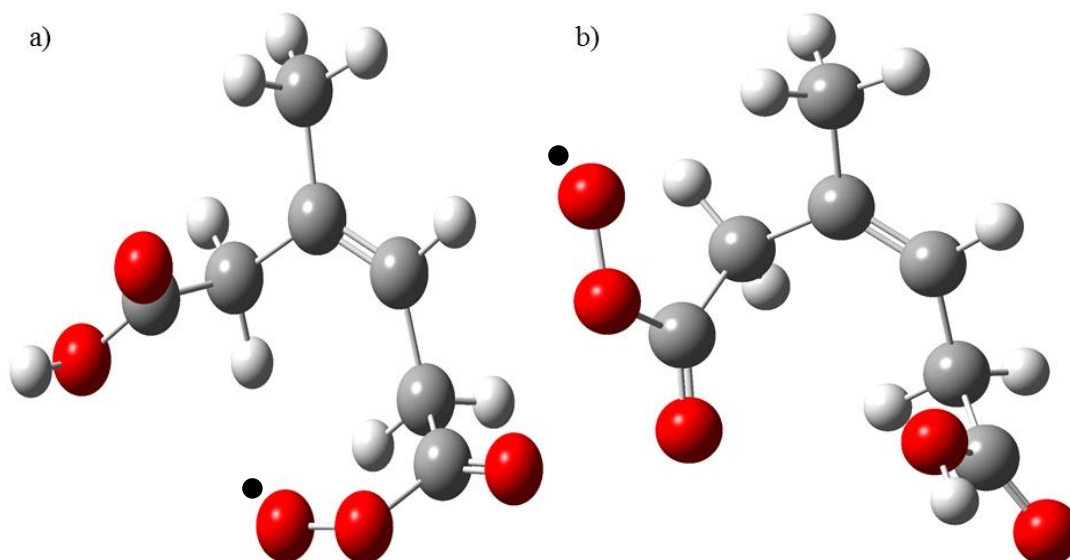
Figure 8.34: Structures of a) A-PR 24 and b) A-PR 30 optimised at the B3LYP/6-31++G(d,p) level of theory

The decomposition pathway of A-PR 25 requires the addition or RO_2 (where R=CH$_3$), via Ts 57 to form an acyl-oxy radical (A-OR 11). Loss of RO_3 from A-OR 11 via Ts 58, results in second acyl-oxy radical, A-OR 12, being formed. Abstraction of a H-atom by A-OR 12 from the lost RO_3 radical (Ts 59) yields a preliminary structure of terpinolic acid (terpinolic acid 2) along with the loss of RO_3 (where R=CH$_2$). A final H-migration yields the 3-methyl-3-hexenedoic acid (terpinolic acid 3) structure (Figure 8.35) suggested by Ma *et al.* The corresponding reaction originating from A-OR 15 does not require this additional H-migration step so 3-methyl-3-hexenedoic acid is formed directly from the abstraction of a H-atom on the RO_3 by A-OR 16.
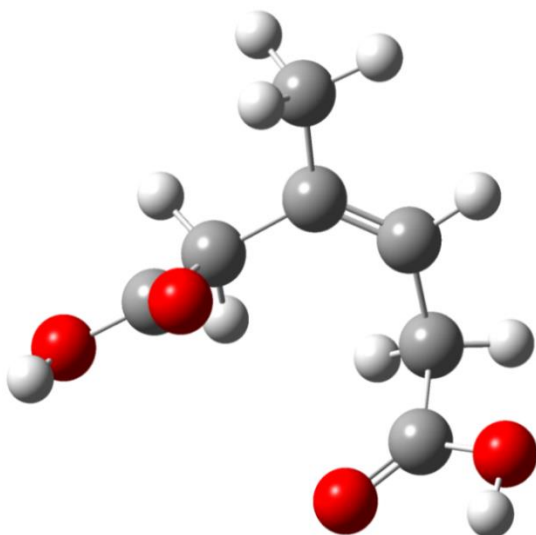
Figure 8.35: Structure of 3-methyl-3-hexenedoic acid optimised at the B3LYP/6-31++G(d,p) level of theory

8.2.4.5 Alternative formation pathway of terpinolic acid

The alternative formation of Terpinolic acid 3, proposed by Koch *et al.*[22], is shown in Figure 8.36.
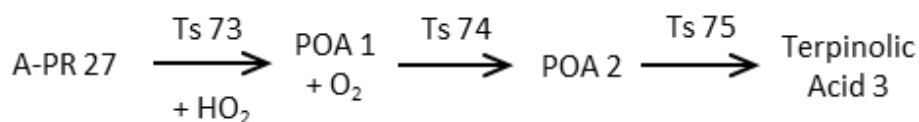
Figure 8.36: Flow chart showing the alternative formation of Terpinolic acid 3, proposed by Koch *et al.*[22]

Additionally to the hydroperoxide channels suggested by Ma *et al.*[18], Koch *et. al.* proposed an alternative mechanism in their study of monoterpene ozonolysis.[22] A structure akin to A-PR 27 undergoes addition of HO_2 via Ts 73 to form a peroxo acid (POA 1) accompanied by the loss of O_2. Isomerisation via Ts 74 yields a second cyclic peroxo acid (POA 2) (Figure 8.37) which is more stable than POA 1 by ~15 kJ mol^{-1}. Further isomerisation of POA 2 yields 3-methyl-3-hexenedoic acid (terpinolic acid 3).
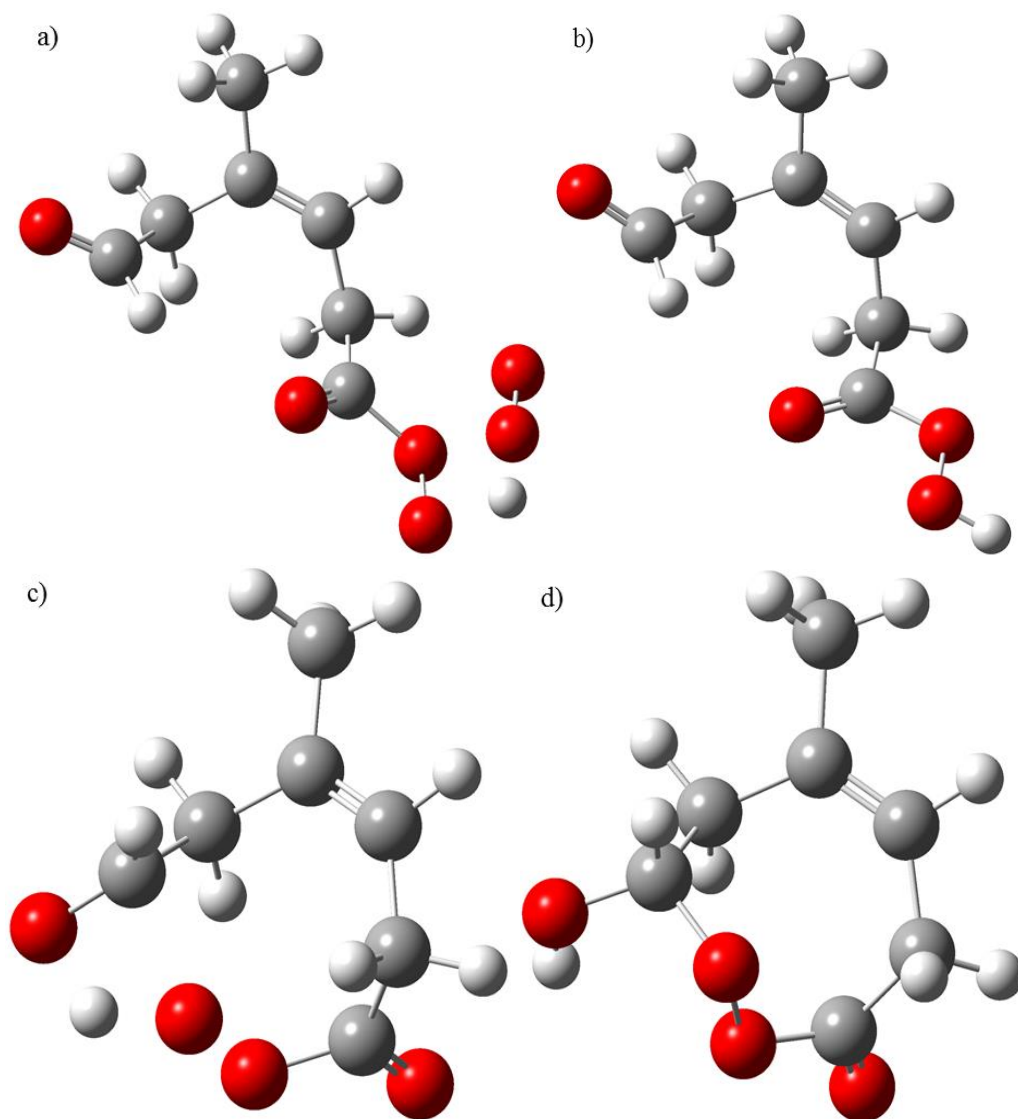
Figure 8.37: Structures of a) Ts 73, b) POA 1, c) Ts 74 and d) POA 2 optimised at the B3LYP/6-31++G(d,p) level of theory

The activation energies for each of the transition states 45-60 and the corresponding transition states 61-72 from the other hydroperoxide channel, calculated at three different levels of theory are listed in Table 8.3. The activation energies for each of the transition states 73-75 from the additional channel, calculated at three different levels of theory, are also listed in Table 8.3.

Table 8.3: Activation energies for the processes joining RO RAD 4 to the products Terpinolalic Acid and Terpinolic Acid with zero-point correction included (kJ mol^{-1})

Transition State	B3LYP/ 6-31++G(d,p)	MPW1K/ 6-31++G(d,p)	MPW1K/ 6-311++G(3df,3pd)
44	18.58	49.93	45.88
45	0.10	0.13	2.57
46	56.64	66.49	81.49
47	-0.60	-0.62	0.54
48	-	-	-
49	21.60	24.28	27.77
50	-11.84		
51	42.97		
52	78.18		
53	1.27	11.61	8.58
54	133.15	140.37	152.85
55	-	-	-
56	23.23	24.90	28.18
57	-9.74		
58	46.44		
59	80.65		
60	132.43	141.19	153.24
61	-	-	-
62	25.43	28.70	33.16
63	-11.23		
64	14.45		
65	77.34	143.90	129.85
66	3.22	13.81	17.90
67	-1.32	-1.42	1.35
68	-	-	-
69	19.69	22.06	25.90
70	4.44		
71	11.52		

Table 8.3: Cont.

Transition State	B3LYP/ 6-31++G(d,p)	MPW1K/ 6-31++G(d,p)	MPW1K/ 6-311++G(3df,3pd)
72	91.47		
73	63.74	141.56	138.07
74	154.89	174.30	188.43
75	-203.46	-215.47	-207.02

8.2.5 Unexpected results

The values highlighted in red in Tables 8.1 – 8.3 display those transition states which have negative activation energies. A transition state is the maximum point on a potential energy surface joining two minima; therefore the difference in energy between the energy minima and maximum, the activation energy, should be positive. It could be argued that in fact these structures are not transition states; however, all possess a single imaginary frequency for which the vibrational mode is at the appropriate location within the molecule, the importance of which was shown in Figure 8.8.

The addition of the RO_2 radical (where $R=CH_3$) was the most common process yielding a negative activation energy, transition states 14, 29, 36, 50, 57 and 63. Other processes that show occasion of negative activation energies are flipping of an O-C bond (transition states 47 and 67) and isomerisation (transition states 75 and 80). For transition states 47 and 67 the presence of a negative activation energy is highly dependent on the level of theory used; using both B3LYP and MPW1K with the 6-31++G(d,p) basis set yield negative activation energies for the flipping of the O-C bond, however when the same structure undergoes a single point energy calculation at the MPW1K/6-311++G(3df,3pd) level of theory then calculated activation energy is positive.

Unfortunately such as comparison cannot be made, for all of the transition states; whilst all 80 transition states (apart from those involving the addition of O_2) have been located using the B3LYP functional; however, the same cannot be said for the MPW1K functional. The transition states that cannot be located with this functional can be catalogued into three groups: the loss of RO_3 (10, 15, 23, 30, 37, 43, 51, 58, 64 and 71), the addition of RO_2 (14, 22, 29, 36, 50, 57, 63 and 70) and the addition of H+ forming terpinolalic and terpinolic acids. With regards to the addition of RO_2, it is noteworthy that

these transition states also fall into the previous category of having a negative activation energy.

8.3 Conclusions

Density functional theory calculations, utilising the B3LYP and MPW1K functionals with the 6-31++G(d,p) basis set, have elucidated the reaction mechanism for the ozonolysis of terpinolene. The B3LYP functional produced the same defect with regards to ozone, as was reported in previous theoretical works. Two successfully solutions to this defect have been determined here; either the MPW1K functional or the unrestricted B3LYP functional will better represent the electron configuration of ozone and produce more accurate barrier heights for the entrance channel process.

Besides the ozone addition process, the B3LYP functional is the most effective functional for the establishment of the whole ozonolysis reaction mechanism. The B3LYP functional locates a transition state structure for each individual reaction step of the mechanism; the MPW1K functional fails to locate a transition state for the reaction steps involving the addition of RO_2, loss of RO_3 and the addition of H^+, if more time had permitted a detailed investigation could have been undertaken to understand why this functional struggles in these instances. There is one instance where B3LYP does fail to locate a transition state, the addition of O_2; regardless of the technique used (fully described in Chapter 3) no reaction barrier can be calculated. Other literature also fails to propose a transition state structure for this addition process and no reaction barrier heights are noted.

The final and most unexpected finding of this investigation is that certain barrier heights are negative. This opposes the expectation as transition states are the energy maxima on the potential energy surface. The presence of an imaginary frequency, vibrating at the appropriate location suggests that the transition state has been located. The majority of the negative barrier heights occur for the addition of RO_2, and further investigation would be required to understand why the calculation yields a negative reaction barrier. Similarly to the addition of ozone, these negative activation energies could be a result of a defect in the B3LYP functional when describing a RO_2 radical.

8.4 References

1. A. D. Becke, *Journal of Chemical Physics*, 1993, **98**, 5648-5652.

2. P. J. Stephens, F. J. Devlin, C. F. Chabalowski and M. J. Frisch, *Journal of Physical Chemistry*, 1994, **98**, 11623-11627.

3. Harihara.Pc and J. A. Pople, *Theoretica Chimica Acta*, 1973, **28**, 213-222.

4. M. J. Frisch, G. W. Trucks, H. B. Schlegel, G. E. Scuseria, M. A. Robb, J. R. Cheeseman, J. A. M. Jr., T. Vreven, K. N. Kudin, J. C. Burant, J. M. Millam, S. S. Iyengar, J. Tomasi, V. Barone, B. Mennucci, M. Cossi, G. Scalmani, N. Rega, G. A. Petersson, H. Nakatsuji, M. Hada, M. Ehara, K. Toyota, R. Fukuda, J. Hasegawa, M. Ishida, T. Nakajima, Y. Honda, O. Kitao, H. Nakai, M. Klene, X. Li, J. E. Knox, H. P. Hratchian, J. B. Cross, V. Bakken, C. Adamo, J. Jaramillo, R. Gomperts, R. E. Stratmann, O. Yazyev, A. J. Austin, R. Cammi, C. Pomelli, J. W. Ochterski, P. Y. Ayala, K. Morokuma, G. A. Voth, P. Salvador, J. J. Dannenberg, V. G. Zakrzewski, S. Dapprich, A. D. Daniels, M. C. Strain, O. Farkas, D. K. Malick, A. D. Rabuck, K. Raghavachari, J. B. Foresman, J. V. Ortiz, Q. Cui, A. G. Baboul, S. Clifford, J. Cioslowski, B. B. Stefanov, G. Liu, A. Liashenko, P. Piskorz, I. Komaromi, R. L. Martin, D. J. Fox, T. Keith, M. A. Al-Laham, C. Y. Peng, A. Nanayakkara, M. Challacombe, P. M. W. Gill, B. Johnson, W. Chen, M. W. Wong, C. Gonzalez and J. A. Pople, Gaussian, Inc., Wallingford CT, 2004, vol. Revision E.01.

5. B. J. Lynch, P. L. Fast, M. Harris and D. G. Truhlar, *Journal of Physical Chemistry A*, 2000, **104**, 4811-4815.

6. P. Y. Ayala and H. B. Schlegel, *Journal of Chemical Physics*, 1997, **107**, 375-384.

7. C. Y. Peng, P. Y. Ayala, H. B. Schlegel and M. J. Frisch, *Journal of Computational Chemistry*, 1996, **17**, 49-56.

8. C. Y. Peng and H. B. Schlegel, *Israel Journal of Chemistry*, 1993, **33**, 449-454.

9. C. Gonzalez and H. B. Schlegel, *Journal of Chemical Physics*, 1989, **90**, 2154-2161.

10. C. Gonzalez and H. B. Schlegel, *Journal of Physical Chemistry*, 1990, **94**, 5523-5527.

11. R. Krishnan, J. S. Binkley, R. Seeger and J. A. Pople, *Journal of Chemical Physics*, 1980, **72**, 650-654.

12. T. L. Nguyen, R. Winterhalter, G. Moortgat, B. Kanawati, J. Peeters and L. Vereecken, *Physical Chemistry Chemical Physics*, 2009, **11**, 4173-4183.

13. R. Dennington, T. Keith and J. M. Millam, Shawnee Mission, KS, 2009, vol. Version 5.

14. D. Zhang and R. Y. Zhang, *Journal of the American Chemical Society*, 2002, **124**, 2692-2703.

15. D. Zhang and R. Zhang, *Journal of Chemical Physics*, 2005, **122**.

16. S. Ayadi and M. Abderrabba, *Canadian Journal of Chemistry-Revue Canadienne De Chimie*, 2011, **89**, 703-708.

17. F. Herrmann, R. Winterhalter, G. K. Moortgat and J. Williams, *Atmospheric Environment*, 2010, **44**, 3458-3464.

18. Y. Ma and G. Marston, *Physical Chemistry Chemical Physics*, 2009, **11**, 4198-4209.

19. J. C. Harrison and J. R. Wells, *Atmospheric Environment*, 2013, **80**, 524-532.

20. R. Atkinson and J. Arey, *Chemical Reviews*, 2003, **103**, 4605-4638.

21. D. J. Stewart, S. H. Almabrok, J. P. Lockhart, O. M. Mohamed, D. R. Nutt, C. Pfrang and G. Marston, *Atmospheric Environment*, 2013, **70**, 227-235.

22. S. Koch, R. Winterhalter, E. Uherek, A. Kolloff, P. Neeb and G. K. Moortgat, *Atmospheric Environment*, 2000, **34**, 4031-4042.

23. H. Hakola, J. Arey, S. M. Aschmann and R. Atkinson, *Journal of Atmospheric Chemistry*, 1994, **18**, 75-102.

24. R. Gutbrod, E. Kraka, R. N. Schindler and D. Cremer, *Journal of the American Chemical Society*, 1997, **119**, 7330-7342.

25. D. Cremer, E. Kraka, M. L. McKee and T. P. Radhakrishnan, *Chemical Physics Letters*, 1991, **187**, 491-493.

26. D. Cremer, J. Gauss, E. Kraka, J. F. Stanton and R. J. Bartlett, *Chemical Physics Letters*, 1993, **209**, 547-556.

27. D. Cremer, *Journal of Chemical Physics*, 1979, **70**, 1911-1927.

28. P. Aplincourt and M. F. Ruiz-Lopez, *Journal of the American Chemical Society*, 2000, **122**, 8990-8997.

29. T. L. Nguyen, J. Peeters and L. Vereecken, *Physical Chemistry Chemical Physics*, 2009, **11**, 5643-5656.

30. Y. Zhao, R. X. Zhang, X. M. Sun, M. X. He, H. Wang, Q. Z. Zhang and M. Y. Ru, *Journal of Molecular Structure:THEOCHEM*, 2010, **947**, 68-75.

31. Y. Zhao, R. X. Zhang, H. Wang, M. X. He, X. M. Sun, Q. Z. Zhang, W. X. Wang and M. Y. Ru, *Journal of Molecular Structure:THEOCHEM*, 2010, **942**, 32-37.

32. M. S. Stark, *Journal of the American Chemical Society*, 2000, **122**, 4162-4170.

33. I. R. Slagle, Q. Feng and D. Gutman, *Journal of Physical Chemistry*, 1984, **88**, 3648-3653.

34. C. A. Morgan, M. J. Pilling, J. M. Tulloch, R. P. Ruiz and K. D. Bayes, *Journal of the Chemical Society-Faraday Transactions Ii*, 1982, **78**, 1323-1330.

35. J. W. Bozzelli and J. Lee, *Abstracts of Papers of the American Chemical Society*, 2004, **227**, U1100-U1100.

36. P. D. Lightfoot, R. Lesclaux and B. Veyret, *Journal of Physical Chemistry*, 1990, **94**, 700-707.

Future Direction

In future this thesis could be expanded by firstly completing the 64 m White type cell, including the internal mirror systems used to manipulate the radiation into and out of the cell. This cell, in conjunction with infrared spectroscopy, mass spectrometry and BTEM analysis, could then be utilised to examine the ozonolysis reaction of terpinolene, as well as other terpenes. Not only could ozonolysis of other terpenes be observed, but oxidation products of terpinolene (and other terpenes) could be monitored with OH radicals and NO_3 radicals.

There are many avenues of the theoretical examination of terpinolene ozonolysis that could be explored. The proposed defect in the B3LYP functional, when describing the addition of RO_2 radicals, could be explored as the negative activation energies obtained in this thesis, were not expected. The MPW1K functional also requires further exploration. The literature review in Chapter 3 suggest that MPW1K is a good alternative to B3LYP for locating transition states; however, in this thesis the MPW1K functional failed to locate a number of transition state structures. The supposedly ineffective B3LYP functional, does however locate all the transition states for the reaction processes discussed in this thesis.